IODINE, BROMINE, AND CHLORINE IN THE ARCTIC ATMOSPHERE – EMISSION RATES, SOURCES, AND IMPACTS

by

Angela R. W. Raso

A Dissertation

Submitted to the Faculty of Purdue University

In Partial Fulfillment of the Requirements for the degree of

Doctor of Philosophy

Department of Chemistry

West Lafayette, Indiana

December 2018

THE PURDUE UNIVERSITY GRADUATE SCHOOL
STATEMENT OF COMMITTEE APPROVAL

Dr. Paul B. Shepson, Chair

Department of Chemistry

Department of Earth, Atmospheric, and Planetary Sciences

Purdue Climate Change Research Center

Dr. Kerri A. Pratt

Department of Chemistry, University of Michigan

Department of Earth & Environmental Sciences, University of Michigan

Dr. Scott A. McLuckey

Department of Chemistry

Dr. Timothy R. Filley

Department of Earth, Atmospheric, and Planetary Sciences

Department of Agronomy

Approved by:

Dr. Christine Hrycyna

Head of the Graduate Program

To Sam, for making this possible.

ACKNOWLEDGMENTS

I would like to acknowledge, and thank from the bottom of my heart, all the layers of support that I've had throughout my work. The Purdue support staff who knew what I needed almost before I did, especially the Jonathan Amy Facility for Chemical Instrumentation, without which this dissertation would have been innumerably more difficult. I want to thank Polar Field Services, and UIC Science for being prepared to fight off a bear, even though they never had to, or a rabid fox, which they did have to, as well as NEON for helping me develop my problem-solving skills in the field.

Of course, none of this would have been possible without our collaborators in the field. My Advisors Kerri and Shep, who helped when I was confused, counseled when I was conflicted, and above all advised my scientific development. Jose Fuentes, who showed patience in explaining micrometeorology to me. Kyle Custard & Sham Thanekar who suffered me in the Arctic, and Stephen McNamara who flew up on short notice to be my relief.

I would also like to thank my family, for inspiring me to continue my education, and my mother for teaching how to be a strong woman. And my pets, past and present, for their unconditional love and support. Finally, I need to thank my husband, who started this all as a boyfriend tagging along with me and has now wound up a life partner, just as excited about my research as I am, even if he doesn't fully understand it after proofreading too many drafts of too many papers.

TABLE OF CONTENTS

LIST OF TABLES

LIST OF FIGURES

ABSTRACT

Author: Raso, Angela, Rose Watson. PhD
Institution: Purdue University
Degree Received: December 2018
Title: Iodine, Bromine, and Chlorine – Emission Rates and Sources
Committee Chair: Paul B. Shepson

Halogen chemistry in the Arctic boundary layer catalytically destroys O_3 and impacts the chemical lifetimes of hydrocarbons, the HO_x-NO_x cycle, and atmospheric mercury. While many advances have been made in the last several decades in understanding the sources, sinks, and recycling pathways of halogens in the Arctic there are still many unknowns. Previous studies have shown that Br_2, BrCl and Cl_2 are produced photochemically in the Arctic tundra snowpack, but the magnitude of this production is still poorly understood. Additionally, while there have been suggestions that the tundra snowpack should also produce I_2, there have been no previous measurements of I_2 in the Arctic. The lack of measurements of the halogen production capacity of Arctic snowpacks has left the community to rely on one-dimensional modeling to estimate the impact of snowpack-derived halogen chemistry on the Arctic atmosphere. Because modeling is inherently dependent on understanding recycling mechanisms, mixing processes, and sinks this leaves the effect of halogens on atmospheric chemistry in the Arctic highly uncertain.

This work describes efforts to address these uncertainties through measurements made during two field campaigns in Utqiaġvik (formerly Barrow), Alaska in January – February 2014, and February – May 2016. The first measurements of I_2 in the Arctic, both in the snowpack interstitial air, and in the air above the snowpack demonstrate that iodine chemistry is active in the Arctic atmosphere, and that I_2 is produced photochemically in the tundra snowpack. The effects of active iodine chemistry on both O_3 and bromine chemistry is examined through zero- and one-

dimensional modeling. The first speciated measurements of snowpack phase iodine reveal that much like previous reports of iodine enriched aerosols, the Arctic snowpack is highly enriched in iodine. Vertical profiles of I^- in the snowpack suggest that there is a consistent, non-radiation dependent source of iodine to the Arctic environment. It seems likely that this source is transport of iodine-enriched aerosols from the mid-latitudes. However, unlike the Antarctic, and previous observations in the mid-latitudes, most Arctic snowpack phase iodine is inorganic, which may contradict transport from the mid-latitudes as a source. One-dimensional modeling was also utilized, in conjunction with the first vertical profile measurements of Br_2 and Cl_2 between 1 and 7 m above the snowpack surface to examine the community's understanding of recycling mechanisms, mixing, sources, and sinks of halogens in the Arctic Atmosphere.

CHAPTER 1. INTRODUCTION

1.1 The Atmospheric Boundary Layer

Gasses are confined near the surface of the earth by gravity, forming the atmosphere, with the highest density, or pressure, closest to the earth. Pressure (density) decreases exponentially with height, as per the hydrostatic Equation (Equation 1.1).

$$P_z = P_0 e^{-\frac{M*g*z}{R*T}} \quad \text{E1.1}$$

Here P_z is the pressure at height z, P_0 is the pressure at the surface, M is the molar mass of air, g is the gravitational constant, z is the height above the surface, R is the gas constant, and T is the temperature. The part of the atmosphere that is heavily influenced by the earth's surface is the known as the atmospheric (or planetary) boundary layer [Stull, 1988]. It is generally accepted that the boundary layer is the region that responds to the surface of the earth within the timescale of about an hour or less [Stull, 1988; Kaimal and Finnigan, 1994], but this region is practically defined using the change in temperature with height (Figure 1.1). During the daytime, the sun warms the earth, and air in contact with the surface is warmed and humidified. Because warm air and water vapor are less dense than cold, dry air, surface warming and humidification causes air to rise. As an air parcel rises it experiences lower pressure, expands, and cools. Air rises and cools to the point where it is saturated with water vapor. At some height any more rising (and thus cooling) will cause water vapor to condense, forming clouds. Condensation is exothermic, and the heat released from water condensing induces a local increase in temperature. When this occurs, the atmospheric temperature increases with height rather than decreases with height, which is an inversion layer. The inversion layer caps the top of the boundary layer and is stable against vertical mixing, effectively holding relatively short-lived gasses that are emitted at the earth's surface

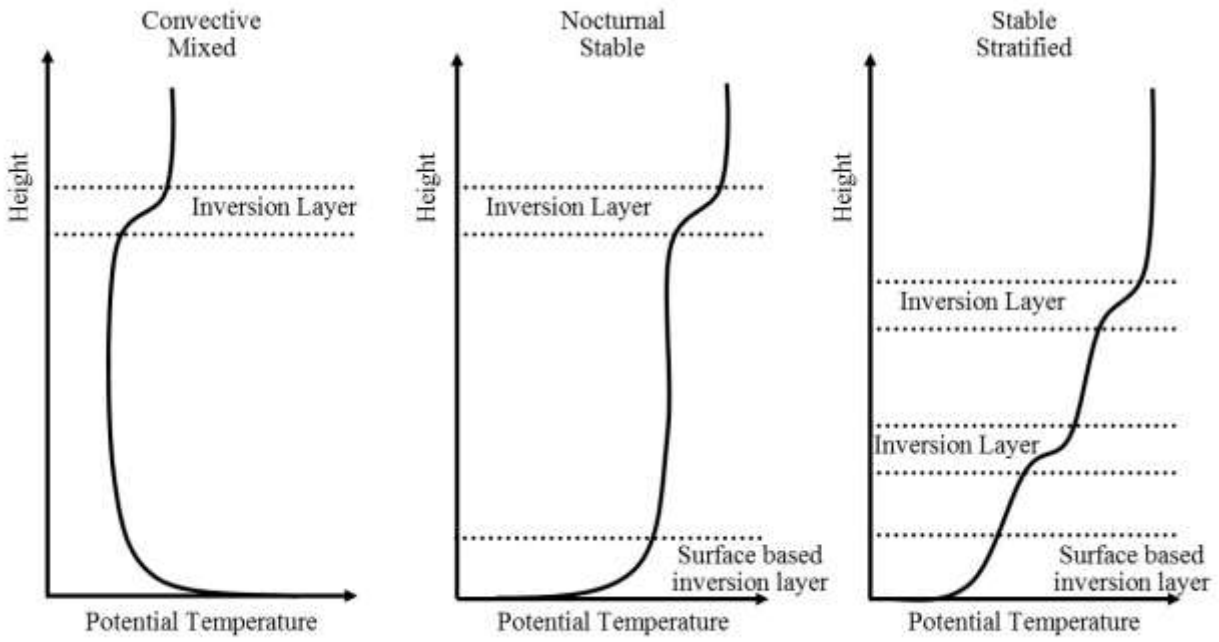

Figure 1.1 Idealized potential temperature profiles for the convective (mixed) boundary layer, the stable nocturnal boundary layer, and the long-lived stable stratified boundary layer. Adapted from Stull [1988], Kaimal and Finnegan [1994], and Anderson and Neff [2008].

within the boundary layer. The process of convective mixing defines the mixed (or convective) boundary layer [Stull, 1988].

At night, a stable nocturnal boundary layer forms when the ground cools faster than the air above it, and air in contact with the surface is colder than the air above. This leads to a surface-based inversion layer and a lack of convective mixing (Figure 1.1 middle panel). When the boundary layer collapses at night it often leaves behind a residual layer, which is decoupled from the surface but still trapped by a temperature inversion. The composition of the residual layer is generally the same as the mixed layer at sunset. In the morning when the ground begins to heat from the sun again, the residual layer and the stable surface layer re-mix to make a mixed boundary layer. Convective mixing is dependent on the earth's surface warming the air above, and thus the nature of the earth's surface can have a substantial effect on the state of the boundary layer. Over

snow-covered ground there is minimal convective mixing because the surface is often colder than the air above. Because of the cold surface, the polar boundary layer is stable as a rule, rather than an exception, even during the daytime [Anderson and Neff, 2008]. The long-term stable boundary layer has a surface-based inversion and temperatures generally rise with height, maintaining stability. This stability can be punctuated by several inversion layers, effectively stratifying the boundary layer.

The stable boundary layer limits the vertical mixing of gasses, both trapping gasses emitted near the surface, and limiting losses of gasses to the surface. Characterization of mixing and understanding the height of the stable and sometimes stratified polar boundary layer is difficult [Andreas, 2002; Grachev et al., 2007; Anderson and Neff, 2008; Mazzola et al., 2016]. Atmospheric mixing models have been parameterized primarily for the convective mixed layer, and rely on Monin - Obukhov similarity theory, which assumes that turbulent flow in the surface layer (the bottom 1/10 of the boundary layer) is homogeneous and fully developed [Kaimal and Finnigan, 1994]. The assumption of stationary turbulent flow in the surface layer is frequently violated when turbulence is intermittent, or when stable stratification occurs and layers of air become decoupled from the surface [Mahrt, 1999]. The community's lack of an ability to model the stable boundary layer poses an ongoing problem with understanding the concentration gradients of species emitted from the surface and confined by a stable boundary layer.

1.2 Chemical Composition of the Boundary Layer

Within the boundary layer concentrations of reactive gasses are controlled by the rates at which they are produced, the rates that they are removed, the volume through which they mix, and the rate of that mixing. Considering the removal of a species X to have the first order rate k, and

assuming that the concentration is not changing significantly with time, then the production and removal terms must be equal (Equation 1.2)

$$k[X] = \frac{F_x}{z} \quad \text{E1.2}$$

Where z is the height over which the species mixes, and F_x is the rate at which the species is introduced into the atmosphere (the flux). Rearranging we can see that the concentration of a species in the atmosphere is directly proportional to its emission (or production) rate (F_x) and its atmospheric lifetime ($\tau = 1/k$), and inversely proportional to the height over which it mixes (z).

$$[X] = \frac{F_x}{z} * \tau \quad \text{E1.3}$$

Sources of gasses to the atmosphere are either human (anthropogenic), biological (biogenic), or geological (geogenic). Removal pathways for gasses – often referred to as sinks – can be chemical or physical. Physical removal takes the form of deposition, either through precipitation (wet deposition) or through adsorption to surfaces (dry deposition). Wet deposition and dry deposition are both highly dependent on chemical structure through water solubility and the adsorptivity of the species to the surface respectively. Chemical properties, such as polarity and hydrogen bonding control the water solubility and absorptivity of compounds, therefore understanding the chemistry that alters the state of pollutants in the atmosphere is very important to understanding the sinks of trace gasses in the atmosphere and their atmospheric lifetime.

Neglecting water content, the atmosphere is composed of 78.08% molecular nitrogen (N_2), 20.95% molecular oxygen (O_2), and 0.93% argon (Ar) by volume [Finlayson-Pitts and Pitts, 2000]. Argon, being a noble gas, is almost wholly chemically unreactive. N_2 is almost as unreactive as argon. However, under both natural high heat, such as lightning strikes (<5% of total emissions), and man-made high heat, such as fossil fuel combustion (>95% of total emissions) [Finlayson-

Pitts and Pitts, 2000], N_2 and O_2 can react to form nitric oxide ($NO^{\cdot}$, reaction 1.1, $k = 1.47\ x\ 10^{13}\ T^{0.3}\ e^{-75286.81/RT}$ $cm^3\ mol^{-1}\ s^{-1}$ [Hewson and Bollig, 1996]).

$$N_2 + O_2 \xrightarrow{\Delta} 2\ NO^{\cdot} \qquad \text{R1.1}$$

In the presence of O_3, $NO^{\cdot}$ is in rapid equilibrium with $NO_2^{\cdot}$. Together $NO^{\cdot}$ and $NO_2^{\cdot}$ are collectively referred to as NO_x. $NO_2^{\cdot}$ can react with sunlight (photolysis) to form $NO^{\cdot}$ and a ground state triplet oxygen atom ($O(^3P)$) (reaction 1.2 J= $1.04x10^{-2}$ s^{-1} at a solar zenith angle of 17.5°), which can then react with O_2 to form ozone (O_3) (reaction 1.3, k =$7.22x10^{-11}$ cm^3 $molecule^{-1}$ s^{-1} at 1 atm [Burkholder et al., 2015]). O_3 can then further photolyze to form an excited state singlet oxygen atom ($O(^1D)$) (reaction 1.4, J= $4.24x10^{-5}$ s^{-1} at a solar zenith angle of 17.5°). $O(^1D)$ relaxes rapidly upon collision with N_2 to $O(^3P)$ (reaction 1.5 k = $6.1x10^8$ s^{-1} at room temperature and pressure [Burkholder et al., 2015]) but can also react with water to form the hydroxyl radical ($OH^{\cdot}$) (reaction 1.6 k = $2x10^{-10}$ cm^3 $molecule^{-1}$ s^{-1} [Burkholder et al., 2015]).

$$NO_2^{\cdot} \xrightarrow{h\nu} NO^{\cdot} + O(^3P) \qquad \text{R1.2}$$

$$O(^3P) + O_2 \xrightarrow{M} O_3 \qquad \text{R1.3}$$

$$O_3 \xrightarrow{h\nu\ (\lambda<340nm)} O_2 + O(^1D) \qquad \text{R1.4}$$

$$O(^1D) \xrightarrow{N_2} O(^3P) \qquad \text{R1.5}$$

$$O(^1D) + H_2O \rightarrow 2\ OH^{\cdot} \qquad \text{R1.6}$$

$OH^{\cdot}$ is the primary oxidant in the atmosphere [Thompson, 1992], acting as a detergent to clean the atmosphere. $OH^{\cdot}$ cleans the atmosphere via oxidation of pollutants, including volatile organic compounds (VOCs), which are mainly emitted from biogenic activity [Guenther et al., 1995].

Oxidation of VOCs forms more water soluble, surface reactive species and is the chemical process that allows for their ultimate removal from the atmosphere [Thompson, 1992].

However, in the presence of $NO^{\cdot}$, each hydrocarbon (RH) that is oxidized produces two O_3 molecules, through the oxidation of $NO^{\cdot}$ to $NO_2^{\cdot}$ (via reactions 1.7-1.10), followed by reactions 1.2-1.3.

$$OH^{\cdot} + RH + O_2 \rightarrow H_2O + RO_2^{\cdot} \quad \text{R1.7}$$

$$RO_2^{\cdot} + NO^{\cdot} \rightarrow NO_2^{\cdot} + RO^{\cdot} \quad \text{R1.8}$$

$$RO^{\cdot} + O_2 \rightarrow HO_2^{\cdot} + carbonyl\ compound \quad \text{R1.9}$$

$$HO_2^{\cdot} + NO^{\cdot} \rightarrow NO_2^{\cdot} + OH^{\cdot} \quad \text{R1.10}$$

$$Net: RH + 2\,O_2 + 2\,NO^{\cdot} \rightarrow H_2O + carbonyl\ compound + 2\,NO_2 \quad \text{R1.11}$$

The formation of O_3 and the subsequent oxidation reactions are highly dependent on light and temperature. In urban environments, large O_3 concentrations can be produced [Molina et al., 2010]. Under most conditions, the production of O_3 is limited by NO_x [Lin et al., 1988; Thompson, 1992]. High O_3 concentrations can be detrimental to human and plant health, and the US has successfully reduced O_3 concentrations in cities through the regulation of NO_x production [Simon et al., 2015]. However, small concentrations of O_3 are necessary for the removal of pollutants from the atmosphere.

1.3 Chemical Composition and Phenomena of the Arctic Atmosphere

The Arctic, which is a mostly ice-covered ocean surrounded by the continents of the northern hemisphere, is a unique environment with a unique atmosphere. Unlike the mid-latitudes, it is cold, the atmosphere is very dry, it is completely dark during the winter, and it is mostly uninhabited. It the most similar to the Antarctic, which is also cold, dry, seasonally dark, and

sparsely inhabited. However, unlike the Antarctic, which is a continent surrounded by ocean, the Arctic is an ice-covered ocean surrounded by industrialized continents that contribute large amounts of transported gaseous and particulate pollution [Barrie et al., 1989; Worthy et al., 1994]. Because the Arctic is covered in snow and ice with a sTable sometimes stratified boundary layer, there is very little convective mixing, and the boundary layer is often very shallow (100-300 m) [Brost and Wyngaard, 1978; Kaimal and Finnigan, 1994]. This can isolate species near the surface where they are emitted. The cold dark atmosphere can also slow the chemical transformation and deposition of pollutants in the Arctic. The Arctic atmosphere thus accumulates anthropogenic emissions, which are transported from Eurasia throughout the winter [Rahn and Borys, 1977; Macdonald et al., 2000; Quinn et al., 2007], and is primed for rapid changes in the springtime when the sun rises. Arctic haze, first characterized in modern scientific literature in 1957 [Schnell, 1984], is a smog-like phenomenon where aerosols form in the springtime significantly reducing visibility. It is caused mostly by the oxidation of gas-phase sulfur dioxide (SO_2) to particle phase sulfate (SO_4^{2-}) [Worthy et al., 1994], and appears when photochemical oxidation begins in the springtime [Quinn et al., 2009]. Observations of Arctic haze lead to increased interest in the phenomenon of the Arctic atmosphere.

In 1986 Oltmans and Komhyr [1986] and Bottenheim et al. [1986] reported intriguing observations in Barrow (now Utqiaġvik), Alaska (71°N), and Alert, Northwest Territories, Canada (82.5°N) respectively. In contrast to the relatively long lifetime (1-2 weeks) of tropospheric O_3 in most of the lower troposphere, the concentrations of O_3 in the Arctic occasionally plummet from background concentrations (30 to 40 ppb) to near 0 ppb during the springtime after sunrise. More than ten years later Schroeder et al. [1998] observed that total gaseous mercury (TGM), which usually has a lifetime of >6 months [Steffen et al., 2015], rapidly depleted along with O_3 in the

spring (Figure 1.2). Schroeder et al. [1998] also showed that TGM and O_3 concentrations in the springtime were highly correlated (Figure 1.2, inset), suggesting a similar mechanism for both depletions. Figure 1.2 shows TGM, air temperature, and O_3 concentrations at Alert, Canada for the 1995 calendar year. Depletion events can be observed during the springtime (March-May), identifiable by the variability of the observations during this period. When depletion events occur, O_3 is rapidly reduced to O_2, and mercury is rapidly oxidized from gaseous elemental mercury (GEM) to reactive gaseous mercury (RGM) [Schroeder et al., 1998; Steffen et al., 2008]. RGM can then be removed from the atmosphere via deposition, potentially entering the Arctic biosphere [Skov et al., 2004]. The depletion of O_3 affects the oxidative capacity of the atmosphere reducting its ability to oxidize and remove pollutants. Atmospheric mercury depletion events and ozone depletion events (ODEs) are among the most interesting phenomenon that has been observed only in polar environments because they are unexpected, and we still lack the ability to predict them.

Reactive halogen chemistry started gaining interest with the suggestion of Molina and Rowland [1974] that commercial chlorofluorocarbons (CFCs), such as Freon-12 (e.g., CFC-12, CF_2Cl_2), could catalytically destroy stratospheric O_3 (reactions 1.12-1.14).

$$CF_2Cl_2 \xrightarrow{h\nu\ (\lambda=175-220\ nm)} CF_2Cl^{\cdot} + Cl^{\cdot} \qquad \text{R1.12}$$

$$Cl^{\cdot} + O_3 \rightarrow ClO^{\cdot} + O_2 \qquad \text{R1.13}$$

$$ClO^{\cdot} + O \rightarrow Cl^{\cdot} + O_2 \qquad \text{R1.14}$$

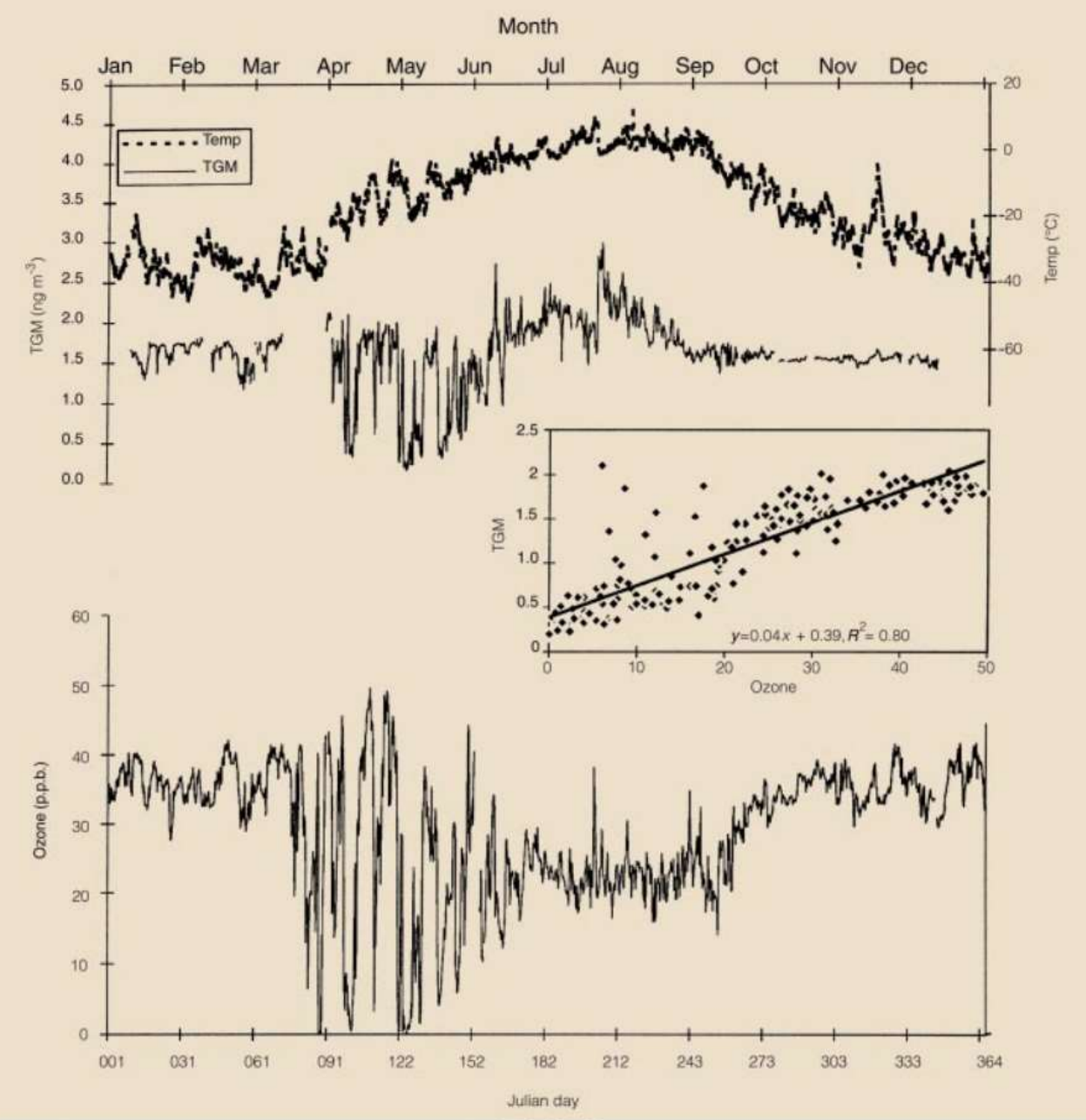

Figure 1.2 Time series of air temperature and total gaseous mercury (TGM) (top panel), and O_3 (bottom panel) during 1995 at Alert, Canada. The middle inset shows the correlation between total gaseous mercury and O_3 concentrations for the period from April 09, 1995, to May 29, 1995. Reproduced from Schroeder et al. [1998].

The initiation step, the photolysis of the CFC (reaction 1.12), requires light in the far ultraviolet, which does not reach the surface of the earth, so CFCs do not photolyze in the lower atmosphere. However ultraviolet light is present in the stratosphere, and a small amount of CFC photolysis can lead to large amounts of O_3 destruction. Destruction of stratospheric O_3 was confirmed by observing a hole in the Antarctic ozone layer during the springtime [Farman et al., 1985] around the same time ODEs were first observed in the Arctic boundary layer [Bottenheim et al., 1986]. Barrie et al. [1988] observed a strong anti-correlation between filterable bromine (i.e. bromine containing fine aerosol) and O_3 during ODEs (Figure 1.3), and postulated that NO_x moderated bromine chemistry (shown in reactions 1.15 – 1.27 below) was responsible for O_3 destruction in the springtime Arctic.

$$CHBr_3 \xrightarrow{h\nu} Br^{\cdot} + CHBr_2^{\cdot} \quad \text{R1.15}$$

$$Br^{\cdot} + O_3 \rightarrow BrO^{\cdot} + O_2 \quad \text{R1.16}$$

$$BrO^{\cdot} + BrO^{\cdot} \rightarrow 2Br^{\cdot} + O_2 \quad \text{R1.17}$$

$$BrO^{\cdot} + NO^{\cdot} \rightarrow Br^{\cdot} + NO_2^{\cdot} \quad \text{R1.18}$$

$$BrO^{\cdot} \xrightarrow{h\nu} Br^{\cdot} + O(^3P) \quad \text{R1.19}$$

$$NO_2^{\cdot} \xrightarrow{h\nu} NO^{\cdot} + O(^3P) \quad \text{R1.2}$$

$$O(^3P) + O_2 \xrightarrow{M} O_3 \quad \text{R1.3}$$

$$NO^{\cdot} + O_3 \rightarrow NO_2^{\cdot} + O_2 \quad \text{R1.20}$$

$$BrO^{\cdot} + NO_2^{\cdot} \xrightarrow{M} BrONO_2 \quad \text{R1.21}$$

$$BrONO_2 \xrightarrow{h\nu} BrO^{\cdot} + NO_2^{\cdot} \quad \text{R1.22}$$

$$Br^{\cdot} + CH_2O \rightarrow HBr + CHO^{\cdot} \quad \text{R1.23}$$

$$Br^{\cdot} + HO_2^{\cdot} \rightarrow HBr + O_2 \quad \text{R1.24}$$

$$CH_2O \xrightarrow{h\nu} CO + H_2$$

$$\xrightarrow{h\nu} H^{\cdot} + CHO^{\cdot} \rightarrow 2HO_2^{\cdot} \quad \text{R1.25}$$

$$O_3 \xrightarrow{h\nu} O(^1D) \quad \text{R1.4}$$

$$O(^1D) + H_2O \rightarrow 2OH^{\cdot} \quad \text{R1.6}$$

$$HBr + OH^{\cdot} \rightarrow Br^{\cdot} + H_2O \quad \text{R1.26}$$

$$BrO^{\cdot} + HO_2^{\cdot} \rightarrow Br^{\cdot} + OH^{\cdot} \quad \text{R1.27}$$

Sturges and Barrie [Sturges and Barrie, 1988] reported in the same year that filterable bromine showed strong seasonal trends, peaking in the springtime (Figure 1.4). Given the halogen-induced depletion of O_3 in the Antarctic stratosphere, the correlation between filterable bromine and O_3 (Figure 1.3)[Barrie et al., 1988], and highly seasonal levels of filterable bromine in the Arctic (Figure 1.4) [Sturges and Barrie, 1988] understanding halogen chemistry in the Arctic seems particularly relevant to study of ODEs.

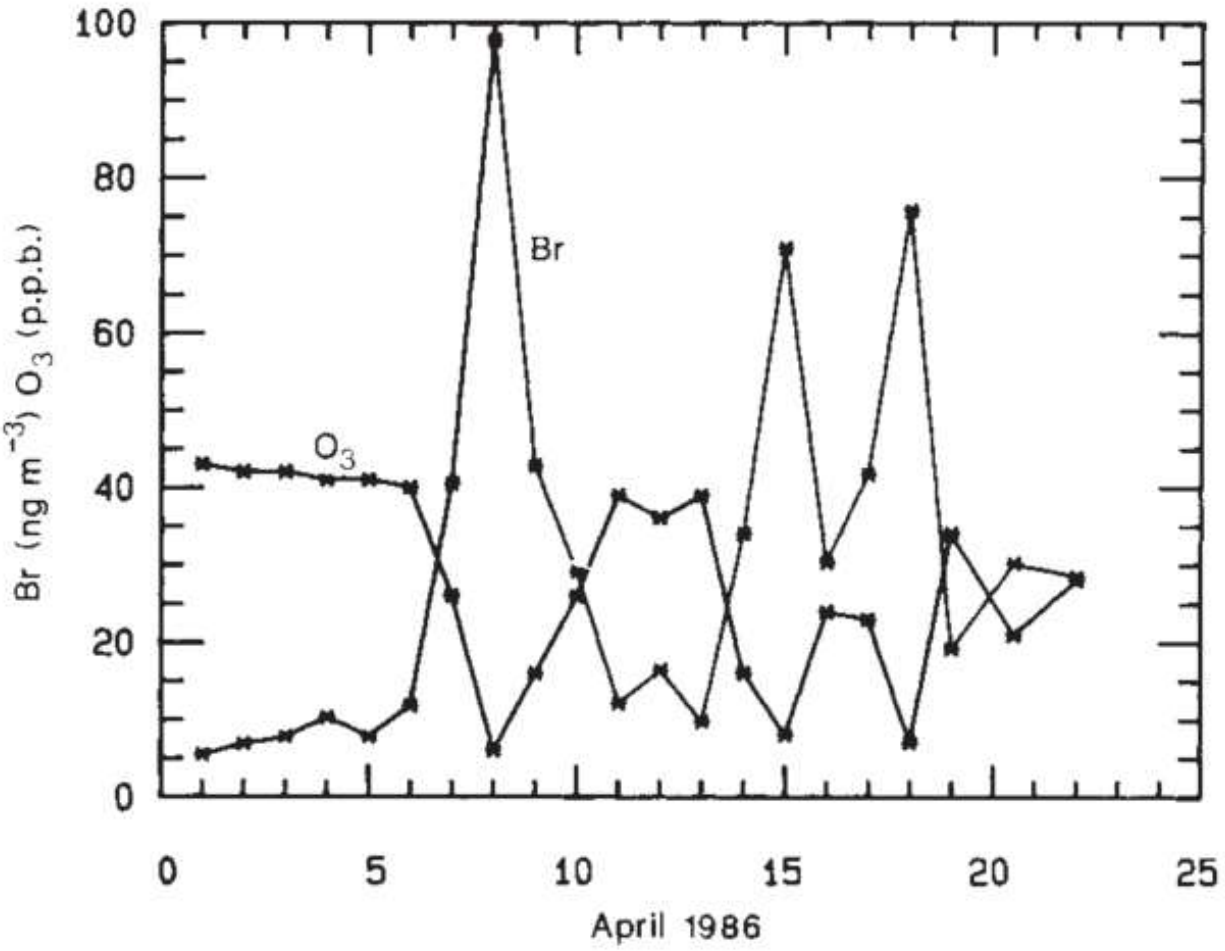

Figure 1.3 Correlation of filterable bromine and O_3 measured in April of 1986. Reproduced from Barrie et al. [1988]

Figure 1.4 The top panel shows enrichment of filterable bromine expressed as the ratio of measured bromine to expected bromine from both marine and combustion sources. The middle and bottom panel show enrichment of chlorine and iodine respectively expressed relative to the halogen / sodium ratio in seawater. Measurements were conducted at Alert, Canada. Note the logarithmic scale. Lines are placed on April 1 (approximate date for 24-hr sunlight) for each year. Reproduced from Sturges and Barrie [1988].

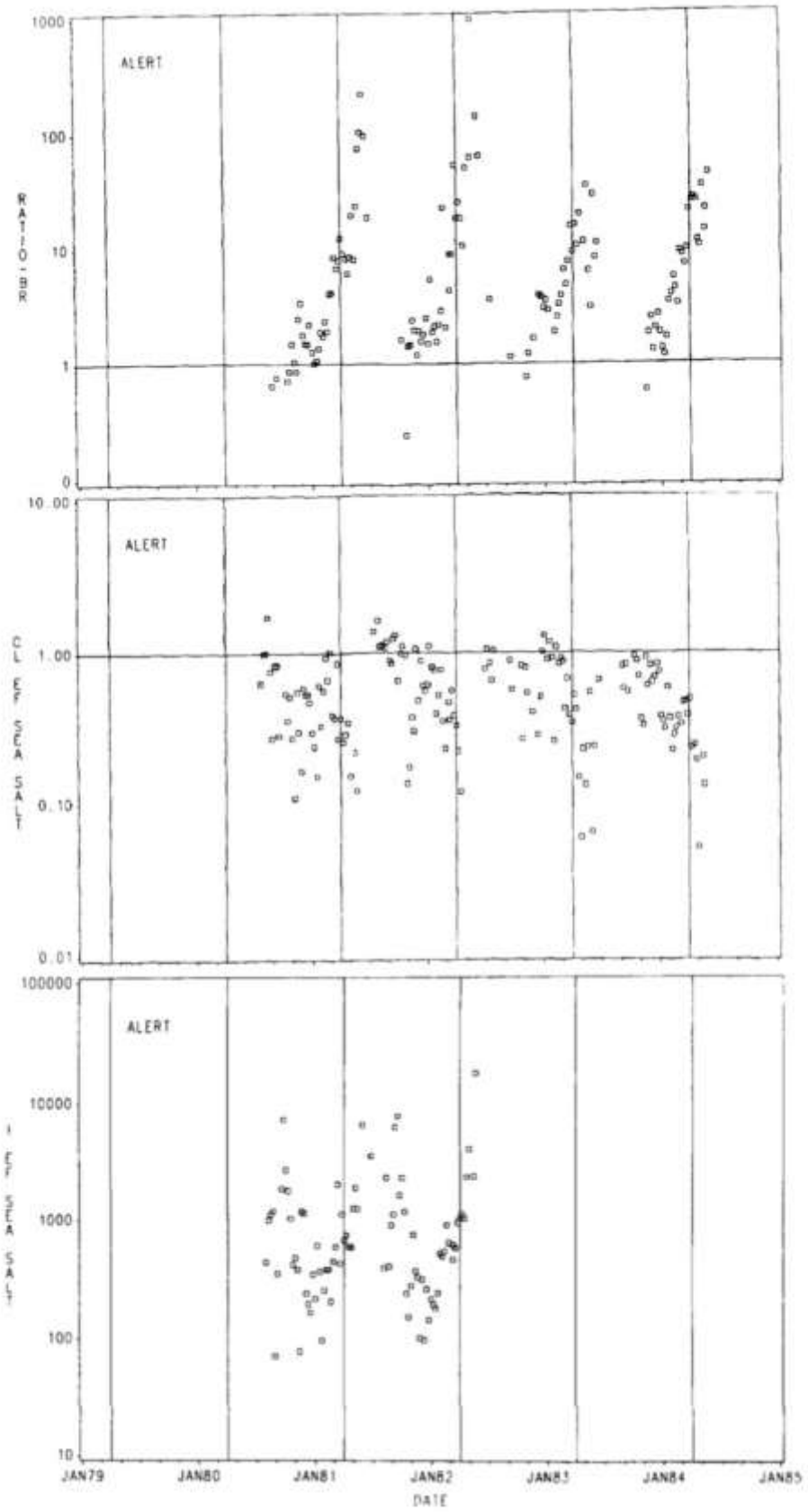
ALERT
RATIO1BR
1000
100
10
1
0
ALERT
CL ES UCA SAT
10.00
1.00
0.10
0.01
ALERT
100000
10000
1000
100
10
JAN79
JAN80
JAN81
JAN82
JAN83
JAN84
JAN85
DATE

1.4 Bromine Chemistry

Barrie et al. [1988] postulated that organobromine compounds, such as methyl bromide (CH_3Br) and bromoform ($CHBr_3$), were responsible for observations of enhanced filterable bromine. These species can be converted to filterable species, such as hydrobromic acid (HBr), via photochemical reactions, that begins with the photolysis of the organobromine compound to form a bromine atom (reaction 1.15).

$$CHBr_3 + hv \rightarrow Br^{\cdot} + CHBr_2^{\cdot} \qquad \text{R1.15}$$

However, organobromine concentrations are not high enough, and the photolysis lifetime is too long (~100 days) to explain the observed concentrations of filterable bromine, so another source is necessary [Barrie et al., 1988; McConnell et al., 1992]. This soon lead to speculation that inorganic bromine, specifically Br_2, may be the primary factor in O_3 depletion rather than organic bromine [Fan and Jacob, 1992; McConnell et al., 1992]. McConnell et al. [1992] and Fan and Jacob [1992] proposed that HOBr could oxidize bromide under acidic conditions in snow and aerosols, respectively (reaction 1.28).

$$HOBr + Br^-_{(aq)} + H^+_{(aq)} \rightarrow Br_2 + H_2O \qquad \text{R1.28}$$

Fan and Jacob [1992] also suggested that $BrONO_2$ could also oxidize bromide in aerosols, by first producing HOBr in the aerosol phase. However, it was later suggested that $BrONO_2$ could interact directly with halide containing surfaces to produce Br_2 (reaction 1.29) [Deiber et al., 2004].

$$BrONO_2 + Br^- \rightarrow Br_2 + NO_3^- \qquad \text{R1.29}$$

These reactions cause exponential growth of gas phase bromine due to autocatalytic liberation from bromide-containing surfaces, which effectively turns one gas phase bromine atom into two. The autocatalytic liberation of Br^- from snow and aerosols is often referred to as a 'bromine

explosion' [Barrie and Platt, 1997]. However, for these bromine explosion reactions to occur, gas phase bromine must already be present in the atmosphere.

The catalytic cycle for O_3 destruction by bromine atoms follows the form of a radical chain reaction. Initiation of the chain reaction occurs by photolysis of Br_2 (reaction 1.31) or another inorganic bromine species (reactions 1.32-1.34). Br_2 undergoes rapid photolysis (reaction 1.31) in the Arctic springtime with a photochemical lifetime of only 23 seconds at the end of March [Thompson et al., 2015]. Other inorganic bromine species (e.g., $BrONO_2$, $BrNO_2$, and HOBr) have much longer photolytic lifetimes than Br_2 (1.3 hours, 1.8 hours, and 7.2 minutes respectively [Thompson et al., 2015]).

Initiation:

$$Br_2 + hv \rightarrow 2\,Br^{\cdot} \qquad \text{R1.31}$$

$$BrONO_2 + hv \rightarrow Br^{\cdot} + NO_3^{\cdot} \qquad \text{R1.32}$$

$$BrNO_2 + hv \rightarrow Br^{\cdot} + NO_2^{\cdot} \qquad \text{R1.33}$$

$$HOBr + hv \rightarrow Br^{\cdot} + OH^{\cdot} \qquad \text{R1.34}$$

$BrONO_2$, $BrNO_2$, and HOBr are likely not sources of bromine to the atmosphere, but rather intermediately reactive species that are produced in the gas phase and can act as reservoirs of reactive bromine.

Propagation of the radical chain reaction is the stage that catalytically destroys O_3. First, a bromine atom reduces O_3 to O_2, producing bromine monoxide ($BrO^{\cdot}$) (reaction 1.16, k = $6.8\text{x}10^{-11}$ cm^3 $molecule^{-1}$ s^{-1} [Atkinson et al., 2007]). $BrO^{\cdot}$ can be converted back to a bromine atom through photolysis (reaction 1.19) with a lifetime of 33 seconds [Thompson et al., 2015], or by reacting with $NO^{\cdot}$ to form $NO_2^{\cdot}$ (reaction 1.18, k = $2.1\text{x}10^{-11}$ cm^3 $molecule^{-1}$ s^{-1} [Atkinson et

al., 2007]). However, both pathways tend to be null, reproducing O_3 through reactions 1.2 and 1.3. The catalytic cycle primarily occurs through the self-reaction of $BrO^{\cdot}$ (reaction 1.17, k = $9.3x10^{-13}$ $cm^3molec^{-1}s^{-1}$ [Sander et al., 2006]), which reproduces bromine atoms.

Propagation:

$$Br^{\cdot} + O_3 \rightarrow BrO^{\cdot} + O_2 \quad \text{R1.16}$$

$$BrO^{\cdot} \xrightarrow{h\nu} Br^{\cdot} + O(^3P) \quad \text{R1.19}$$

$$BrO^{\cdot} + NO^{\cdot} \rightarrow Br^{\cdot} + NO_2^{\cdot} \quad \text{R1.18}$$

$$BrO^{\cdot} + BrO^{\cdot} \rightarrow 2Br^{\cdot} + O_2 \quad \text{R1.17}$$

The net effect of a cycle through reactions 1.16 and 1.17 is the reduction of two O_3 molecules to three O_2 molecules. However, modeling has suggested that the chain reaction isn't very efficient, with an average radical chain length (the number of times that the radical cycle is completed before a termination reaction occurs) for bromine atoms in the Arctic of only 0.85-1.79 [Thompson et al., 2017]. This suggests that the rapid destruction of O_3 requires efficient recycling of reactive bromine back to Br_2, which can rapidly reinitiate the chain reaction.

Termination of the bromine chain reaction occurs when bromine atoms or $BrO^{\cdot}$ reacts to form a non-radical bromine species. In some cases, this will form a reservoir species (reactions 1.21, 1.35, 1.27), that can then reinitiate the chain reaction (reactions 1.32-1.34). When bromine abstracts a hydrogen atom from an aldehyde (reaction 1.36) HBr is formed.

Termination:

$$BrO^{\cdot} + NO_2^{\cdot} \rightarrow BrONO_2 \quad \text{R1.21}$$

$$Br^{\cdot} + NO_2^{\cdot} \rightarrow BrNO_2 \quad \text{R1.35}$$

$$BrO^{\cdot} + HO_2 \rightarrow HOBr + OH^{\cdot} \quad \text{R1.27}$$

$$Br^{\cdot} + aldehyde \rightarrow HBr + R^{\cdot} \quad \text{R1.36}$$

HBr is much more stable than the other termination products, and its main sink is uptake to the aerosol phase, where it is effectively lost from the atmosphere by dry deposition unless reactivated by an oxidation pathway.

Before the implementation of portable or semiportable mass spectrometers, measurements of various forms of total inorganic bromine were common. Barrie et al. [1994], utilized a denuder and filter combination system to determine the relative amounts of gas and particle phase inorganic bromine. Impey et al. [1997] measured total photolyzable bromine (most likely a weighted sum of Br_2, $BrONO_2$, $BrNO_2$, and HOBr) by utilizing a Xe arc lamp in a flow cell to convert bromine species to bromine atoms. The bromine atoms were then mixed with propene to form sTable bromoketones. Bromoketones were then detected using gas chromatography with electron capture detection (GC-ECD). The first species-specific gas phase inorganic bromine measurement was reported by Hausmann and Platt [1994], who measured $BrO^{\cdot}$ using long path differential adsorption spectroscopy (LP-DOAS), and found that $BrO^{\cdot}$ concentrations alone did not account for the rapidity of ozone depletion. This finding suggested that advection of air masses and atmospheric dispersion were also required to explain ODEs. However averaging times for the first DOAS $BrO^{\cdot}$ measurements were long (sometimes up to 24 hours), and it is likely that peaks in $BrO^{\cdot}$ were averaged out. The implementation of mass spectrometry techniques for the measurement of Br_2 and BrCl increased measurement frequency and showed that Br_2 increases throughout the Arctic spring [Foster et al., 2001], and tends to peak when ozone depletion occurs (Figure 1.5) [Spicer et al., 2002].

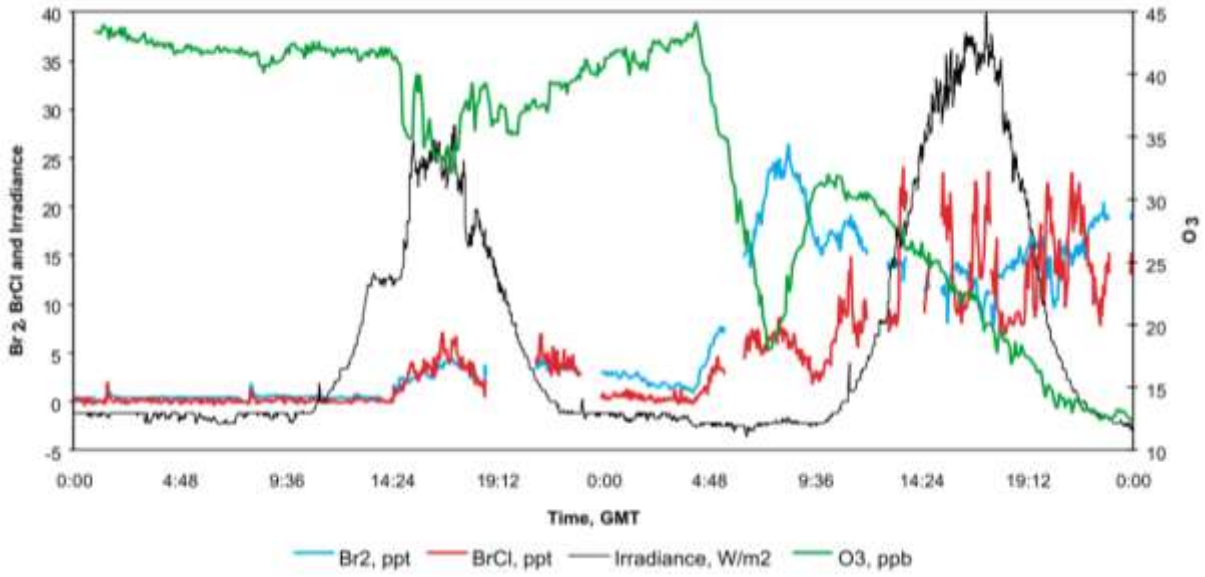

Figure 1.5 Br_2 (blue), BrCl (red), irradiance (black), and O_3 (green) on March 10-11, 2000 in Alert Canada. Reproduced from Spicer et al. [2002].

Ten years later, with the development of a compact high sensitivity chemical ionization mass spectrometer, Liao et al. [2012] reported direct measurements of inorganic bromine species (Br_2, $BrO^{\cdot}$, and HOBr) at Utqiaġvik, Alaska, which they further validated by comparison with DOAS measurements [Liao et al., 2011]. These measurements allowed for an understanding of the diurnal evolution of bromine species (Figure 1.6). Daytime correlations between HOBr and $BrO^{\cdot}$ with O_3 are difficult to interpret since rapid conversion between species occur. Br_2 and O_3 showed a strong anticorrelation [Liao et al., 2011] at night when bromine is present almost entirely as Br_2 (as shown in Figure 1.6).

While there is a consensus that Br_2 is the main bromine species that is emitted to the Arctic atmosphere [Simpson et al., 2015], the substrate that produces Br_2 has been a matter of some debate. Total bromine (the sum of bromine species in both the gas and aerosol phase) increases during ODEs suggesting that bromine is activated from a source that is inactive at other times [Barrie et

al., 1994; Li et al., 1994]. Ice surfaces such as sea ice, frost flowers, coastal snow, wind lofted snow, and snow above sea ice, along with sea salt aerosols, have been the main suggestions for halogen activation substrates. In 1999 a major discovery was made that changed the pursuit of understanding of bromine recycling – that some species, including formaldehyde [Sumner and Shepson, 1999], and NO_x [Honrath et al., 1999], are photochemically produced in the sunlit snowpack. Peterson and Honrath [2001] reported that O_3 in the Arctic snowpack interstitial air shows a diurnal trend, and is ~1/2 of the O_3 concentration above the snowpack (Figure 1.7), suggesting that O_3 is destroyed within the snowpack during the daytime. Br_2 is present at much higher concentrations within the snowpack interstitial air than above the snow [Foster et al., 2001] (Figure 1.8). Together these observations suggest that Br_2 is photochemically produced by the snowpack and is responsible for O_3 destruction in the snowpack interstitial air.

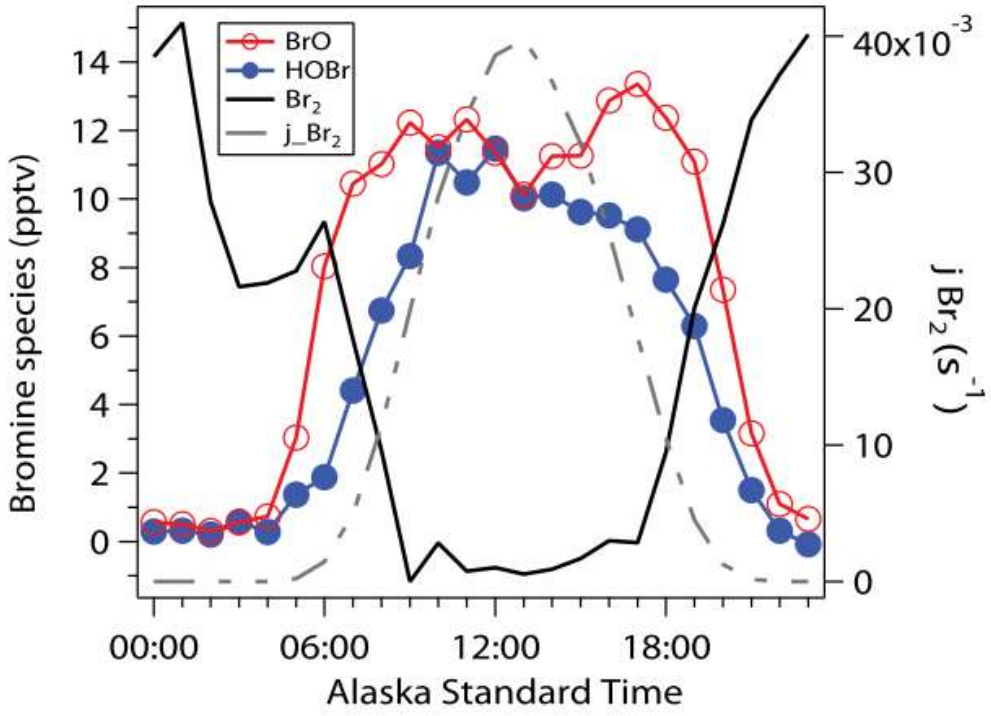

Figure 1.6 Diurnal average evolution of Br_2, $BrO^{\cdot}$, and HOBr at Utqiaġvik Alaska for March 18 – April 14, 2009. Reproduced from Liao et al. [2012].

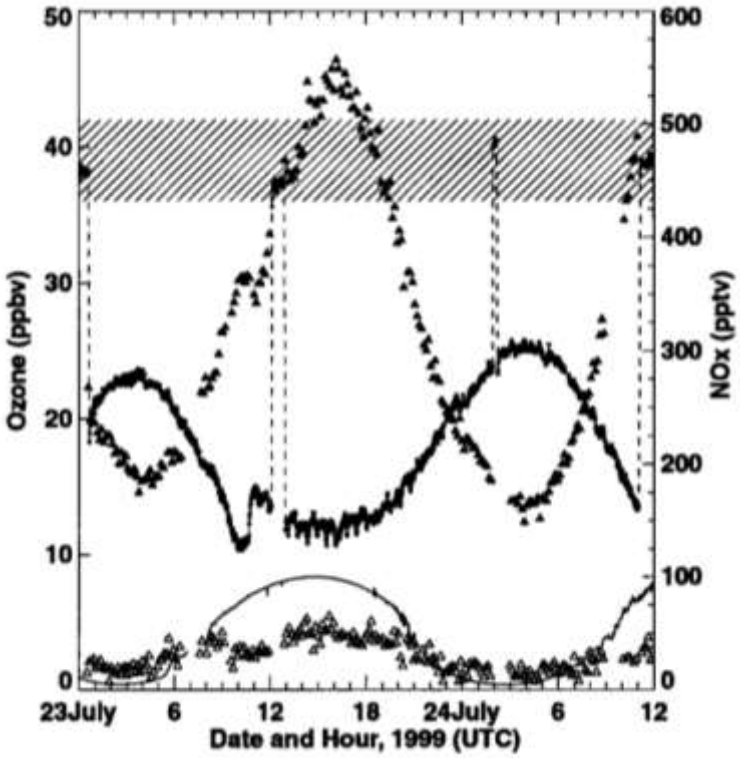

Figure 1.7 O_3 (filled circles) and NO_x (filled triangles) at a depth of 30 cm in the snowpack, NO_x at 1 m above the snowpack (open triangles), and $NO_2^{\cdot}$ photolysis rates (solid lines). The shaded area represents background atmospheric O_3 concentrations, which were measured three times over the course of the data shown. Reproduced from Peterson and Honrath [2001].

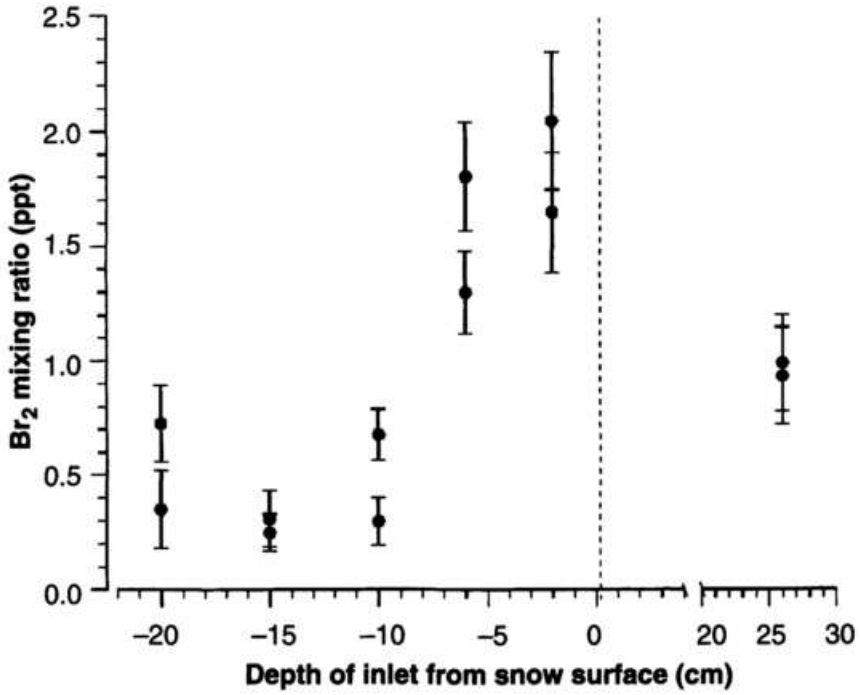

Figure 1.8 Br_2 within the snowpack interstitial air, and just above the snowpack surface. Br_2 is at peak concentrations within the snowpack interstitial air near the surface. Reproduced from Foster et al. [2001]

Pratt et al. [2013] demonstrated the direct production of Br_2 from Arctic coastal snow, using a snow chamber in which clean air could be flowed over snow samples. This system allowed the snowpack to first be isolated from gas phase bromine species, removing the possibility of bromine explosion chemistry, before Br_2 was photochemically produced. Br_2 production was tested in coastal snow, snow from above sea ice, brine icicles, and sea ice. Br_2 production was not observed from sea ice, brine icicles, sea ice, or snow that was in direct contact with the sea ice. However, both coastal snow, and surface snow above sea ice (which is separated from the ice and brine), showed Br_2 production when exposed to light. The two snow types that demonstrated Br_2 production are more acidic than the substrates that did not demonstrate Br_2 production, suggesting that the production mechanism is pH dependent. The observations support the previously

proposed pH dependent photochemical oxidation mechanism to form Br_2 from Br^- [Huff and Abbatt, 2002; George and Anastasio, 2007; Sjostedt and Abbatt, 2008; Abbatt et al., 2010].

$$NO_2^- + hv \rightarrow NO^{\cdot} + O^{\cdot -} \quad \text{R1.37}$$

$$O^{\cdot -} + H^+ \rightarrow OH^{\cdot} \quad \text{R1.38}$$

$$H_2O_2 + hv \rightarrow OH^{\cdot} \quad \text{R1.39}$$

$$OH^{\cdot} + Br^- \leftrightarrow HOBr^{\cdot -} \quad \text{R1.40}$$

$$HOBr^{\cdot -} + H^+ \rightarrow Br^{\cdot} + H_2O \quad \text{R1.41}$$

$$Br^{\cdot} + Br^- \rightarrow Br_2^{\cdot -} \quad \text{R1.42}$$

$$2Br_2^{\cdot -} \rightarrow Br_3^- + Br^- \quad \text{R1.43}$$

$$Br_3^- \leftrightarrow Br_2 + Br^- \quad \text{R1.44}$$

This mechanism is also illustrated in the top left of Figure 1.9, which summarizes bromine production pathways in the Arctic snowpack.

While it now seems clear that the snowpack is the direct source of Br_2 to the Arctic atmosphere, there have been few measurements of the vertical extent of halogen chemistry. The dearth of measurements examining the vertical extent of halogens limits our knowledge of the impact of the snowpack source, and the importance of various recycling mechanisms. Recently DOAS studies have suggested that recycling on aerosols is necessary to explain observations of $BrO^{\cdot}$ aloft [Peterson et al., 2017]. However, DOAS has limited vertical resolution (~100 m), and most mass spectrometry measurements have been only conducted at 1 m above the snowpack surface. Thus either the field must improve the scale and resolution of speciated measurements, or studies of vertical recycling and propagation of halogen chemistry will have to continue to be pursued using one-dimensional models [Thomas et al., 2011; Toyota et al., 2014], which

necessarily assume that the community's understanding of halogen recycling mechanisms and atmospheric mixing in a stably stratified boundary layer is somewhat complete.

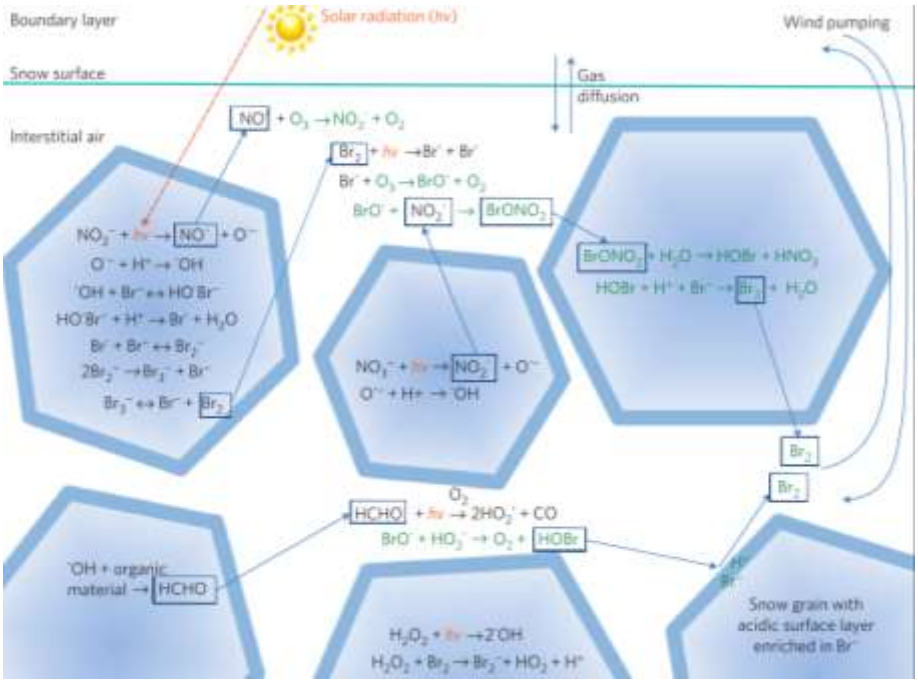

Figure 1.9 Summary of production mechanisms from the photochemical production of Br_2 on snow surfaces. Reproduced from Pratt et al. [2013].

1.5 Chlorine Chemistry

Halogen chemistry initiated by the photolysis of CFCs is largely responsible for the destruction of O_3 in the stratosphere [Molina and Rowland, 1974; Solomon et al., 2016]. However, CFCs do not photolyze in the troposphere, and filterable chlorine is generally similar to what would be expected from sea salt (Figure 1.2) [Sturges and Barrie, 1988]. While bromine chemistry is mostly responsible for ODEs, chlorine is much more effective at oxidation of VOCs, because the HCl bond strength is similar to (or greater than) the bond strength of a hydrogen-carbon bond. Thus, chlorine tends to destroy VOCs rather than O_3 [Platt and Honniger, 2003], especially under depleted ozone conditions [Jobson et al., 1994]. Jobson et al. [1994] first reported active chlorine chemistry in the Arctic troposphere, estimating $Cl^{\cdot}$ atom concentrations of 0.13 – 2.7 ppq using the 'hydrocarbon clock method'. This method utilizes the known reaction rate constants with $OH^{\cdot}$, $Br^{\cdot}$, and $Cl^{\cdot}$ to calculate the concentrations of halogens that must be present for the observed relative removal rates of non-methane hydrocarbons (C_2-C_6). While $Cl^{\cdot}$ concentrations are low (0.13-2.7 ppq), chlorine chemistry still accounts for most hydrocarbon oxidation in the Arctic under depleted ozone conditions [Jobson et al., 1994; Boudries and Bottenheim, 2000].

Impey et al. [1997] observed that photolyzable chlorine species could experience concentrations as high as 100 ppt, however, chlorine was generally high before sunrise, and low after, implying different production mechanisms for Br_2 and Cl_2. Liao et al. [2014] observed Cl_2 at Utqiaġvik during the OASIS campaign in 2009, at concentrations sometimes as high as 400 ppt, but concentrations were highly sporadic (Figure 1.10). In contrast to Br_2, Cl_2 is highest during the daytime, and near zero overnight Figure 1.10, middle inset). Custard et al. [2016] reported the first simultaneous measurements of $ClO^{\cdot}$ and Cl_2 using mass spectrometry measurements during the 2012 BROMEX campaign. $ClO^{\cdot}$ had previously been observed using optical spectroscopy

[Tuckermann et al., 2017], and gas chromatography [Stephens et al., 2012; Thompson et al., 2015], however never at the same site as Cl_2 measurements. During the 2009 OASIS campaign both $ClO^{\cdot}$ [Stephens et al., 2012] and Cl_2 [Liao et al., 2014] were observed, but $ClO^{\cdot}$ measurements made using gas chromatography have low time resolution (1 measurement every ~1 hour). The simultaneous measurements using mass spectrometry yielded relatively high frequency (1 measurement every ~10 seconds) data, which allowed for confirmation that Cl_2 is the main source of $Cl^{\cdot}$ atoms to the Arctic atmosphere using zero-dimensional modeling. $ClO^{\cdot}$ concentrations were as high as 28 ppt during the BROMEX campaign, and showed a similar diurnal trend to Cl_2 and BrO [Custard et al., 2016], with the highest concentrations during the daytime, when photolysis is actively occurring. Wang and Pratt [2017] suggest that the difference in diurnal profiles is due to both the longer photolytic lifetime of Cl_2 and the ability of Cl_2 to oxidize aerosol Br^-, liberating BrCl (reaction 1.45).

$$Cl_2 + Br^- \rightarrow BrCl + Cl^- \qquad \text{R1.45}$$

This reaction leads to the loss of Cl_2 overnight, while the longer photolysis lifetime allows Cl_2 to be present in the daytime at 1 m above the snowpack surface.

Pratt et al. [2013] reported the formation of Br_2 from tundra snow within a chamber experiment but did not observe the formation of Cl_2 or BrCl. Custard et al. [2017] observed that Br_2, Cl_2, and BrCl were all generated in the snowpack interstitial air. However, Cl_2 formation was not consistent between observations. The difference between Br_2 and Cl_2 production may be due to the effective enrichment of Br^- relative to Cl^- in the snowpack under cold conditions [Mcnamara et al., in prep.; Custard et al., 2017]. The eutectic point for the formation of $NaCl \cdot 2H_2O$ (251 K) is higher than the eutectic point for the formation of $NaBr \cdot 2H_2O$ (245 K) [Koop et al., 2000], and when the snowpack is between these temperatures the effective Br^-/Cl^- ratio may be enhanced.

The enhanced Br^-/Cl^- ratio may account for observations of seemingly erratic chlorine chemistry in the Arctic. If this is true, then as the Arctic warms chlorine chemistry will play an increasingly important role in Atmospheric oxidation processes.

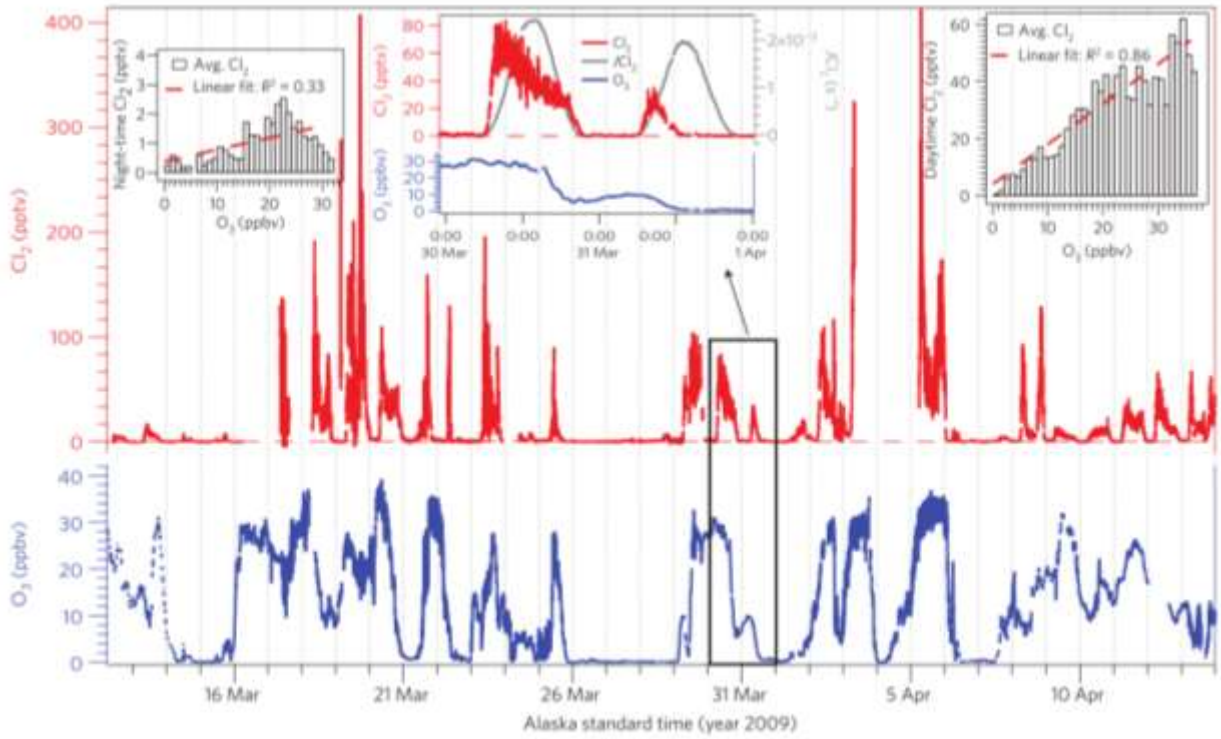

Figure 1.10 Measurements of Cl_2 (red, top panel) and O_3 (blue, bottom panel) in 2009. Top right and top left insets show the relationship of O_3 with nighttime and daytime Cl_2 respectively. The middle inset shows the diurnal profile of Cl_2 for two days. Reproduced from Liao et al. [2014].

1.6 Iodine Chemistry

While it has long been speculated that iodine may also play a role in ozone depletion, its role has not been as extensively researched. I_2 photolyzes (reaction 1.46) more rapidly than Br_2, with a lifetime of only 6.7 seconds during the springtime at Utqiaġvik (compared to Br_2's photolysis lifetime of 23 seconds) [Thompson et al., 2015]. Iodine can also reduce O_3 (reaction 1.47, k = 7.4×10^{-13} cm^3 $molecule^{-1}$ s^{-1} [Atkinson et al., 2007]) as rapidly as bromine (reaction 1.16, k = 6.8×10^{-13} cm^3 $molecule^{-1}$ s^{-1} [Atkinson et al., 2007]).

$$I_2 \xrightarrow{h\nu} 2I^{\cdot} \qquad \text{R1.46}$$

$$I^{\cdot} + O_3 \rightarrow IO^{\cdot} + O_2 \qquad \text{R1.47}$$

$$Br^{\cdot} + O_3 \rightarrow BrO^{\cdot} + O_2 \qquad \text{R1.16}$$

However, the presence of active gas-phase iodine chemistry in the Arctic has not previously been firmly established.

Gas-phase inorganic iodine has been measured in coastal and marine areas around the world [Saiz-Lopez et al., 2012]. In the Antarctic, many measurements of gas phase inorganic iodine have been reported. Iodine monoxide ($IO^{\cdot}$) [Frieß et al., 2001] and I_2 [Atkinson et al., 2012] have both been observed during the springtime, and $IO^{\cdot}$, in particular, has been studied extensively using satellite measurements [Saiz-Lopez et al., 2007b; Schonhardt et al., 2008]. I_2 and 'activated iodine compound' (assumed to be HOI + ICl) measurements were conducted during a cruise on the Weddell sea [Atkinson et al., 2012] using a denuder system. While this denuder system was designed to account for iodine oxides (e.g., I_xO_y), it fails to account for HI, HIO_3, or iodine atoms, which might have been collected as part of either I_2 or activated iodine compounds, possibly giving erroneous results. Iodine chemistry in the Antarctic does seem to be quite active, with $IO^{\cdot}$

concentrations of 10-20 ppt [Frieß et al., 2001; Saiz-Lopez et al., 2007a, 2007b; Schonhardt et al., 2008].

While iodine chemistry in the Antarctic seems to be quite abundant and has even been referred to as 'the most iodine active environment in the world' [Saiz-Lopez et al., 2012], iodine chemistry in the Arctic has only been observed on a much smaller scale. $IO^{\cdot}$ has been measured in the sub-arctic (at Kuujjuarapik, Hudson Bay, Canada) [Mahajan et al., 2010], at concentrations up to 3.4 ppt. Johannes Zielcke reported in his dissertation [Zielcke, 2015] observations of $IO^{\cdot}$ in the high Arctic at Alert, Canada, but concentrations were consistently ≤ 1 ppt, and these observations have not undergone peer review. Sipilä et al. [2016] reported up to 1 ppt of iodic acid (HIO_3) in the Arctic (northern Greenland), coincident with a new particle formation event (Figure 1.11). Iodine-containing molecular halogen compounds (I_2, IBr, ICl) have not previously been reported in the Arctic, and other species seem to be present at low concentrations. Still, observations of high concentrations of iodine in particles [Berg and Sperry, 1983; Sturges and Barrie, 1988] and snow [Duce et al., 1966] suggest that active iodine chemistry may be occurring.

Filterable iodine was seen at the same time as bromine and chlorine in aerosol [Sturges and Barrie, 1988] (Figure 1.2). These measurements were remarkable because they showed that, relative to the iodine to sodium (I/Na^+) ratio of seawater, the I/Na^+ ratio in aerosols showed considerable enhancement, up to 10,000 times what would be expected if seawater was the only source of iodine. Iodine photochemistry has been implicated in new particle formation events in both the mid-latitudes [O'Dowd et al., 1999] and the Arctic [Allan et al., 2014; Sipilä et al., 2016]. Until recently the chemical mechanism for the formation of iodine-oxide polymers which eventually form ultrafine particles was not well understood. Sipilä et al. [2016] used chemical

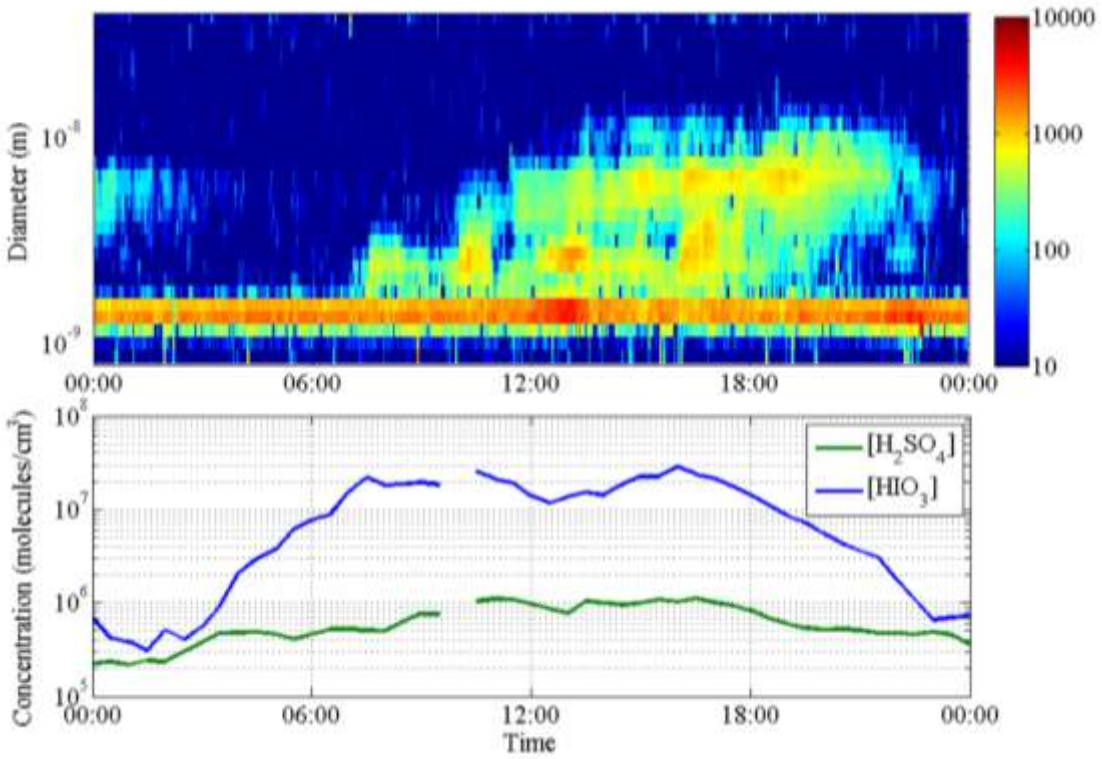

Figure 1.11 New particle formation (upper panel) observed in Northern Greenland concurrently with HIO_3 (blue trace, bottom panel) on March 31, 2015. Reproduced from Sipilä et al. [2016]

ionization time of flight mass spectrometry to observe the change in mass defect as iodine-oxide clusters grew in the Arctic (northern Greenland) and the mid-latitudes (coastal Ireland). From the correlation between the mass defect and mass/charge ratio, they determined that the formation of iodine-oxide clusters occurs via the sequential addition of HIO_3 (Figure 1.12).

In most mid-latitude coastal observations of I_2 and $IO^{\cdot}$, the source of inorganic iodine is believed to be macroalgae under oxidative stress during low tide [McFiggans et al., 2004; Saiz-Lopez and Plane, 2004; Saiz-Lopez et al., 2006]. Carpenter et al. [2013] proposed that the direct oxidation of I^- by O_3 (reactions 1.48-1.49) could account for up to 75% of the observed iodine in macroalgae-free marine areas.

$$H^+ + I^- + O_3 \rightarrow HOI + O_2 \qquad \text{R1.48}$$

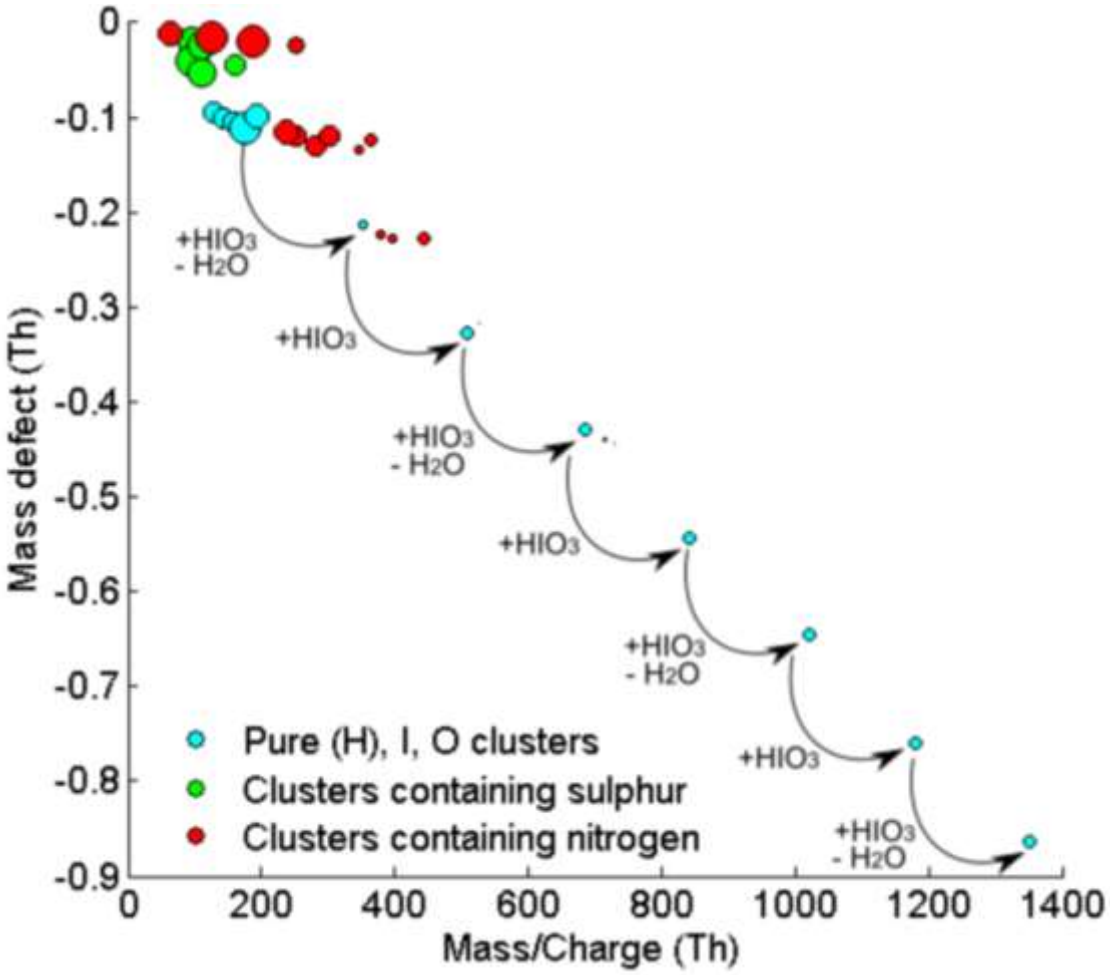

Figure 1.12 Mass defect vs. mass/charge ratio for 16:00-18:00 on March 31, 2015, in Northern Greenland. Reproduced from Sipilä et al. [2016].

$$HOI + I^- + H^+ \leftrightarrow I_2 + H_2O \qquad \text{R1.49}$$

In the Antarctic, production of I_2 has been previously ascribed to sea ice diatoms, which are commonly found on the underside of both Arctic and Antarctic sea ice [Atkinson et al., 2012; Saiz-Lopez et al., 2012, 2015; Saiz-Lopez and Blaszczak-Boxe, 2016]. I_2 could then diffuse through open brine channels to the sea ice surface [Saiz-Lopez et al., 2015; Saiz-Lopez and Blaszczak-Boxe, 2016]. However, this method of I_2 production has not been confirmed by measurements of either I_2 production by sea ice diatoms, or measurements of I_2 diffusion through brine channels. I_2 has been photochemically produced in laboratory studies of frozen salt solutions [Kim et al., 2016;

Halfacre et al., 2018]. Triiodide (I_3^-), which is in rapid equilibrium with I_2, formation was also observed in I^- spiked and refrozen Antarctic snow samples [Kim et al., 2016], and iodate (IO_3^-) has been shown to be photochemically converted to other species in frozen salt solutions [Gálvez et al., 2016]. The chemical mechanism suggested for photochemical production of I_2 has varied. Kim et al. [2016] suggested that the primary pathway might be the ordinarily slow oxidation of I^- by O_2 (reaction 1.50), which is accelerated by the exclusion of salts to the ice grain boundary.

$$O_2 + 4H^+ + 6I^- \rightarrow 2H_2O + 2I_3^- \quad \text{R1.50}$$

Halfacre et al. [2018] found that in frozen solution I_2 was preferentially produced before Br_2. I_2 and Br_2 production were also influenced by condensed-phase $OH^{\cdot}$, which supports a similar reaction mechanism to Br_2 in the snowpack (reactions 1.51-1.55).

$$OH^{\cdot} + I^- \rightarrow HOI^{\cdot -} \quad \text{R1.51}$$

$$HOI^{\cdot -} + H^+ \rightarrow I^{\cdot} + H_2O \quad \text{R1.52}$$

$$I^{\cdot} + I^- \rightarrow I_2^{\cdot -} \quad \text{R1.53}$$

$$2I_2^{\cdot -} \rightarrow I_3^- + I^- \quad \text{R1.54}$$

$$I_3^- \leftrightarrow I_2 + I^- \quad \text{R1.55}$$

Models have also suggested that bromine chemistry alone does not explain the full extent of ODEs [Saiz-Lopez et al., 2007a; Thomas et al., 2011; Toyota et al., 2014; Thompson et al., 2015], and that even low concentrations of gas phase inorganic iodine could have a significant impact on rates of O_3 depletion [Calvert and Lindberg, 2004; Saiz-Lopez et al., 2014; Thompson et al., 2015], due to the relatively large rate constant for the reaction of $BrO^{\cdot}$ with $IO^{\cdot}$ (reaction 1.56 k = 9.4×10^{-11} $cm^3 molec^{-1} s^{-1}$ [Rowley et al., 2001]) compared to the $BrO^{\cdot}$ self-reaction (reaction 1.17 k = 9.3×10^{-13} $cm^3 molec^{-1} s^{-1}$ [Sander et al., 2006]).

$$IO^{\cdot} + BrO^{\cdot} \rightarrow Br^{\cdot} + OIO^{\cdot} \quad \text{R1.56}$$

$$BrO^{\cdot} + BrO^{\cdot} \rightarrow 2Br^{\cdot} + O_2 \qquad \text{R1.17}$$

Thompson et al. [2017] reported that the iodine chain length could be up to 10 times longer than the bromine chain length, and thus can have a significant effect on bromine chemistry even under low concentrations ($IO^{\cdot}$ < 1ppt). The results of these models suggest that further measurements of small concentrations of inorganic iodine, while elusive, could be critical to understanding the impact of halogen chemistry on the composition of the Arctic atmosphere.

1.7 Research Purpose

While the community's understanding of Arctic halogen chemistry has grown significantly in the last few decades through the use of mass spectrometry and long path adsorption spectroscopy, there are still several areas where our understanding is inadequate. In this thesis, I will discuss my efforts to improve understanding of the oxidation processes that occur in the springtime Arctic with an emphasis on the relative importance of the snowpack as a reactive surface that can produce and recycle molecular halogens. Specifically, the following scientific questions are addressed.

1. Is I_2 present at detectable concentrations in the Arctic boundary layer?
2. Is I_2, like Br_2, BrCl, and Cl_2, produced photochemically in the Arctic snowpack?
3. What is the impact of I_2 on ozone depletion the Arctic boundary layer?
4. What is the rate of halogen emissions from the Arctic snowpack?
5. What is the vertical extent of bromine and chlorine chemistry in the Arctic boundary layer?
6. Does our current understanding of halogen sources, sinks and recycling explain observations of the vertical evolution of Br_2 and Cl_2 in the Arctic boundary layer?

These questions are addressed using data collected during two field campaigns in Utqiaġvik, Alaska in Jan - March 2014 and February - May 2016.

Questions one and two are addressed in chapter 2, where I show and discuss the first measurements of I_2 in the Arctic both near the snowpack surface, and within the snowpack interstitial air. The second question is further addressed in chapter 3, where the first measurements of iodide in Arctic snow are described. The third question is discussed in chapter 4, which utilizes zero-dimensional modeling to demonstrate the impact of iodine chemistry on O_3 both in the boundary layer and in the snowpack interstitial air. The fourth question is addressed in chapter 5, where the first eddy covariant fluxes of Cl_2 and an estimate of Br_2 fluxes are shown, and the difficulties of measuring snowpack fluxes are discussed. Chapter 6 shows the first vertical profile measurements of Br_2 and Cl_2 between 1 and 7 m above the snowpack and utilizes one-dimensional modeling to test our ability to explain these vertical profiles. The one-dimensional model used in chapter 6 is also used to discuss the community's understanding of the production, loss, and turbulent mixing of halogens produced by the Arctic snowpack.

CHAPTER 2. GAS PHASE IODINE CHEMISTRY IN THE ARCTIC

2.1 Introduction

Recently inorganic iodine (IO, HIO_3) [Zielcke, 2015; Sipilä et al., 2016] has been observed in the Arctic, adding support to signs of the importance of iodine chemistry from early aerosol measurements [Berg and Sperry, 1983; Sturges and Barrie, 1988]. While molecular iodine (I_2) has not previously been observed in the Arctic, it has been observed at several mid-latitude marine and coastal sites [Saiz-Lopez et al., 2012] and along the Antarctic coast [Atkinson et al., 2012], and IO has been observed in the Antarctic [Saiz-Lopez et al., 2007a, 2007b; Frieß et al., 2010] and in the sub-Arctic [Mahajan et al., 2010]. During recent measurements at Alert, Canada, IO was observed at levels up to 1.5 ppt [Zielcke, 2015]. Iodine has recently been observed to contribute to atmospheric new particle formation [Allan et al., 2014] in the Arctic through the sequential addition of iodic acid (HIO_3) at maximum mole ratios of ~1 ppt [Sipilä et al., 2016], giving further evidence to the presence and importance of Arctic iodine chemistry.

While there is clear indications of iodine chemistry in the Arctic, the source of the inorganic iodine has not been apparent. In most mid-latitude observations of I_2 and IO, the source of inorganic iodine is believed to be macroalgae under oxidative stress during low tide [McFiggans et al., 2004; Saiz-Lopez and Plane, 2004; Saiz-Lopez et al., 2006]. In the Antarctic, observations have previously been ascribed to I_2 production by sea ice diatoms, which are commonly found on the underside of both Arctic and Antarctic sea ice, followed by I_2 diffusion through open brine channels to the sea ice surface [Saiz-Lopez et al., 2015; Saiz-Lopez and Blaszczak-Boxe, 2016]. However, while the diffusion of I_2 through brine channels has been modeled [Saiz-Lopez et al., 2015], it has not been directly observed. Whether iodine precursors in the Arctic are emitted from

the open ocean [Mahajan et al., 2010; Zielcke, 2015] or from sea ice covered regions [Sipilä et al., 2016] has remained unclear. There are potential mechanistic pathways for both sources. Br_2, Cl_2, and BrCl production via photochemical reactions has been demonstrated in the Arctic saline snowpack [Foster et al., 2001; Pratt et al., 2013; Custard et al., 2017] and from frozen substrates in laboratory experiments [Adams et al., 2002; Huff and Abbatt, 2002; Sjostedt and Abbatt, 2008; Abbatt et al., 2010; Oldridge and Abbatt, 2011; Wren et al., 2013; Halfacre et al., 2018]. I_2 has also been produced photochemically from frozen substrates in the laboratory [Kim et al., 2016; Halfacre et al., 2018], and triiodide (I_3^-) was recently been shown to be photochemically produced in Antarctic snow spiked with iodide (I^-) (1-1000 μM) [Kim et al., 2016]. These studies show condensed phase iodine photochemistry, and although previous samples have lacked the physical and chemical characteristics of snow, they suggest that photochemical production of I_2, similar to that of Br_2 and Cl_2 production in the Arctic surface snowpack [Pratt et al., 2013; Custard et al., 2017], is probable. However, neither atmospheric I_2 nor the photochemical production of I_2 from snow samples with natural I^- levels, has ever been reported.

Given the expected importance of iodine chemistry in the atmosphere, snowpack iodine chemistry was investigated near Utqiaġvik (formerly Barrow), AK in January and February 2014. Here, we report the first Arctic I_2 measurements, in both the boundary layer and snowpack interstitial air. The effect of radiation on halogen mole ratios in the snowpack interstitial air was examined through sunlit experiments, artificial irradiation experiments, and snowpack vertical profiles.

2.2 Methods

2.2.1 CIMS Instrumental Methods

Trace halogen gases were measured using chemical ionization mass spectrometry (CIMS), as described by Liao et al. [2011, 2012], Peterson et al. [2015], and Custard et al. [2016], on the Barrow Environmental Observatory (BEO), 5 km inland over tundra snowpack near Utqiaġvik, Alaska. Figure 2.1 shows a diagram of flows through the CIMS instrument. A constant flow rate of 7.5 lpm was continuously sampled into a custom made three-way valve at the CIMS inlet, after which air was drawn through a 0.51 mm diameter orifice to the CIMS flow reactor, where electron transfer to the analyte using excess SF_6^- was achieved. SF_6^- was produced by passing 1.7 lpm of 5 ppm SF_6 in N_2 through a ^{210}Po ionizer. The flow of N_2 was controlled to maintain a pressure of 13 torr in the flow reactor. The CIMS instrument was modified from the previous studies [Liao et al., 2011, 2012; Pratt et al., 2013; Peterson et al., 2015] by the addition of an 18 cm long PTFE coated flow double nipple to the original 4.5 cm flow reactor. The longer flow reactor yielded increased sensitivity to I_2. A dry scroll pump (Agilent Triscroll 300) was utilized for the first stage of pumping. From the flow reactor analytes were sampled through an orifice to the collision dissociation chamber (CDC), which is maintained at ~0.5 torr by an Adixen 5011 turbopump. Ions are then transmitted through a third orifice to the octupole ion guide. Both the octupole and quadrupole regions are pumped by Agilent TV81 turbopumps. The quadrupole ion selector is maintained at a pressure of ~$6x10^{-5}$ torr. Ion detection is achieved through an Exelis CeraMax electron multiplier tube (EMT).

Masses 146 amu (SF_6^-), 254 amu ($^{127}I_2^-$), 160 amu ($^{81}Br^{79}Br^-$), and 158 amu ($^{79}Br_2^-$) were monitored. All analyte masses were normalized to the ionization agent mass (SF_6, 146 amu) to account for changes in ion production and transmission. Br_2 mole ratios were calculated using mass 160 amu; masses 158 and 160 showed the same trends ($R^2 = 0.977$) and had an isotope ratio

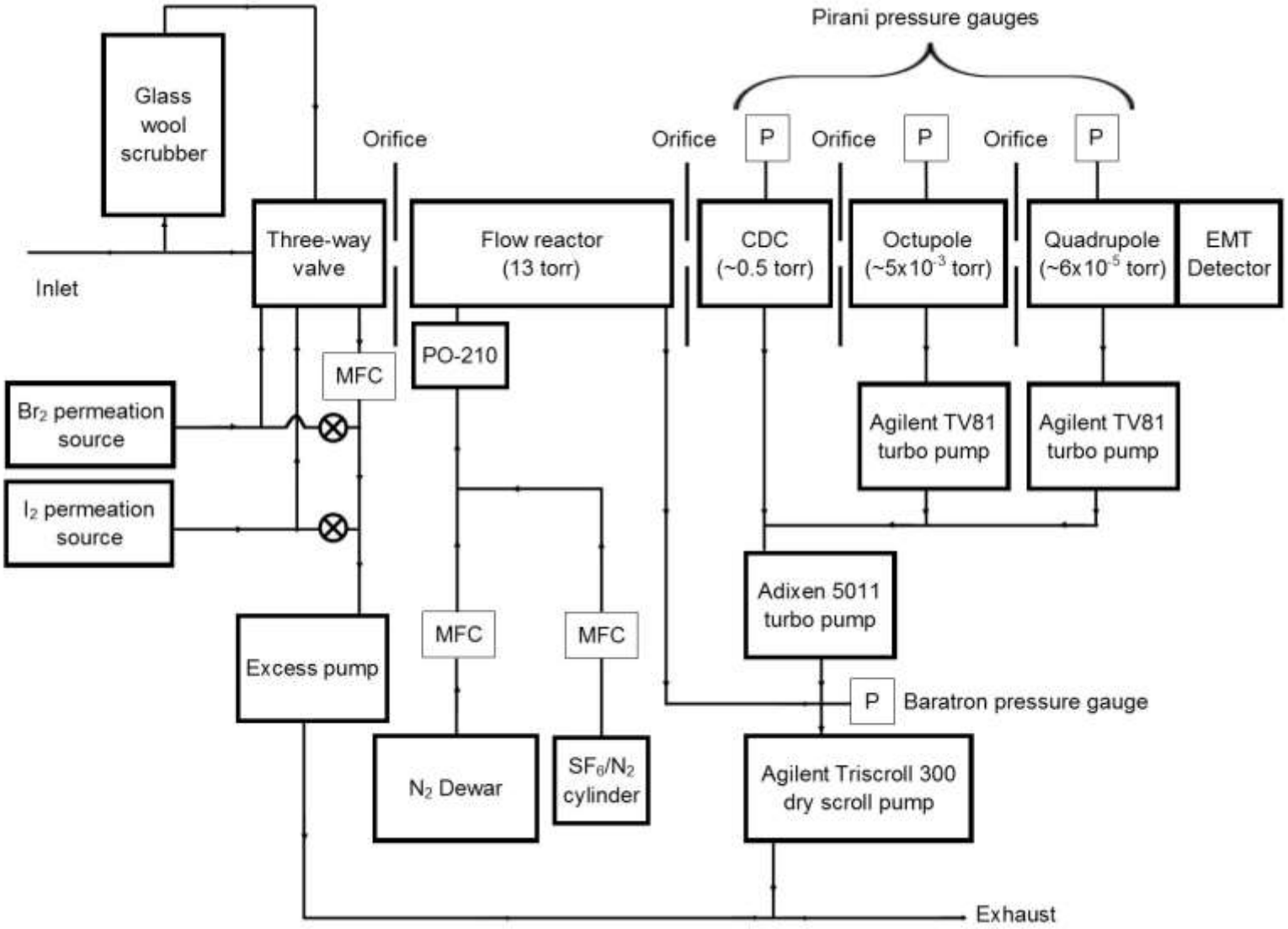

Figure 2.1 Flow diagram of the CIMS instrument for measurements in 2014

(158 amu/160 amu) of 0.5300 ±0.0003 (natural isotope ratio =0.5140). The duty cycle was 10 s, with a dwell time of 6 s for I_2 (254 amu), 300 ms for each of the Br_2 masses (158 amu and 160 amu), and 100 ms for the reagent ion (146 amu). Other masses made up the remainder of the duty cycle. However, none of these masses yielded measurable concentrations.

2.2.2 Background and Calibration Methods

Single point calibrations were performed using I_2 and Br_2 permeation devices (VICI Metronics) every 30 min – 2 h. Figure 2.2 shows a four-point calibration curve for I_2, and Figure 2.3 shows the sensitivity of the instrument to I_2 and Br_2 throughout the study. The output gas of the I_2 permeation device flowed through an impinger into a $NaHCO_3$ (30mM)/$NaHSO_3$ (5mM) reducing solution. This solution quantitatively reduces I_2 to I^-, which was then analyzed using a Dionex DX500 ion chromatography system with an AG11 guard column and an AS11 analytical column with a sodium hydroxide gradient. The output gas of the Br_2 and Cl_2 permeation devices flowed through impingers into a 2% (by weight) potassium iodide solution. The Br_2/Cl_2 then oxidizes I^- to I_3^- which is quantified using a UV/visible spectrometer (Spectronic 20 Genesys) at 352 nm. The permeation rates were found to be 2.3(±0.8) x 10^{-11}, 4.9(±0.6) x 10^{-10}, and 8.1(±0.8) x 10^{-10} moles min^{-1} of I_2, Br_2, and Cl_2, respectively.

Background measurements were performed by passing the air flow through a glass wool scrubber, which quantitatively (>99%) destroyed all three halogens, every 20 min – 1 h for 7-20 minutes, corresponding to a 14.4 s - 28.1 s integration period for each Br_2 mass and a 252 - 720 s integration period for the I_2 mass. It has previously been shown that glass wool has >99% efficiency at removing halogen species [Neuman et al., 2010; Liao et al., 2011], and we found this to be true for I_2, as well as Br_2 and Cl_2. There were no observable increases in the monitored masses when 62 ppt, 3.3 ppb, and 3.0 ppb of I_2, Br_2, and Cl_2, respectively, were passed through

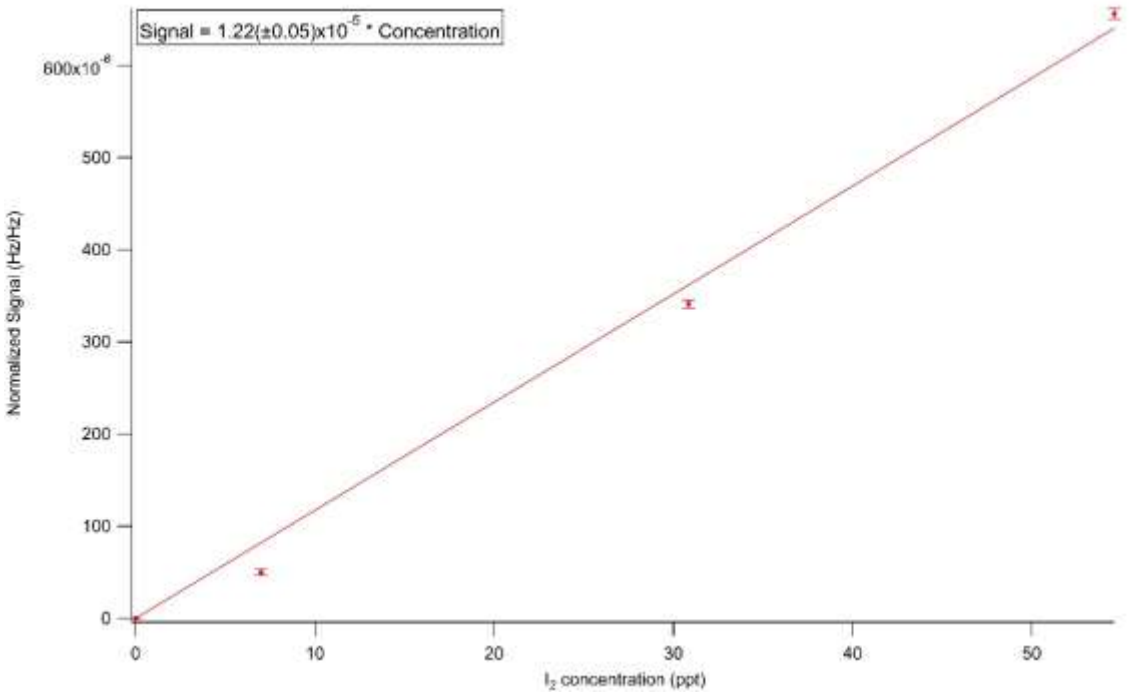

Figure 2.2 Four-point calibration curve for I_2. The sensitivity of the instrument to I_2, in this case, was 1.22(±0.05) x 10^{-5} Hz Hz^{-1} ppt^{-1}.

the scrubber. There was some variation between mass 254 amu ($^{127}I_2^-$) background measurements, both with ambient and ultra-zero grade air (Air Liquide), suggesting that there may be an interference created by the glass wool at mass 254 amu. This was particularly apparent during background measurements of the snowpack interstitial air, which were often higher than

interference in the Arctic air, as scrubbed ambient air backgrounds and ultra-zero grade air backgrounds agreed well during individual tests, and no diurnal pattern was observed in background signals. It is also unlikely that this variability is due to inefficiency of the glass wool scrubber, which was found to remove>99% of 62 ppt of I_2. Therefore, periodic background measurements in the ambient air were utilized for background subtraction for both the ambient air and snowpack interstitial air measurement data. The difference between these backgrounds and

measured backgrounds in the snowpack interstitial air was accounted for in the measurement uncertainty expressed in Figures, as calculated below.

The Br_2 3σ limit of detection (LOD) for these measurements ranged from 1.5 - 3.9 ppt. The I_2 3σ LOD ranged from 0.2 – 1 ppt. The 20-minute averaged 3σ LOD for Br_2 and I_2 ranged from and 1.5 – 2.0 ppt and 0.2 – 0.5 ppt respectively. Limits of detection for unaveraged data throughout the field study are seen in Figure 2.3.

2.2.3 Ambient and Snowpack Interstitial Air Sampling

Interstitial snowpack air and depth profile sampling was conducted using a 380 cm long, 1.3 cm ID FEP-Teflon line heated to 25°C, which was attached directly to the CIMS sampling inlet. The sampling end of this line was fitted with a 7 cm long, 5 cm OD custom machined PTFE snow probe (Figure 2.4), intended to prevent snow from entering the sampling line. A custom built 61 cm x 61 cm Acrylite OP-4 cover (80% transmittance at 300 nm, and ~92% at 395 nm) with a 7.6 cm aluminum lip was pressed into the snow surface to prevent ambient air from being pulled directly into the snowpack and mixing with the interstitial air being sampled below (Figure 2.5). While dilution of the snowpack interstitial air by ambient air will occur to some extent, the O_3 mole ratios measured during in-snowpack experiments were consistently much lower than those. observed in the air above the snowpack and agreed with previous snowpack O_3 observations [Peterson and Honrath, 2001; Van Dam et al., 2015], suggesting that the mixing of ambient air into the snowpack was minimal. Any mixing of air within the snowpack due to high sampling rates would be expected to lessen the gradients shown in the snowpack vertical profiles (Figure 2.8).

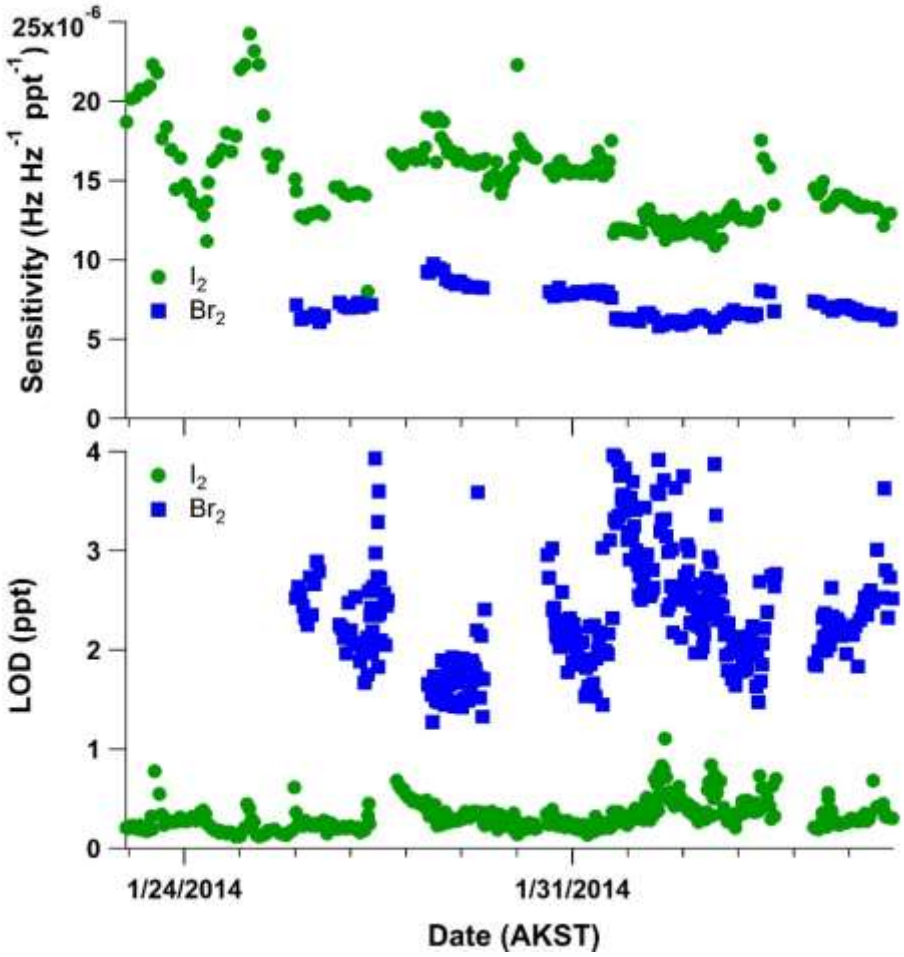

Figure 2.3 Instrumental sensitivity (top panel) and limit of detection (LOD, bottom panel) for unaveraged I_2 (green) and Br_2 (blue) for SF_6 measurements during the 2014 field campaign (January 23 – February 05, 2014).

Artificial light was supplied by six UVA-340 halogen light bulbs (Q-Lab Corp.) housed in a custom built heated and insulated fixture. The radiation spectrum of the UVA-340 light bulbs is shown in Figure 2.6. The light exited the fixture through a sheet of Acrylite OP-4, which insulated the light bulbs from the cold environment. The lamp housing was suspended approximately 10 cm above the snow cover (Figure 2.5).

Holes in the snowpack for interstitial air measurements were drilled 2–3 cm deeper than the maximum depth to which the snow probe was inserted via a sea ice drill bit. Ambient measurements were conducted at 1 m above the snowpack surface for 30 min every 90 min during the day and two times overnight for the two-day diurnal profile (Figure 2.7). For vertical profile measurements (Figure 2.8), each height was sampled for 9 – 22 min, with sampling alternating between the overlying boundary layer and snowpack interstitial air. Interstitial measurements started closest to the snowpack surface and proceeded downward, while ambient measurements were done in no particular order. The heights shown in Figure 2.8 are the midline position of the snow probe, either in or above the snowpack. Due to the relatively high flow rate of air (7.5 lpm) being pulled from the snowpack, there was likely some vertical transport of species. The snowpack where sampling occurred was >70 cm deep for the duration of the campaign.

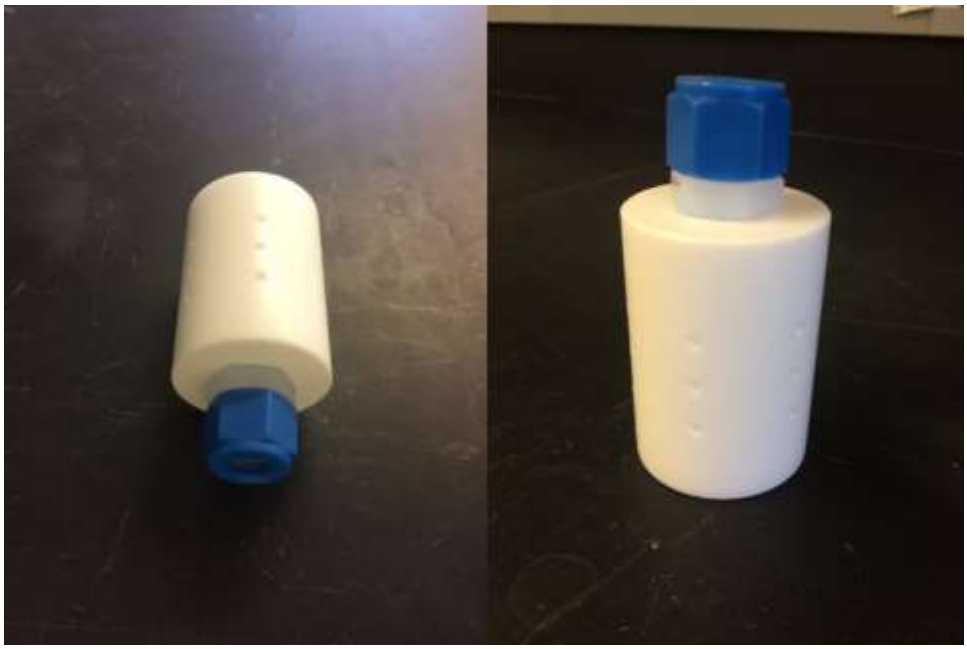

Figure 2.4 Custom machined snow-probe used to prevent snow from entering the sampling line during measurements. Photo credit: S. McNamara (Univ. of Michigan).

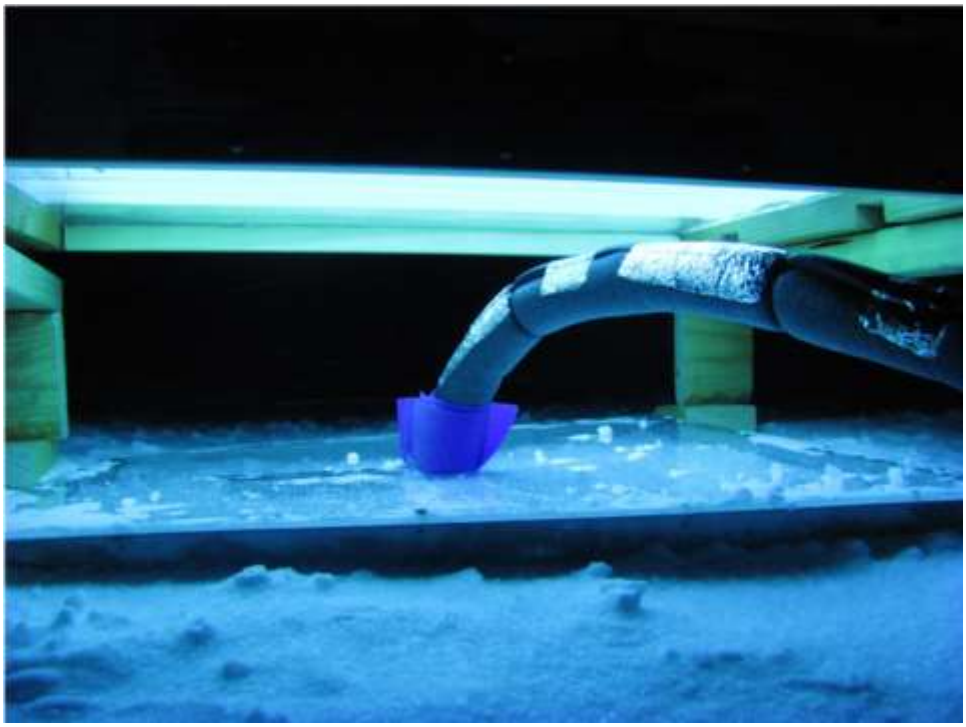

Figure 2.5 Sampling from the snowpack interstitial air. The sampling line was inserted into the hole in the snowpack through a ~6 cm diameter hole, which was partially sealed using silicone sheets. The artificial light fixture was suspended ~10 cm above the Acrylite snow cover.

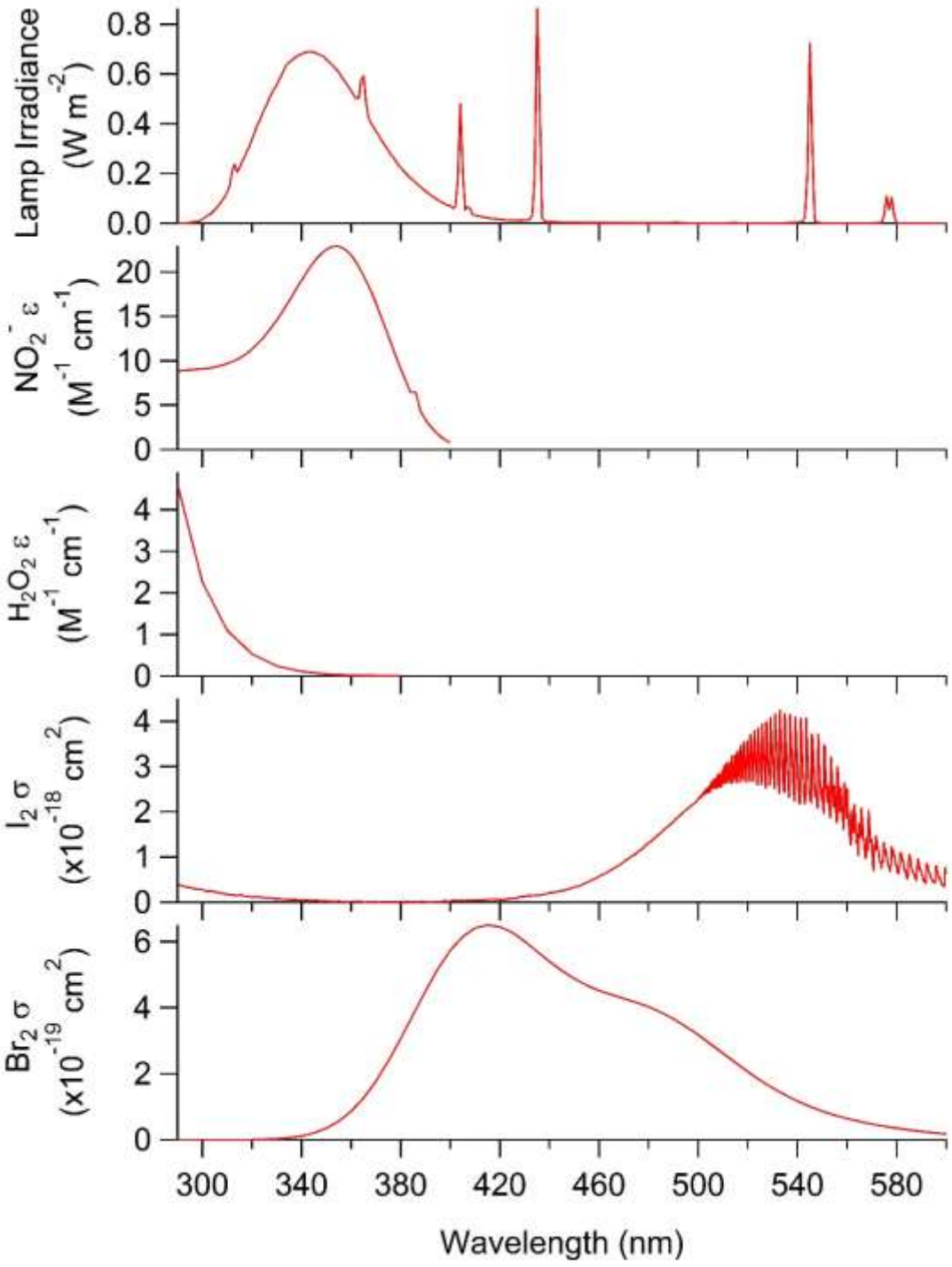

Figure 2.6 Radiation spectrum of the UVA 340 lamps used for artificial irradiation and absorption spectra of species of interest. The lamps have a peak irradiation wavelength at 340 nm. The molar absorptivity of aqueous nitrite (NO_2^-) peaks at a similar wavelength [Sander et al., 2006]. The molar absorptivity of aqueous hydrogen peroxide (H_2O_2) is highest at wavelengths less than 320 nm [Sander et al., 2006]. Gas phase I_2 and Br_2 have peak absorbance cross sections at 530 nm and 420 nm, respectively [Saiz-Lopez et al., 2004; Sander et al., 2006].

2.2.4 Line Loss and Method Uncertainties

To minimize line losses [Neuman et al., 2010], the line was periodically rinsed with Milli-Q water and dried with ultra-high purity nitrogen (Air Liquide). Estimated line losses, based on laboratory and field testing of the lines with permeation devices, were accounted for in the method uncertainties. Tests for molecular halogen losses to the sampling line were completed both before the campaign in the laboratory and during the field campaign. In the laboratory, tests were done using several lengths of the 1.3 cm ID FEP line ranging from 2.44 m to 7.32 m at room temperature (~20°C). The greatest losses observed were 10% for I_2 and 4% for Br_2. In the field, line loss tests were performed at the end of the study with the same line as for sampling. Losses of 14% and 10% were observed for I_2 and Br_2, respectively. Because of the variability observed in line losses, the measurements presented in this paper have not been corrected for line losses. Instead, the maximum loss has been accounted for in the calculated measurement uncertainties. As all line tests showed molecular halogen loss, rather than gain, on the sampling lines, this has only been incorporated into the reported negative method uncertainties.

CIMS method uncertainties are propagated from the uncertainties of the ambient measurement, background, calibration, permeation source, SF_6 signal, and line losses. This is expressed in Equation 2.1 below.

$$\%\ unc. = \sqrt{\frac{\sigma_{amb}^2+\sigma_{bkg}^2}{(amb-bkg)^2} + \frac{\sigma_{cal}^2+\sigma_{amb}^2}{(cal-amb)^2} + \frac{\sigma_{perm}^2}{perm^2} + 2 * \frac{\sigma_{SF_6}^2}{SF_6^2} + line\ loss^2} \qquad \text{E2.1}$$

Where σ_{amb} and amb are the standard deviation of the ambient signal and the ambient signal, σ_{bkg} and bkg are the standard deviation of the background measurement and the background measurement, σ_{cal} and cal are the standard deviation of the calibration signal and the calibration signal, σ_{perm} and $perm$ are the standard deviation of the permeation device output and the

permeation device output, and, σ_{SF_6} and SF_6 are the standard deviation of the SF_6 signal and the SF_6 signal. The propagated uncertainties, including line losses, in the I_2 and Br_2 mole ratios are calculated to be (-33%/+35% + LOD), and (-19%/+21% + LOD), respectively. The snowpack interstitial air I_2 uncertainties shown in Figures reflect these uncertainties, as well as the difference between the snowpack interstitial air and above-snowpack background signals, applied to the negative uncertainty.

2.2.5 Auxiliary Measurements

O_3 measurements were obtained using a dual-beam O_3 monitor (2B Technologies model 205), which sampled from the same airflow as the CIMS instrument. After the 3-way valve on the CIMS inlet, 1.3 lpm of air was diverted for O_3 measurement. Radiation data were obtained from the NOAA Global Monitoring Division Earth Systems Research Laboratory (http://www.esrl.noaa.gov/gmd/). The NOAA measurement site was approximately 5 km across the flat tundra to the northeast (upwind) of the CIMS measurement site.

2.3 Results and Discussion

Gas phase I_2 was observed in the snowpack interstitial air at 10 cm below the sunlit snowpack surface on February 1 and 2, 2014 near Utqiaġvik, AK (Figure 2.7). I_2 mole ratios in the snowpack interstitial air peaked at 2.7 – 5.1 ppt in the early afternoon, just following the solar radiation maxima. Coincident with these daytime maxima, I_2 was observed in the boundary layer, 1 m above the snowpack surface, at mole ratios of ~0.3 – 1.0 ppt. Significantly more I_2 was observed in the snowpack interstitial air on February 2 (maximum I_2 5.1 ppt), which was sunny and clear (maximum radiation 172 W/m^2), compared to February 1 (maximum I_2 2.7 ppt), which was overcast (maximum radiation 18 W/m^2), further supporting a photochemical production

mechanism. Laboratory studies have shown that I_2 can be produced from aqueous samples containing I^- in the presence of O_3 without light, via Reactions 6-8 (Figure 2.10) [Carpenter et al., 2013]. During the night of February 1-2, average wind speeds rose from 2.0 m s^{-1} to 5.9 m s^{-1} leading to increased wind pumping, resulting in increasing O_3 from 5 ppb to 25 ppb in the snowpack interstitial air over the course of ~30 min (22:00 – 22:30 AKST, Figure 2.7). This presents an opportunity to examine the influence of O_3 on dark oxidation and subsequent I_2 formation. However, while an apparent small increase in I_2 signal at a snowpack depth of 10 cm was observed during this time (Figure 2.7), the I_2 levels were never statistically significant different from zero. These observations suggest that snowpack photochemical reactions were the predominant source of the observed I_2 in the Arctic boundary layer.

The photochemical nature of I_2 production in the snowpack is further demonstrated by the differences in the vertical profiles of I_2 and molecular bromine (Br_2) within the snowpack interstitial air (Figure 2.8). Gas phase I_2 and Br_2 were simultaneously quantified at mole ratios up to 22 ppt and 43 ppt, respectively, under sunlit conditions in the snowpack interstitial air on February 04. Br_2 showed peak mole ratios (43 ppt on February 04, and 27 ppt on February 03) just below the snowpack/atmosphere interface (within the top ~10 cm) (Figure 2.8). This is consistent with previous measurements, which showed a maximum in Br_2 mole ratios within the top 7 cm of the snowpack air at Alert, Canada [Foster et al., 2001]. In contrast, the I_2 peak mole ratio (22 ppt) was observed at ~40 cm below the snowpack surface, at least 30 cm deeper than the Br_2 maximum on February 04 (Figure 2.8). On February 03 the vertical profile measurements did not extend deep enough into the snowpack to capture the peak I_2 concentrations, but the observation of the Br_2 peak was replicated. At 40 cm below the snowpack surface, ambient light was attenuated (at 40 cm ~2% of 400 nm light remains [King and Simpson, 2001]). The difference

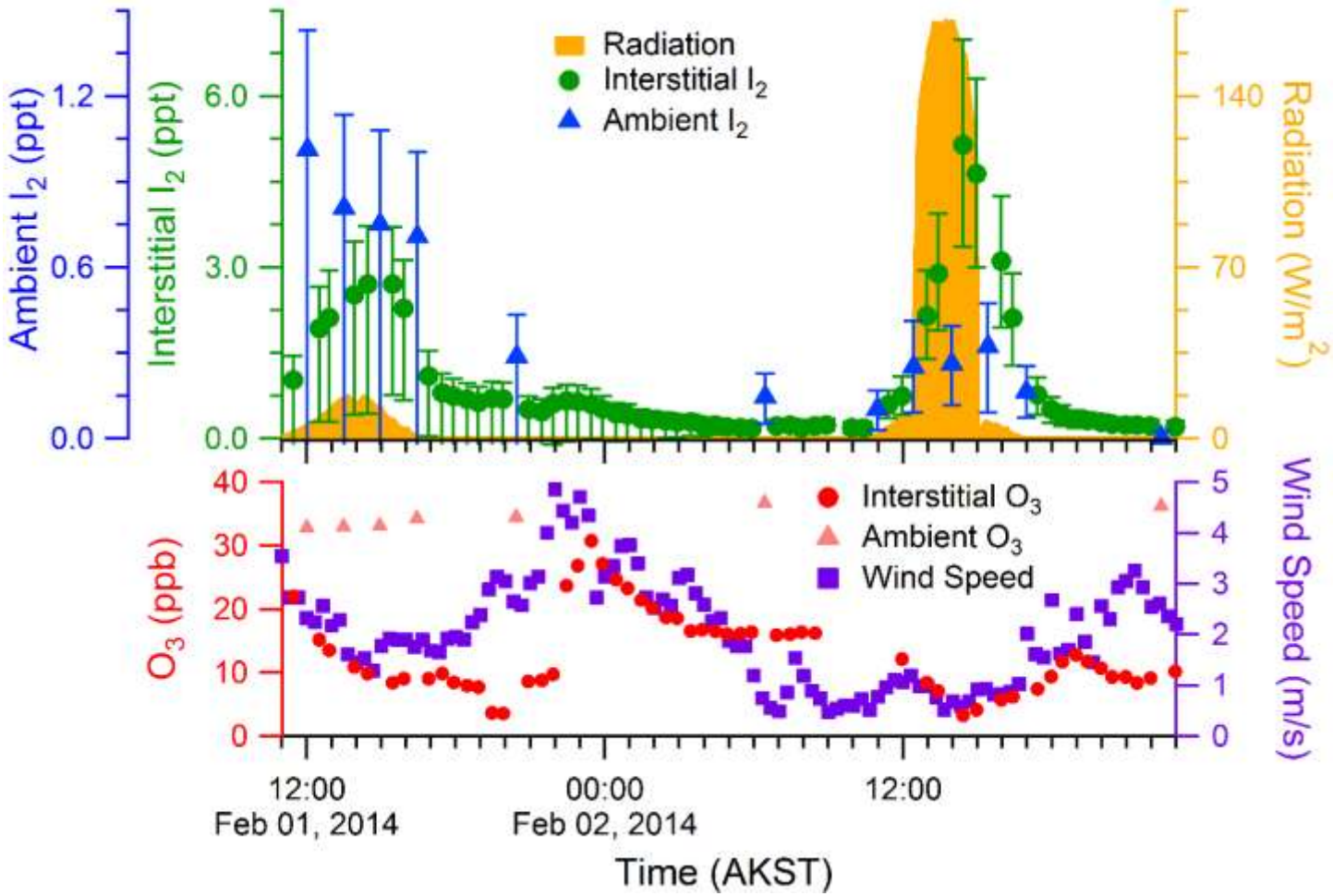

Figure 2.7 I_2, O_3, radiation, and wind speeds during February 1-2, 2014. The diurnal profiles for I_2 and O_3 mole ratios, as well as the radiation and wind speeds, are shown as 20 min averages from Feb. 1-2, 2014. Error bars are propagated uncertainties. Ambient measurements were conducted 1 m above the snowpack surface. Interstitial air measurements were conducted 10 cm below the snowpack surface. Fluctuations in interstitial air O_3 mole ratios correlate with high wind speeds and are therefore likely due to wind pumping.

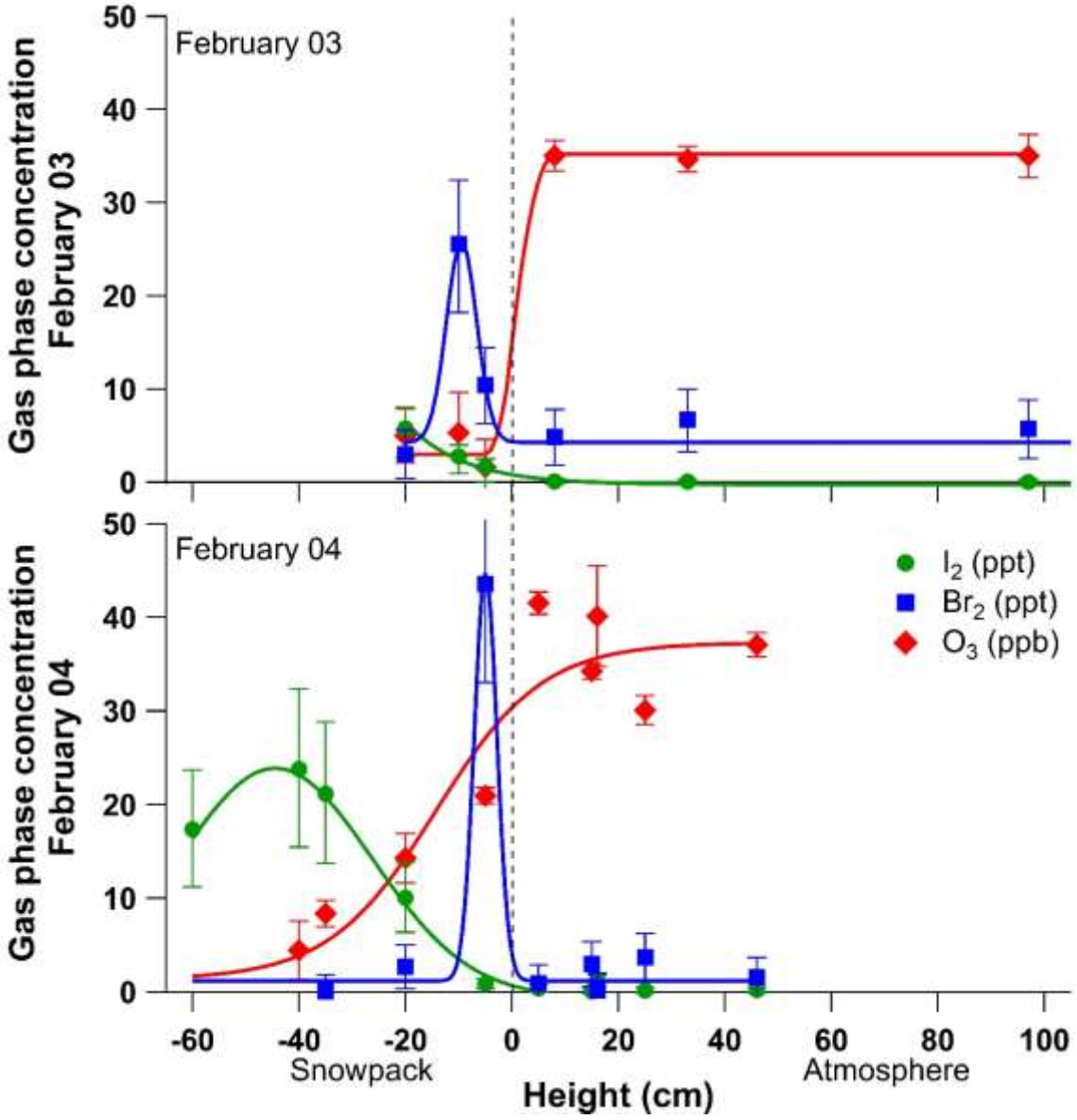

Figure 2.8 Depth profiles of near-surface atmospheric and snowpack interstitial air I_2, Br_2, and O_3 mole ratios. Measurements were made during daylight February 03 and 04, 2014 at heights above (positive) and below (negative) the snowpack surface. Error bars for species measured with CIMS (I_2 and Br_2) are propagated uncertainties. Error bars on the O_3 measurements are the standard deviations of 9 – 22 min averages at each height.

in behavior between I_2 and Br_2 with depth reflects two factors. First, I_2 photolyzes nearly four times faster than Br_2 (I_2 J_{max} = $2.9x10^{-3}$ s^{-1} vs Br_2 J_{max} = $8.6x10^{-4}$ s^{-1} for above the snowpack on February 2, 2014). Second, the multiphase recycling efficiency may be different for Br_2 and I_2, as discussed in chapter 3 of this work.

To further investigate photochemical I_2 production, the snowpack was exposed to artificial ultraviolet light (Figure 2.9). This experiment was conducted during the night and morning when solar radiation was low (<20 W/m^2). When exposed to artificial light, the snowpack rapidly produced up to 35 ppt of gas-phase I_2 at a depth of 10 cm (Figure 2.9). The radiation spectrum of the lights used (Figure 2.6) is adequate for the photolytic production of hydroxyl radicals from hydrogen peroxide and nitrite (Figure 2.10, reactions 21-23), but not for significant I_2 photolysis, which occurs most efficiently at wavelengths greater than 400 nm [Saiz-Lopez et al., 2004; Sander et al., 2006]. Upon snow illumination, Br_2 was also quickly produced in the snowpack interstitial air, yielding mole ratios of 40–80 ppt (Figure 2.9). With halogen production in the snowpack, O_3 decayed rapidly, via the chemistry shown in Figure 2.10. When the lights were turned off, both Br_2 and I_2 mole ratios decayed, and O_3 partially recovered. This molecular halogen decline was likely controlled by dilution with ambient air (wind pumping), a lack of photochemical halogen production, and adsorption/desorption of halogen species onto the snow. While snow grain chemical composition and exchange processes are complex [Bartels-Rausch et al., 2014], the rate of desorption from aqueous surfaces is often described as inversely proportional to the Henry's Law constant for that species [Jacob, 2000]. Since I_2 is more soluble (k_H = 41.9 M/atm at -20°C [Sander, 2015]) than Br_2 (k_H = 8.4 M/atm at -20°C [Sander, 2015]), its rate of desorption from the disordered snow interface is expected to be slower, as shown in Figure 2.9 by the slower decay in I_2 mole ratios after illumination ceases, and from the slower initial rise in I_2 mole ratios upon

illumination. I_2 and Br_2 were again observed upon snowpack re-illumination (Figure 2.9). This demonstrates that I_2 and Br_2 are both characterized by condensed-phase photochemical production mechanisms.

The I_2 multiphase photochemical production mechanism proposed here (Figure 2.10) is analogous to that for Br_2 production, which occurs first by condensed-phase photochemistry and then is greatly enhanced by gas-phase recycling of Br atoms in the presence of O_3 [Pratt et al., 2013; Wren et al., 2013]. The suggested mechanism for I_2 production begins in the disordered

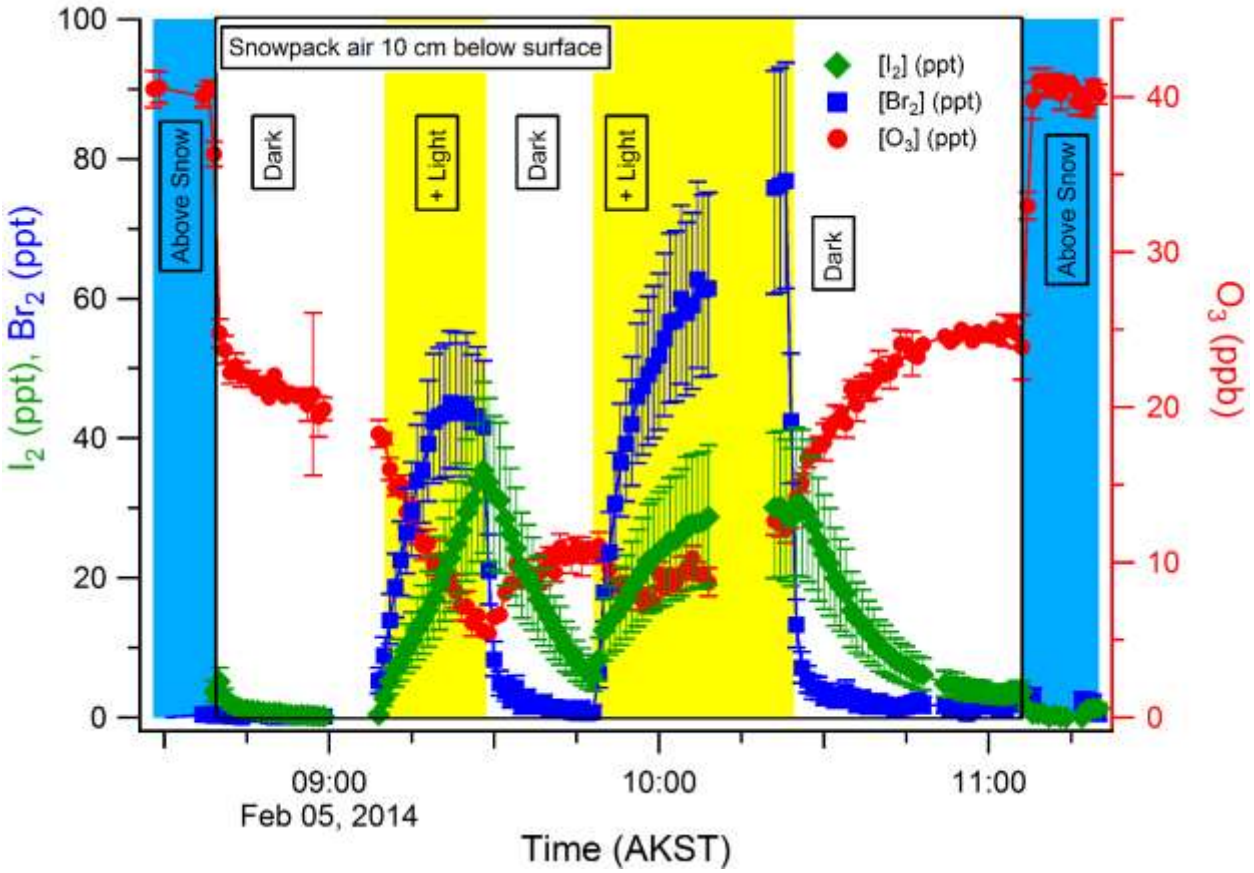

Figure 2.9 Snowpack artificial irradiation experiment. Snowpack interstitial air Br_2, I_2, and O_3 mole ratios are shown as 1 min averages for dark and artificial light measurement periods during an experiment on Feb. 5, 2014. Error bars for I_2 and Br_2 are propagated uncertainties. The interstitial air measurements were bracketed by near-surface (5 cm above the snowpack surface) measurements of boundary layer air. The duration of the experiment occurred before the sun rose, allowing for complete darkness when the artificial lights were off.

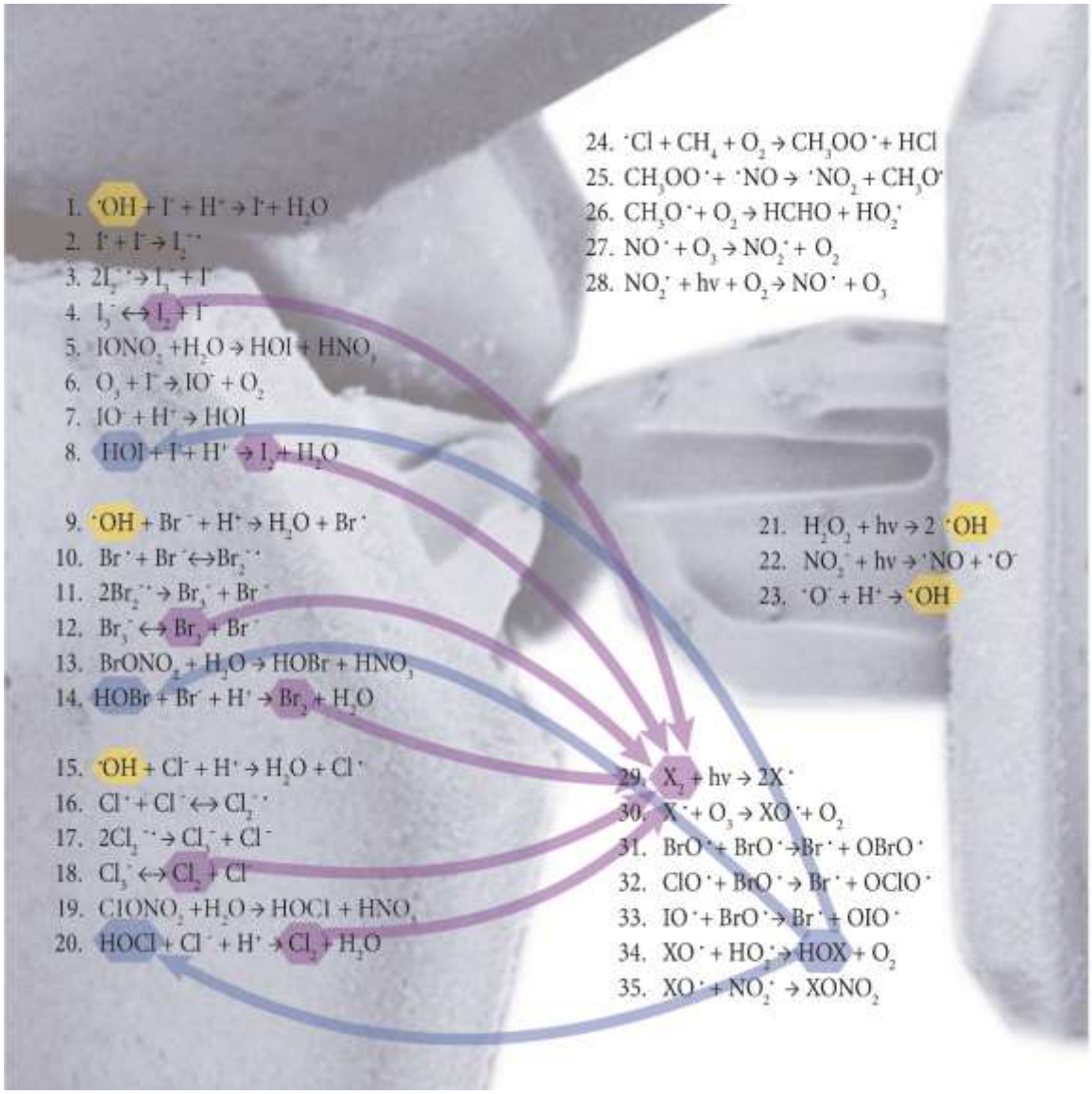

Figure 2.10 Snowpack halogen production and interstitial air halogen reactions. Major halogen reactions proposed to occur in the interstitial snowpack air, and within the snow surface are shown. Oxidation of I^- in the dark (reactions 6-8) is based on *Carpenter et al.* [2013]. Photochemical oxidation of Br^- (reactions 9-12) is based on *Abbatt et al.* [2010]. Cl^- and I^- photochemical oxidation reactions (reactions 15-18 and reactions 1-4, respectively) are suggested to be analogous. Snow crystal scanning electron microscopy image is an open source image from the Electron and Confocal Microscopy Laboratory, Agricultural Research Service, U. S. Department of Agriculture.

interface of the aqueous phase on the snow grain surface [Bartels-Rausch et al., 2014] with oxidation of I^- to an iodide radical by a photochemically produced oxidant (reaction 1), likely the hydroxyl radical, produced by nitrite photolysis in Utqiaġvik snow (reactions 22-23) [France et al., 2012]. The iodide radical then further reacts in solution to form I_3^- (reactions 2-3), which has been recently observed in snow samples spiked with I^- [Kim et al., 2016]. I_3^- then decomposes, forming I_2 (reaction 4). I_2 can then be released from the condensed phase to the gas phase, where it rapidly photolyzes in the presence of sunlight. The resulting iodine atoms react with O_3 to form IO (reaction 30). IO can then react with HO_2 to form HOI (reaction 34) or NO_2 to form $IONO_2$ (reaction 35), which can each then be re-deposited onto the snow grain surface to reproduce I_2 in a catalytic cycle similar to the 'bromine explosion' [Simpson et al., 2015]. Interhalogen reactions may also participate in the production of molecular halogens. HOBr has also been shown to oxidize Cl^- on frozen surfaces to form BrCl when the Br^-/Cl^- ratio is low [Adams et al., 2002; Huff and Abbatt, 2002; Wren et al., 2013]. Similarly, HOI or $IONO_2$ can react on frozen salty surfaces with Br^- and Cl^- to form IBr and ICl [Holmes et al., 2001]. The production of IBr via the reaction of HOI and Br^- is up to 200 times faster ($k=3.3 \times 10^{12}$ M^{-2} s^{-1} [Troy et al., 1991]) than the production of Br_2 via the reaction of HOBr and Br^- (reaction 14, $k=1.6 \times 10^{10}$ M^{-2} s^{-1} [Beckwith et al., 1996]). While the interactions between halogen species in the gas phase have received some study, the condensed phase interactions of halogens have been significantly understudied [Simpson et al., 2015].

2.4 Conclusions

Low mole ratios (0.3-1.0 ppt) of I_2 in the boundary layer air coupled with elevated I_2 mole ratios in the snowpack interstitial air suggest that the snowpack is a source of I_2 to the Arctic boundary layer. I_2 is observed in the snowpack interstitial air under naturally sunlit conditions,

and under artificial irradiation, but not in the dark, suggesting a photochemical production mechanism. The profiles of I_2 and Br_2 in and above the snowpack show significant differences, suggesting that the multiphase chemistry of iodine within the snowpack is different from that of bromine. The differences in iodine and bromine multiphase recycling are further addressed in chapter 3 of this work, which shows and discusses the first measurements of iodide in Arctic snow and contrasts them with measurements of bromide.

While the I_2 observed here is present in quite small concentrations above the snowpack relative to Br_2, they may still have a significant effect on the oxidation capacity of the Arctic boundary layer. The effect of the small concentrations of I_2 observed above the snowpack chemistry of the Arctic boundary layer is addressed in Chapter 4 of this work, which in which zero-dimensional modeling is used to evaluate the importance of iodine on O_3 depletion rates. Chapter 4 also utilizes zero-dimensional modeling to evaluate the impact of iodine chemistry on the daytime destruction of O_3 in the snowpack interstitial air. The effects of iodine chemistry on the Arctic boundary layer is further explored in chapter 6, which utilizes one-dimensional modeling to evaluate the vertical scale of iodine chemistry from a snowpack source, and the impact of a snowpack source of iodine on the vertical scale of bromine chemistry in the Arctic Boundary layer.

CHAPTER 3. MEASUREMENTS OF SPECIATED SNOWPACK PHASE IODINE

3.1 Introduction

Snowpack measurements of Br^- have been used as critical evidence that Br_2 production occurs in the snowpack [Simpson et al., 2005; Pratt et al., 2013]. Simpson et al. [2005] conducted a survey of the Cl^- and Br^- content of snow in the North Slope of Alaska (Figure 3.1), using Na^+ as a conserved tracer of sea salt aerosol. They found that the Cl^-/Na^+ ratio in Arctic snow was consistently close to the Cl^-/ Na^+ ratio of Arctic seawater. The Br^-/Na^+ ratio, on the other hand, varied widely, and was quite different from the seawater Br^-/Na^+ ratio. Simpson et al. [2005] also observed that the Br^- content of snow decayed much slower with distance from the coast than the Na^+ content. This can be seen in Figure 3.1, which shows that samples taken

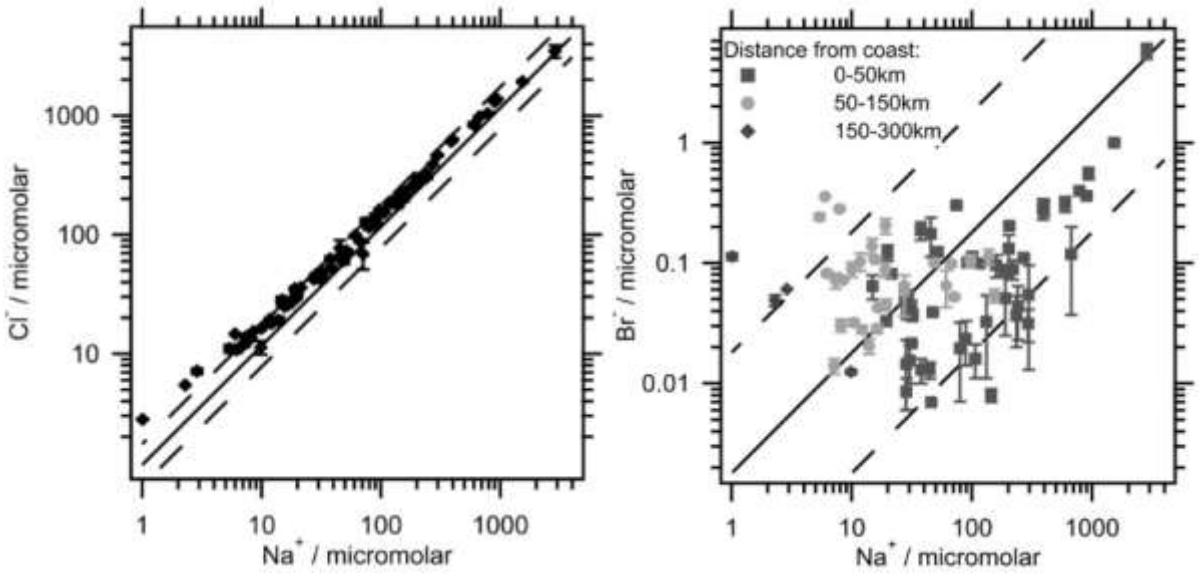

Figure 3.1 Cl^- (left) and Br^- (right) relative to Na^+ in snow samples from the North Slope of Alaska. Solid lines are the Cl^-/Na^+ and Br^-/Na^+ ratio of Arctic seawater. Dashed lines are 1.5 and 2/3 times the sea salt ratio for Cl^-, and 10 and 0.1 times the sea salt ratio for Br^-. Reproduced from Simpson et al. [2005].

farther from the coast are likely to be above the sea salt ratio line, while samples collected near the coast are likely to be below the sea salt ratio line. This observation strongly suggests that bromine is chemically released from snow independently of Na^+ and travels inland either in the gas phase or in bromine enriched aerosols. The mixture of enrichment and depletion observed suggests that sea salt is the initial source of Br^- and photochemistry causes redistribution to downwind sites.

While measurements of Br^- in snow have helped to elucidate the snowpack as both a source and sink of inorganic bromine to the atmosphere, very few measurements of iodide (I^-) in snow exist. Low concentrations of I^-, relative to Br^- and Cl^-, in snow make measurements by ion chromatography with electrochemical detection, which is generally used to measure Br^- and Cl^-, very difficult. Measurements of total soluble iodine in snow samples have been reported, however, using either neutron activation analysis or inductively coupled plasma mass spectrometry (ICPMS). Gilfedder et al. [2007a, 2007b, 2008] coupled ion chromatography with ICPMS to report measurements of speciated iodine from snow, rain, and aerosols in the mid-latitudes. They found that ~54% of iodine present in precipitation in inland Germany is present in the form of an unidentified organic iodine compound [Gilfedder et al., 2007b]. It is likely that organic iodine species, if present in polar snow, would require additional steps before it could photochemically oxidize and release to the atmosphere than inorganic species. However, it is unknown if organic iodine is prominent in polar snow, as no speciated measurements have been reported, and sources of iodine at the poles and in the mid-latitudes may be entirely different.

Relatively high concentrations of iodine in aerosols in the Arctic [Duce et al., 1966; Berg and Sperry, 1983; Sturges and Barrie, 1988], Antarctic [Duce et al., 1973], and mid-latitudes [Komabayasi, 1962; Duce et al., 1965] were among the first observations that suggested iodine chemistry is active in the boundary layer. In the Arctic Sturges and Barrie [1988] found that iodine

aerosols showed highest concentrations in the springtime at inland sites, but not at coastal sites. This is supported by the observations of Berg and Sperry [1983], who found that at Barrow (now Utqiaġvik) there was very little seasonality of iodine-containing aerosols. While there is no seasonal record of iodine-containing particles at a single site in Antarctica, Roscoe et al. [2015] found that springtime peaks in aerosol number concentrations at Halley and Neumayer correlated well with IO concentrations, suggesting that local production of iodine oxide particles may occur in the spring. At Aboa research station (Queen Maud Land, Antarctica), which is ~130 km inland from the Antarctic coast, Sipilä et al. [2016] observed HIO_3 in the gas phase but did not observe iodine new particle formation. In the mid-latitudes, it has been demonstrated that the main source of iodine to the atmosphere is macroalgae under oxidative stress [O'Dowd et al., 2002]. However, macroalgae are less common in polar regions [Keith et al., 2014]. Despite suggestions that microalgae colonies on the bottom of sea ice ("ice algae") could be the source of iodine to polar atmospheres [Saiz-Lopez and Blaszczak-Boxe, 2016], it has not been experimentally demonstrated that these species are capable of iodine production. Additionally, sea ice microalgae are only active when light penetrates the sea ice [Campbell et al., 2017], and not during the wintertime. It follows that local biological production of iodine would cease during the winter, and seasonality of iodine enrichment would be observed. The lack of a local source and mixed observations of the seasonality of iodine enriched leaves the sources of iodine to the Arctic atmosphere unclear.

Duce et al. [1966] reported the first and only previous measurements of iodine in Arctic snow. Using neutron activation analysis, they measured total chlorine, total bromine, and total iodine in snow sampled in transects away from the west coast (Chukchi sea) at Barrow (now Utqiaġvik) on January 30, 1965 (Figure 3.2). The wintertime collection of samples was intended

to isolate possible mechanisms of atmospheric iodine production suggested for mid-latitude observations at the time – sea surface bubble bursting and photochemical oxidation of I^- in the sea. The wintertime Arctic atmosphere is isolated from the ocean by sea ice, so bubble bursting does not occur, and is completely dark, so photochemistry is impossible. They observed that all three halogens decrease with distance from the coast (Figure 3.2). However, the decrease in iodine is much slower than that for bromine and chlorine. The I/Cl and I/Br ratios increase with

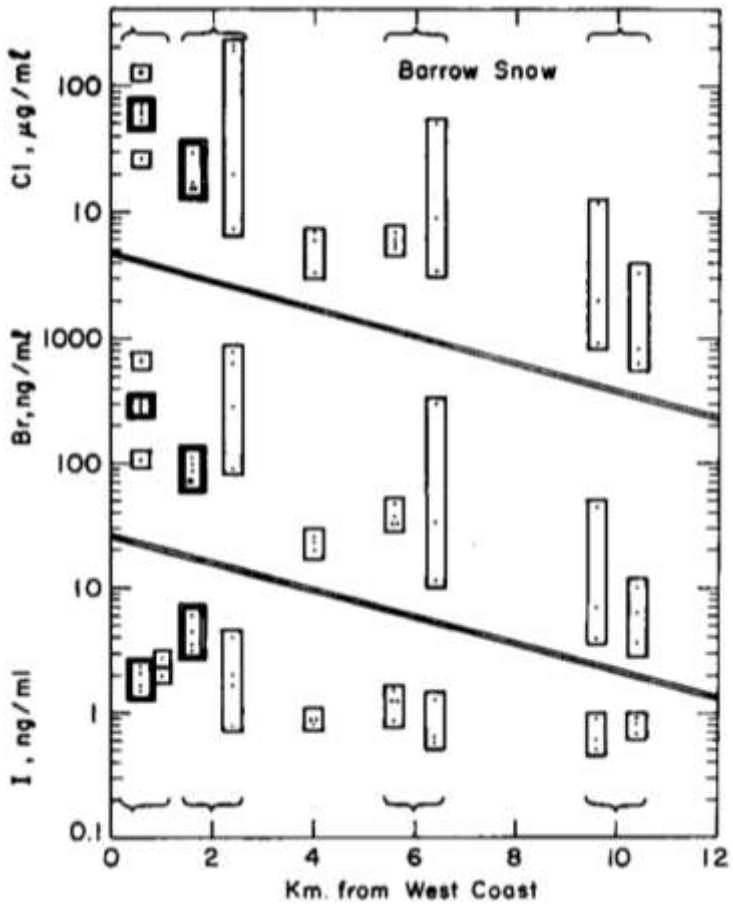

Figure 3.2 Total chlorine, total bromine, and total iodine measured from transects in Barrow (now Utqiaġvik). Plotted against distance from the west coast (Chukchi Sea). Single boxes are from ground lying snow, and double boxes are from blowing snow. Points within boxes represent measurements from 1-75 cm depths in the snowpack (ground lying snow) or heights from 30 – 210 cm (blowing snow). Reproduced from Duce et al. [1966]

increasing distance from the sea, implying two sources of halogens to the snow. First, a sea salt component, which accounts for nearly all the chlorine, some of the bromine, and very little of the iodine. Second an "atmospheric" component, containing nearly none of the chlorine, some of the bromine, and nearly all the iodine. This "atmospheric" component can be interpreted as a combination of gas and non-sea salt aerosol phase transport.

The Br/Cl ratio deviations from seawater observed by Duce et al. [1966] (Figure 3.3) are minor compared to the Br^-/Na^+ deviations observed by Simpson et al. [2005] (Figure 3.1). This is likely due to the wintertime sampling by Duce et al. [1966], and further supports the hypothesis that bromine enrichment and depletion in Arctic snow can be explained by photochemical Br_2 production. The I/Cl ratios deviate greatly from seawater (Figure 3.3). Unlike the Br/Cl ratios, they are not centered around the seawater ratio (black line); Rather, all of the samples measured are enriched with iodine. Additionally, while I does show some correlation with Cl, the intercept is non-zero. This suggests that iodine has a separate source or enrichment mechanism from bromine, such as the 'atmospheric component' described above. This mechanism may be either local enrichment of iodine from the sea, such as the biological mechanism proposed by Saiz-Lopez et al. [2015], or transport from lower latitudes in the gas – or more likely aerosol – phase. Duce et al. [1966] observed little variation of iodine content with depth in the snowpack relative to the variation of bromine and chlorine (Figure 3.2), suggesting that deposition of iodine to the snowpack is constant throughout snowfall in the fall and winter. This agrees with the coastal observations of iodine enriched aerosols by Sturges and Barrie [1988], and Berg and Sperry [1983]. A local biological production mechanism cannot explain wintertime enrichment, as light is necessary for algal growth [Campbell et al., 2017].

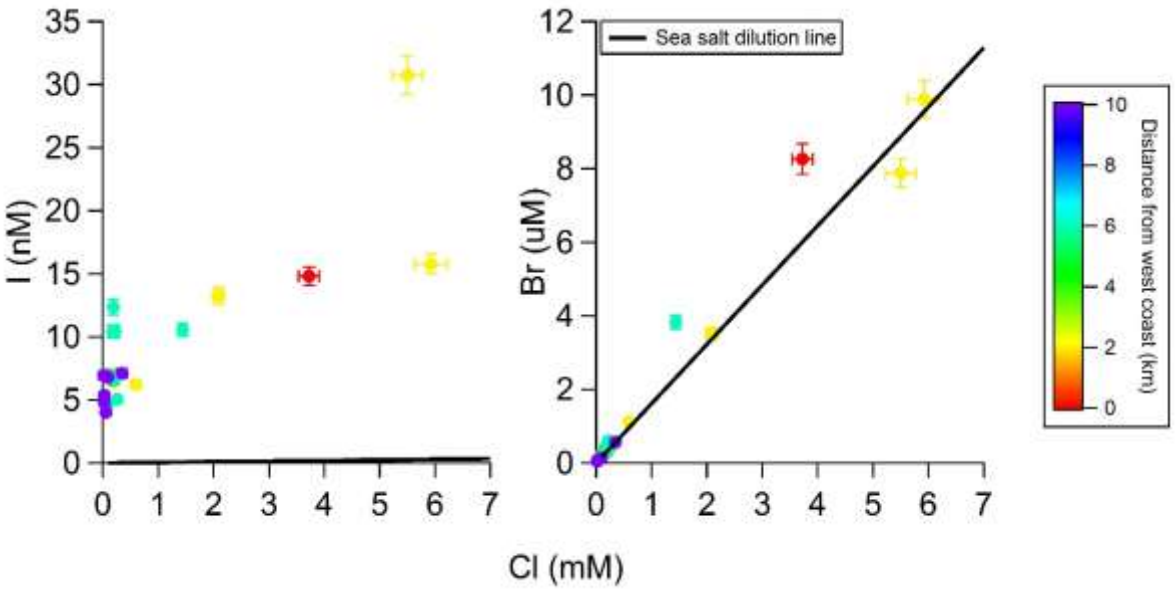

Figure 3.3 Total iodine and total bromine vs. total chlorine in snow samples from Utqiaġvik. Replotted data from Duce et al. [1966]

Total soluble iodine measurements in snow have also been reported in the Antarctic [Heumann et al., 1987; Frieß et al., 2010]. Heumann et al. [1987] were the first to measure iodine in Antarctic snow, reporting enrichments of I/Cl of 10-190 times the I/Cl ratio found in seawater. Frieß et al. [2010] sampled snow from a snow pit at Neumayer station, and found that they could trace the seasonality of snowpack iodine, with the highest iodine concentrations (up to 5 nM) in snow samples that were at the surface during the winter, as determined using $\delta^{18}O$, nitrate and methyl sulfonic acid content. They suggest that efficient photochemical release of iodine from the snowpack leads to low concentrations of iodine in snow that was at the surface during the summertime. This implies the same constant seasonality in the source that can be drawn from the data of Duce et al. [1966] for the Arctic.

Transport of iodine oxide particles from the mid-latitudes is a likely source for at least some of the observed iodine in the Arctic. However, mixed observations of iodine seasonality of aerosols, paired with the relatively sparse measurements of gas and snowpack phase iodine, and

the complete lack of speciated iodine measurements in both the Arctic and Antarctic, leaves uncertainty in the sources of iodine to polar environments. Here we discuss the iodine content and speciation of snow from the Arctic and Antarctic. Forty-eight snow samples from the Arctic and Antarctic were analyzed for I^-, iodate (IO_3^-), and organic iodine composition using ion chromatography coupled with inductively coupled plasma mass spectrometry (IC-ICPMS). Samples were from a variety of locations, including the Arctic tundra near the CIMS sampling site described in chapter 2, multiyear and first-year sea ice in the Arctic, and a variety of coastal and sea ice sites in the Antarctic. Vertical profiles of the snowpack were also conducted at the Arctic tundra site, allowing for analysis of the seasonality of iodine deposition in the Arctic.

3.2 Methods

3.2.1 Snow Sample Collection

Sample locations and descriptions are shown in Table 3.1. Utqiaġvik surface snow samples were collected ~50 m upwind (N-NE) of the CIMS sampling site on the Barrow Environmental Observatory (BEO) using a polypropylene scoop, which was rinsed with ACS grade methanol and air dried before sampling. Snow core samples were retrieved using an ice corer from the snowpack ~10 m upwind of the CIMS sampling site. Snow core samples were broken into ~10 cm sections. Samples were stored frozen (-10 °C to -40 °C) in polyethylene bags until the day of analysis. The sampler wore disposable gloves and remained downwind of the sampling site. Other Arctic samples, from snow on top of first-year sea ice and multi-year sea ice, were also collected in polyethylene bags with a clean polypropylene scoop. Some samples had been previously melted for analysis before refreezing. Antarctic snow samples were collected in polypropylene tubes from various locations (Table 3.1). Antarctic samples were stored frozen but briefly melted in shipping before being re-frozen.

Table 3.1 Snow sample Identifiers and descriptions. Samples marked with * were previously melted.

Sample identifier	Date collected	Location	Description
20140126EX01	January 26, 2014	BEO	Vertical profile surface snow
20140126EX03	January 26, 2014	BEO	12-17 cm inside diurnal profile hole
20140127EX01	January 27, 2014	BEO	Surface snow, 9:45AM
20140127EX02	January 27, 2014	BEO	Surface snow, 2:30PM
20140128EX01	January 28, 2014	BEO	Surface snow, 9:45AM
20140128EX02	January 28, 2014	BEO	Surface snow, 2:45PM
20140203EX01	February 03, 2014	BEO	Inside diurnal profile hole from February 1-2
20140203EX02	February 03, 2014	BEO	Surface snow
20140204EX01	February 04, 2014	BEO	Surface near vertical profile hole
20140204EX02	February 04, 2014	BEO	Inside vertical profile hole
20140205EX01	February 05, 2014	BEO	Surface snow
20140205EX02	February 05, 2014	BEO	Midway in vertical profile hole
20140205EX03	February 05, 2014	BEO	Deep in vertical profile hole
20140205EX04	February 05, 2014	BEO	Lights in snow hole ~3pm
20140209EX01	February 09, 2014	BEO	~10am overnight lights surface sample
20140223EX01	February 23, 2014	BEO	Snow core first 10 cm
20140223EX02	February 23, 2014	BEO	Snow core 10-20 cm
20140223EX03	February 23, 2014	BEO	Snow core 20-30 cm
20140223EX04	February 23, 2014	BEO	Snow core 30-40 cm
20140223EX05	February 23, 2014	BEO	Surface snow, ~4:30PM
20140224EX01	February 24, 2014	BEO	Surface snow, ~8:00AM
20140226EX01	February 26, 2014	BEO	Surface snow, from lights
20140228EX01	February 28, 2014	BEO	Snow core first 10 cm
20140228EX02	February 28, 2014	BEO	Snow core 10-20 cm
20140228EX03	February 28, 2014	BEO	Snow core 20-30 cm

Table 3.1 Continued.

20140228EX04	February 28, 2014	BEO	Snow core 30-40 cm
20140416EX01	April 16, 2014	Barneo Lat 87 01.00N Lon 90 35E	20-30 cm depth surface
20140418EX01	April 18, 2014	Barneo Lat 89 59.118N Lon 01 29.5801W	15 cm snow depth
*20130511MYISY	May 11, 2013	Switchyard UW-10 Lat 83 00.320N Lon 55 01.439W	6.5 cm
*20130515MYISY	May 15, 2013	Switchyard UW-15 Lat 86 20.923N Lon 29 04.944W	9 cm
*20140510MYIIG	May 10, 2014		#6 MY ice 5-10 cm
*20141015MYIIG	October 15, 2014		#7 MY ice 10-15 cm
20140227FYI01	February 27, 2014		First-year ice site 1
20140227FYI02	February 27, 2014		First-year ice site 2
*S121011I1 - 10	October 11, 2012	Antarctica	Iceberg surface – OBBARD Site 2
*S121015B1 - 24	October 15, 2012	Butter Pt., Antarctica	Butter Pt. surface – snow 4 cm thick
*S121015B2 - 21	October 15, 2012	Butter Pt., Antarctica	Butter Pt. on ice – bottom 8 cm thick
*S121025B2 - 40	October 25, 2012	Butter Pt., Antarctica	Butter Pt. surface
*S121025B3 - 42	October 25, 2012	Butter Pt., Antarctica	Butter Pt. surface
*S121025I1 - 43	October 25, 2012	Antarctica	Iceberg surface 36 cm depth
*S121025I2 - 35	October 25, 2012	Antarctica	Iceberg 22 cm depth
*S121020E1 - 20	October 20, 2012	Cape Evans, Antarctica	Cape Evans – surface
*S121102B1 - 113	November 02, 2012	Butter Pt., Antarctica	Butter Pt. surface
*S12110502C - 72	November 05, 2012	Antarctica	DOAS 2 -3rd 50cm depth
*S121106B1 - 81	November 06, 2012	Butter Pt., Antarctica	Butter Pt. surface
*S121106I1 - 75	November 06, 2012	Antarctica	Iceberg surface – tips of sastrugi
*S121107C1 - 106	November 07, 2012	Cape Bird, Antarctica	Cape Bird surface
*S121107C3 - 103	November 07, 2012	Cape Bird, Antarctica	Cape Bird surface

3.2.2 IC-ICPMS Analysis of Speciated Iodine

Measurements of inorganic iodine were conducted at the Pacific Northwest National Laboratory Environmental and Molecular Sciences User Facility from October 21, 2015 – October 31, 2015. An Agilent Technologies 1200 series ion chromatograph (IC) equipped with a Thermo Scientific AS16 analytical column and an AG16 guard column was utilized to separate iodine species, including I^-, IO_3^-, and organic iodine. These are the same analytical columns used by Gilfedder et al. [2007a, 2007b, 2008]. An ESI Apex IR nebulizer was used to couple the IC with a Thermo Scientific Element XR inductively coupled plasma mass spectrometer (ICPMS) for quantification. 100 µL injections of snowmelt samples, standards, and blanks were made using an Agilent 1260 series autosampler which was temperature controlled to 18°C. A calibration curve, consisting of NaI, was constructed containing samples with concentrations in the range of 1 - 20 nM. A blank sample chromatogram, and one for the 1.0 nM standard are shown in Figure 3.4. The NaI calibration was applied to all iodine species, as ICPMS sensitivity does not vary with iodine speciation. An example calibration curve from October 22, 2015, is shown as Figure 3.5. The area under the curves was used for quantification. The calibration curve was obtained at least daily, with periodic lone standards interspersed with samples for sensitivity checks. The variation of the sensitivity of the instrument is shown in Figure 3.6. 3σ limits of detection for I^- and IO_3^- were 54-96 pM, and 63-270 pM respectively. The difference between the I^- and IO_3^- limits of detection are due to noise in the background signal, which can be seen in Figure 3.3. I^- enrichment factors relative to seawater were calculated using the ratio of I^- to Na^+ in seawater off the coast of Iceland ($^{I^-}/_{Na^+}{}_{sw}$ = 6.2 x 10^{-8}) [Waite et al., 2006] and Equation 3.1.

$$Enrichment\ Factor = \frac{{}^{I^-}/_{Na^+}{}_{snow}}{{}^{I^-}/_{Na^+}{}_{sw}} \qquad \text{E3.1}$$

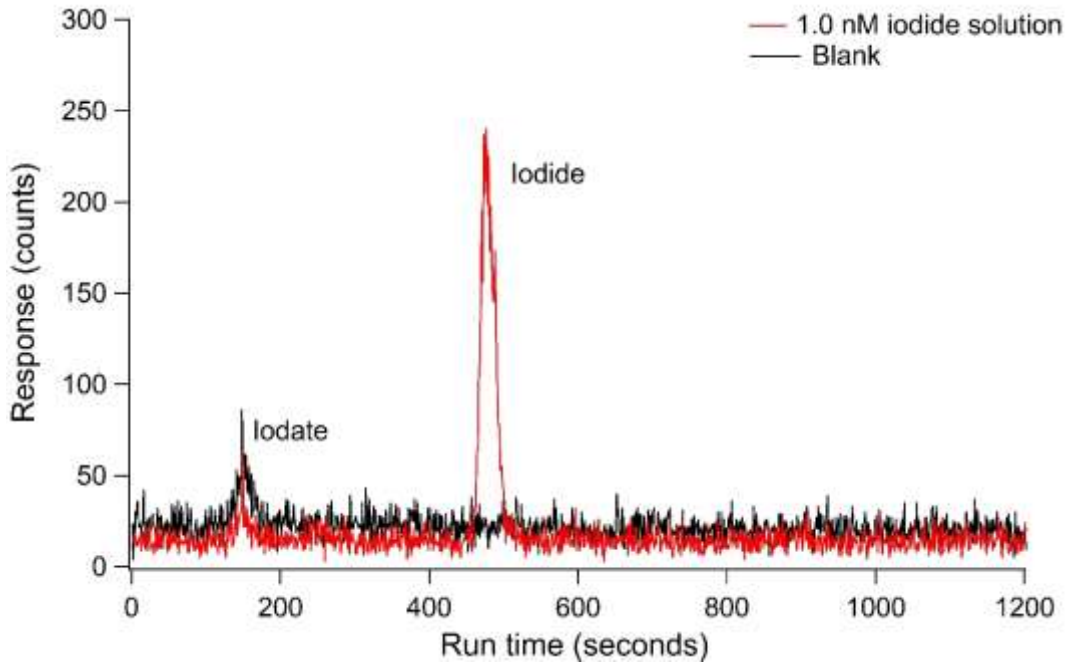

Figure 3.4 Chromatogram for the lowest concentration calibration standard (1 nM), along with a blank measurement.

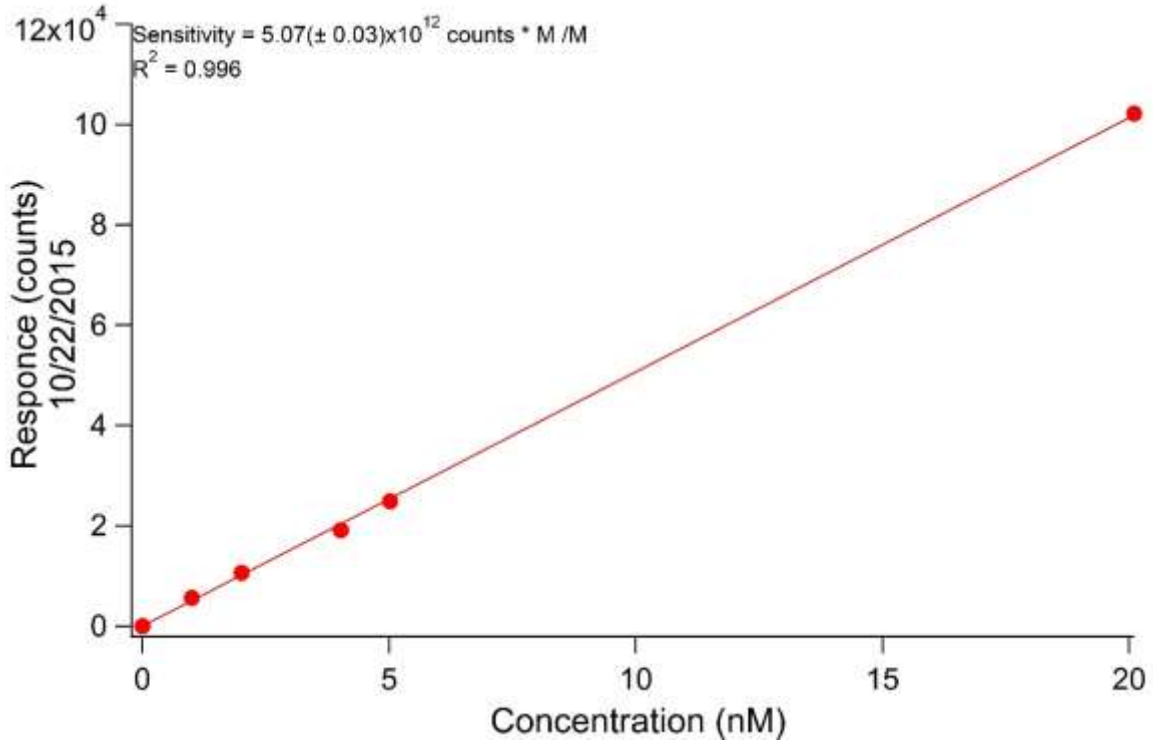

Figure 3.5 Linear calibration curve example from October 22, 2015. The sensitivity of the instrument for this calibration is 5.07(±0.03) x10^{12} counts*M/M.

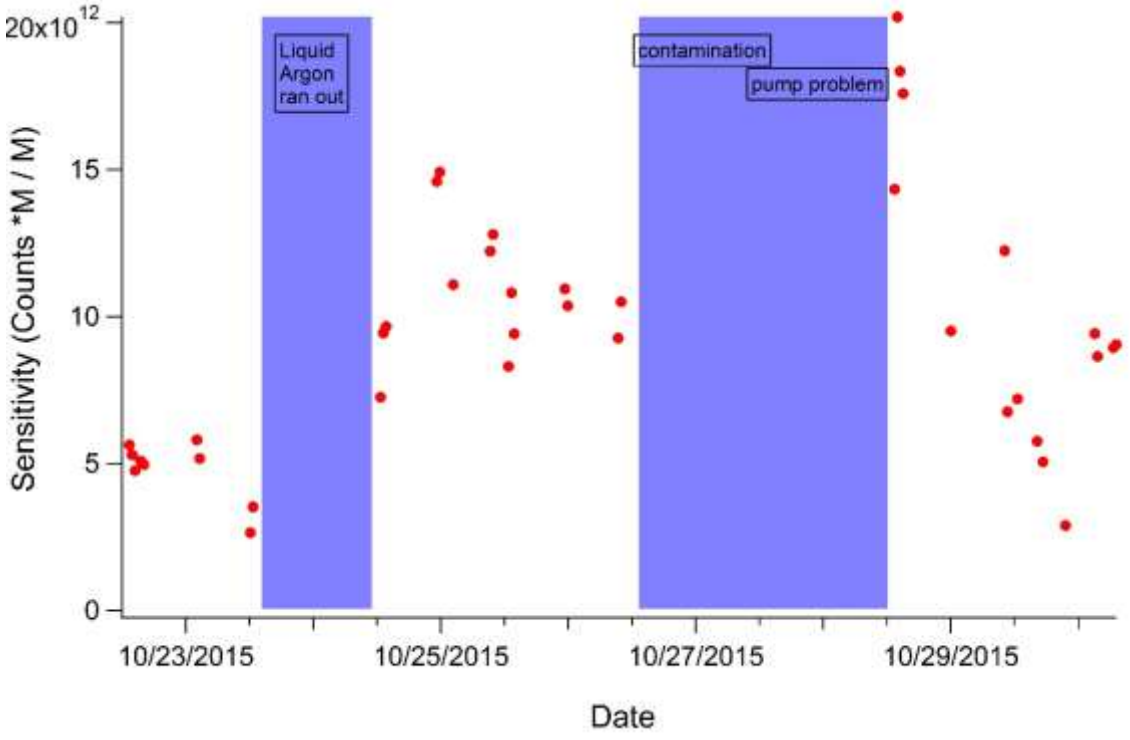

Figure 3.6 Sensitivity of the IC-ICPMS system to iodide over the measurement period.

1100 system with an ultralow pressure trace cation concentrator column (TCC-ULP1, Dionex), a CG12A guard column (Dionex), and a CS12A analytical column (Dionex); Methanesulfonic acid (20mM) was used as an eluent. Br^- and Cl^- were measured on an ICS-2100 system with an ultralow pressure trace anion concentrator column (UTAC-ULP1, Dionex), an AG18 guard column (Dionex), and an AS18 analytical column (Dionex); A potassium hydroxide gradient generated by an EGC III KOH system was used as an eluent. Both the ICS-1100 and ICS-2100 systems use heated conductivity cells (DS6, Dionex) for detection. Br^- enrichment factors were calculated based on seawater off the coast of Utqiaġvik ($Br^-/Na^+ = 2.0 \times 10^{-3}$) [Simpson et al., 2005].

3.2.3 Theoretical Limit on Snowpack Interstitial Air I_2

The theoretical maximum mole ratio of I_2 in the snowpack interstitial air if I^- were completely converted to I_2, and completely contained in the snowpack interstitial air is shown by Equation 3.2 below.

$$[I_2]_{max} = [I^-]_{avg} * \frac{1\ mol\ I_2}{2\ mol\ I^-} * f_s * \frac{1}{f_a} * mv_{air} \qquad \text{E3.2}$$

Where $[I^-]_{avg}$ is the average concentration of I^- in the surface snowpack, f_s is the liquid water content of the snowpack as a unitless fraction (0.4), f_a is the air fraction of the snowpack (0.6), and mv_{air} is the mole volume of air at -20°C (20.8 L/mol).

3.3 Results and Discussion

3.3.1 Iodine Content and Speciation of BEO Snow Samples

The iodine content of snow samples collected in the BEO during the 2014 campaign was primarily present as I^- and IO_3^-, with very little evidence of organic iodine. This can be seen in Figure 3.7, which shows overlaid chromatograms of the BEO samples. There was wide variation in the fraction of iodine present as I^- and IO_3^- in the samples and neither correlated well with Na^+ (Figure 3.8), suggesting that sea salt is not a strong direct source of either species to the snowpack. Table 3.2 contains the iodine content of all snow samples analyzed. The total I in Table 3.2 is the sum of I^- and IO_3^-.

Figure 3.9 shows the Cl^- (top), Br^-, (middle), and I^- (bottom) content of snow vs. the Na^+ content of snow for BEO samples. The Cl^-/Na^+ ratio shows little deviation from the seawater ratio, except at low salt content, as shown by low Na^+ content, when Cl^- is slightly depleted. The Br^-/Na^+ ratio shows a greater variation, with the Br^-/Na^+ ratio being 0.58 - 2.0 times the seawater Br^-/Na^+ ratio, suggesting that redistribution of snowpack bromine is occurring. However, the

enrichment of Br^- is small compared to that of I^-. All the snow samples collected in 2014 from BEO show a considerable enrichment (20-2000 times the seawater ratio) of I^-/Na^+.

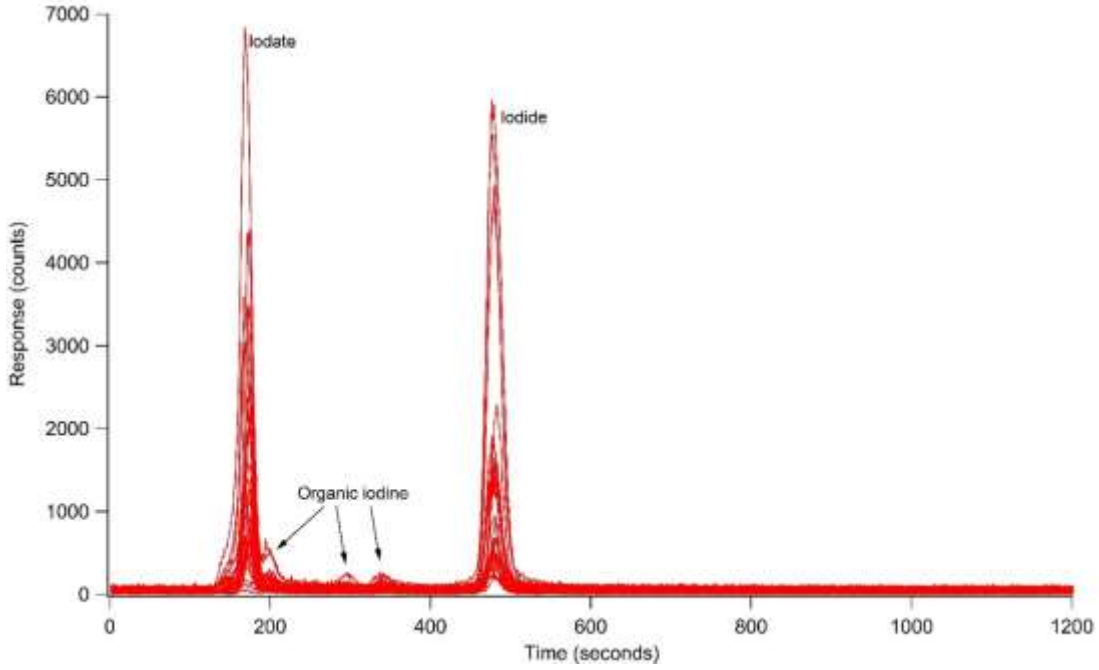

Figure 3.7 Chromatogram of BEO samples. Iodate, iodide and organic iodine peaks are labeled.

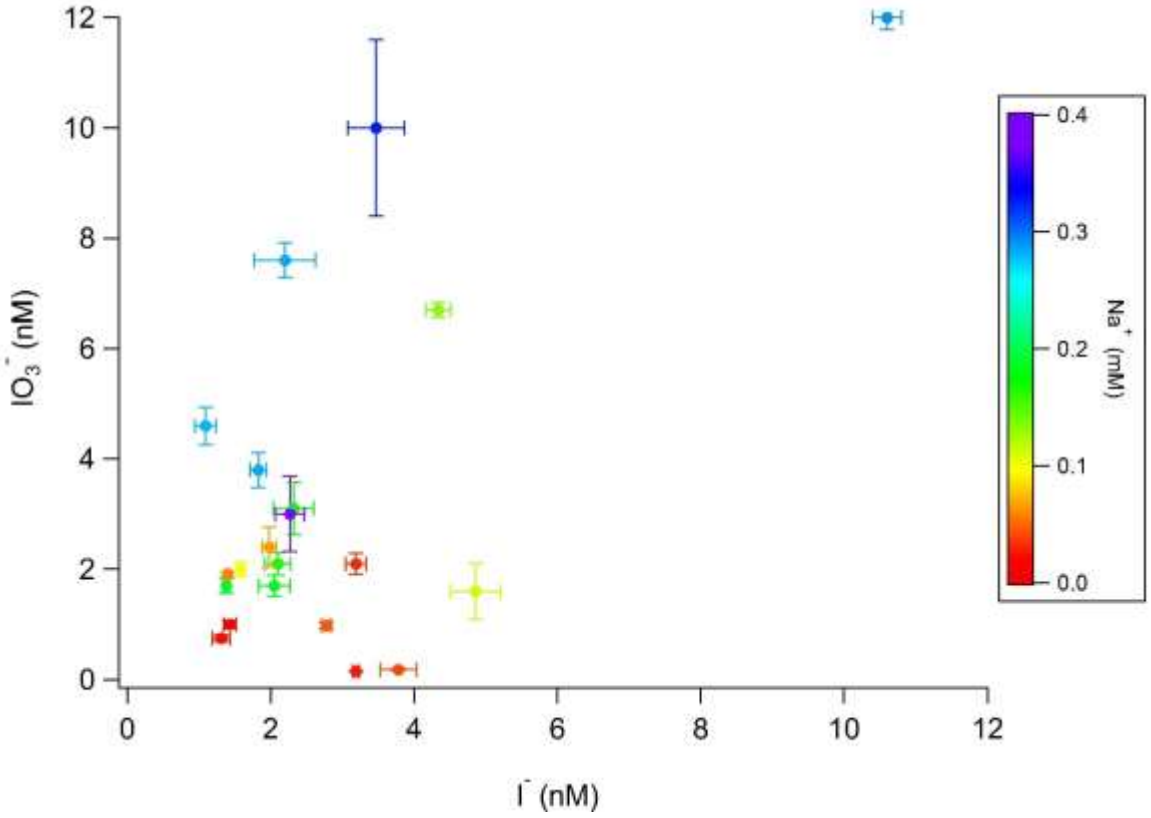

Figure 3.8 Iodate vs. iodide and sodium in BEO samples. Error bars are the standard deviation of triplicate measurements.

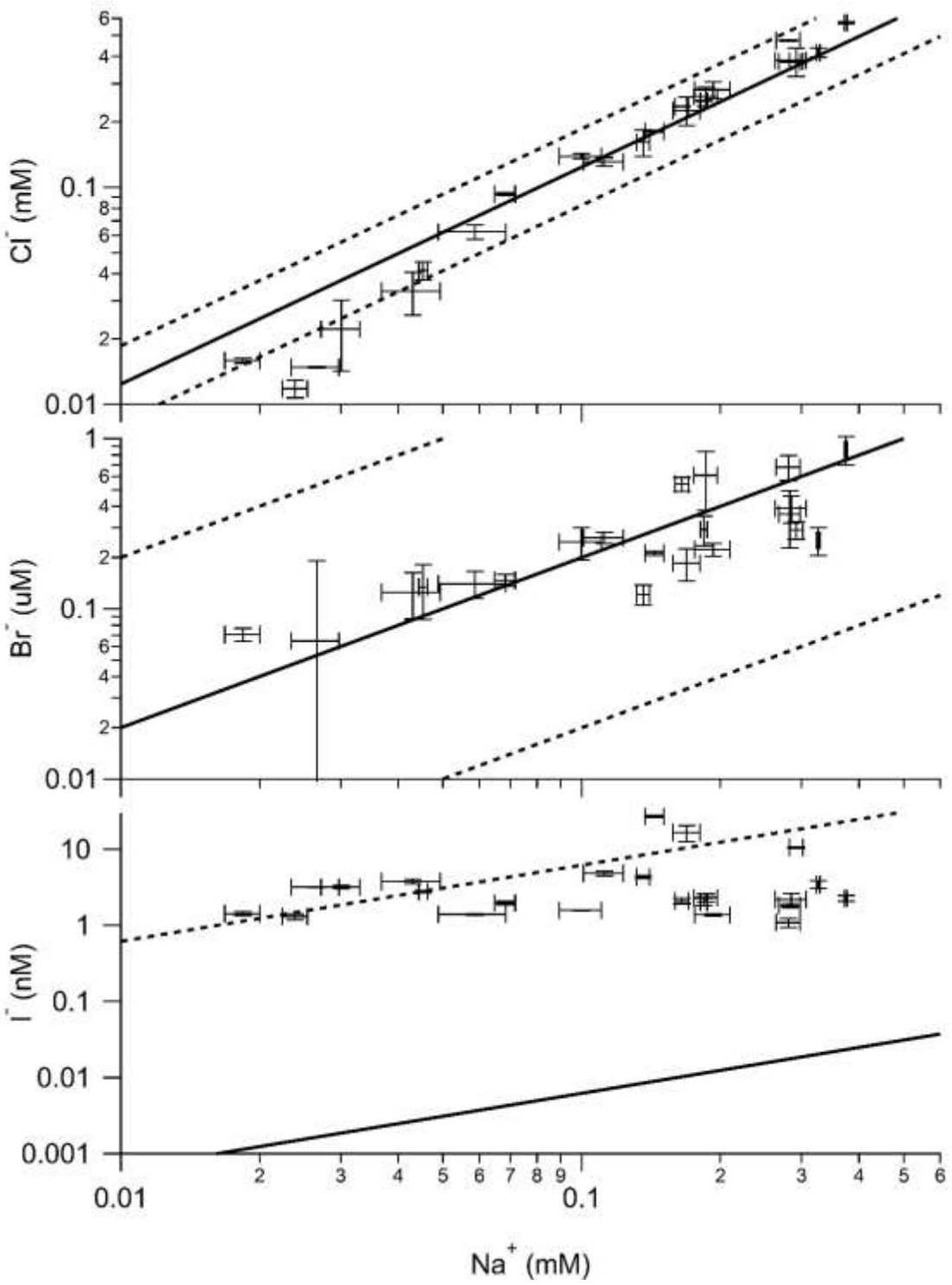

Figure 3.9 Cl^- (top), Br^- (middle), and I^- (bottom) relative to Na^+ in snow samples collected in the BEO in Spring 2014. Error bars are the standard deviation of triplicate measurements. Solid lines represent the halide/Na^+ ratio from Arctic sea water. Dashed lines are 3/2 and 2/3 times the seawater ratio for Cl^-, 10 and 1/10 times the seawater ratio for Br^-, and 1000 times the seawater ratio for I^-.

3.3.2 Vertical Profiles of I^- and Br^- at the BEO

While bromide (Br^-) shows no consistent enrichment (relative to the seawater Br^-/Na^+ ratio) with snowpack depth (Figure 3.10), I^- was more enriched deep in the snowpack than at the surface in January and February 2014 snow meltwater (Figure 3.10). Here we primarily discuss the content of snow present as I^-, as it is the most directly comparable to Br^-. I^- was observed at concentrations of 0.8 – 27.3 nM (Figure 3.9, Table 3.2) that are substantially enriched relative to sodium (Na^+), at up to ~1900 times the seawater ratio (I^-/Na^+) (Figure 3.9). The I^- concentrations in the surface (top 7 cm) snowpack meltwater (2.0 ± 0.6 nM, Figure 3.9, Table 3.2) were sufficient to produce ~1600 ppt of I_2 if I^- were wholly converted to I_2 and contained in the snowpack interstitial air. In comparison, snow meltwater Br^- ranged from partially depleted to double that in seawater (0.58 - 2.0 times the seawater Br^-/Na^+ ratio, Figure 3.9). Previous measurements of Br^-/Na^+ ratios in coastal surface snow have shown bromide enrichments to increase from late winter (1.5-5 times the seawater Br^-/Na^+ ratio) through early spring (20-72 times the Br^-/Na^+ ratio in seawater), which is consistent with active heterogeneous recycling of bromine on the snowpack [Simpson et al., 2005; Xu et al., 2016]. The decreased enrichment of I^- at the surface indicates that iodine near the surface has migrated, either redepositing deeper in snowpack or being lost from the snowpack surface to the atmosphere, following polar sunrise. While the source of I^- enrichment in the Arctic snowpack requires further investigation, deposition of gas or particle phase iodine is consistent with earlier findings of aerosol enriched in iodine up to 20,000 times the I/Na ratio of seawater [Sturges and Barrie, 1988]. The relative consistency of I^- enrichment with depth past the surface layer is also consistent with the findings of Duce et al. [1966], who say very little change in the iodine content of snow with depth in samples from the wintertime. Future measurements of the spatial and temporal heterogeneity of snowpack I^- enrichment after sunrise are needed to elucidate the migration of iodine in the Arctic system.

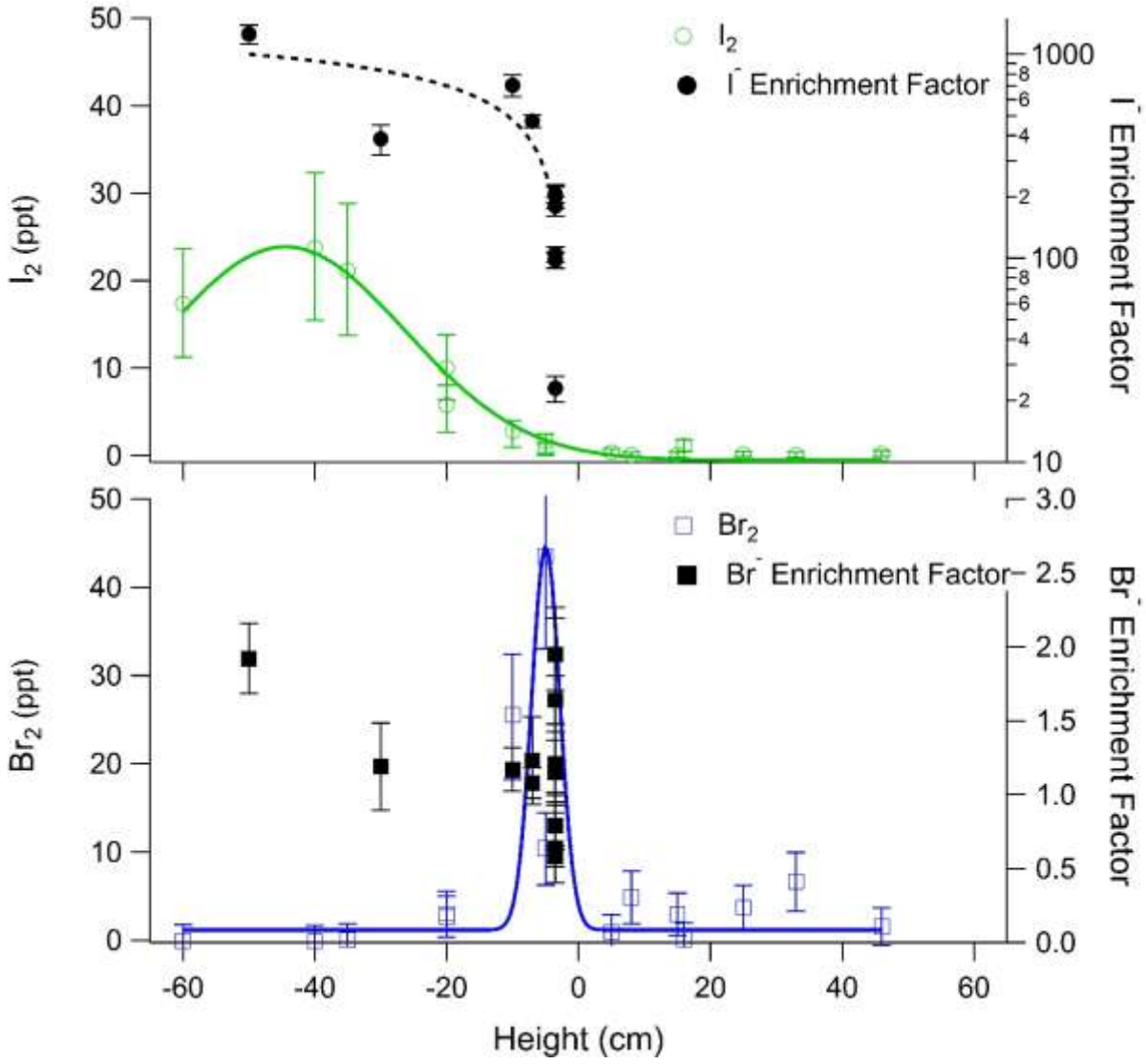

Figure 3.10 Br_2 and I_2 measurements from vertical profiles on February 03 and 04, 2014 (see chapter 2). Br^- and I^- enrichment factors relative to seawater from vertically resolved snow samples between January 26 and February 09, 2014. Error bars on enrichment factors are propagated uncertainties from triplicate analysis of I^-, Br^- and Na^+ analysis.

3.3.3 Iodine Content and Speciation of Snow Samples from on Top of Arctic Sea Ice

Eight samples from other Arctic locations were analyzed for speciated iodine. These consisted of two samples of snow from on top of first-year sea ice and six samples from snow on top of multiyear sea ice. The two samples from atop first-year ice were collected during the 2014 campaign and are directly comparable to the BEO snow samples. The samples from atop multiyear ice were collected later in the year (two from May 2013, two from April 2014, one from May 2014, and one from October 2014). As with the snow samples from the BEO most iodine was present as I^- and IO_3^- in all of the Arctic samples. The two samples from atop first-year ice showed similar I^- and IO_3^- concentrations to the BEO samples (total I 7.3 & 3.8 nM vs. 1.0-30.5 nM for BEO samples, Table 3.2). The samples from on top of multiyear ice, on the other hand, showed lower concentrations of iodine (total I 0.18 – 14 nM). It may be tempting to conclude that, as Simpson et al. [2005] observed for Br^-, there could be spatial variability in snow I^- concentrations – indicating that active redistribution of iodine occurs from coastal to inland snow. However, the vertical profile observations suggest that, as reported by Frieß et al. [2010], significant loss of iodine from the snowpack occurs when sunlight is available leading to temporal variability in the iodine content of surface snow. Since the collection dates of these samples are later in the year than other samples, photochemical loss of iodine from snow to the gas phase is the likely cause of lower iodine content. Without further sampling, it is impossible to tell if there is significant spatial variability in the iodine content of Arctic snow.

3.3.4 Iodine Content and Speciation of Antarctic Snow Samples

Fourteen Antarctic snow samples collected in spring (October – November) 2012 were analyzed for speciated iodine. Table 3.2 contains the iodine content of all snow samples analyzed. Unlike the Arctic samples, which showed little organic iodine content, the Antarctic samples

almost universally contained organic iodine. The organic iodine was present as a single peak, which nearly coeluted with IO_3^- (Figure 3.11). Because the IO_3^- and organic iodine peak lacked resolution, the reported values for IO_3^- in Table 3.2 are of the sum of the organic and IO_3^- concentrations. Generally, the total iodine content of the Antarctic samples was higher than that observed for the Arctic samples, averaging 50 nM vs. 10 nM for the Arctic samples. The total iodine concentrations are also larger than those observed by Frieß et al. [2010] (max 5.1 nM) or by Heumann et al. [1987] (max 14.2 nM). However, the I^- content of the Antarctic samples is smaller than the Arctic samples, averaging only 0.7 nM (The Arctic average was 3.5nM). Because the sampling procedures were different for Antarctic samples and Arctic samples, contamination of one and not the other is possible.

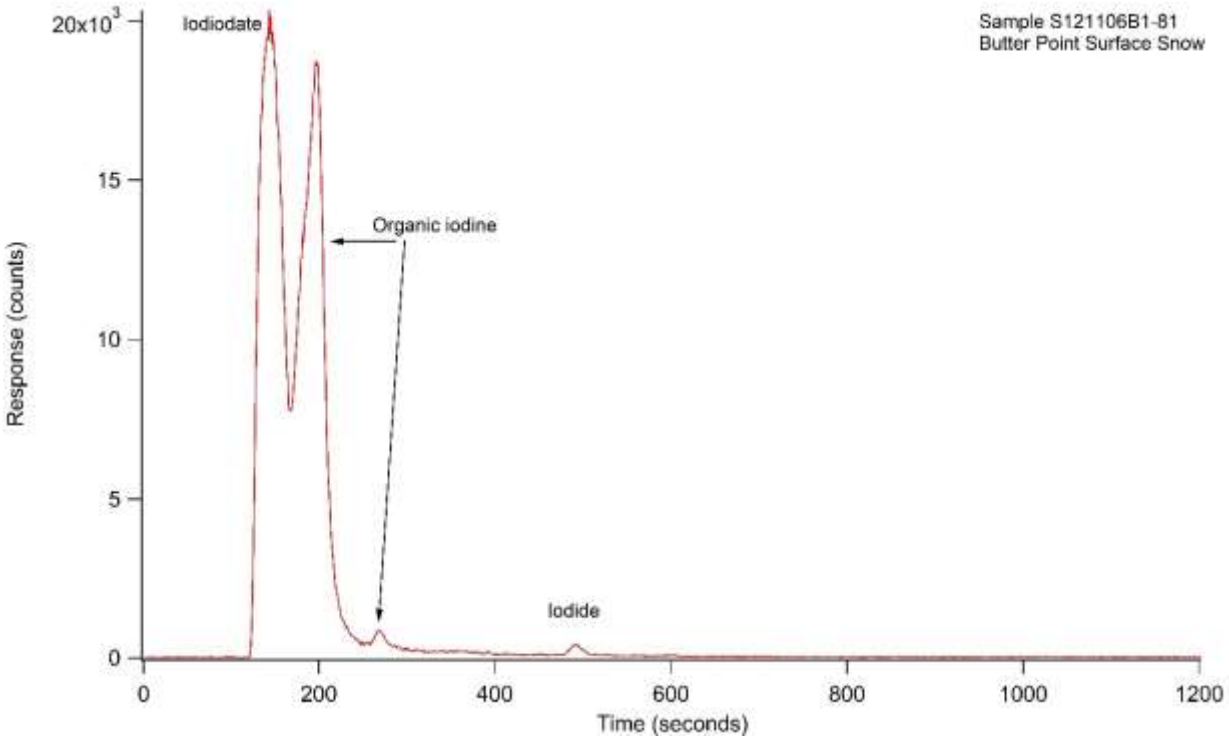

Figure 3.11 Chromatogram of a snow sample from Butter Point, Antarctica.

Table 3.2 I^-, IO_3^-, and total I content of analyzed samples. * Sample had been previously melted.

Sample identifier	I^- (nM)	±	%	IO_3^- (nM)	±	%	Total I (nM)	±	%
20140126EX01	1.1	0.1	13%	4.6	0.3	7%	5.7	0.4	8%
20140126EX03	0.89	0.09	11%	0.07	0.03	44%	1.0	0.1	11%
20140127EX01	2.0	0.2	11%	1.7	0.2	12%	3.7	0.4	11%
20140127EX02	1.8	0.1	6%	3.8	0.3	8%	5.6	0.4	7%
20140128EX01	2.3	0.3	12%	3.1	0.5	15%	5.4	0.7	13%
20140128EX02	2.1	0.2	8%	2.1	0.2	9%	4.2	0.3	8%
20140203EX01	2.0	0.1	5%	2.4	0.4	15%	4.4	0.3	7%
20140203EX02	0.8	0.2	28%	1.6	0.5	32%	2.4	0.7	29%
20140204EX01	3.2	0.3	8%	6.7	0.4	6%	9.9	0.6	6%
20140204EX02	4.9	0.4	7%	1.6	0.1	7%	6.5	0.5	7%
20140205EX01	2.3	0.2	9%	3.0	0.7	23%	5.3	0.8	16%
20140205EX02	1.40	0.03	2%	1.92	0.05	3%	3.31	0.08	2%
20140205EX03	1.43	0.08	6%	1.03	0.08	7%	2.5	0.1	6%
20140205EX04	1.58	0.02	1%	2.0	0.1	7%	3.5	0.1	4%
20140209EX01	1.38	0.05	4%	1.7	0.1	8%	3.0	0.1	4%
20140223EX01	4.3	0.2	4%	6.7	0.1	2%	11.0	0.3	3%
20140223EX02	3.8	0.3	7%	0.18	0.02	11%	4.0	0.2	6%
20140223EX03	3.19	0.04	1%	0.15	0.01	5%	3.34	0.04	1%
20140223EX04	3.2	0.1	5%	2.1	0.2	9%	5.3	0.2	4%
20140223EX05	3.5	0.4	11%	10.0	1.6	16%	13	2	15%
20140224EX01	2.2	0.4	20%	7.6	0.3	4%	9.8	0.7	7%
20140226EX01	27.3	0.9	3%	3.15	0.01	0.4%	30.5	0.9	3%
20140228EX01	10.6	0.2	2%	12.2	0.2	2%	22.83	0.08	0.3%
20140228EX02	11.5	7.6	66%	12.8	4.2	32%	24.3	5.4	22%
20140228EX03	2.78	0.07	2%	0.98	0.06	6%	3.77	0.04	1%
20140228EX04	1.3	0.1	9%	0.75	0.06	8%	2.1	0.2	9%
20140416EX01	0.62	0.03	5%	1.6	0.2	10%	2.2	0.2	9%
20140418EX01	0.45	0.03	7%	0.58	0.03	5%	1.03	0.04	4%

Table 3.2 Continued.

*20130511MYISY	0.8	0.2	24%	13	2	17%	14.1	2.4	17%
*20130515MYISY	0.51	0.02	5%	4.4	0.8	18%	5.0	0.8	16%
*20140510MYIIG	0.5	0.1	19%	0.10	0.06	63%	0.65	0.06	10%
*20141015MYIIG	0.14	0.05	38%	0.04	0.04	87%	0.18	0.08	46%
20140227FYI01	1.8	0.1	8%	111	7	6%	113	7	6%
20140227FYI02	0.7	0.3	42%	17	4	21%	18	4	22%
*#S121011I1 - 10	0.5	0.1	22%	46	2	4%	47	2	4%
*#S121015B1 - 24	0.35	0.02	6%	61	8	12%	62	8	12%
*#S121015B2 - 21	0.5	0.1	23%	58	4	7%	59	4	7%
*#S121025B2 - 40	0.53	0.07	14%	45.3	0.7	2%	45.8	0.7	2%
*#S121025B3 - 42	1.3	0.1	8%	79.6	0.7	1%	81.0	0.7	1%
*#S121025I1 - 43	0.69	0.07	10%	45	3	6%	45	3	6%
*#S121025I2 - 35	0.35	0.04	11%	17	1	6%	18	1	6%
*#S121020E1 - 20	0.43	0.05	12%	40.1	0.9	2%	40.5	0.9	2%
*#S121102B1 - 113	0.6	0.2	31%	68.6	0.5	1%	69.2	0.5	1%
*#S12110502C - 72	0.19	0.03	14%	1.9	0.7	35%	2.1	0.7	32%
*#S121106B1 - 81	0.98	0.04	4%	140	10	11%	140	10	11%
*#S121106I1 - 75	0.85	0.08	9%	85.9	3.0	4%	87	3	3%
*#S121107C1 - 106	1.2	0.2	19%	12.9	2.6	20%	14	3	19%
*#S121107C3 - 103	1.95	0.02	1%	44.0	1.1	2%	46	1	2%

3.4 Conclusions

The first Arctic snowpack measurements of I^- were greatly enriched relative to seawater Na^+, and more so with increasing depth. Differences in the snowpack depth profiles of bromine and iodine species within both the snow phase (Br^- and I^-), and gas phase (Br_2 and I_2, shown in chapter 2) suggest that there are significant differences in bromine and iodine multiphase chemistry. The assumption that these species act similarly may be an oversimplification – one which can only be remedied through further measurements of production and recycling. The total iodine content of the Arctic snow measured here is consistent with the only previous observation. Almost all the iodine present in Arctic snow is inorganic (I^- & IO_3^-), suggesting that measurements of total iodine may continue to be a good proxy. Both the observations presented here and those of Duce et al. [1966] also show nearly constant concentrations below the surface layer. The near constant concentrations of iodine with depth suggest that the source of iodine to the snowpack does not decrease significantly in the fall and winter. This is consistent with observations of the lack of seasonality in iodine enriched aerosols in coastal Arctic areas [Berg and Sperry, 1983; Sturges and Barrie, 1988]. These observations together make enrichment mechanisms that rely on light, including photochemical production and local biological production, seem unlikely. Rather, it seems likely that iodine is transported to the Arctic from lower latitudes as iodine enriched aerosols. However, this source has not been fully resolved yet. The lack of an organic iodine component in the Arctic snow is not consistent with measurements in snow samples in inland Germany [Gilfedder et al., 2007b], where the iodine is also presumably transported from the midlatitude coast. In contrast to the Arctic samples, Antarctic snow showed large concentrations of an organic iodine species. These contrasting results suggest that caution is required when considering iodine enrichment mechanisms. While biological enrichment of iodine is likely a strong source,

production from different species and chemical transformation during global transport may play a large role in the chemical composition of global iodine enrichment.

CHAPTER 4. ZERO-DIMENSIONAL MODELING OF IODINE WITHIN AND ABOVE THE SNOWPACK

4.1 Introduction

While high concentration of iodine in Arctic aerosols was first reported in the late 1980's [Berg and Sperry, 1983; Sturges and Barrie, 1988], other measurements of iodine in the Arctic have been sparse until quite recently. In the last several years there have been several reports of active iodine chemistry in the Arctic. Allan et al. [2014] reported observations of iodine within small particles during a persistent new particle formation event near the sea ice off the coast of Greenland. Sipilä et al. [2016] then showed that new particle formation in the Arctic can occur via sequential addition of HIO_3. In the gas phase, there have been only four reported measurements. First, observations of gas phase IO have been reported both in the sub-Arctic (Kuujjuarapik, Hudson Bay, Canada) [Mahajan et al., 2010], and the Arctic (Greenland) [Zielcke, 2015]. Second, Sipilä et al. [2016] observed HIO_3 in the gas phase concurrently with their observations of new particle formation. Finally, the measurements of I_2 reported in this dissertation (chapter 2), and Raso et al. [2017]. These diverse measurements of iodine species point to the importance of iodine chemistry in the Arctic. But because few of them are of the same species, modeling is required to understand the magnitude of importance.

The presence of iodine compounds, even at small mole ratios, may significantly increase the rate of O_3 destruction during ODEs [Calvert and Lindberg, 2004; Saiz-Lopez et al., 2014; Thompson et al., 2015, 2017], due to the relatively large rate constant for the reaction of BrO with IO ($k = 9.4 \times 10^{-11}$ cm^3 $molecule^{-1}$ s^{-1} [Rowley et al., 2001]), compared to the BrO self-reaction ($k = 9.3 \times 10^{-13}$ cm^3 $molecule^{-1}$ s^{-1} [Sander et al., 2006]). However, few Arctic models have included iodine chemistry, at least in part because of the previous shortage of gas phase measurements.

Saiz-Lopez et al. [2014] examined the global effect of iodine chemistry on tropospheric ozone, focusing primarily on the tropical and mid-latitude boundary layer. They found that within the marine boundary layer 9-27% of ozone loss is due to iodine chemistry. Calvert and Lindberg [2004] simulated the effect of iodine chemistry on polar ozone depletion events, finding that small inputs of I_2, IBr, and ICl each significantly enhance the ozone depletion caused by bromine chemistry, though iodine chemistry in the absence of bromine chemistry has a smaller effect. Thompson et al. [2015, 2017] used a zero-dimensional (0-D) box model to investigate the interactions between halogens, and the effect of iodine on the bromine radical chain length, agreeing with Calvert and Lindberg that small amounts of iodine can significantly enhance bromine mediated ozone destruction. However, these modeling studies were conducted before measurements of I_2 in the Arctic were published and did not include testing of the sensitivity of the system to I_2 concentration.

Snowpack interstitial air chemistry impacts boundary layer O_3 molar ratios through the distribution and amount of molecular halogens that exit the snowpack [Abbatt et al., 2012; Thomas et al., 2012; Pratt et al., 2013; Simpson et al., 2015], and through heterogeneous production of halogens. Previously it has been observed that O_3 in the naturally lit snowpack is usually depleted [Peterson and Honrath, 2001; Albert and Shultz, 2002; Van Dam et al., 2015]. Chapter 2 of this work shows this phenomenon, concurrent with high molecular halogen concentrations in the snowpack interstitial air. The O_3 depletion observed in both naturally and artificially lit snowpack interstitial air cannot be explained by NO_x and HO_x chemistry alone [Peterson and Honrath, 2001], and is likely due to reactions with halogen atoms in the snowpack interstitial air, as well as decreased wind penetration into the snowpack interstitial air with depth [Albert and Shultz, 2002; Albert et al., 2002; Van Dam et al., 2015], and longer times for loss processes. Few previous

studies [Thomas et al., 2011, 2012; Toyota et al., 2014] have simulated O_3 destruction in the snowpack interstitial air, and none have previously simulated O_3 destruction in the snowpack interstitial air including iodine chemistry. Here we apply a 0-D photochemical model, based on that of Thompson et al. [2015, 2017], to understanding ozone destruction within the interstitial snowpack air, including iodine chemistry. The same model is utilized to test the sensitivity of ozone depletion rates to I_2 concentration in the ambient boundary layer above the snowpack.

4.2 Methods

4.2.1 Zero-Dimensional Modeling

The model consists of a series of gas phase chemical reactions, which are compiled into a 0-D photochemical model by the commercial software FACSIMILE. Thermal chemical reactions can be found in Table 4.1. Photolytic reactions and maximum photolysis rates can be found in Table 4.2. For modeling of the snowpack interstitial air, the model was constrained to I_2 measurements from February 2, 2014, while Br_2 and Cl_2 are constrained to measurements from February 11, 2014. For modeling of boundary layer ozone depletion rates, the model was constrained to measurements from March 11, 2012. Methods for these measurements are described below. Initial gas phase mole ratios (for species not constrained to observations) can be found in Table 4.3.

Previous models that simulated snowpack interstitial air [Thomas et al., 2011; Toyota et al., 2014] have assumed a constant e-folding depth for actinic radiation to obtain snowpack photolysis rates. In this study, we accounted for differences in molecular absorbance, and wavelength-dependent e-folding depths, to yield species-specific photolysis rates at a depth of 10 cm in the snowpack interstitial air. The peak absorbance wavelength and quantum yield for each reaction were considered to estimate compound spectral e-folding depths. The e-folding depth for

this wavelength was then determined by applying a linear fit to the data presented by *King and Simpson* [2001], who demonstrated the wavelength dependence of e-folding depths. Optimal wavelengths and e-folding depths used are shown in Table 4.4. These were used to scale ambient air photolysis rates for modeling in the snowpack interstitial air. Ambient photolysis constants were obtained using the National Center for Atmospheric Research tropospheric and ultraviolet (TUV) radiation model (http://cprm.acd.ucar.edu/Models/TUV/) and scaled to radiation measurements from the NOAA Global Monitoring Division Earth Systems Research Laboratory (http://www.esrl.noaa.gov/gmd/).

Table 4.1 Non-photolytic chemical reactions used in the ambient and interstitial snowpack models.

Reaction	Rate Constant	Reference
$O[^1D] + M \rightarrow O[^3P]$	7.22×10^{-11}	[Dunlea and Ravishankara, 2004]
$O[^3P] + O_2 \rightarrow O_3$	2.12×10^{-14}	[Atkinson et al., 2004]
$O[^1D] + H_2O \rightarrow 2OH$	2.2×10^{-10}	[Atkinson et al., 2004]
$OH + O_3 \rightarrow HO_2$	3.84×10^{-14}	[Atkinson et al., 2004]
$OH + HO_2 \rightarrow H_2O$	1.34×10^{-10}	[Atkinson et al., 2004]
$OH + H_2O_2 \rightarrow HO_2 + H_2O$	1.52×10^{-12}	[Atkinson et al., 2004]
$OH + O[^3P] \rightarrow O_2$	3.74×10^{-11}	[Atkinson et al., 2004]
$OH + OH \rightarrow H_2O + O[^3P]$	1.74×10^{-12}	[Atkinson et al., 2004]
$OH + OH \rightarrow H_2O_2$	1.86×10^{-11}	[Atkinson et al., 2004]
$OH + NO_3 \rightarrow HO_2 + NO_2$	2.0×10^{-11}	[Atkinson et al., 2004]
$HO_2 + NO_3 \rightarrow HNO_3$	4.0×10^{-12}	[Atkinson et al., 2004]
$HO_2 + O_3 \rightarrow OH + 2O_2$	1.39×10^{-15}	[Atkinson et al., 2004]
$HO_2 + HO_2 \rightarrow H_2O_2 + O_2$	2.58×10^{-12}	[Atkinson et al., 2004]
$NO + OH \rightarrow HONO$	3.49×10^{-11}	[Atkinson et al., 2004]
$NO + HO_2 \rightarrow NO_2 + OH$	9.59×10^{-12}	[Atkinson et al., 2004]
$NO + O_3 \rightarrow NO_2$	7.09×10^{-15}	[Sander et al., 2006]
$NO + NO_3 \rightarrow NO_2 + NO_2$	2.98×10^{-11}	[Sander et al., 2006]
$NO_2 + OH \rightarrow HNO_3$	1.2×10^{-10}	[Atkinson et al., 2004]
$NO_2 + HO_2 \leftrightarrow HNO_4$	f: 8.6×10^{-12} r: 1.32×10^{-4}	[Atkinson et al., 2004]
$NO_2 + O_3 \rightarrow NO_3$	6.15×10^{-18}	[Sander et al., 2006]
$NO_2 + NO_3 \leftrightarrow N_2O_5$	f: 1.83×10^{-12} r: 3.76×10^{-5}	[Atkinson et al., 2004]
$NO_2 + CH_3COOO \leftrightarrow PAN$	f: 1.4×10^{-11} r: 3.1×10^{-8}	[Atkinson et al., 2004]
$NO_3 + NO_3 \rightarrow NO_2 + NO_2$	4.36×10^{-17}	[Sander et al., 2006]
$N_2O_5 + H_2O \rightarrow HNO_3 + HNO_3$	2.6×10^{-22}	[Atkinson et al., 2004]
$HONO + OH \rightarrow NO_2 + H_2O$	3.74×10^{-12}	[Sander et al., 2006]
$HNO_3 + OH \rightarrow NO_3 + H_2O$	1.5×10^{-13}	[Atkinson et al., 2004]
$HNO_4 + OH \rightarrow NO_2 + H_2O$	6.2×10^{-12}	[Atkinson et al., 2004]
$CO + OH \rightarrow HO_2 + CO_2$	2.4×10^{-13}	[Atkinson et al., 2004]
$CH_4 + OH \rightarrow CH_3OO + H_2O$	1.87×10^{-15}	[Sander et al., 2006]
$C_2H_2 + OH \rightarrow C_2H_2OH$	7.8×10^{-13}	[Atkinson et al., 2004]
$C_2H_6 + OH \rightarrow C_2H_5OO$	1.18×10^{-13}	[Lurmann et al., 1986]

Table 4.1 Continued.

$C_2H_4 + OH \rightarrow C_2H_4OH$	1.02×10^{-11}	[Vakhtin et al., 2003]
$C_3H_8 + OH \rightarrow nC_3H_7O_2$	1.56×10^{-13}	[Harris and Kerr, 1988]
$C_3H_8 + OH \rightarrow iC_3H_7O_2$	6.64×10^{-13}	[Harris and Kerr, 1988]
$C_3H_6 + OH \rightarrow C_3H_6OH$	3.63×10^{-11}	[Atkinson et al., 2004]
$C_3H_6O + OH \rightarrow$ Products	2.51×10^{-11}	[Atkinson et al., 2004]
$nC_3H_7O_2 + NO \rightarrow NO_2 + C_3H_6O + HO_2$	5.4×10^{-11}	[Eberhard and Howard, 1996]
$iC_3H_7O_2 + NO \rightarrow NO_2 + CH_3COCH_3 + HO_2$	1.2×10^{-11}	[Eberhard and Howard, 1996]
$nC_4H_{10} + OH \rightarrow nC_4H_9OO$	1.64×10^{-12}	[Donahue et al., 1998]
$iC_4H_{10} + OH \rightarrow CH_3COCH_3 + CH_3OO$	1.65×10^{-12}	[Donahue et al., 1998]
$nC_4H_9OO + NO \rightarrow$ n-Butanal $+ NO_2 + HO_2$	5.4×10^{-11}	[Michalowski et al., 2000]
$nC_4H_9OO + CH_3OO \rightarrow$ n-Butanal $+ HCHO + HO_2 + HO_2$	6.7×10^{-13}	[Michalowski et al., 2000]
$nC_4H_9OO + CH_3OO \rightarrow$ n-Butanal $+ CH_3OH$	2.3×10^{-13}	[Michalowski et al., 2000]
$nC_4H_9OO + CH_3OO \rightarrow nC_4H_9OH + HCHO$	2.3×10^{-13}	[Michalowski et al., 2000]
$CH_3OH + OH \rightarrow CH_3O$	7.09×10^{-13}	[Atkinson et al., 2004]
n-Butanal + OH → Products	2.0×10^{-11}	[Michalowski et al., 2000]
$CH_3OO + HO_2 \rightarrow CH_3OOH$	1.01×10^{-11}	[Atkinson et al., 2004]
$C_2H_5OO + HO_2 \rightarrow C_2H_5OOH$	9.23×10^{-12}	[Atkinson et al., 2004]
$CH_3COOO + HO_2 \rightarrow CH_3COOOH$	2.54×10^{-11}	[DeMore et al., 1997]
$C_2H_5OOH + OH \rightarrow C_2H_5OO$	6.0×10^{-12}	[Atkinson et al., 2004]
$CH_3OO + CH_3OO \rightarrow HCHO + HO_2$	3.64×10^{-13}	[Lurmann et al., 1986]
$CH_3OOH + OH \rightarrow HCHO + H_2O + OH$	2.54×10^{-12}	[Sander and Crutzen, 1996]
$CH_3OOH + OH \rightarrow CH_3OO + H_2O$	6.01×10^{-12}	[Sander and Crutzen, 1996]
$CH_3OO + HO_2 \rightarrow CH_3OOH$	1.01×10^{-11}	[Atkinson et al., 2004]
$CH_3OO + NO \rightarrow HCHO + HO_2 + NO_2$	8.76×10^{-12}	[Atkinson et al., 2004]
$CH_3OO + nC_3H_7O_2 \rightarrow HCHO + C_3H_6O + HO_2 + HO_2$	6.70×10^{-13}	[Lightfoot et al., 1992]
$CH_3OO + nC_3H_7O_2 \rightarrow C_3H_6O + CH_3OH$	2.3×10^{-13}	[Lightfoot et al., 1992]
$CH_3OO + nC_3H_7O_2 \rightarrow HCHO + nC_3H_7OH$	2.3×10^{-13}	[Lightfoot et al., 1992]
$CH_3OO + iC_3H_7O_2 \rightarrow HCHO + CH_3COCH_3 + HO_2 + HO_2$	1.2×10^{-14}	[Lightfoot et al., 1992]
$CH_3OO + iC_3H_7O_2 \rightarrow CH_3COCH_3 + CH_3OH$	4.1×10^{-15}	[Lightfoot et al., 1992]
$CH_3OO + iC_3H_7O_2 \rightarrow HCHO + iC_3H_7OH$	4.1×10^{-15}	[Lightfoot et al., 1992]
$CH_3OO + C_2H_5OO \rightarrow CH_3CHO + HCHO + HO_2 + HO_2$	2.0×10^{-13}	[Kirchner and Stockwell, 1996]

Table 4.1 Continued.

$CH_3OO + CH_3COOO \rightarrow HCHO + CH_3OO + HO_2$	1.58×10^{-11}	[Kirchner and Stockwell, 1996]
$C_2H_5OO + NO \rightarrow CH_3CHO + HO_2 + NO_2$	8.68×10^{-12}	[Lurmann et al., 1986]
$C_2H_5OO + HO_2 \rightarrow C_2H_5OOH$	9.23×10^{-12}	[Atkinson et al., 2004]
$C_2H_5OO + CH_3COOO \rightarrow CH_3CHO + CH_3COO + HO_2$	4.0×10^{-12}	[Michalowski et al., 2000]
$iC_3H_7O_2 + HO_2 \rightarrow$ iPerox	9.23×10^{-12}	[Michalowski et al., 2000]
$nC_3H_7O_2 + HO_2 \rightarrow$ nPerox	9.23×10^{-12}	[Michalowski et al., 2000]
$HCHO + OH \rightarrow HO_2 + CO$	9.3×10^{-12}	[Atkinson et al., 2004]
$HCHO + HO_2 \rightarrow HOCH_2O_2$	7.53×10^{-14}	[Sander et al., 2006]
$HCHO + NO_3 \rightarrow HNO_3 + HO_2 + CO$	5.8×10^{-16}	[DeMore et al., 1997]
$CH_3CHO + OH \rightarrow CH_3COOO + H_2O$	1.98×10^{-11}	[Atkinson et al., 2004]
$CH_3CHO + NO_3 \rightarrow HNO_3 + CH_3COOO$	1.4×10^{-15}	[DeMore et al., 1997]
$CH_3COCH_3 + OH \rightarrow H_2O + CH_3COCH_2$	1.37×10^{-13}	[Atkinson et al., 2004]
$HOCH_2O_2 + NO \rightarrow HCOOH + HO_2 + NO_2$	8.68×10^{-12}	[Lurmann et al., 1986]
$HOCH_2O_2 + HO_2 \rightarrow HCOOH + H_2O$	2.0×10^{-12}	[Lurmann et al., 1986]
$HOCH_2O_2 + HOCH_2O_2 \rightarrow HCOOH + HCOOH + HO_2 + HO_2$	1.0×10^{-13}	[Lurmann et al., 1986]
$HCOOH + OH \rightarrow HO_2 + H_2O + CO_2$	4.0×10^{-13}	[DeMore et al., 1997]
$CH_3COOO + NO \rightarrow CH_3OO + NO_2 + CO_2$	2.4×10^{-11}	[Atkinson et al., 2004]
$CH_3COOO + HO_2 \rightarrow CH_3COOH + O_3$	1.87×10^{-11}	[Kirchner and Stockwell, 1996]
$CH_3COOO + CH_3COOO \rightarrow CH_3COO + CH_3COO$	2.5×10^{-11}	[Kirchner and Stockwell, 1996]
$Cl_2 + OH \rightarrow HOCl + Cl$	2.85×10^{-14}	[Atkinson et al., 2004]
$Cl + O_3 \rightarrow ClO$	1.02×10^{-11}	[Atkinson et al., 2004]
$Cl + H_2 \rightarrow HCl$	3.5×10^{-15}	[Atkinson et al., 2004]
$Cl + HO_2 \rightarrow HCl$	3.57×10^{-11}	[Sander et al., 2006]
$Cl + HO_2 \rightarrow ClO + OH$	6.68×10^{-12}	[Sander et al., 2006]
$Cl + H_2O_2 \rightarrow HCl + HO_2$	2.11×10^{-13}	[Atkinson et al., 2004]
$Cl + NO_3 \rightarrow ClO + NO_2$	2.4×10^{-11}	[Atkinson et al., 2004]
$Cl + CH_4 \rightarrow HCl + CH_3OO$	3.99×10^{-14}	[Sander et al., 2006]
$Cl + C_2H_6 \rightarrow HCl + C_2H_5OO$	5.36×10^{-11}	[Sander et al., 2006]

Table 4.1 Continued

$Cl + C_2H_4 \rightarrow HCl + C_2H_5OO$	1.0×10^{-10}	[Atkinson et al., 2004]
$Cl + MEK \rightarrow HCl$	4.21×10^{-11}	[Atkinson et al., 2004]
$Cl + C_2H_2 \rightarrow ClC_2CHO$	2.5×10^{-10}	[Atkinson et al., 2004]
$Cl + C_3H_6 \rightarrow HCl + C_3H_6Cl$	2.7×10^{-10}	[Keil and Shepson, 2006]
$Cl + C_3H_8 \rightarrow HCl + iC_3H_7O_2$	1.65×10^{-10}	[DeMore et al., 1997]
$Cl + C_3H_8 \rightarrow HCl + nC_3H_7O_2$	1.65×10^{-10}	[DeMore et al., 1997]
$Cl + C3H6O \rightarrow HCl$	1.1×10^{-10}	[Wallington et al., 1988]
$Cl + iC_4H_{10} \rightarrow HCl + C_4H_9$	1.3×10^{-10}	[Hooshiyar and Niki, 1995]
$Cl + nC_4H_{10} \rightarrow HCl + C_4H_9$	2.15×10^{-10}	[Tyndall et al., 1997]
Cl + n-Butanal → HCl + Products	1.1×10^{-10}	[Michalowski et al., 2000]
$Cl + HCHO \rightarrow HCl + HO_2 + CO$	7.18×10^{-11}	[Sander et al., 2006]
$Cl + CH_3CHO \rightarrow HCl + CH_3COOO$	8.08×10^{-11}	[Atkinson et al., 2004]
$Cl + CH_3COCH_3 \rightarrow HCl + CH_3COCH_2$	1.39×10^{-12}	[Atkinson et al., 2004]
$Cl + CH_3OOH \rightarrow CH_3OO + HCl$	2.36×10^{-11}	[Atkinson et al., 2004]
$Cl + CH_3OOH \rightarrow CH_2OOH + HCl$	3.54×10^{-11}	[Atkinson et al., 2004]
Cl + CHBr3 → HCl + Br + CBr2O	2.9×10^{-13} [at 298 K]	[Kamboures et al., 2002]
$Cl + OClO \rightarrow ClO + ClO$	6.35×10^{-11}	[Atkinson et al., 2004]
$Cl + ClNO_3 \rightarrow Cl_2 + NO_3$	1.12×10^{-11}	[Sander et al., 2006]
Cl + PAN → HCl + HCHO + NO_3	1.0×10^{-14}	[Tsalkani et al., 1988]
$Cl + HNO_3 \rightarrow HCl + NO_3$	1.0×10^{-16}	[Wine et al., 1988]
$Cl + NO_2 \rightarrow ClNO_2$	1.4×10^{-12} [at 298 K]	[Ravishankara et al., 1988]
Cl + HBr → HCl + Br	4.48×10^{-12}	[Nicovich and Wine, 1990]
$ClO + O[^3P] \rightarrow Cl + O_2$	1.6×10^{-11}	[Atkinson et al., 2004]
$ClO + OH \rightarrow Cl + HO_2$	2.45×10^{-11}	[Atkinson et al., 2004]
ClO + OH → HCl	2.37×10^{-13}	[Sander et al., 2006]
$ClO + HO_2 \rightarrow HOCl$	8.67×10^{-12}	[Atkinson et al., 2004]
$ClO + CH_3OO \rightarrow Cl + HCHO + HO_2$	2.08×10^{-12}	[Sander et al., 2006]
$ClO + CH_3COOO \rightarrow Cl + CH_3OO + CO_2$	2.03×10^{-12}	[Michalowski et al., 2000]
$ClO + NO \rightarrow Cl + NO_2$	2.04×10^{-11}	[Atkinson et al., 2004]
$ClO + NO_2 \rightarrow ClNO_3$	7.1×10^{-12}	[Atkinson et al., 2004]
$ClO + ClO \rightarrow Cl_2$	1.64×10^{-15}	[Atkinson et al., 2004]
ClO + ClO → Cl + Cl	1.54×10^{-15}	[Atkinson et al., 2004]
ClO + ClO → Cl + OClO	1.40×10^{-15}	[Atkinson et al., 2004]
OClO + OH → HOCl	1.13×10^{-11}	[Atkinson et al., 2004]

Table 4.1 Continued

$HOI + OH \rightarrow IO$	2.0×10^{-13}	[McFiggans, 2002]
$IO + OIO \rightarrow I_2O_3$	1.5×10^{-10}	[McFiggans, 2002]
$OIO + OIO \leftrightarrow I_2O_4$	f: 1.0×10^{-10} r: 4.4×10^{-4}	[Gómez Martín et al., 2005]
$IOOI + O_3 \rightarrow I_2O_3$	1.0×10^{-12}	[Sander et al., 2006]
$I_2O_3 + O_3 \rightarrow I_2O_4$	1.0×10^{-12}	[Saunders and Plane, 2005]
$I_2O_4 + O_3 \rightarrow I_2O_5$	1.0×10^{-12}	[Saunders and Plane, 2005]

Table 4.2 Maximum photolysis constants for both the ambient air and interstitial snowpack air models. Many photolysis rate constants were scaled to Thompson et al. *[2015]* by multiplying by the ratio of maximum NO_2 photolysis rates.

Reaction	J_{max} (s^{-1}) Ambient	J_{max} (s^{-1}) Interstitial	Ambient Source
$I_2 \rightarrow 2I$	$3.76x10^{-2}$	$1.69x10^{-2}$	Scaled to *[Thompson et al., 2015]*
$IO \rightarrow I + O(^3P)$	$4.50x10^{-2}$	$2.02x10^{-2}$	Scaled to *[Thompson et al., 2015]*
$OIO \rightarrow IO + O(^3P)$	$3.84x10^{-4}$	$1.73x10^{-4}$	Scaled to *[Thompson et al., 2015]*
$OIO \rightarrow I + O_2$	$8.09x10^{-3}$	$3.64x10^{-3}$	Scaled to *[Thompson et al., 2015]*
$IOOI \rightarrow 2IO$	$3.71x10^{-3}$	$1.67x10^{-3}$	Scaled to *[Thompson et al., 2015]*
$IOOI \rightarrow 2I + O_2$	$3.71x10^{-3}$	$1.67x10^{-3}$	Scaled to *[Thompson et al., 2015]*
$HOI \rightarrow I + OH$	$1.26x10^{-3}$	$5.66x10^{-4}$	Scaled to *[Thompson et al., 2015]*
$INO \rightarrow I + NO$	$2.07x10^{-2}$	$9.30x10^{-3}$	Scaled to *[Thompson et al., 2015]*
$INO_2 \rightarrow I + NO_2$	$5.53x10^{-4}$	$2.48x10^{-4}$	Scaled to *[Thompson et al., 2015]*
$INO_3 \rightarrow IO + NO_2$	$1.77x10^{-4}$	$7.95x10^{-5}$	Scaled to *[Thompson et al., 2015]*
$INO_3 \rightarrow I + NO_3$	$7.21x10^{-5}$	$3.24x10^{-5}$	Scaled to *[Thompson et al., 2015]*
$IBr \rightarrow I + Br$	$1.69x10^{-2}$	$7.62x10^{-3}$	Scaled to *[Thompson et al., 2015]*
$Br_2 \rightarrow 2Br$	$1.09x10^{-2}$	$4.92x10^{-3}$	Scaled to *[Thompson et al., 2015]*
$BrO \rightarrow Br + O(^3P)$	$7.49x10^{-3}$	$3.37x10^{-3}$	Scaled to *[Thompson et al., 2015]*
$HOBr \rightarrow Br + OH$	$5.74x10^{-4}$	$2.58x10^{-4}$	Scaled to *[Thompson et al., 2015]*
$BrNO_2 \rightarrow Br + NO_2$	$3.75x10^{-5}$	$1.68x10^{-5}$	Scaled to *[Thompson et al., 2015]*
$BrNO_3 \rightarrow BrO + NO_2$	$2.90x10^{-4}$	$1.30x10^{-4}$	Calculated using TUV and radiation data
$BrNO_3 \rightarrow Br + NO_3$	$5.12x10^{-5}$	$2.30x10^{-5}$	Calculated using TUV and radiation data
$ICl \rightarrow I + Cl$	$5.46x10^{-3}$	$2.46x10^{-3}$	Scaled to *[Thompson et al., 2015]*
$BrCl \rightarrow Br + Cl$	$3.12x10^{-3}$	$1.40x10^{-3}$	Scaled to *[Thompson et al., 2015]*
$Cl_2 \rightarrow 2Cl$	$5.10x10^{-4}$	$2.29x10^{-4}$	Calculated using TUV and radiation data
$ClO \rightarrow Cl + O(^3P)$	$6.06x10^{-6}$	$2.72x10^{-6}$	Scaled to *[Thompson et al., 2015]*
$OClO \rightarrow ClO + O(^3P)$	$3.04x10^{-2}$	$1.37x10^{-2}$	Calculated using TUV and radiation data
$HOCl \rightarrow Cl + OH$	$3.44x10^{-5}$	$1.54x10^{-5}$	Scaled to *[Thompson et al., 2015]*
$ClNO_2 \rightarrow Cl + NO_2$	$1.09x10^{-5}$	$4.91x10^{-6}$	Scaled to *[Thompson et al., 2015]*
$ClNO_3 \rightarrow ClO + NO_2$	$8.33x10^{-7}$	$3.75x10^{-7}$	Calculated using TUV and radiation data
$ClNO_3 \rightarrow Cl + NO_3$	$7.25x10^{-6}$	$3.26x10^{-6}$	Calculated using TUV and radiation data
$O_3 \rightarrow O_2 + O(^1D)$	$1.31x10^{-4}$	$5.87x10^{-5}$	Calculated using TUV and radiation data
$H_2O_2 \rightarrow 2OH$	$8.45x10^{-7}$	$3.80x10^{-7}$	Calculated using TUV and radiation data
$NO_2 \rightarrow NO + O(^3P)$	$2.13x10^{-3}$	$9.59x10^{-4}$	Calculated using TUV and radiation data
$NO_3 \rightarrow NO + O_2$	$1.11x10^{-2}$	$5.01x10^{-3}$	Calculated using TUV and radiation data
$N_2O_5 \rightarrow NO_2 + NO_3$	$3.78x10^{-6}$	$1.70x10^{-6}$	Calculated using TUV and radiation data

Table 4.2 Continued.

$HNO_2 \rightarrow NO + OH$	$4.47x10^{-4}$	$2.01x10^{-4}$	Calculated using TUV and radiation data
$HNO_3 \rightarrow NO_2 + OH$	$3.62x10^{-8}$	$1.63x10^{-8}$	Calculated using TUV and radiation data
$HNO_4 \rightarrow NO_2 + HO_2$	$1.81x10^{-7}$	$8.14x10^{-8}$	Calculated using TUV and radiation data
$HCHO \rightarrow CO + 2HO_2$	$3.65x10^{-6}$	$1.63x10^{-6}$	Calculated using TUV and radiation data
$HCHO \rightarrow CO + H_2$	$7.81x10^{-6}$	$3.51x10^{-6}$	Calculated using TUV and radiation data
$CH_3CHO \rightarrow CH_3O_2+CO+HO_2$	$2.65x10^{-7}$	$1.19x10^{-7}$	Calculated using TUV and radiation data
$CH_3OOH \rightarrow HCHO+HO_2+OH$	$7.85x10^{-7}$	$3.53x10^{-7}$	Calculated using TUV and radiation data
$C_3H_6O \rightarrow C_2H_5OO+CO+HO_2$	$3.46x10^{-7}$	$1.55x10^{-7}$	Calculated using TUV and radiation data
$PAN \rightarrow CH_3COOO+NO_2$	$4.33x10^{-8}$	$1.95x10^{-8}$	Calculated using TUV and radiation data

Table 4.3 Constant (or *starting) molar ratios used in modeling. Species not shown had a starting concentration of zero. For several species, the same mole ratio was used in both the ambient air and interstitial snowpack air models. This is due either to a lack of interstitial snowpack air measurements of those species, or a low variability between ambient and interstitial mixing ratios.

Species	Ambient mixing ratio	Interstitial mixing ratio	References for ambient and interstitial (when different) mixing ratios
Hg	122 ppqv	122 ppqv	[Thompson et al., 2015]
NO_2	43.9 pptv	250 pptv	[Thompson et al., 2015] [Peterson and Honrath, 2001]
NO	26.3 pptv	150 pptv	[Thompson et al., 2015] [Peterson and Honrath, 2001]
HONO	203 pptv	203 pptv	[Thompson et al., 2015]
H_2O	907 ppmv	907 ppmv	
H_2	663 ppbv	663 ppbv	
O_2	252 ppthv	252 ppthv	
O_3 *	21.7 ppbv	12.0 ppbv	Chapter 2, and CIMS Measurements
CO_2	472 ppmv	472 ppmv	[Thompson et al., 2015]
CO	228 ppbv	228 ppbv	[Thompson et al., 2015]
CH_4	2.28 ppmv	2.28 ppmv	[Thompson et al., 2015]
CH_3Br	14.2 pptv	14.2 pptv	[Thompson et al., 2015]
$CHBr_3$	4.06 pptv	4.06 pptv	[Thompson et al., 2015]
C_2H_2	317 pptv	317 pptv	[Thompson et al., 2015]
C_2H_4	24.4 pptv	24.4 pptv	[Thompson et al., 2015]
C_2H_6	2.11 ppbv	2.11 pptv	[Thompson et al., 2015]
C_3H_6	13.4 pptv	13.4 pptv	[Thompson et al., 2015]
C_3H_8	610 pptv	610 pptv	[Thompson et al., 2015]
PAN *	200 pptv	200 pptv	[Dassau et al., 2004]
MEK	250 pptv	250 pptv	[Thompson et al., 2015]
HCHO	12.2 pptv	200 pptv	[Thompson et al., 2015] [Sumner and Shepson, 1999]
CH_3CHO	16.3 pptv	16.3 pptv	[Thompson et al., 2015]
CH_3COCH_3	976 pptv	976 pptv	[Thompson et al., 2015]
n-C_4H_{10}	244 pptv	244 pptv	[Thompson et al., 2015]
i-C_4H_{10}	179 pptv	179 pptv	[Thompson et al., 2015]

Table 4.4 Wavelengths of light and e-folding depths used to determine photolysis reaction rates in the interstitial snowpack air.

Reaction	e-Folding Depth	λ_{max} used	Reference
$I_2 \rightarrow 2I$	7.21cm	530nm	[Gómez Martín et al., 2005]
$IO \rightarrow I + O[^3P]$	6.10cm	430nm	[Laszlo et al., 1995]
$OIO \rightarrow IO + O[^3P]$	7.64cm	568nm	[Ashworth et al., 2002]
$OIO \rightarrow I + O_2$	7.64cm	568nm	[Ashworth et al., 2002]
$IOOI \rightarrow 2IO$	6.88cm	500nm	Estimate
$IOOI \rightarrow 2I + O_2$	6.88cm	500nm	Estimate
$HOI \rightarrow I + OH$	5.27cm	355nm	[Bauer et al., 1998]
$INO \rightarrow I + NO$	3.99cm	240nm	[Forte et al., 1981]
$INO_2 \rightarrow I + NO_2$	4.65cm	300nm	[Mossinger et al., 2002]
$INO_3 \rightarrow IO + NO_2$	4.65cm	300nm	[Mossinger et al., 2002]
$INO_3 \rightarrow I + NO_3$	4.65cm	300nm	[Mossinger et al., 2002]
$IBr \rightarrow I + Br$	6.88cm	500nm	[Wrede et al., 2001]
$Br_2 \rightarrow 2Br$	5.99cm	420nm	[Maric et al., 1994]
$BrO \rightarrow Br + O[^3P]$	5.10cm	340nm	[DeMore et al., 1997]
$HOBr \rightarrow Br + OH$	4.43cm	280nm	[Ingham et al., 1998]
$BrNO_2 \rightarrow Br + NO_2$	5.43cm	370nm	[Scheffler et al., 1997]
$BrNO_3 \rightarrow BrO + NO_2$	4.43cm	280nm	[Harwood et al., 1998]
$BrNO_3 \rightarrow Br + NO_3$	4.74cm	308nm	[Harwood et al., 1998]
$ICl \rightarrow I + Cl$	6.55cm	470nm	[Seery and Britton, 1964]
$BrCl \rightarrow Br + Cl$	5.54cm	380nm	[Maric et al., 1994]
$Cl_2 \rightarrow 2Cl$	4.99cm	330nm	[Maric et al., 1994]
$ClO \rightarrow Cl + O[^3P]$	4.38cm	275nm	[DeMore et al., 1997]
$OClO \rightarrow ClO + O[^3P]$	5.21cm	350nm	[Wahner et al., 1987]
$HOCl \rightarrow Cl + OH$	4.10cm	250nm	[Burkholder, 1993]
$ClNO_2 \rightarrow Cl + NO_2$	4.65cm	300nm	[Ghosh et al., 2012]
$ClNO_3 \rightarrow ClO + NO_2$	3.79cm	222nm	[Yokelson et al., 1997]
$ClNO_3 \rightarrow Cl + NO_3$	3.99cm	240nm	[Yokelson et al., 1997]
$O_3 \rightarrow O_2 + O[^1D]$	4.77cm	310nm	[Molina and Molina, 1986]
$H_2O_2 \rightarrow 2OH$	6.88cm	500nm	[Vaghjiani and Ravishankara, 1989]
$NO_2 \rightarrow NO + O[^3P]$	5.77cm	400nm	[Schneider et al., 1987]
$NO_3 \rightarrow NO + O_2$	7.77cm	580nm	[Graham and Johnston, 1978]
$N_2O_5 \rightarrow NO_2 + NO_3$	4.65cm	300nm	[Graham and Johnston, 1978]
$HONO \rightarrow NO + OH$	5.26cm	354nm	[Bongartz et al., 1991, 1994]
$HNO_3 \rightarrow NO_2 + OH$	4.82cm	315nm	[Burkholder et al., 1993]

Table 4.4 Continued

$HO_2NO_2 \rightarrow NO_2 + HO_2$	4.08cm	248nm	[Singer et al., 1989]
$HCHO \rightarrow CO + 2HO_2$	4.65cm	300nm	[DeMore et al., 1997]
$HCHO \rightarrow CO + H_2$	5.08cm	338nm	[DeMore et al., 1997]
$CH_3CHO \rightarrow CH_3O_2 + CO + HO_2$	4.43cm	280nm	[Martinez et al., 1992]
$CH_3OOH \rightarrow HCHO + HO_2 + OH$	4.65cm	300nm	Estimate
$C_3H_6O \rightarrow C_2H_5OO + CO + HO_2$	4.60cm	295nm	[Martinez et al., 1992]
$PAN \rightarrow CH_3COOO + NO_2$	12.33cm	990nm	[Talukdar et al., 1995]

4.2.2 2014 CIMS Measurements

Snowpack interstitial air modeling was constrained using radiation data and I_2 measurements from 11:30 – 15:00 AKST on February 2, 2014. February 2 measurements are from the second day of the diurnal profile discussed in chapter 2 of this work. As described in chapter 2, SF_6^- ion chemistry was used in 2014 to measure I_2 at mass 254 amu ($^{127}I_2^-$) with a 6 s dwell time. Due to detector voltage settings, Br_2 data from February 2, 2014, was not available. Br_2 and Cl_2 mole ratios were constrained using measurements from 11:30 – 15:00 AKST on February 11, 2014, which utilized hydrated I^- ($I(H_2O)_n^-$) as a reagent ion. Masses 287 amu ($I^{81}Br^{79}Br^-$), 289 amu ($I^{81}Br^{81}Br^-$), 197 amu ($I^{35}Cl^{35}Cl^-$), and 199 amu ($I^{37}Cl^{35}Cl^-$) were monitored, each with a 500 ms dwell time. $I(H_2O)_n^-$ was produced in the flow reactor by passing 1.7 lpm of 5 ppm methyl iodide (CH_3I) in N_2 through a ^{210}Po ionizer. To avoid any fluctuations due to ambient relative humidity, water was added in N_2 (0.12 lpm) from a ~20°C bubbler to the flow reactor, which was held at a constant pressure of 13 Torr. All other instrumental and measurement details are as described in Chapter 2. Snowpack interstitial air measurements were conducted with a heated 180 cm long sampling line, which was inserted 10 cm into the snowpack. CIMS measurements used for modeling the snowpack interstitial air are shown in Figure 4.1.

4.2.3 2012 (BROMEX) CIMS Measurements

As an ozone depletion event did not occur during the 2014 campaign, data from the 2012 BROMEX campaign was utilized to simulate the effect of iodine on the rate of ozone depletion. CIMS data gathered on March 11-12, 2012 were used for boundary layer modeling. This data can be seen in Figure 4.2. In 2012 data were obtained using hydrated I^- ($I(H_2O)_n^-$) chemistry. Masses 287 amu ($I^{81}Br^{79}Br^-$), 289 amu ($I^{81}Br^{81}Br^-$), 223 amu ($IHO^{79}Br^-$), 225 amu ($IHO^{81}Br^-$), 197 amu

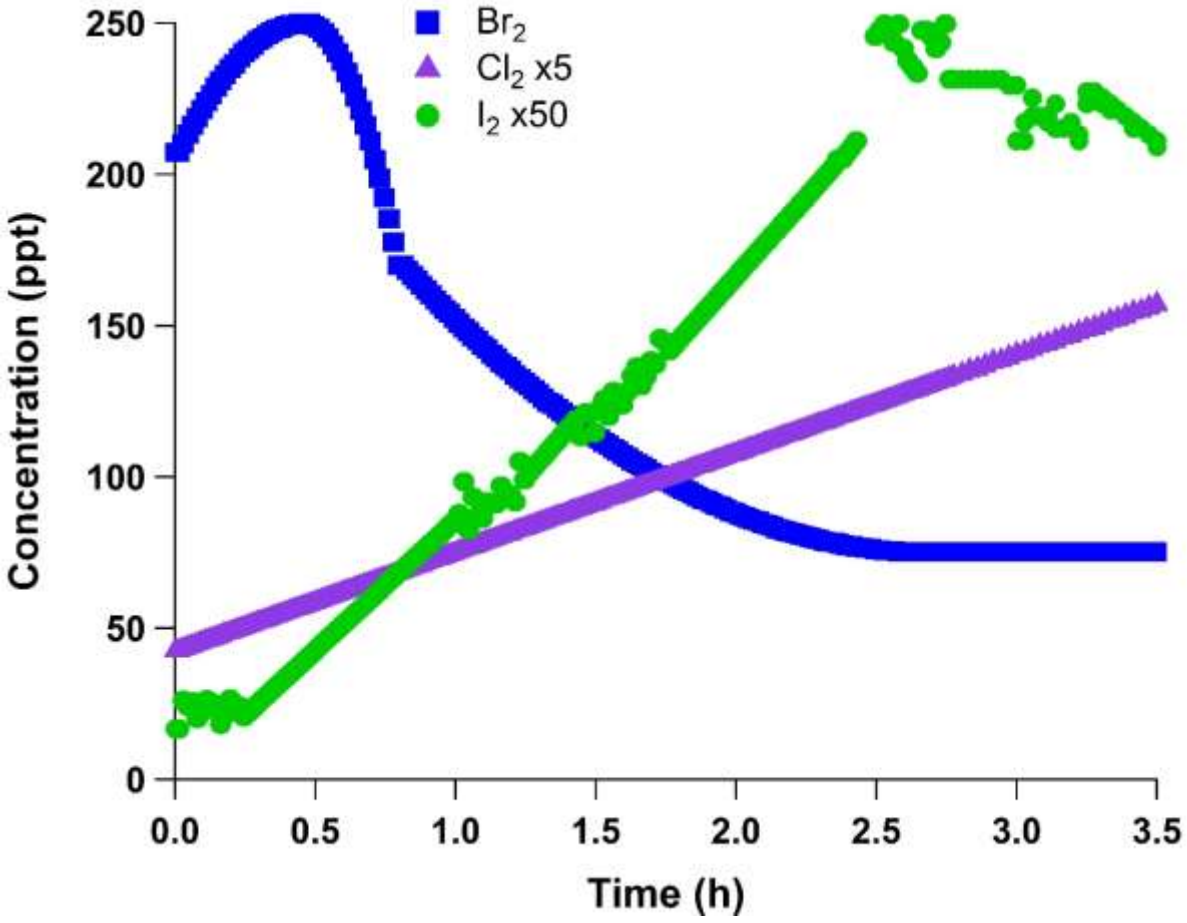

Figure 4.1 Measurement data from 11:30 – 15:00 AKST February 2, 2014 (I_2), and 11:30 – 15:00 AKST February 11, 2014, used to constrain snowpack interstitial air photochemical modeling. Other starting mole ratios for the model can be found in Table 4.3.

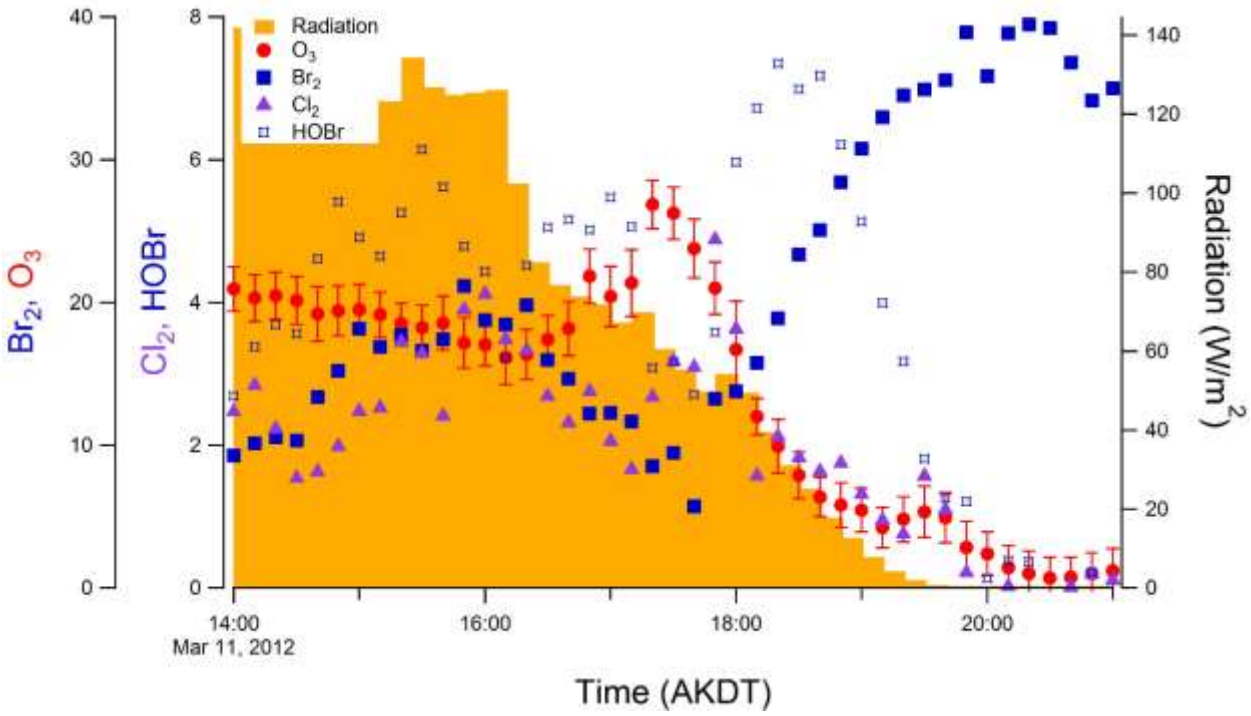

Figure 4.2 Measurement data from Mar. 11, 2012 used to constrain boundary layer photochemical modeling. Other starting mole ratios for the model can be found in Table 4.3.

($I^{35}Cl^{35}Cl^-$), and 199 amu ($I^{37}Cl^{35}Cl^-$) were monitored. As by Liao et al. *[2011]*, Peterson et al. *[2015]*, and Custard et al.[2016], measurements were conducted by sampling from a 33 cm long 4.6 cm ID aluminum pipe that extended ~9 cm beyond the wall of the building. A blower was used to pull a total flow rate of ~300 lpm through the pipe, and 7.5 lpm was sub-sampled from the centerline to the 3-way valve. Reagent ions were generated as above, using CH_3I, a ^{210}Po ionizer, and humidified nitrogen. Background measurements were completed by flowing ambient air through a glass wool scrubber, as completed in 2014 and described by Liao et al. [2012]. Br_2 and Cl_2 permeation devices were used for calibration, with the permeation rate measured as described in chapter 2 and by Liao et al. [2012]. The sensitivity of HOBr (225 amu) relative to Br_2 (287 amu) of 0.5 was utilized for HOBr quantification [Liao et al., 2012].

The 3σ limits of detection with $I(H_2O)_n^-$ chemistry for Br_2 (287 amu), Cl_2 (197 amu), and HOBr (225 amu) were calculated to be 3.9 ppt, 1.5 ppt, and 3.1 ppt, respectively, on average for 1 min. of CIMS measurements (corresponding to 2.8 s integration periods for each mass). Since the variation in the background is likely due to counting statistics [Liao et al., 2012], the limits of detection for the 10 min averaged data used for simulation are estimated at 1.2 ppt, 0.5 ppt, and 1.0 ppt for Br_2, Cl_2, and HOBr, respectively. The uncertainties in the 10 min averaged Br_2, Cl_2, and HOBr molar ratios used are calculated to be 14% + LOD, 25% + LOD, and (-28%/+34%) + LOD, respectively.

4.3 Results and Discussion

4.3.1 The Effect of Iodine on Ozone Destruction in the Snowpack Interstitial Air

Snowpack interstitial air chemistry impacts boundary layer O_3 molar ratios through the distribution and amount of molecular halogens that exit the snowpack [Abbatt et al., 2012; Thomas et al., 2012; Pratt et al., 2013; Simpson et al., 2015], and through heterogeneous production of halogens. In the naturally lit snowpack, O_3 is depleted, and I_2 and Br_2 production occur (chapter 2). O_3 molar ratios decrease with depth in the snowpack (chapter 2). The O_3 depletion observed in both naturally and artificially lit snowpack interstitial air is likely due to reactions with halogen atoms in the snowpack interstitial air, as well as decreased wind penetration into the snowpack interstitial air with depth [Albert and Shultz, 2002; Albert et al., 2002; Van Dam et al., 2015], and longer times for loss processes. It cannot be explained by NO_x and HO_x chemistry alone [Peterson and Honrath, 2001]. In comparison, previous boundary layer atmospheric models have found that even small molar ratios (~0.3 - 1 ppt of I atom equivalent) of inorganic iodine can result in significant enhancements of O_3 depletion [Calvert and Lindberg, 2004; Thompson et al., 2015]. Few previous studies [Thomas et al., 2011, 2012; Toyota et al., 2014] have simulated O_3

destruction in the snowpack interstitial air, and none have previously simulated O_3 destruction in the snowpack interstitial air including iodine chemistry. Therefore, to examine the impact of iodine in the snowpack interstitial air, the interstitial O_3 depletion with and without the presence of iodine chemistry was simulated (Figure 4.3).

To simulate snowpack interstitial air O_3 destruction, the 0-D model was constrained to I_2 measurements from February 2, 2014, and Br_2 and Cl_2 measurements from February 11, 2014. At up to 250 ppt, Br_2 molar ratios were about ~50 times those of I_2 (Figure 4.1) in the snowpack interstitial air, and bromine chemistry dominated O_3 depletion (Figure 4.3) making the overall impact of Br chemistry greater. However, due to generally faster reaction rates of iodine atoms, compared to bromine atoms, the presence of even this relatively low molar ratio of I_2 (up to 5 ppt) still increased the destruction of O_3 significantly (+ 4% of total measured depletion). Iodine chemistry may also support the recycling of bromine on the snow surfaces, magnifying the interstitial air bromine explosion. Because the model is constrained to measured Br_2 molar ratios and does not include heterogeneous reactions, the enhancement of heterogeneous chemistry due to interhalogen reactions is not tested by our model. While the presence of iodine chemistry did increase significantly increase the modeled daytime ozone destruction in the snowpack interstitial air, the modeled O_3 is still much higher than the observed. This suggests that other processes that are not included in the model, such as heterogeneous reactions of O_3 on the snow grains could play an important role. The heterogeneous chemistry and recycling in the snowpack is so complex, including an ill-defined surface substrate, that the community lacks a model with predictive qualities [Domine et al., 2013].

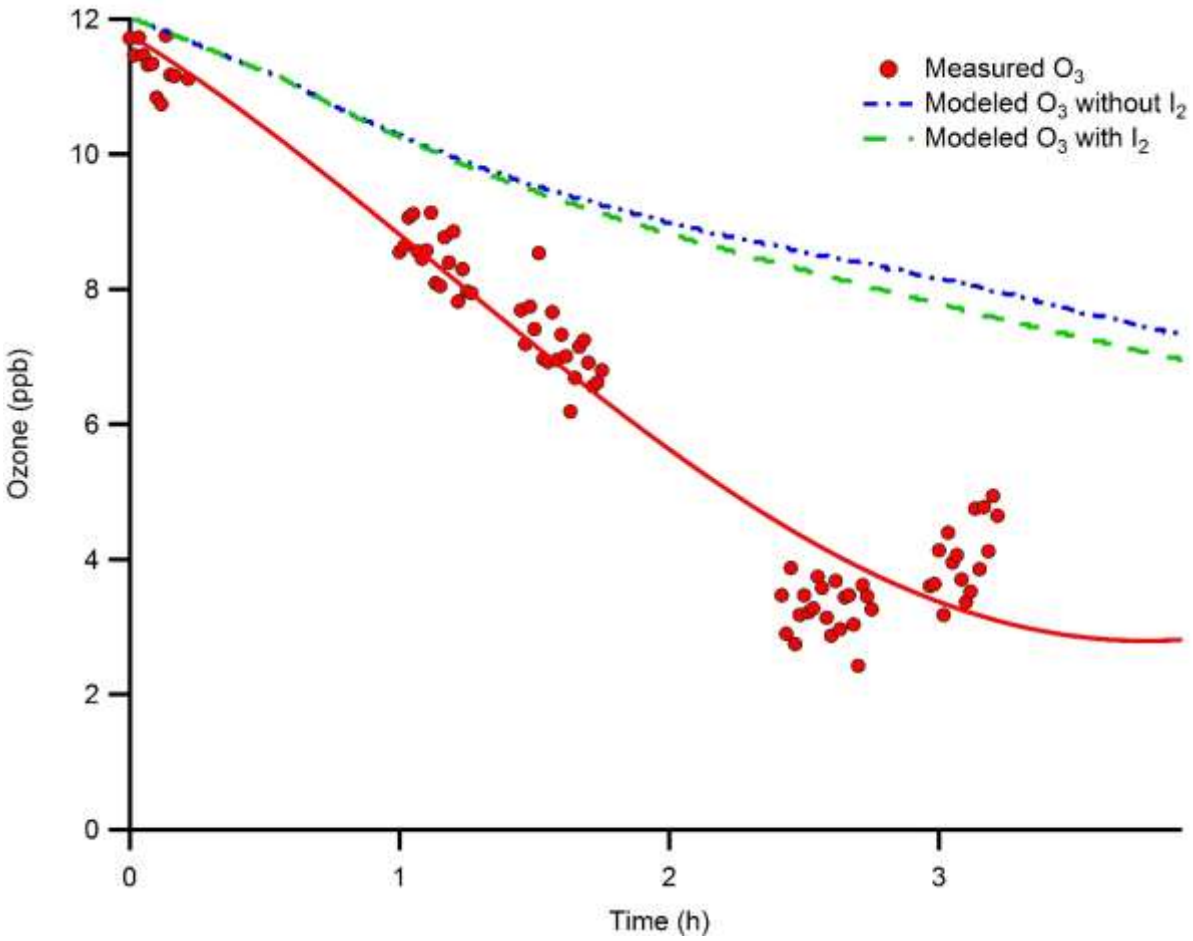

Figure 4.3 Model results showing the influence of iodine on ozone chemistry in the snowpack interstitial air.

4.3.2 The Effect of Iodine on Boundary Layer Ozone Depletion Rate

Since even small levels of I_2 can significantly impact Arctic atmospheric chemistry, a 0-D photochemical model was employed to simulate O_3 depletion and IO production. Since an ODE was not observed during the January-February 2014 study (ODEs typically begin in March in Barrow [Oltmans, 1981]), previous observations of atmospheric Br_2, Cl_2, and HOBr from the same location on March 11, 2012, were used to constrain the model (Figure 4.2). On this day, atmospheric O_3 decreased from ~20 ppb to <1 ppb over the course of 7 h (Figure 4.4a), with winds blowing from north-northeast over the consolidated snow-covered ice on the Beaufort Sea. The overall observed ozone depletion rate (3.0 ppb h^{-1} over the seven h period) is typical of a large number of ODEs observed over the snow-covered sea ice on the Arctic Ocean (average of 3.5 ppb h^{-1}) [Halfacre et al., 2014]. The initial depletion (from 14:00 – 16:10 AKST) occurred at a rate of 2.2 ppb h^{-1} and was interrupted by a local atmospheric mixing event (16:10 – 18:00 AKST), which is not possible to simulate with a 0-D model.

Given that I_2 was only measured in early February in this study, it is plausible that higher mole ratios are present in March when ODEs regularly occur. Therefore, the model was used to test the sensitivity of O_3 depletion rates to I_2 mole ratios from 0 – 2.4 ppt (Figure 4.4a). Without the inclusion of iodine chemistry, O_3 was simulated to deplete initially (14:00 – 16:10 AKST) at a rate of 1.3 ppb h^{-1} (Figure 4.4a), mostly from bromine atom chemistry. However, as shown in the Figure 4.4a, the addition of 0.3 ppt of I_2 (as observed on Feb. 2, 2014) increases the initial rate of ozone depletion by 24%, to 1.7 ppb h^{-1}. The best fit to the observed initial ozone depletion rate (2.2 ppb h^{-1}) corresponds to the inclusion of 0.6 ppt of I_2, which causes the model to simulate the initial depletion at a rate of at 2.1 ppb h^{-1}. The significant increase in the simulated ozone depletion rate with the inclusion of only 0.6 ppt I_2 demonstrates the importance of even a small amount of iodine on the depletion of boundary layer O_3. Higher, but still very modest and plausible, I_2 mole

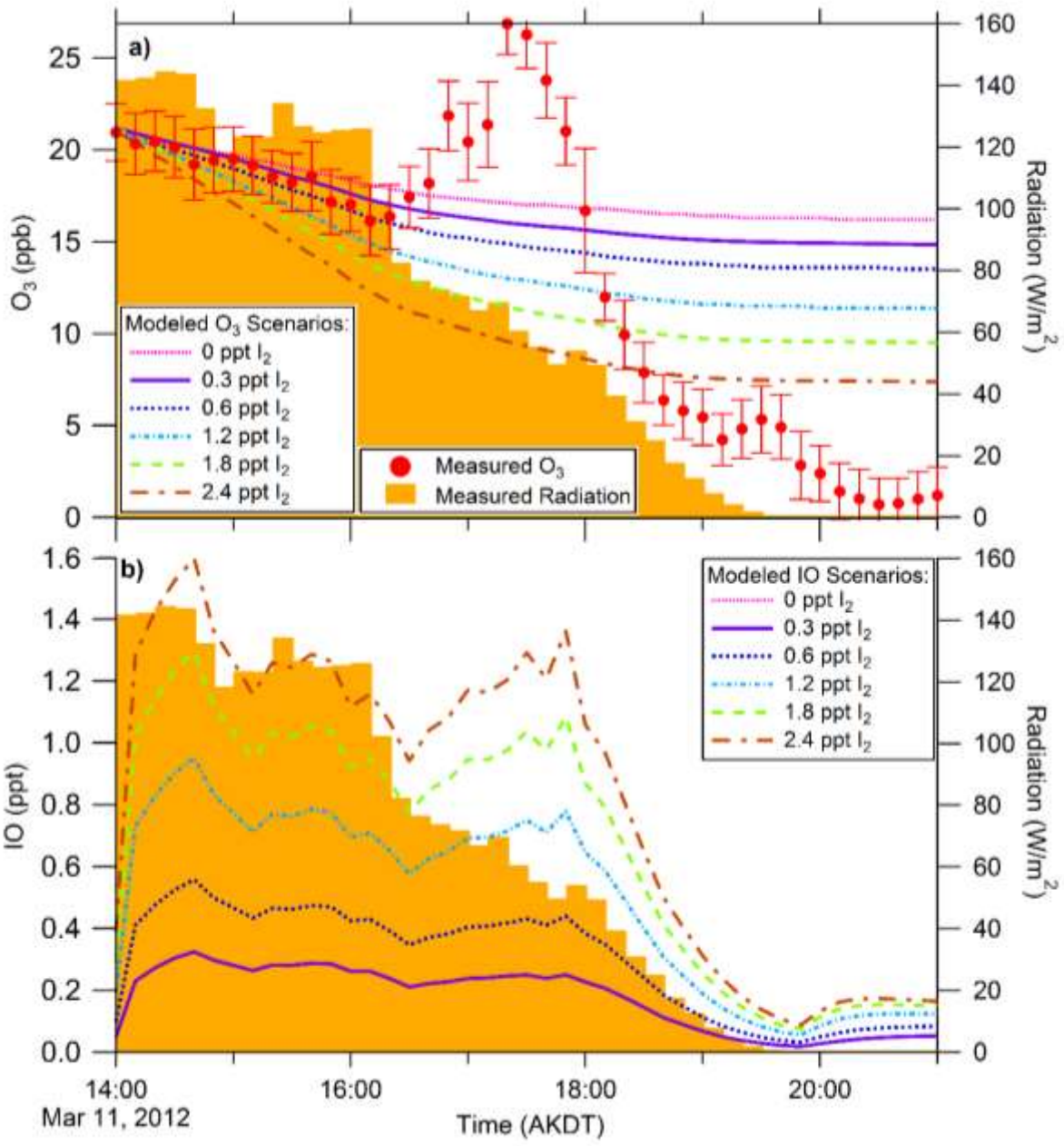

Figure 4.4 Model results show the influence of I_2 on a) tropospheric ozone depletion rates and b) IO mole ratios. An ozone depletion event occurring on March 11, 2012, was simulated with I_2 mole ratios between 0 ppt and 2.4 ppt. Cl_2, Br_2, and HOBr were constrained to measurements as shown in Figure 4.2 a) Measured O_3 with standard deviations of the 10 min average, and model results showing simulated O_3 mole ratios. b) Simulated IO mole ratios during the same period.

ratios (compared to the ~18 ppt of Br_2 present) have a pronounced effect on the predicted O_3. The addition of 2.4 ppt of I_2 triples the rate of O_3 depletion for the initial period (14:00-16:10 AKST) to 4.0 ppb h^{-1}.

The sensitivity of simulated IO concentrations to varying amounts of I_2 on March 11, 2012, was also examined (Figure 4.4b). The simulation containing 2.4 ppt of I_2 produced a maximum of 1.6 ppt of IO, which is near the highest mole ratios observed (1.5 ppt) in Alert, Canada [Zielcke, 2015]. The simulation with 0.3 ppt of I_2 (Feb. 2, 2014 maximum mole ratio) revealed IO mole ratios similar to those most commonly observed at Alert (~0.3 ppt) [Zielcke, 2015]. It should be noted, however, that there are significant uncertainties associated with modeling gas-phase iodine chemistry. Variations in the branching ratio for the products of the reaction of IO with itself can significantly change predicted IO mole ratios. The branching ratios used here (38% I+OIO, 16% I+I, 46% IOOI) may cause overestimation of IO by up to ~10 % [Sommariva et al., 2012]. Additionally, since the photolysis of higher order iodine oxides (I_2O_3 and larger) could cause the simulated O_3 depletion ratio to be underestimated [Saiz-Lopez et al., 2014], sub-ppt levels of I_2 may result in even greater ozone depletion rates than predicted here. Even with these uncertainties in simulating iodine chemistry, our snowpack and ambient I_2 observations along with our model results demonstrate that even a small amount of I_2, at the observed levels, can significantly increase O_3 depletion rates, while also producing realistic IO mole ratios.

4.4 Conclusions

Even at sub-ppt levels in the Arctic atmosphere, iodine chemistry is predicted to have significant impacts on atmospheric boundary layer oxidation capacity and composition, impacting pollutant fate and particle formation. The inclusion of observed molar ratios of I_2 in a 0-D model increases the ability of the model to simulate the initial rate of an observed ozone depletion event

and produces IO concentrations consistent with recent observations. These first measurements of Arctic snowpack interstitial air I_2 and snow I^-, combined with photochemical modeling suggests that iodine (even at <1 ppt) is vital in explaining observed snowpack ozone depletion, as well as springtime destruction of Arctic boundary layer ozone. However, much is still not known about iodine chemistry in the Arctic, and further investigation is needed. Specifically, further understanding of the behavior of higher order iodine oxides may allow for better modeling and understanding of iodine chemistry both in the Arctic and worldwide.

CHAPTER 5. MEASURMENTS OF SNOWPACK MOLECULAR HALOGEN FLUXES

5.1 Introduction

While it has been demonstrated that I_2 [Raso et al., 2017], Br_2 [Pratt et al., 2013], BrCl, and Cl_2 [Custard et al., 2017] are produced photochemically in the Arctic snowpack, the magnitude of that production is not well known. The production rate is usually expressed as a flux, or the amount produced per area per amount of time – in this case, molecules cm^{-2} s^{-1}. One dimensional models have been used to estimate the Br_2 flux from the snowpack that would be necessary to explain observations of BrO and Br_2 [Lehrer et al., 2004; Piot and von Glasow, 2008; Piot and Glasow, 2010; Thomas et al., 2011; Toyota et al., 2014]. Estimates of Cl_2 fluxes from modeling have not been reported in the literature, as measurements of BrO make up most available halogen measurements, and 1-dimensional models have not focused on chlorine chemistry. Model-estimated fluxes of Br_2 have ranges covering two orders of magnitude (9.0×10^7 – 2.7×10^9 molecules cm^{-2} s^{-1}) [Lehrer et al., 2004; Piot and von Glasow, 2008; Piot and Glasow, 2010; Toyota et al., 2014]. However, significant uncertainty exists in both multiphase recycling of halogens on aerosols and vertical mixing in the Arctic, and models that fit the flux to measurements must assume some best estimate of turbulent mixing. Therefore, an independent measurement of the flux is necessary to understand the magnitude and impact of halogen chemistry in the Arctic.

Only one such measurement of halogen fluxes exists in the Arctic. Custard et al. [2017] reported fluxes of Br_2 and Cl_2 from the snowpack in Utqiaġvik (Barrow), measured during the 2014 campaign described in Chapter 2 of this work. Fluxes are often defined using Fick's law of diffusion (Equation 5.1), which postulates that the molecules will diffuse from areas of high

concentration to areas of low concentration with a magnitude that is proportional to the concentration gradient (dC/dx).

$$diffusive\ flux = -D\frac{dC}{dx} \quad \text{E5.1}$$

This diffusion flux is also controlled by the diffusivity of the species in the substrate (D). In the atmosphere mixing is largely controlled by turbulence, rather than molecular diffusion, but the turbulent flux can be defined similarly (Equation 5.2).

$$turbulent\ flux = -K\frac{dC}{dz} \quad \text{E5.2}$$

Here the diffusivity, known as eddy diffusivity (K) in this case, is a property of the amount of turbulent mixing in the environment rather than a property of the substance being mixed within the fluid medium. Custard et al. [2017] utilized this definition and calculated fluxes by measuring the gradients of Br_2 and Cl_2 above the snowpack. The eddy diffusivity (K) is usually calculated using the flux of momentum above the surface, however, calculation of the momentum flux requires high frequency wind measurements, which Custard et al. [2017] did not have. Instead, they utilized wind speed measurements from the National Oceanographic and Atmospheric Administration (NOAA) Global Monitoring Division (GMD) site, which is nearly 5km away. The friction velocity (u^*) is calculated using Equation 5.3, which utilizes the van Karman constant ($\kappa = 0.4$), the NOAA wind speeds at 10 m above the ground ($U(10m)$), and the logarithmic ratio of the wind speed height (10 m) to the measurement height (z_0).

$$u^* = \frac{\kappa U(10m)}{\ln(\frac{10m}{z_0})} \quad \text{E5.3}$$

The eddy diffusivity can then be calculated using this friction velocity, the logarithmic mean height of the measurement (z_s), and the von Karmen constant (Equation 5.4).

$$K = \kappa z_s u^* \quad \text{E5.4}$$

Because this eddy diffusivity is calculated using data that is not collocated with the measurements, it may be much more uncertain than simple propagation of error can account for and introduces significant uncertainties that are not well expressed in the paper. Additionally, the measurements of Br_2 and Cl_2 gradients were conducted within a few meters of the laboratory building, which significantly affects the turbulent eddies that transport the flux from the snowpack [Burba, 2005]. Despite these likely underreported uncertainties, Custard et al. [2017] report the first, and currently only fluxes of halogens in the Arctic. The resulting Br_2 fluxes (0.69 – 12x10^8 molecules cm^{-2} s^{-1}, Figure 5.1) are similar to, if slightly lower than, those predicted by models. The relatively low fluxes may be in part due to the measurements occurring in February, while most model predictions are for March – April when halogen chemistry is most active. Cl_2 was only above the CIMS detection limit one of the two days on

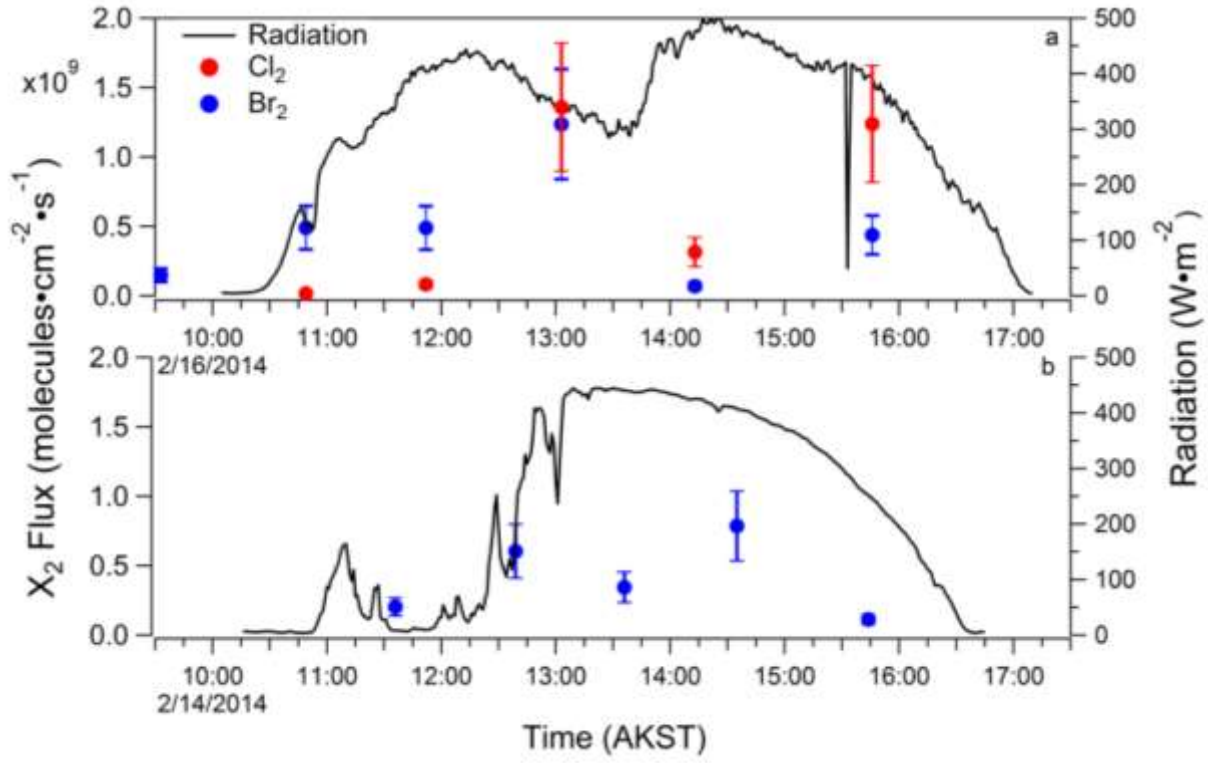

Figure 5.1 Calculated fluxes for Br_2 (blue) and Cl_2 (red) on February 16 (top) and 14 (bottom) 2014. Reproduced from Custard et al. [2017].

which measurements were conducted, with a flux of the same order of magnitude as the Br_2 fluxes (0.16-14x10^8 molecules cm^{-2} s^{-1} Figure 5.1). Fluxes with both higher time resolution and lower uncertainty would greatly increase our understanding of the magnitude and diurnal pattern of halogen fluxes in the Arctic. As there is no current comparison for the Cl_2 fluxes observed by Custard et al. [2017], further measurements are necessary to verify the order of magnitude of chlorine produced in and emitted by the Arctic tundra snowpack.

The eddy covariance method for calculating fluxes [Wofsy et al., 1993] allows for much higher frequency of fluxes, as it does not have to rely on measurements of concentrations at multiple heights. The foundation of this method is that turbulent mixing occurs through eddies in the atmosphere, and that the upward flux depends on the steepness of the gradient, and the magnitude of the turbulent eddies. These eddies can be visualized as irregular three-dimensional swirls of air. When a surface produces the species of interest a gradient occurs, with the highest concentrations close to the surface. This gradient means that upward eddy motions will contain higher concentrations than downward eddy motions. The method calculates the correlation between the variances (covariance) of the vertical wind speed (u) and the concentration of the species of interest (C) over some averaging period. This is expressed in Equation 5.5, where the overbar represents an average and the prime symbol ($'$) represents the variance.

$$Flux = \overline{(\bar{u} - u) * (\bar{C} - C)} = \overline{u'C'} \qquad \text{E5.5}$$

A similar method is usually used to determine the momentum flux ($\overline{u'w'}$) mentioned above for calculation of the eddy diffusivity (K).

The eddy covariance method of determining fluxes has several advantages, including increased frequency of flux data. However, its implementation is dependent on the ability to make precise, high frequency (usually ~10 Hz) measurements of both the vertical wind speed and the

species of interest. As the availability of commercial high frequency 3-dimensional sonic anemometers and gas sensors has bloomed in recent decades, the eddy covariance method has gained popularity [Baldocchi, 2013]. Because the eddy covariance method relies on the variance of the measurement, precision is essential to not under or overestimate the covariance. High-frequency measurements are essential to capture the portion of the flux that is carried by small eddies. This can be especially important in the wintertime Arctic, where there is little turbulence because of the lack of convective mixing. Only one previous measurement of eddy covariance fluxes in the wintertime Arctic has been reported. Zona et al. [2016] reported that the production of methane by the tundra is much more prominent during the wintertime than previously assumed. However, they did not include significant discussion of the effect of reduced turbulence over a frozen surface. An example of the spectrum of eddies present over the wintertime Arctic tundra can be seen in Figure 5.4. Even close to the surface (0.6 m) most eddies have a frequency of 1 Hz or less. The closeness of the surface is important, as the concentration of the halogens produced by the snowpack decays with height due to photolysis. Sampling near

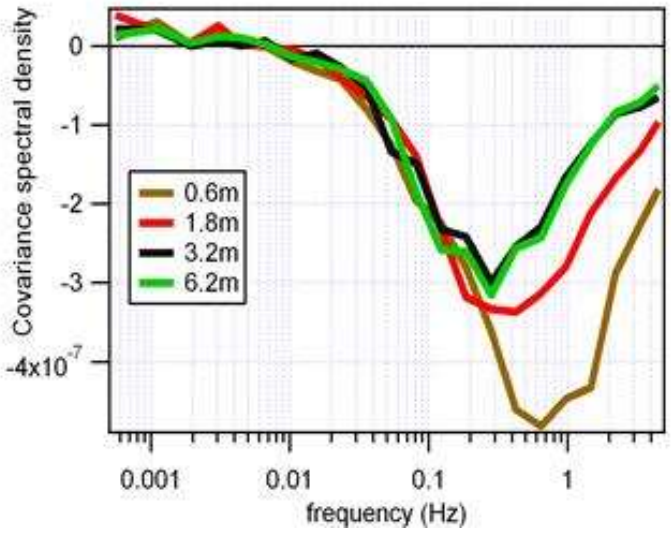

Figure 5.2 Spectral densities of eddies in the Arctic at various heights above the tundra. Courtesy of Ralph Staebler of Environment Canada (Personal Communication, May 25, 2015)

the snowpack must occur at a rate of at least 2 Hz to capture most of the transport that occurs because of the Nyquist frequency. It is only recently that measurements of halogens have progressed from gas chromatography based methods, with a typical measurement frequency of ~10 min [Impey et al., 1997], to mass spectrometry, with a typical measurement frequency of ~10s [Liao et al., 2011]. Even this sixty times increase in measurement frequency is not sufficient for eddy covariance.

Here we describe method development and implementation of the use of a chemical ionization mass spectrometer (CIMS) instrument to collect data used to calculate fluxes of Cl_2 and Br_2 using the eddy covariance method. Measurements were conducted during the 2016 PHOX:MELT (Photochemical Halogen and Ozone eXchange: a Meteorological Experiment on Layer Turbulence) campaign in Utqiaġvik, Alaska in February – May 2016. These are the second wintertime eddy covariance fluxes in the Arctic, and the first eddy covariance fluxes of molecular halogens. The calculations for these fluxes are described thoroughly. The resulting fluxes are shown and discussed, and future directions for the measurements of Arctic halogen fluxes are suggested.

5.2 Field Campaign and Data Collection

5.2.1 Field Site Description

Measurements of fluxes were conducted on ten days in March and April 2016 during the PHOX:MELT (Photochemical Halogen and Ozone eXchange: a Meteorological Experiment on Layer Turbulence) campaign on the Barrow Environmental Observatory (BEO) near Utqiaġvik, Alaska (Figure 5.3). Because of instrumental limitations (discussed below), only one halogen could be measured at a time. Therefore we measured Cl_2 fluxes on two of these ten days and Br_2

Figure 5.3 Map of field site near the Barrow Environmental Observatory. Wind rose is courtesy of the NOAA global monitoring division.

Fluxes on eight days. At the field site winds are predominantly from the north to northeast. The upwind fetch of the measurements extended over the BEO, containing mostly homogeneous tundra. However minor disruption of the upwind tundra did occur before flux measurements. This disruption was due to use of snowmobiles to lay a power cable connected to construction of a semi-permanent environmental monitoring station just outside the fetch of the measurement site. Disruption of the upwind tundra was minimal, however, likely including <10% of the measurement area. Measurements conducted at the site included halogens from the chemical ionization mass spectrometry (CIMS) instrument, and height-resolved micrometeorological data from eight 3D sonic anemometers (CSAT3D, Campbell Scientific) placed on a 12 m tall tower. A separate 192 cm tall mast with a single 3D sonic anemometer (SCAT3D, Campbell Scientific) was utilized for eddy covariance flux calculations. Concentrations for eddy covariance flux calculations were measured using a 23 m long 12.7 mm ID heated (30˚C) sampling line connected to the CIMS

instrument, which was located in a building 17 m downwind of the mast. Figure 5.4 shows the mast used for measurements, including the 3-D sonic anemometer, and the colocation of the sampling line inlet.

5.2.2 CIMS Measurements

Br_2 and Cl_2 were measured at 2 Hz using chemical ionization mass spectrometry (CIMS) as described by Liao et al. [2011, 2012], Peterson et al. [2015], Custard et al. [2017], and chapter 2 of this dissertation using hydrated I^- ($I(H_2O)_n^-$) as a reagent ion. Br_2 was detected as $I^{79}Br^{79}Br^-$ (287 amu) and $I^{79}Br^{81}Br^-$(289 amu). Cl_2 was detected as $I^{35}Cl^{35}Cl^-$(197 amu) and $I^{35}Cl^{37}Cl^-$(199 amu). Each signal was normalized to the reagent ion signal in order to account for any changes in ionization efficiency, ion transmission, or multiplier response. The final concentration of each species was calculated following Equation 5.6, which utilizes mass 287 as an example. The instrumental sensitivity is obtained via the response of the instrument during a one-point calibration (Equation 5.7).

$$Concentration = \frac{287\ amu\ signal - background\ 287\ amu\ signal}{147\ amu\ signal} / \ Instrumental\ Sensitivity \quad \text{E5.6}$$

$$Instrumental\ Sensitivity = \frac{287\ amu\ signal}{147\ amu\ signal} / Calibration\ Concentration \quad \text{E5.7}$$

Background measurements were conducted for 30 seconds (60 points) every 10 minutes by flowing the sampled air through a glass wool scrubber, which was heated to 30°C. Glass wool has been previously shown to remove >99% of halogens [Neuman et al., 2010; Raso et al., 2017]. One-point calibrations were conducted with a Br_2 or Cl_2 permeation device (VICI metronics) at 592 ppt and 968 ppt respectively, for 30 seconds every 2 hours. Figure 5.5 shows an in-field calibration curves collected on March 14, 2016. The permeation rates of the permeation

Figure 5.4 Flux measurement mast with sampling line attached (top), and colocation of air sampling and sonic anemometer (bottom)

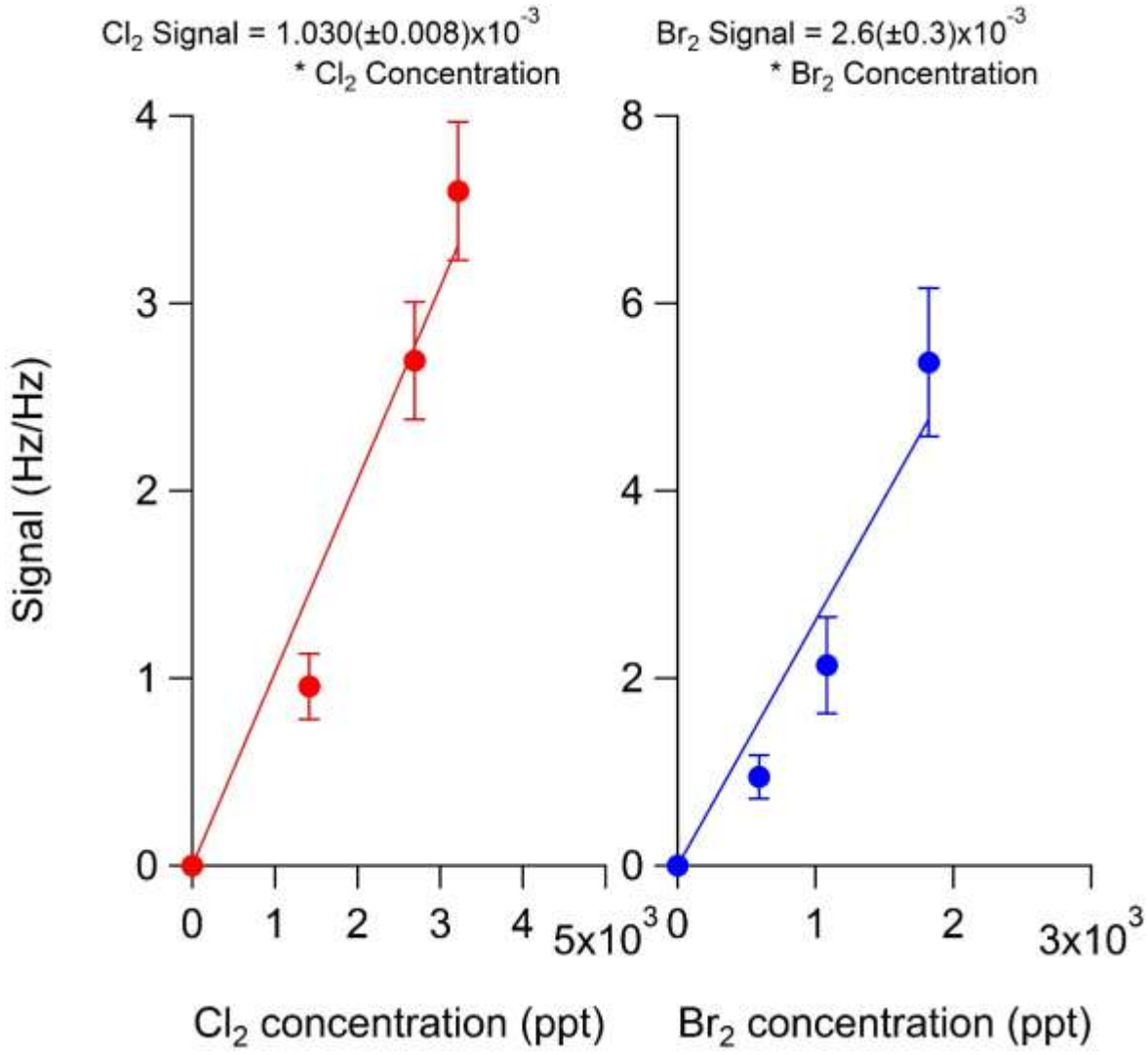

Figure 5.5 Calibration curves for Cl_2 and Br_2 collected at 2 Hz in the field on March 14, 2016.

devices were quantified by flowing their output through an impinger containing a buffered potassium iodide solution. The molecular halogens quantitively convert I^- to I_3^-, which was detected using UV-Visible spectroscopy at 354 nm [Liao et al., 2011]. 3σ limits of detection were 1.9-4.0 ppt and 1.1-2.1 ppt for Br_2 and Cl_2 respectively. The instrumental uncertainties, found by propagating the uncertainties of the background, calibration, and calibration concentration, were ±20%+LOD for Cl_2 and 22%+LOD for Br_2.

A full flow diagram of the flow within the CIMS instrument is shown as Figure 5.5. Arctic air was drawn through the 23 m long sampling line at a rapid but laminar flow (17.1 lpm, Reynolds number 2200). The sampling line was attached to a custom built three-way sampling valve, which allowed for calibration and background measurements. Air was sampled into the flow reactor via a 0.51 mm orifice. The reagent ion ($I(H_2O)_n^-$) was made by passing excess CH_3I through an in-line analyzer containing Po-210. Within the flow reactor the resulting I^- was hydrated by mixing with humidified N_2 which is produced by flowing dry N_2 through a custom built stainless steel impinger. The flow reactor was pressure controlled (13 torr), by varying the N_2 flow through the Po-210 ionization source using a mass flow controller. The transmission efficiency of ions through the CIMS instrument is an essential part of the precision of mass spectrometric measurements. This efficiency is controlled by the voltage gradient from the first voltage on the orifice between the flow reactor and the collision disassociation chamber (CDC, Figure 5.5) and the final voltage placed on the orifice between the octupole ion guide and the mass selecting quadrupole. The four voltages that can be adjusted are labeled in Figure 5.5.

Ion detection was accomplished using an electron multiplier tube (Model 470, Detector Technology Inc.) and mass hopping. Usually, measurements of multiple masses are conducted

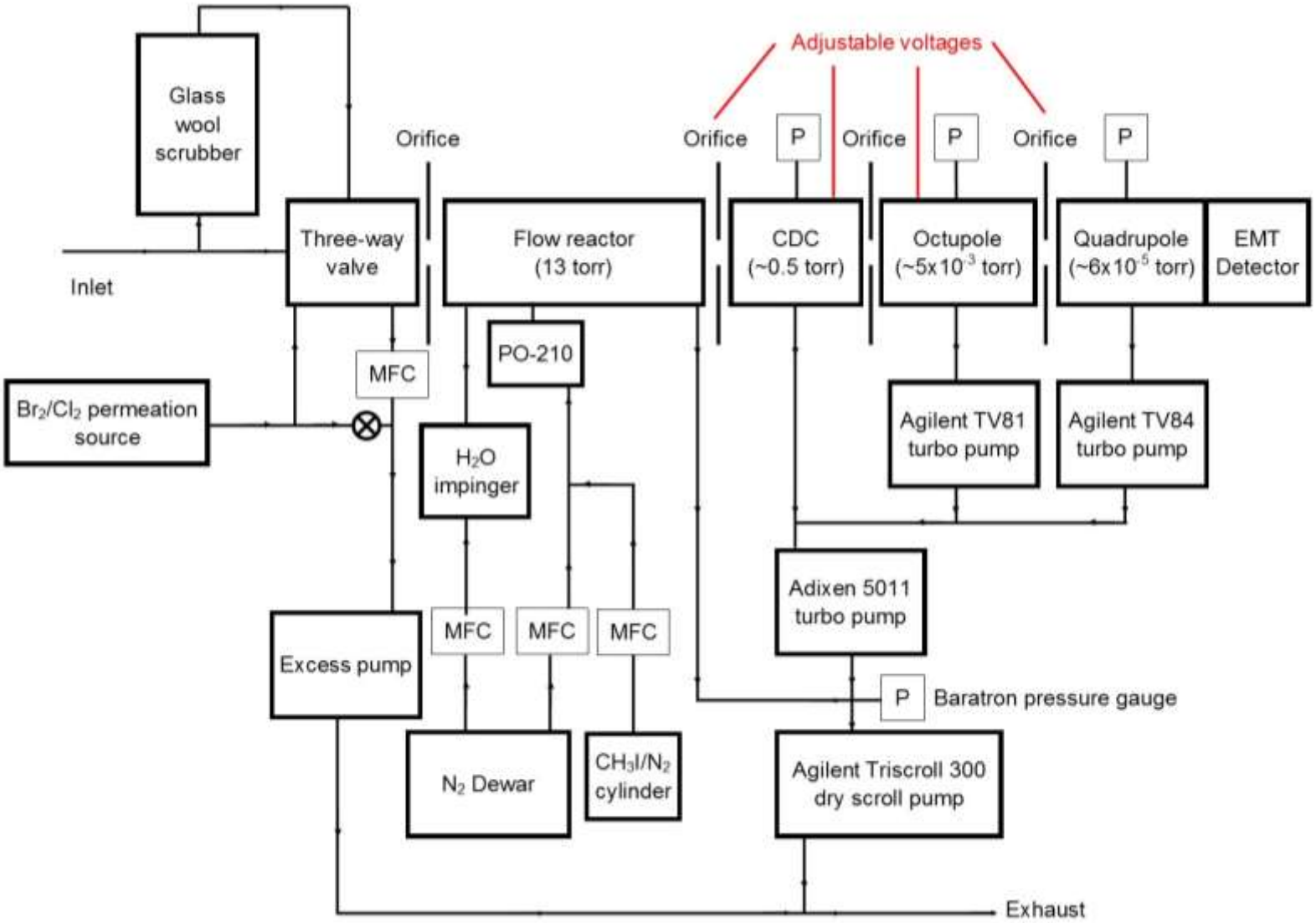

Figure 5.6 Flow diagram for the CIMS instrument for measurements in 2016. Locations of adjustable voltages for ion transition optimization are shown in red.

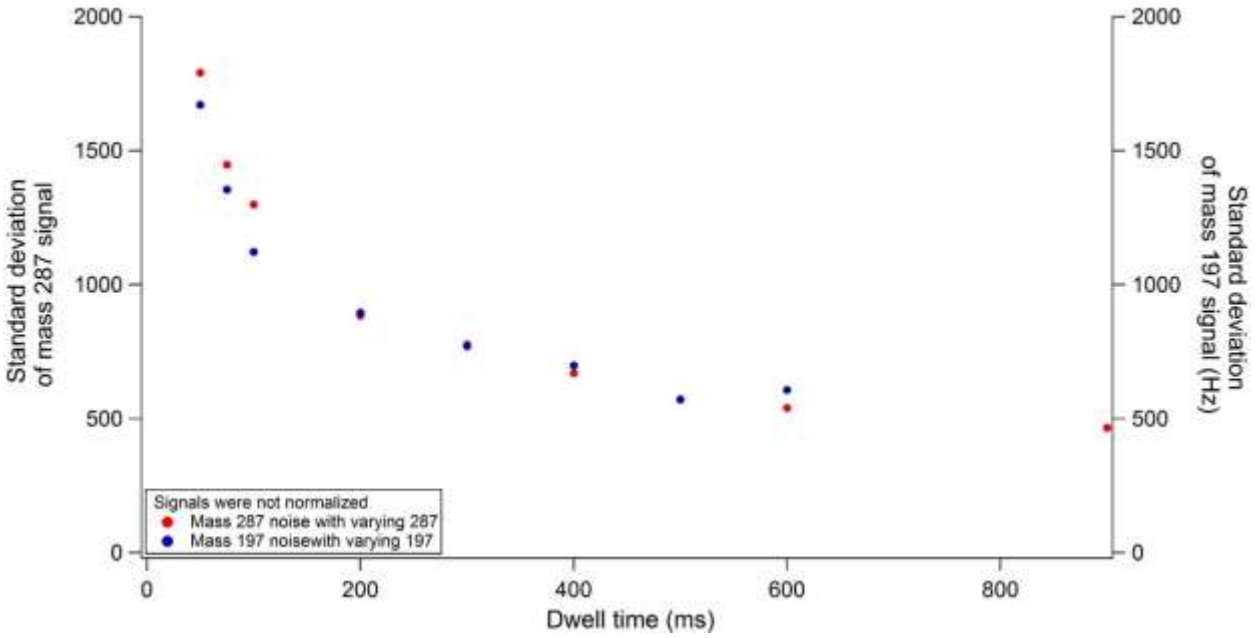

Figure 5.7 Dwell time of masses 287 amu (Br_2) and 197 amu (Cl_2) vs. the standard deviation of the signal.

with dwell times of 500 - 1000 ms [Liao et al., 2011, 2012; Pratt et al., 2013; Custard et al., 2017]. To decrease the duty cycle time, and thus increase the frequency of measurements, only three ions were monitored each day – the $I^-{\cdot}H_2{}^{18}O$ ion (147 amu), the main ion used for calculations (287 amu for Br_2 and 197 amu for Cl_2), and the secondary ion used for isotopic confirmation of the halogen (289 amu for Br_2 and 199 amu for Cl_2). The relationship between frequency and noise for masses 287 amu and 197 amu was investigated using permeation devices. As can be seen in Figure 5.6, for both 287 amu (Br_2) and 197 amu (Cl_2), the standard deviation of the signal increases as $1/\sqrt{t}$ decreasing dwell times (t) due to counting statistics. Figure 5.6 shows that a dwell time of ~200 ms is optimal for high-frequency measurements without sacrificing precision. During measurements, the total duty cycle (sum of dwell times) was 500 ms, for 2Hz frequency of measurements. The reagent ion mass was monitored for 250 ms, the main halogen

mass (287 amu or 197 amu) was monitored for 200 ms, and the secondary halogen mass was monitored for 50 ms.

5.2.3 Line Losses and Recycling

Line losses were tested both in the laboratory before field deployment and in the field. In the laboratory, line losses were tested utilizing the permeation devices. These laboratory tests showed a large range of line losses, but they were not significantly different from zero. Laboratory line losses were 16±22% for Br_2 and -5±32% for Cl_2, with 15 trials. Laboratory line losses also showed no correlation with halogen concentration between 15 ppt and 90 ppt, as demonstrated in Figure 5.7.

It has been previously noted that other bromine species – likely HOBr – can recycle on inlet lines, forming Br_2 from halides residing on the surfaces of the inlet line [Neuman et al., 2010]. To minimize this, the 23 m long sampling line was rinsed with ~2 L of Milli-Q water between experiments. An aliquot of this water was reserved for analysis of Br^- and Cl^- content and the inlet line was heated and dried using ultra high purity nitrogen (Air Liquide). The reserved line rinse samples showed no trend in halide content with either the length of use or the concentration of the halogens measured through the line. Recycling was further tested in the field, along with line losses, by comparison of the concentrations measured through the sampling line and concentrations measured utilizing the ambient measurement method described by Liao et al. [2011], which minimizes interaction between the CIMS sampling interface and the Arctic air sample. The ambient inlet was rapidly changed to the clean 23 m long inlet line, which was then suspended at approximately the same height above the snowpack as the ambient inlet for a minimum of 10 minutes. An experiment was then conducted, which utilized the sampling line for 5-23 hours. At the end of the experiment, the sampling line was again suspended at the same

height as the ambient inlet for a minimum of 10 minutes before the inlet was rapidly exchanged back to the ambient. This test was performed on six days in March and April 2016. A paired two-tailed t-test with 95% confidence showed no significant differences between the concentrations measured using the ambient method and the sampling line either at the beginning or end of an experiment.

Because line losses and recycling were never found to be significantly different from zero either in the laboratory or the field, halogen concentrations have not been corrected for line losses.

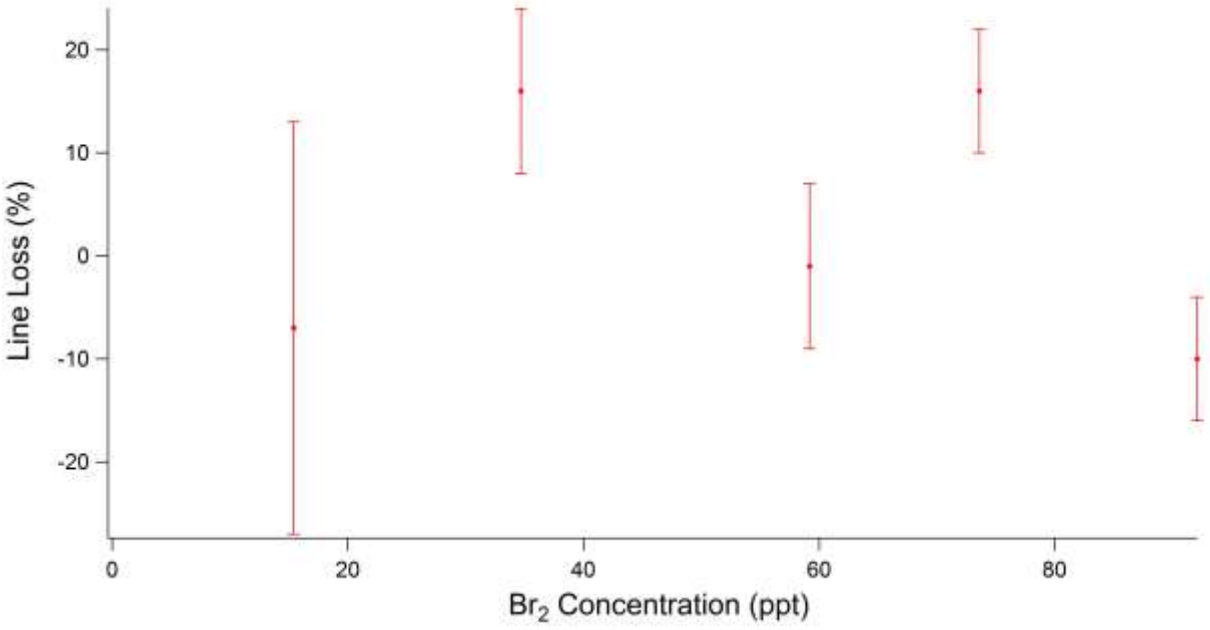

Figure 5.8 Line loss through the 23 m long inlet line in the laboratory for Br_2 as a function of concentration. Each concentration shows the average and standard deviation of three trials.

5.3 Flux Calculations and Results

While 2Hz CIMS measurements were conducted for ten days during the PHOX:MELT campaign, only one day yielded fluxes that were significantly different from zero – March 17, 2016. Therefore, the flux calculations and results below are presented for that day. Cl_2 fluxes and their associated uncertainties are calculated in sections 5.3.1-5.3.5 for March 17. An analysis of the lowest Br_2 flux that we could have detected is discussed in section 5.3.6.

5.3.1 Data preparation

The eddy covariance fluxes were calculated using 30-minute periods of 10 Hz data from the 3-dimensional sonic anemometer, and 2 Hz data from the CIMS. The 10 Hz wind data is broken into three components – w, the vertical wind, u, the horizontal wind, and v, the cross wind. The wind data was coordinate-rotated, so the mean vertical wind speed is zero, and the mean cross wind is zero. The true vertical wind speed must be zero due to conservation of mass – there cannot be a net vertical movement of air. Coordinate rotation of the vertical wind simply corrects for minor deviations in the leveling of the instrument relative to the surface under it. The following Equations (5.8-5.15) are used to perform 3-dimensional 2-step coordinate rotation on the 10Hz winds data, where the subscript 0 indicates the untouched raw data, and the subscripts 1 and 2 indicate the data after the first and second rotation respectively [Kaimal and Finnigan, 1994].

$$u_1 = u_0 cos\theta + v_0 sin\theta \quad \text{E5.8}$$

$$v_1 = -u_0 sin\theta + v_0 cos\theta \quad \text{E5.9}$$

$$w_1 = w_0 \quad \text{E5.10}$$

$$\theta = \tan^{-1}\left(\frac{\bar{v}_0}{\bar{u}_0}\right) \quad \text{E5.11}$$

$$u_2 = u_1 cos\phi + w_1 sin\phi \quad \text{E5.12}$$

$$v_2 = v_1 \quad \text{E5.13}$$

$$w_2 = u_1 sin\phi + w_1 cos\phi \quad \text{E5.14}$$

$$\phi = \tan^{-1}(\frac{\bar{w}_1}{\bar{u}_1}) \quad \text{E5.15}$$

After coordinate rotation, a wavelet filter was used to filter out data that was too quiescent (lacking turbulence) for meaningful fluxes to be measured. The data is filtered using the variable block averaging algorithm proposed by Howell [1995]. A Haar wavelet transform is computed by calculating arithmetic averages over a series of overlapping windows. This divides the data into variable width blocks that are bounded by sharp changes in the data.

Because the two data sets were collected at different frequencies, the 10 Hz wind data must be reduced to 2 Hz for calculating the halogen fluxes. Time matching was accomplished by matching the 10 Hz measurement that occurred within 0.1 seconds of the 2 Hz measurement to the 2Hz measurement. In the final step before the fluxes were calculated, the lag between the 2 data sets was determined. Because the CIMS measurements were conducted after the sample had been pulled through a 23 m long 12.7 mm ID sampling line at 17.1 lpm, there is a theoretical lag of 10.2 seconds ($\pi r^2 l/flowrate$) between the measurements. However other variables can cause additional or reduced lag. For instance, the recorded times on the instrument computers, while set to match, may differ by a few seconds. Additionally, there is a small offset between the sonic anemometer and the start of the inlet line (Figure 5.4) that may cause additional lag. The lag time adjustment between the two data sets is corrected by maximizing the covariance (and therefore the flux) calculated from the two data sets. This is done by changing the time alignment of the two sets by 0.5 seconds (1 data point), calculating the covariance between the two sets, and repeating. Figure 5.7 shows the calculated covariance between Cl_2 and vertical wind speeds in the 30-minute period centered around 18:16 AKDT on March 17, 2016, vs. the number of points Cl_2 has been offset, after correcting for the known 10.2 second lag. The point at zero lag points (circled in red)

is near the maximum, suggesting that additional lag time does not play a significant role. Figure 5.9 shows the 2 Hz data for March 17, 2016 after data preparation.

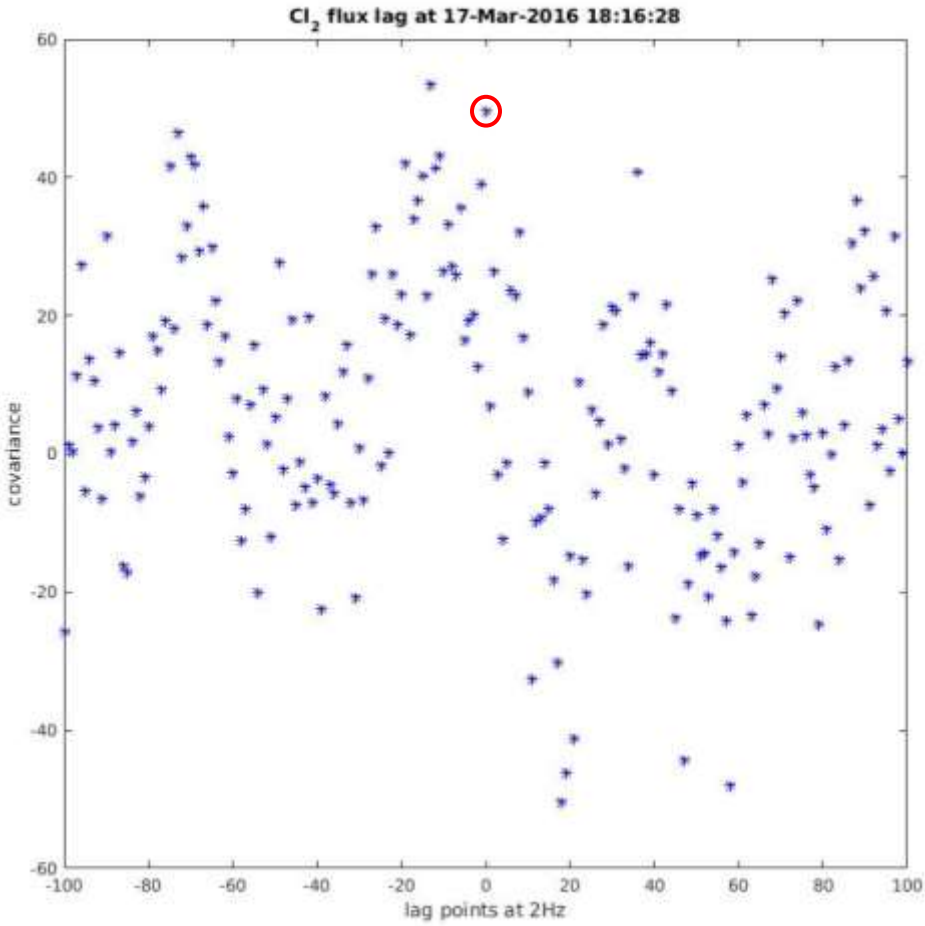

Figure 5.9 Calculated covariance between Cl_2 and *w* in the half hour centered around 18:16 AKDT on March 17, 2016. Cl_2 data had previously been corrected for the known 10.2 second lag. The covariance at zero lab points is circled in red.

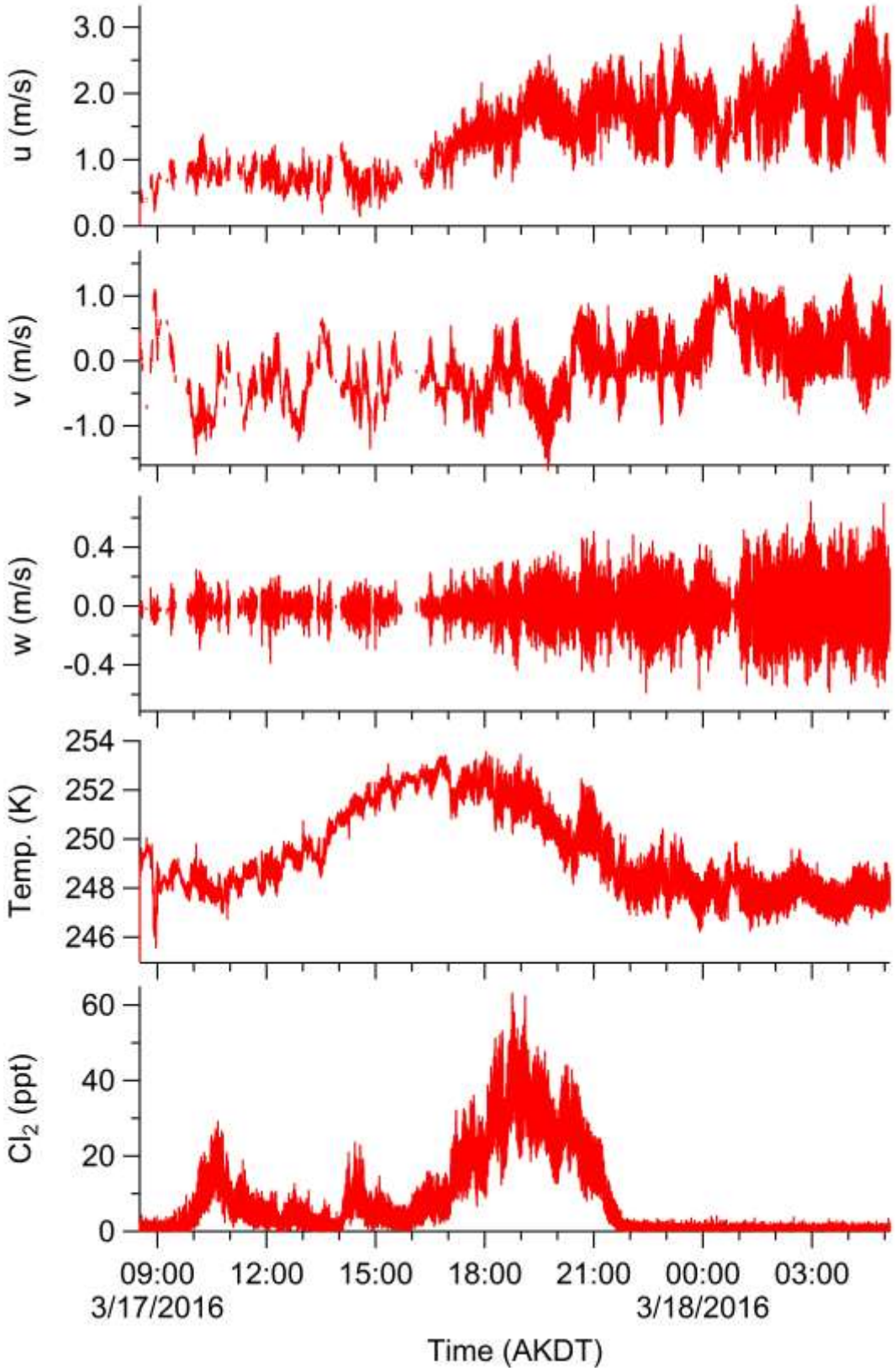

Figure 5.10 2 Hz data after preparation.

5.3.2 Eddy Covariance Calculations

Both the 10 Hz and the 2 Hz time-matched data were broken into 30-minute segments for data calculations and averaging. Each 30-minute segment of data was detrended using a 3rd order polynomial fit. Normally data used for eddy covariance fluxes is either not detrended, or detrended linearly. However linear detrending left several artifacts in the intermittent turbulence, despite the described wavelet filtering. For each data segment the friction velocity (u^*), kinematic heat flux, and eddy covariant flux was calculated using Equations 5.16-5.18. Kinematic heat fluxes were calculated using both 10 Hz and 2 Hz data. Cl_2 fluxes were calculated using 2 Hz data.

$$u^* = [(\overline{u'w'})^2 + (\overline{v'w'})^2]^{\frac{1}{4}} \quad \text{E5.16}$$

$$kinematic\ heat\ flux = \overline{w'T'} \quad \text{E5.17}$$

$$Cl_2Flux = \overline{Cl_2'w'} \quad \text{E5.18}$$

Figure 5.10 shows the calculated friction velocities, kinematic heat fluxes, and Cl_2 fluxes.

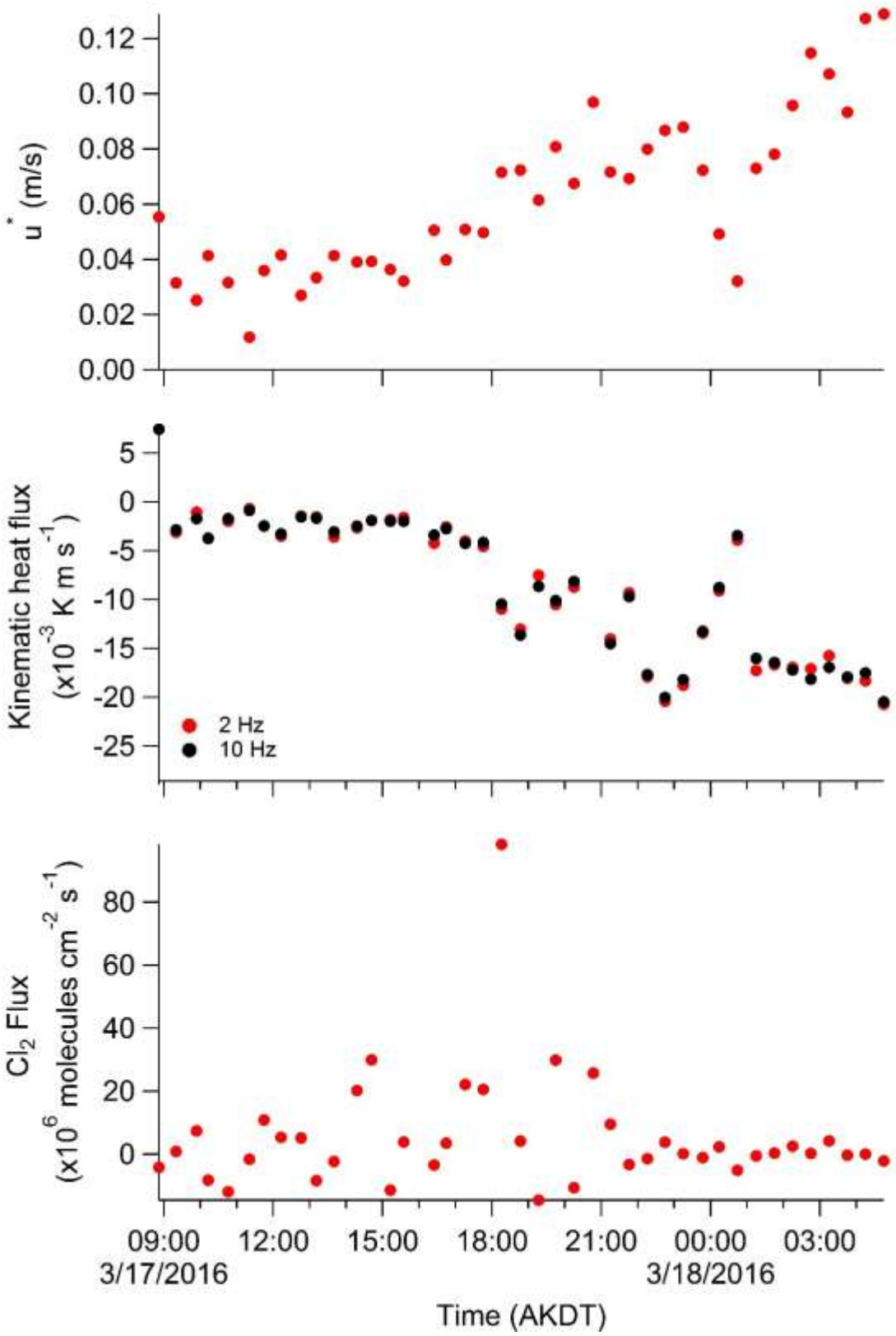

Figure 5.11 Friction velocity, kinematic heat fluxes, and Cl_2 fluxes

5.3.3 Corrections for Systematic Errors

Three systematic errors were present in the measurements made for eddy covariance flux calculations. The first of these was undersampling of the flux carried by high-frequency eddies. As described in the introduction above, the Nyquist frequency requires that sampling occurs at two times the highest frequency present to measure all components of a spectrum. Because sampling of Cl_2 was only possible at 2 Hz, there were likely under sampling of the flux carried by high frequency eddies is likely. This can be seen in Figure 5.10, which shows the co-spectral density of the vertical wind speed and temperature for measurements made at 2 Hz (red) and 10 Hz (blue). The area under the curves is proportional to the kinematic heat flux. The area under the corresponding spectrum of vertical wind and Cl_2 is proportional to the Cl_2 flux. The area underneath the curve corresponding to the 2 Hz measurements is smaller than the area under the curve from the 10 Hz measurements. Because mixing is turbulent, heat and Cl_2 are carried on the same eddies and the difference between the kinematic heat flux at 2Hz and 10 Hz will be the same as the difference between the Cl_2 flux at 2 Hz and 10 Hz. Therefore, the flux can be frequency-corrected following Equation 5.20.

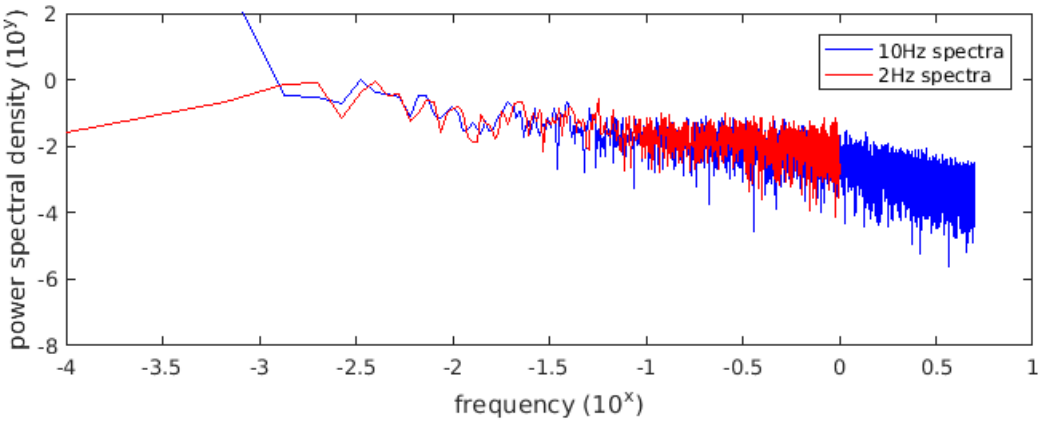

Figure 5.12 power spectral density of the vertical wind speeds at 10 Hz (blue) and 2 Hz (red).

$$Frequency\ corrected\ Cl_2\ flux = Cl_2Flux * \frac{Kinematic\ heat\ flux\ at\ 10\ Hz}{Kinematic\ heat\ flux\ at\ 2\ Hz} \quad \text{E5.20}$$

The second systematic error to correct for is the difference in the placement between the inlet of the CIMS sampling line and the sonic anemometer. This can be observed in Figure 5.4. Because eddies can be smaller than the distance between the inlet and the sensor (and thus missed), and tend to stretch over time, this distance introduces more than just lag between the two measurements. This correction was done following the method of Lee and Black [1994], who sampled a variety of distances from their sonic anemometer and derived Equation 5.21.

$$\frac{Measured\ Flux}{True\ Flux} = e^{-\beta*((D/z)^{4/3})} \quad \text{E5.21}$$

Here β is defined by Equation 5.22.

$$\beta = 1.18(\cos(d)^2 + 2.4\sin(d)^2)^{\frac{2}{3}} \quad \text{E5.22}$$

Here, d is the angle between the wind direction and displacement vector, D is the displacement of the inlet from the anemometer (0.53 m), and z is the height of the measurement (1.24 m).

The third and final systematic error is dampening of variance and attenuation within the sampling line. This is corrected for using the method of Massman and Ibrom [2008] who found an attenuation coefficient that the flux is divided by to correct for attenuation within the line.

$$Attenuation\ Coefficient = 2(Re^{-0.125}) + 33.3(Re^{-0.725}) \quad \text{E5.23}$$

Here Re is the Reynolds number within the sampling line (2200). Figure 5.11 shows the fluxes before and after corrections. The largest correction (lateral displacement) corresponds to up to an 87% increase in the calculated flux. Together the corrections increased the flux by up to 85%.

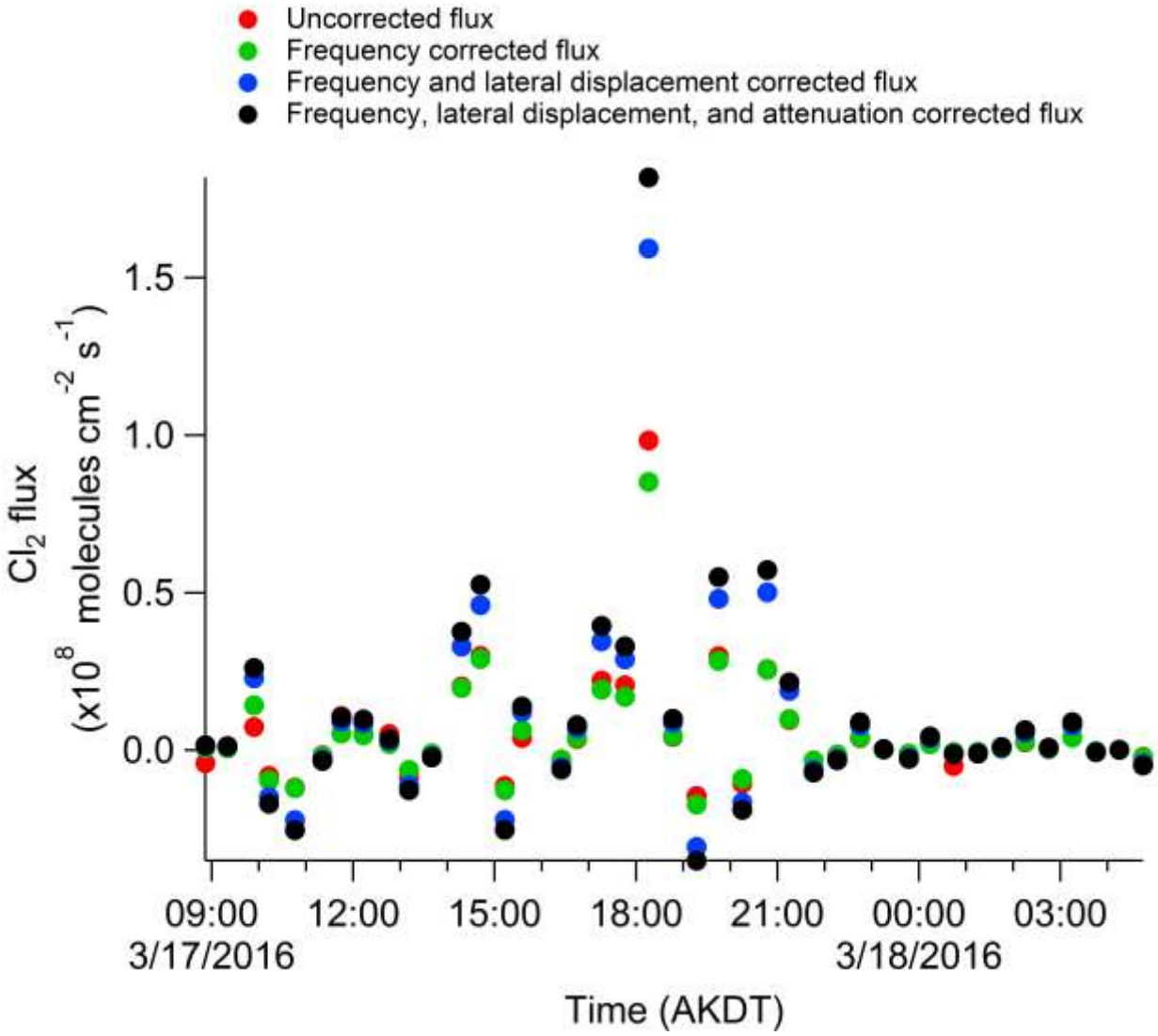

Figure 5.13 Cl_2 fluxes before and after corrections for systematic errors

5.3.4 Uncertainty Calculations

Despite the uncertainties inherent to any calculation of flux, it is surprisingly rare for calculations of eddy covariant fluxes to include the associated uncertainties, likely due to the proliferation of commercial instrumentation, with assumed low uncertainties. However Mauder et al. [2013] and Rannik et al. [2016] supply Equation 5.24 for the calculation of the random uncertainties associated with a flux measurement.

$$\delta_{F,N} = \frac{\sqrt{\sigma_{nwf}^2 \sigma_c^2 + \sigma_w^2 \sigma_{ncf}^2}}{\sqrt{ft}} \quad \text{E5.24}$$

In Equation 5.24 σ_c^2 and σ_w^2 are the variances of the scalar (Cl_2) and the vertical wind, σ_{ncf}^2 and σ_{nwf}^2 are the instrumental noise variances for the scalar (Cl_2) and vertical wind, f is the frequency of the measurement, and t is time of the averaging period. Here we re-derive this expression and show the assumptions that they made.

The error in the flux is calculated by simple propagation, given the flux calculation for Cl_2 (Equation 5.19). The uncertainty in the Cl_2 measurements, σ_{Cl_2}, is 20% + the limit of detection, as described in the CIMS methods above. The resolution of the vertical windspeed measurement is 0.5 mm/s, as given by the manufacturer (Campbell Scientific). Following the rules of error propagation, the variance of the average Cl2 concentration, $\sigma_{\overline{Cl_2}}^2$, is given by Equation 5.26, where N is the number of points in the average, if the uncertainty in the Cl_2 measurement, σ_{Cl_2}, is not changing significantly over time, such that the uncertainty for each point is the same as the average uncertainty, $\overline{\sigma_{Cl_2}^2}$. This assumption is not achieved when the Cl_2 is not constant throughout the averaging period.

$$\sigma_{\overline{Cl_2}}^2 = \frac{\sum \sigma_{Cl_2}^2}{N^2} = \frac{\overline{\sigma_{Cl_2}^2}}{N} \quad \text{E5.25}$$

Because the resolution of the vertical wind speed does not change with time the variance of the average, $\sigma_{\overline{w}}^2$, follows this rule.

$$\sigma_{\overline{w}}^2 = \frac{\sigma_w^2}{N} \quad \text{E5.26}$$

It follows then that the uncertainty in the variances of Cl_2 and w, $\sigma_{Cl_2}^2{}'$, and $\sigma_{w'}^2$, are given by Equations 5.28 and 5.29 respectively.

$$\sigma_{Cl_2}^2{}' = \sigma_{Cl_2}^2 + \sigma_{\overline{Cl_2}}^2 = \sigma_{Cl_2}^2 + \frac{\overline{\sigma_{Cl_2}^2}}{N} \quad \text{E5.27}$$

$$\sigma_{w'}^2 = \sigma_w^2 + \frac{\sigma_w^2}{N} \quad \text{E5.28}$$

The uncertainty in the covariance, $\sigma_{w'Cl_2'}$, is then given by Equation 5.30, and simplified in Equation 5.31.

$$\frac{\left(\sigma_{w'Cl_2'}\right)^2}{w'^2 Cl_2'^2} = \left(\frac{\sigma_{w'}}{w'}\right)^2 + \left(\frac{\sigma_{Cl_2'}}{Cl_2'}\right)^2 \cong \frac{(\sigma_w{}^2 + \frac{\sigma_w{}^2}{N})}{w'^2} + \frac{(\sigma_{Cl_2}^2 + \overline{\frac{\sigma_{Cl_2}^2}{N}})}{Cl_2'^2} \quad \text{E5.29}$$

$$\left(\sigma_{w'Cl_2'}\right)^2 \cong Cl_2'^2\left(\sigma_w^2 + \frac{\sigma_w^2}{N}\right) + w'^2(\sigma_{Cl_2}^2 + \overline{\frac{\sigma_{Cl_2}^2}{N}}) \quad \text{E5.30}$$

The flux is the average of the covariances for the period. Therefore the uncertainty in the flux is given by Equation 5.31.

$$\sigma_{flux}^2 = \frac{\sum_n \sigma_{w'Cl_2'}^2}{N^2} \quad \text{E5.31}$$

To relate this expression to that derived by Mauder et al. [2013] (Equation 5.23), the assumption must be made that N is large so that 1/N is negligible, and thus, $\frac{Cl_2'^2\sigma_w^2}{N}$ and $\frac{w'^2\sigma_{Cl2}^2}{N}$ are negligible. Following this Equation 5.30 can be simplified to Equation 5.31.

$$\sigma_{flux}^2 = \frac{\sigma_w^2}{N}\frac{\sum_n Cl_2'^2}{N} + \frac{\overline{\sigma_{Cl_2}^2}}{N}\frac{\sum_n w'^2}{N} \quad \text{E5.32}$$

Noting that instrumental noise variance of a measurement (σ_{nxf}^2) is defined as

$$\sigma_{nxf}^2 = \frac{\sum_n x'^2}{N-1} \quad \text{E5.33}$$

and assuming that N is large enough that $N \cong N - 1$, and that there is no gaps in the data, such that the frequency (f) times the time period (t) is equal to the number of data points (N).

$$\sigma_{flux}^2 = \frac{\sigma_w^2 * \sigma_{nCl_2f}^2 + \overline{\sigma_{Cl_2}^2} * \sigma_{nwf}^2}{f * t} \quad \text{E5.34}$$

Equation 5.34 is the equivalent of Equation 5.24.

However, a number of assumptions were required in order to find the equivalent of the random uncertainty suggested by Mauder et. al [2013] and Rannik et al. [2016], which may apply well to typical flux measurements, but may not apply well to the measurements made with the CIMS in the Arctic environment. Therefore, the uncertainty in the fluxes was also calculated using Equation 5.34, which does not make these assumptions.

$$\sigma_{Flux} = \sqrt{\frac{1}{N^2}\sum(Cl_2' w')^2 \left(\frac{(\sigma_{Cl_2}^2 + \frac{\sum \sigma_{Cl_2'}^2}{N^2})}{{Cl_2'}^2} + \frac{(\sigma_w^2 + \frac{\sigma_w^2}{N})}{w'^2} \right)} \qquad \text{E5.35}$$

The first assumption is that the uncertainty in the individual Cl_2 measurements at 2Hz (σ_{Cl_2}) does not change over time, and thus is the same as the average uncertainty in the Cl_2 measurements at 2 Hz ($\overline{\sigma_{Cl_2}}$). The uncertainty in CIMS measurements is defined as a percent uncertainty (20% + LOD), because it is a propagated error from the uncertainty in the calibration and background measurements. However, in order to satisfy the stationarity principle, and calculate meaningful fluxes, the Cl_2 concentrations over the averaging period cannot change significantly. The second assumption which is made is that N is large enough that 1/N is negligible. With 30-minute averaging periods, at 2 Hz there are approximately 3600 data points per averaging period. Figure 5.13 shows the absolute uncertainties in the fluxes, and the percent change of the flux uncertainty due to assumptions. The changes due to the two assumptions discussed above change the uncertainty by less than 10%, with the assumption of Cl2 not changing over the averaging period containing the larger uncertainty.

After the calculation of the random uncertainty associated with the flux measurements the uncertainty associated with the corrections made for systematic errors must also be calculated. The frequency correction uncertainty is the propagated error from both the 10Hz and 2Hz kinematic heat fluxes. The lateral distance correction was calculated using the method of Lee

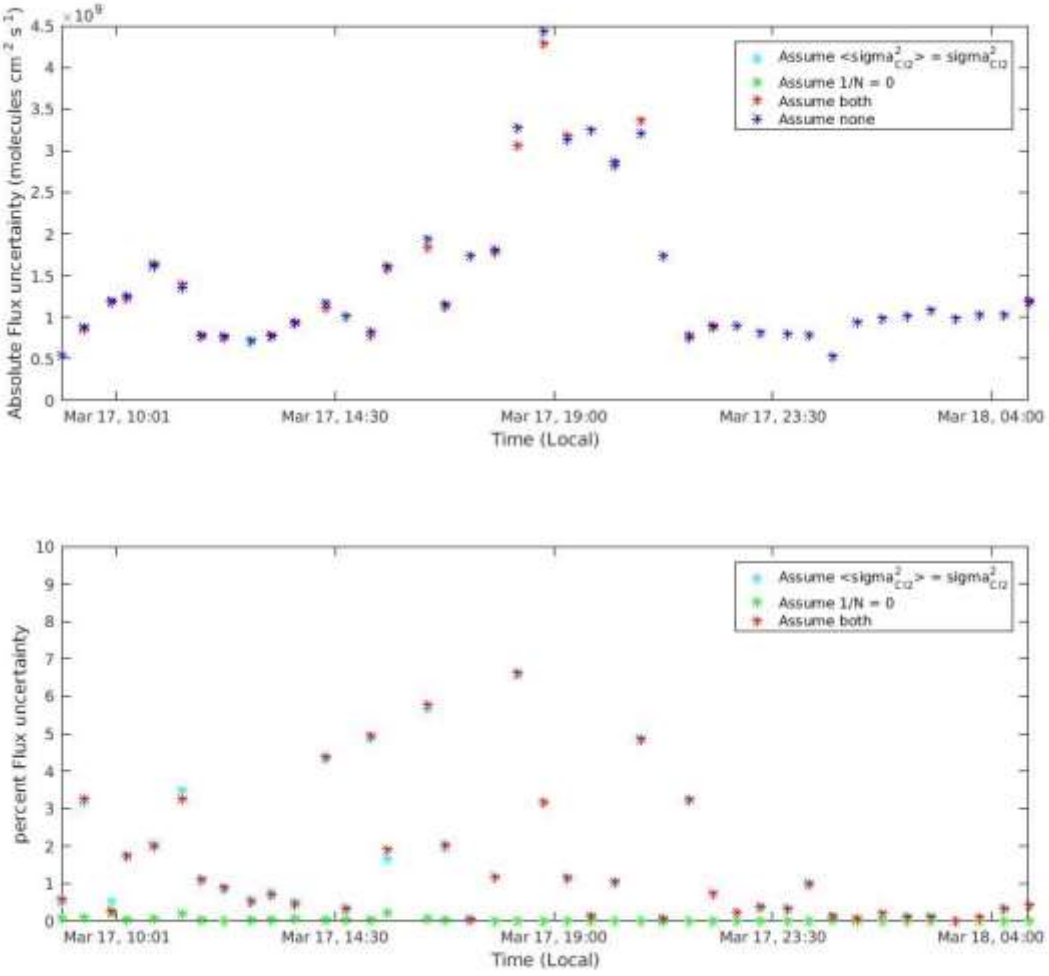

Figure 5.14 The absolute uncertainties in the fluxes with and without assumptions in the propagation of uncertainties (top panel) and the percent change in the flux uncertainties due to assumptions made in the propagation of uncertainties (bottom panel).

and Black [1994]. Kristensen et al. [1997] propose an alternative correction. The difference between these correction methods is taken as the uncertainty in the correction for the lateral displacement between the sonic anemometer and the inlet of the sampling line. The attenuation in the sampling line was corrected following the method of Massman and Ibrom [2008]. They outline a second, less empirical, method to correct for attenuation within the sampling line. The difference

between these two methods is taken as the uncertainty. Figure 5.14 shows the calculated uncertainties before and after adding the uncertainty associated with systematic errors. The uncertainty in the fluxes is generally high, at many points becoming greater than 200%, however, the uncertainty in the corrections of systematic errors plays a small role in the size of the uncertainty. Rather relatively low concentrations of Cl_2 on this day lead to high uncertainties in the Cl_2 data used to calculate the fluxes.

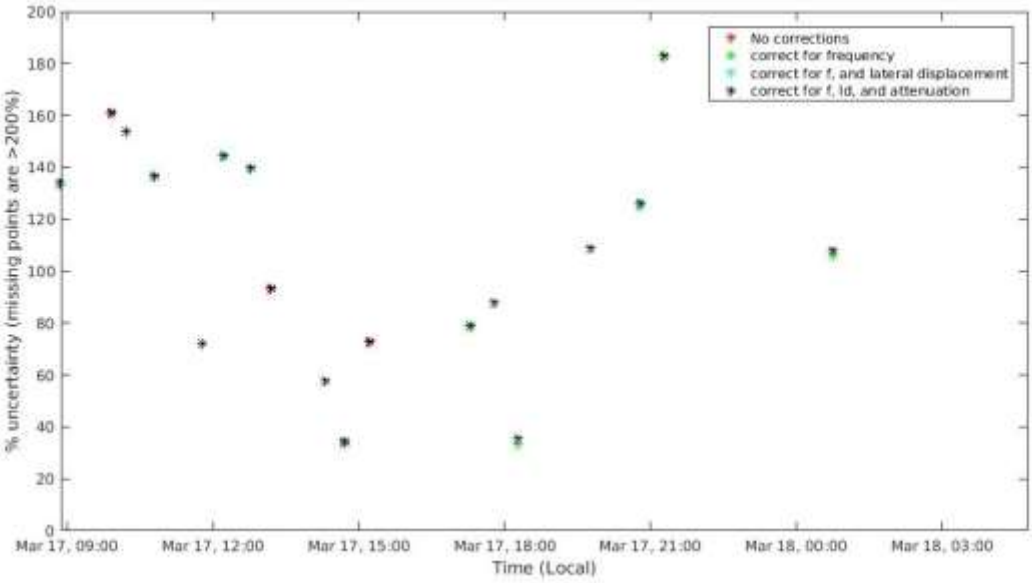

Figure 5.15 Calculated percent uncertainties associated with fluxes of Cl_2 on March 17, 2016. Values up to 20% of the calculated fluxes are shown. Percent uncertainties are shown both before (red) and after the uncertainty with corrections for systematic errors (green, teal, black).

5.3.5 Removal of Fluxes with Insufficient Data

Due to calibrations, background, and the filtering out of quiescent periods described above none of the 30-minute periods used to calculate fluxes contained the theoretical 3600 data points possible for a 30-minute measurement at 2 Hz. Therefore, analysis is necessary to understand the amount of data in the 30-minute averaging period that is required. Using the period around 18:16 AKDT on March 17, 2016, which had the highest Cl_2 fluxes, and nearly complete data (2165 /

3600 possible data points), the number of data points remaining to calculate an accurate flux was evaluated. The magnitude of the Cl_2 flux was $1.8\pm0.6x10^{10}$ molecules cm^{-2} s^{-1} for this 30-minute averaging period. The probability density functions (PDFs) of the vertical winds (w), temperature, and Cl_2 concentrations are shown in Figure 5.14 both with 100% of the data possible (2165 points) and with 74% of the data randomly removed (563 points). Data points were randomly removed from this 30-minute section of data. Between 100 and 2,000 data points were removed. Each number of removals was bootstrapped 1,000 times to account for uncertainty in the random removal. Figure 5.15 shows the percent change in the Cl_2 flux as a function of the number of points removed from the data and the percent of data remaining. For this 30-minute averaging period of data, the uncertainty is 33%, which is lower than many other percent uncertainties shown in Figure 5.13. When 26% of data remains, the change in the flux is 31%+/- 21%, as can be seen in Figure 5.15. Therefore any 30-minute averaging periods with less than 26% of the data remaining were discarded.

5.3.6 Calculation of the Br_2 Flux Limit of Detection

Br_2 data were collected at 2 Hz using the CIMS instrument for seven days during the 2016 PHOX:MELT campaign, specifically, March 09, March 10, April 05, April 07, April 10, April 13, and April 18. Br_2 fluxes were calculated for these days as described for the Cl_2 fluxes on March 17, above. Figure 5.17 shows the calculated fluxes, with their uncertainties as error bars. It should be noted that no fluxes during this period were significantly different from zero.

To understand the magnitude of flux that would be required for measurements to be statistically significant, the lowest possible detectible flux was calculated, following the form of a limit of detection. It was assumed that there was no appreciable flux on March 09 and 10 so that

these data could be considered a blank measurement. The standard deviation of the data on March 09 and 10 was multiplied by three to yield a flux limit of detection of 6.5×10^7 molecules cm^{-2} s^{-1}.

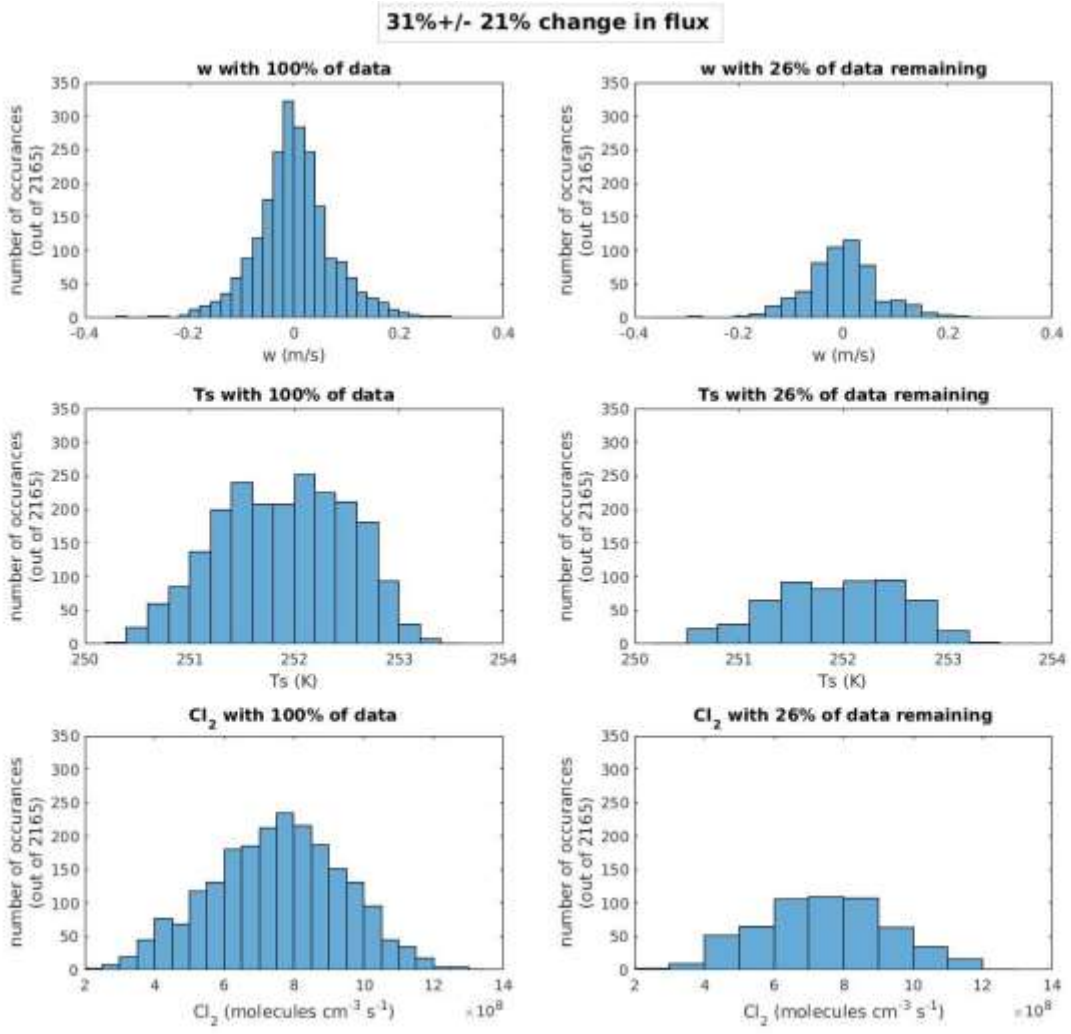

Figure 5.16 The probability densities of the vertical wind speed (w) (top panel), virtual temperature (Ts) (middle panel), and Cl_2 (bottom panel) for the flux period centered around 18:16 AKDT on March 17, 2016. The right side of each panel shows the PDF with 100% of the data available for the period (2165 data points), while the right side of the panel shows the PDF with 74% of the data randomly removed.

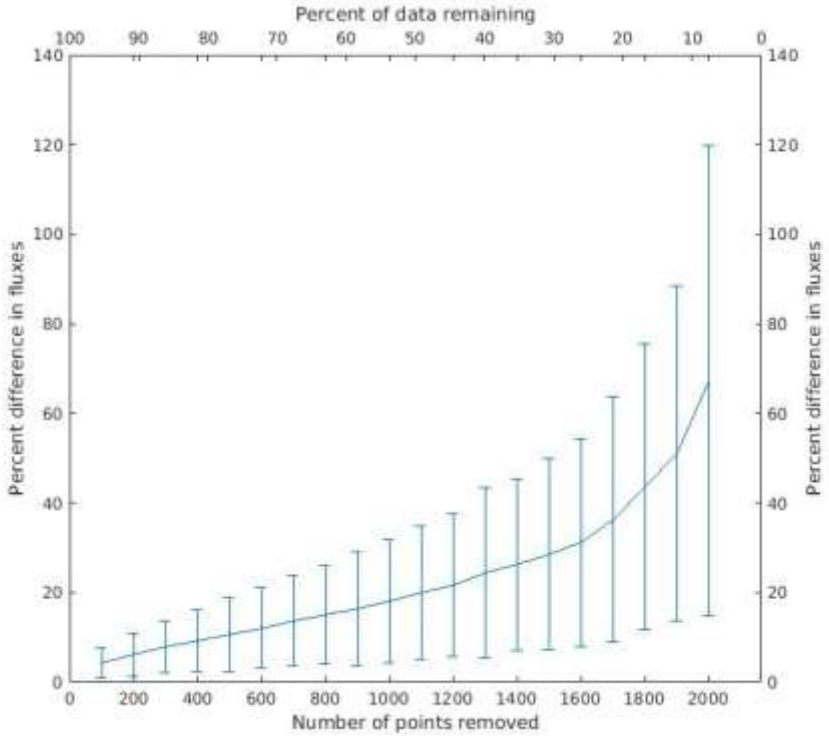

Figure 5.17 Percent change in the flux for the 30-minute averaging period as a function of the number of data points removed, and the percent of data remaining.

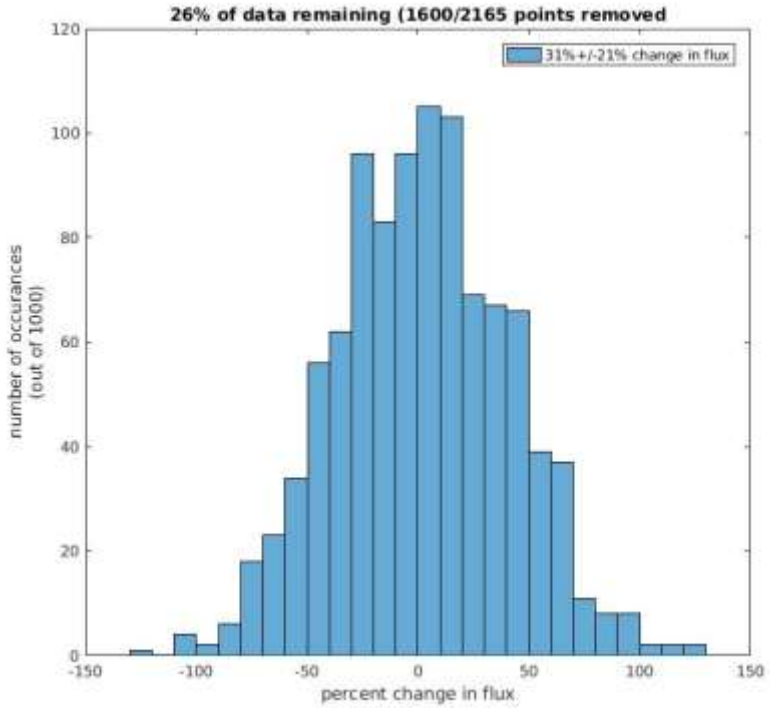

Figure 5.18 The probability density function for the change in the Cl_2 flux when 74% of the data is randomly removed.

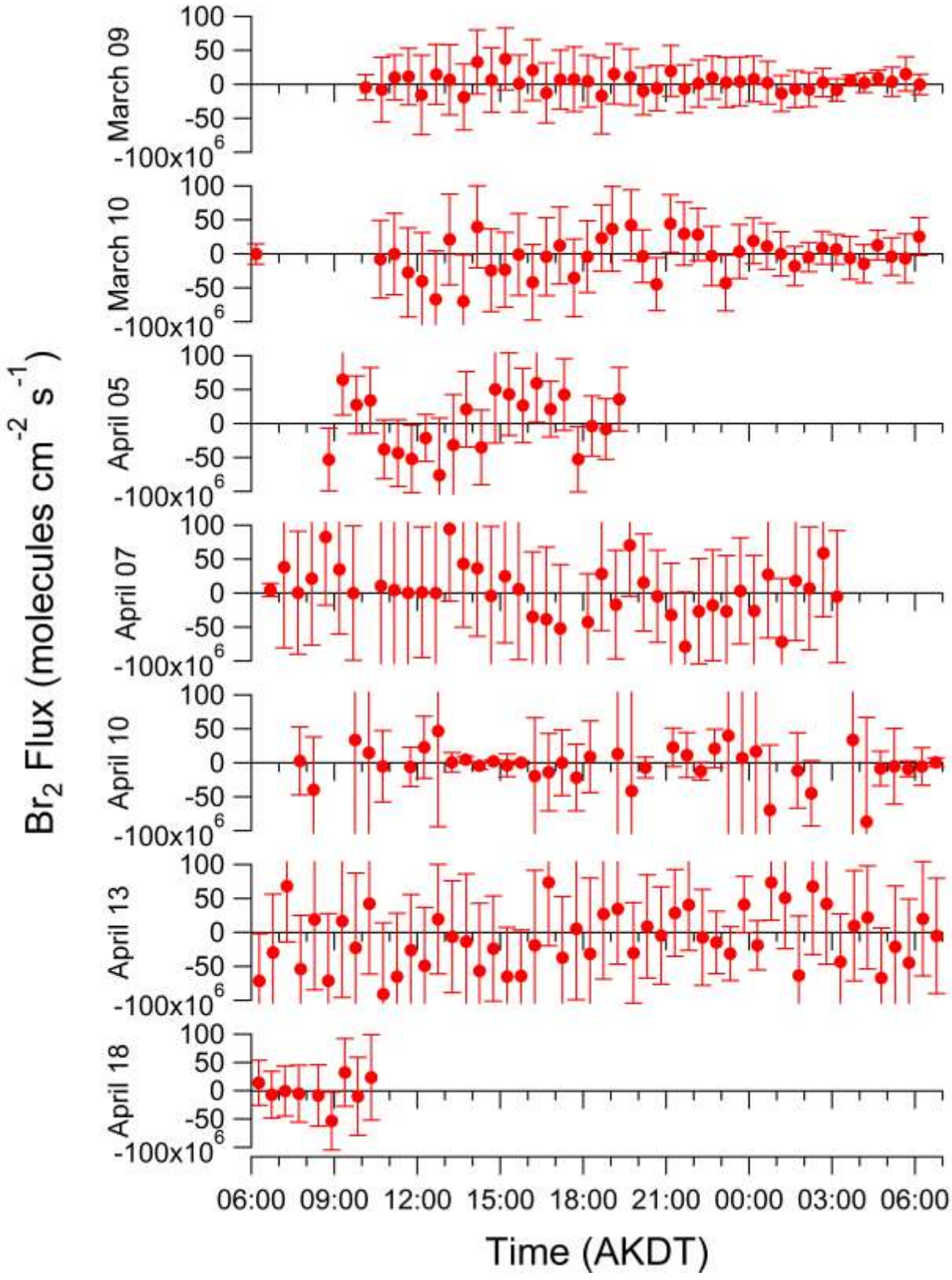

Figure 5.19 Calculated Br_2 fluxes

5.4 Discussion, Conclusions, and Recommendations for Future Measurements

The final Cl_2 fluxes from March 17, 2016, are shown in Figure 5.18. The six averaging periods that show upwards flux from the snowpack and are significantly different from zero are in the range of 0.3-1.8x10^8 molecules cm^{-2} s^{-1}. There is one averaging period that yielded a downward flux to the snowpack of 0.1x10^8 molecules cm^{-2} s^{-1}. The upward fluxes of Cl_2 are within the range reported by Custard et al. [2017] (0.16-14x10^8 molecules cm^{-2} s^{-1}) despite the differences in the measurement dates. Cl_2 concentrations in the Arctic tend to be more episodic than Br_2 concentrations [Liao et al., 2012]. Mcnamara et al. [in prep.] suggest that this is due to NO_x-influenced production within the snowpack via reactions 5.1-5.2.

$$N_2O_5 + Cl^- \rightarrow ClNO_2 + NO_3^- \quad \text{R5.1}$$

$$ClNO_2 + Cl^- \rightarrow Cl_2 + NO_2^- \quad \text{R5.2}$$

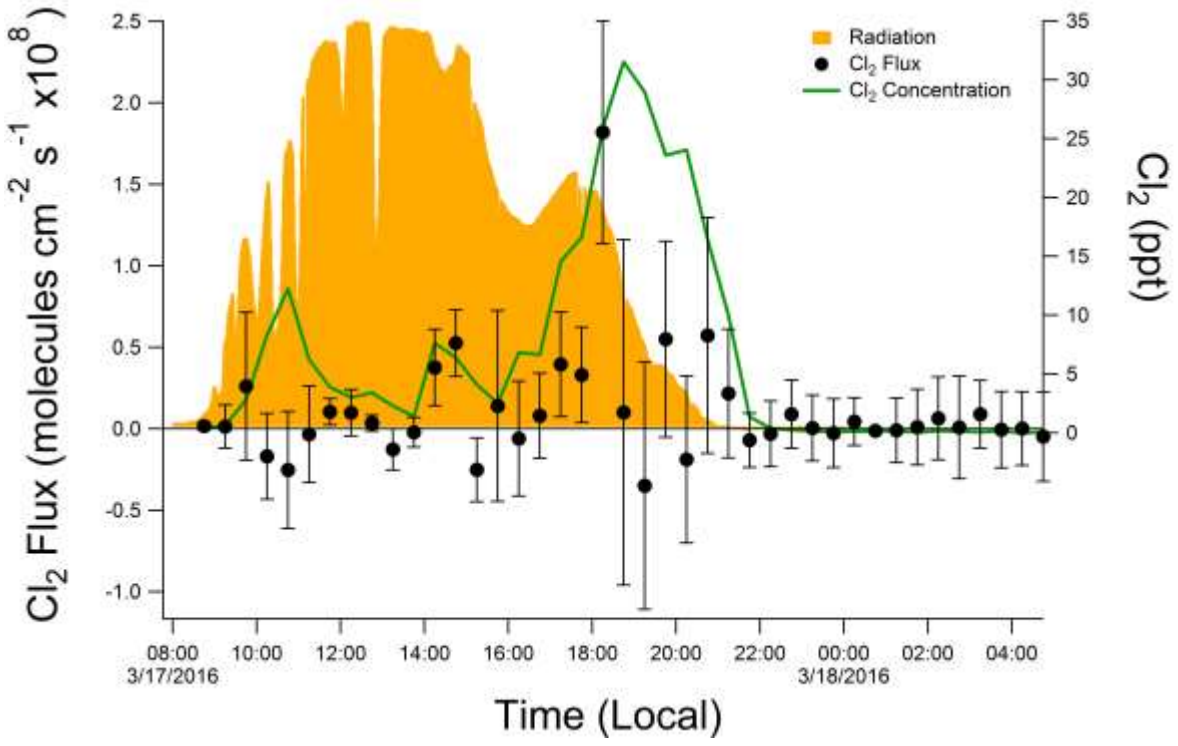

Figure 5.20 Cl_2 fluxes on March 17, 2016

Further measurements of Cl_2 fluxes, in conjunction with fluxes of $ClNO_2$, NO_x and N_2O_5 may confirm the NO_x influenced nature of Cl_2 production on snow, giving further insight into the reasons for the episodic nature of chlorine chemistry in the Arctic.

The Br_2 flux limit of detection was determined to be $6.5x10^7$ molecules cm^{-2} s^{-1}. The method used to calculate this value assumed that there was no flux present on March 09 and 10, and thus likely is an overestimate of the limit of detection, rather than an underestimate. Still, the calculated limit of detection is smaller than the fluxes calculated by Custard et al. [2017] (0.69 – $12x10^8$ molecules cm^{-2} s^{-1}), and those that have been suggested for models [Lehrer et al., 2004; Piot and von Glasow, 2008; Piot and Glasow, 2010; Thomas et al., 2011; Toyota et al., 2014] ($9.0 x10^7$ – $2.7x10^9$ molecules cm^{-2} s^{-1}) suggesting that measurements of the Br_2 flux should have been possible. There are then two possibilities to explain the lack of observances that are significantly different from zero. The first of these is that there is more efficient recycling of bromine in the atmosphere than current models implement, or that there is another source of bromine to the atmosphere that the models do not account for. There is some evidence for this, which is discussed in chapter 6 of this work. This possibility, while likely occurring to some extent does not explain the differences between the lack of non-zero fluxes observed in 2016, and the observed fluxes of Custard et al. [2017] in 2014. The second possible explanation for the differences is that bromine concentrations in 2016 were anomalously low. It was observed that average daytime BrO concentrations were halved in 2016, compared to the average of 2012-2015 [Swanson et al. 2017]. The Br_2 concentrations during the daytime on March 09 and March 10 were <5 ppt, while Custard et al. [2017] observed ~12 ppt of Br_2 at 1 m above the snowpack during the daytime. While the Br_2 flux likely does not scale linearly with observed concentrations of Br_2 and BrO, due to

recycling in the gas and particle phase, the lower concentrations likely do indicate that fluxes of Br_2 from the snowpack were lower in 2016 than in other years.

Future measurements of eddy covariant fluxes in the Arctic could have a large impact on the field's understanding of the sources and sinks of halogens in the Arctic. The episodic nature of chlorine chemistry may be linked to NO_x activation of chlorine compounds in the snowpack. If this is the case, concurrent fluxes of chlorine and nitrogen species may yield significant insight. Recently eddy covariant fluxes of $ClNO_2$ and N_2O_5 above the air-sea interface revealed that N_2O_5 deposition into the sea and that significant production of $ClNO_2$ does not occur at the sea surface [Kim et al., 2014]. Kim et al. [2014] utilized a CIMS instrument with a time of flight mass selector rather than the quadrupole present in the instrument used here. This allowed them to make measurements at a frequency of 80 kHz, which were then averaged to 10 Hz for calculations. This much higher frequency, if applied to measurements intended for eddy covariance calculations in the Arctic, should yield a much less noisy data set.

CHAPTER 6. THE VERTICAL IMPACT OF A SNOWPACK SOURCE OF MOLECULAR CHLORINE, BROMINE, AND IODINE IN THE ARCTIC

6.1 Introduction

Halogen chemistry during the Arctic springtime affects ozone (O_3), the HO_x-NO_x cycle, oxidation of hydrocarbons, and gaseous elemental mercury (GEM) [Steffen et al., 2008; Simpson et al., 2015]. Rapid depletions in boundary layer O_3 during the polar springtime [Barrie et al., 1988] affecting the oxidative capacity of the atmosphere are caused by a radical chain reaction (reactions 6.1-6.4) in which halogens, predominantly bromine, destroy O_3.

$$Br_2 + h\nu \rightarrow 2Br\cdot \quad \text{R6.1}$$

$$2Br\cdot + 2O_3 \rightarrow 2BrO\cdot + 2O_2 \quad \text{R6.2}$$

$$BrO\cdot + BrO\cdot \rightarrow 2Br\cdot + O_2 \quad \text{R6.3}$$

The chain reaction is initiated via the photolysis of Br_2 (reaction 6.1), which is very short-lived, with a midday photolysis lifetime of ~23 seconds. The net effect of the propagation steps (reaction 6.2- 6.3) is that for every cycle of the reaction two O_3 molecules are reduced to three O_2 molecules. Termination of the chain reaction can occur via the abstraction of a hydrogen atom from an aldehyde (reaction 6.4).

$$Br\cdot + RC(O)H \rightarrow RC(O)\cdot + HBr \quad \text{R6.4}$$

Termination steps of the chain reaction can also store bromine in species which photolyze to rapidly reinitiate the chain reaction such as $BrNO_2$ (reaction 6.5), $BrNO_3$ (reaction 6.6), and HOBr (reaction 6.7).

$$Br\cdot + NO_2\cdot \rightarrow BrNO_2 \quad \text{R6.5}$$

$$BrO\cdot + NO_2\cdot \rightarrow BrNO_3 \quad \text{R6.6}$$

$$BrO\cdot + HO_2\cdot \rightarrow HOBr + O_2 \quad \text{R6.7}$$

The main sink of HBr is deposition or uptake to the snowpack and aerosols, while reactive bromine products photolyze relatively rapidly (midday lifetimes of 73 seconds, 13 minutes, and 8 minutes for $BrNO_2$, $BrNO_3$ and HOBr respectively). HOBr and $BrNO_3$ can also undergo multiphase recycling to oxidize bromide (Br^-), which is present in aerosols and snow (reaction 6.8-6.9).

$$HOBr + Br^-_{(aq)} + H^+ \rightarrow Br_2 + H_2O \quad \text{R6.8}$$

$$BrNO_3 + Br^-_{(aq)} \rightarrow Br_2 + NO_3^-{}_{(aq)} \quad \text{R6.9}$$

These reactions, which convert a single gas phase bromine into two, are known as the 'bromine explosion' [Fan and Jacob, 1992; Wennberg, 1999]. The concentrations of reactive bromine species relative to each other can govern the rate at which both bromine explosion and the destruction of O_3 occur.

The interactions of bromine with chlorine and iodine chemistry can affect the distribution of reactive bromine, and the rate of bromine cycling through reactive bromine species. BrCl, with a midday photolysis lifetime of 91 seconds, can be formed by HOCl or $ClNO_3$ reacting with Br^- in the aerosol or snowpack [Abbatt et al., 2012].

$$HOCl + Br^-_{(aq)} + H^+ \rightarrow BrCl + H_2O \quad \text{R6.10}$$

$$ClNO_3 + Br^-_{(aq)} \rightarrow BrCl + NO_3^-{}_{(aq)} \quad \text{R6.11}$$

Chlorine and iodine chemistry can also speed the propagation of the bromine chain reaction by recycling bromine monoxide back to bromine atoms via reactions 6.12-6.13 [Thompson et al., 2015; Raso et al., 2017].

$$BrO\cdot + ClO\cdot \rightarrow Br\cdot + OClO\cdot \quad \text{R6.12}$$

$$BrO\cdot + IO\cdot \rightarrow Br\cdot + OIO\cdot \quad \text{R6.13}$$

Reaction 6.13 is ~100 times faster than the BrO self-reaction (reaction 6.2). Zero-dimensional (0-D) models of iodine chemistry in the Arctic have shown that the speed of iodine chemistry allows it to play a larger role the recycling of bromine in the atmosphere than the small concentrations of observed iodine species would suggest [Calvert and Lindberg, 2004; Saiz-Lopez et al., 2014; Thompson et al., 2015; Raso et al., 2017].

Production of molecular halogens in the Arctic occurs via multiphase mechanisms on ice or snow [Foster et al., 2001; Abbatt et al., 2010, 2012]. The photochemically activated process of halogen production in a salty aqueous-like environment, excluded to the surface of a frozen substrate is shown in reaction 6.14-6.20, where X is an iodine, bromine, or chlorine atom [Abbatt et al., 2010; Pratt et al., 2013; Custard et al., 2017; Raso et al., 2017].

$$NO_2^-{}_{(aq)} + h\nu \rightarrow \cdot NO_{(aq)} + \cdot O^-{}_{(aq)} \quad \text{R6.14}$$

$$\cdot O^-{}_{(aq)} + H^+{}_{(aq)} \rightarrow \cdot OH_{(aq)} \quad \text{R6.15}$$

$$\cdot OH_{(aq)} + X^-{}_{(aq)} + H^+{}_{(aq)} \rightarrow H_2O + \cdot X_{(aq)} \quad \text{R6.16}$$

$$\cdot X_{(aq)} + X^-{}_{(aq)} \leftrightarrow \cdot X_2^-{}_{(aq)} \quad \text{R6.17}$$

$$2 \cdot X_2^-{}_{(aq)} \rightarrow X_3^-{}_{(aq)} + X^-{}_{(aq)} \quad \text{R6.18}$$

$$X_3^-{}_{(aq)} \leftrightarrow X_{2(aq)} + X^-{}_{(aq)} \quad \text{R6.19}$$

$$X_{2(aq)} \leftrightarrow X_{2(g)} \quad \text{R6.20}$$

Many frozen substrates, including frost flowers [Rankin et al., 2002], salty snow on first-year ice [Abbatt et al., 2012], brine on first-year ice [Koop et al., 2000], blowing snow [Yang et al., 2008, 2010; Jones et al., 2009], and coastal snow [Foster et al., 2001; Spicer et al., 2002; Simpson et al., 2005; Pratt et al., 2013; Custard et al., 2017; Raso et al., 2017] have been proposed as the primary source of reactive inorganic halogens to the Arctic. However, Pratt et al. [2013] showed that it does not occur for high pH surfaces, such as sea ice and frost flowers. Recently it has been shown

that the coastal Arctic snowpack produces molecular iodine (I_2) [Raso et al., 2017], molecular bromine (Br_2) [Pratt et al., 2013], molecular chlorine (Cl_2) and bromine chloride (BrCl) [Custard et al., 2017].

While the snowpack is the initial source of reactive bromine [Pratt et al., 2013], the importance of multiphase reactions on aerosols sustenance of halogen chemistry via bromine explosion (reactions 6.8-6.9) has long been studied[Fan and Jacob, 1992; Barrie and Platt, 1997]. Recycling of halogens on aerosol is important to sustain the transport of BrO [Peterson et al., 2017], and potentially explain the duration of O_3 depletion events [Fan and Jacob, 1992]. However, aerosols have been discounted as an initial source of bromine because the sum of gas and aerosol phase bromine has been observed to spike periodically [Barrie and Platt, 1997]. This does not eliminate the possibility that snowpack-derived bromine, lost from the gas phase by HBr deposition, could be reactivated by oxidation pathways such as reaction 6.14-20. The effect of photochemical oxidation of snowpack derived Br^- in the aerosol phase has not been explicitly examined in previous 1-dimensional models.

The vertical extent of halogen chemistry above the snowpack determines the magnitude of the effect halogen chemistry has on the oxidation capacity of the Arctic boundary layer. However, production of molecular halogens in the snowpack, fast photolysis rates of Br_2, and a relatively stable atmospheric boundary layer should result in a steep vertical gradient of halogens in the daytime. However, there have been few measurements of the vertical gradient of molecular halogens above the snowpack surface to verify this. The vertical gradient of molecular halogens near the snowpack surface has only previously been reported to a height of 1 m [Custard et al., 2017]. These measurements showed that Br_2 was highest close the snowpack surface (1cm), however, much less Br_2 was removed by 1 m than would be expected. Measurements of other

species give some information on the vertical extent of halogen chemistry. The vertical gradients of O_3, gaseous elemental mercury (GEM), and hydrocarbons, which are destroyed by halogens, were studied by Tackett et al. [2007], who concluded that halogen chemistry occurs predominantly within the lowest tens of meters above the snowpack surface. Measurements of the BrO vertical gradient via multi axis differential optical adsorption spectroscopy (MAX-DOAS) [Frieß et al., 2011; Peterson et al., 2015; Simpson et al., 2017] lack vertical resolution, only allowing for analysis of the bottom 100 m of the atmosphere near the snowpack as a single bin, but suggest that shallow layers of bromine chemistry (<100 m thick) often occur, while at other times the BrO enriched layer can be 100s of meters thick [Simpson et al., 2017].

The vertical propagation of snowpack-derived halogen chemistry may also be a key diagnostic tool to test our understanding of halogen recycling mechanisms using one-dimensional (1-D) modeling. While there have been many 0-D photochemical models of the coupling of HO_x, NO_x, and halogen chemistry in the Arctic [Bloss et al., 2010; Liao et al., 2012; Cao et al., 2014; Custard et al., 2015; Thompson et al., 2015; Wang and Pratt, 2017], relatively few 1-D models that incorporate vertical mixing have been applied to study of vertical evolution of halogen chemistry [Lehrer et al., 2004; Piot and von Glasow, 2008; Saiz-Lopez et al., 2008; Thomas et al., 2011; Toyota et al., 2014].

Recent 1-D modeling studies [Toyota et al., 2014] and measurements of BrO [Peterson et al., 2015; Simpson et al., 2017] have indicated that the stability of the atmospheric boundary layer, and thus the rate of vertical mixing, is critical to both the extent and magnitude of the halogen chemistry above the snowpack. Measurements have shown that high atmospheric stability causes shallow (<100 m) layers of bromine chemistry, while higher total lower tropospheric column BrO concentration occur when vertical mixing is increased [Peterson et al., 2015]. Previous modeling

has been limited by absence of high quality data on the eddy diffusivity and atmospheric stability as a function of height. Toyota et al. [2014] used the method of Brost and Wyngaard [1978] to calculate eddy diffusivity, varying the surface wind speed and parameterization of the stability correction factor to test the importance of atmospheric stability. However, characterization of the stable and sometimes stratified polar boundary layer is difficult [Andreas, 2002; Grachev et al., 2007; Mazzola et al., 2016]. Atmospheric mixing models rely on Monin - Obukhov similarity theory, which assumes that turbulent flow in the surface layer (the bottom tenth of the boundary layer) is homogeneous and fully developed [Kaimal and Finnigan, 1994]. The assumption of stationary turbulent flow in the surface layer is by definition violated when turbulence is intermittent, or when stable stratification occurs and layers of air become decoupled from the surface [Mahrt, 1999]. As in-situ vertically resolved measurements have not been included in previous 1-D Arctic chemical models, the effects of intermittent mixing and stratification of the atmosphere on the vertical propagation of halogen chemistry have not been examined.

In this work we examine the impact of a surface snowpack source of molecular halogens on the near-surface vertical scale of atmospheric halogen chemistry. A 1-D atmospheric photochemical model is used to explore current understanding of the atmospheric sources and sinks of halogens in the Arctic. The influence of intermittent turbulence and the stably stratified atmospheric boundary layer on halogen chemistry in the Arctic are examined using measurement derived time and height-resolved eddy diffusivities in a 1-D photochemical model for the first time. Within this model framework, we test the influence of iodine chemistry and multiphase aerosol reactions on the vertical evolution of bromine chemistry in the lowest 12 m of the Arctic atmosphere. The effect of aerosol-phase halogen production on the vertical extent of halogens is examined via both multi-phase recycling reactions and the direct aerosol-phase photochemical

oxidation of Br^-. These model results are evaluated using our unique vertical profile measurements of Br_2 and Cl_2 between 1 and 7m above the snowpack surface. Vertical profiles were measured using chemical ionization mass spectrometry (CIMS) during the 2016 PHOX:MELT campaign in Barrow, AK. The ability of a snowpack flux of molecular halogens to explain the observed vertical evolution of halogen chemistry is investigated.

6.2 Measurement Methods

6.2.1 Chemical Ionization Mass Spectrometry (CIMS) Methods

Vertical profiles of Br_2 and Cl_2 were measured on March 21, April 06, April 12, April 18, April 25, April 27, and April 30 2016 during the 2016 PHOX:MELT (Photochemical Halogen and Ozone eXchange: a Meteorological Experiment on Layer Turbulence) campaign on the Barrow Environmental Observatory in northern Alaska (71°16'33.5"N 156°38'10.7"W) using chemical ionization mass spectrometry (CIMS). Arctic air was sampled through a 23 m long 12.7 mm custom FEP inlet line, heated to 30 C, at a rapid but laminar flow rate (17.1 lpm, Reynolds number 2200). The inlet line was connected to the CIMS via a custom made three-way sampling valve [Liao et al., 2011], which allowed for background and calibration measurements. The height of the end of the inlet line was adjusted between six heights between 1 m and 7 m above the snowpack surface in a randomized order (7 m, 5m, 3 m, 1 m, 2 m, 4m) using a pulley attached to a 12 m tall tower. Measurements were conducted at each height for 10 – 13 minutes (97-127 points per average). After each set of vertical profile measurements (3-6 hours) the line was rinsed with milli-q water, to minimize halide buildup and recycling to molecular halogens on the line walls, and dried using ultra-high purity nitrogen.

Line losses were tested both in the laboratory before field deployment and in the field. In the laboratory, line losses were tested utilizing the permeation devices. These laboratory tests

showed a large range of line losses, but they were not significantly different from zero. Laboratory line losses were 16±22% for Br_2 and -5±32% for Cl_2, with 15 trials. Laboratory line losses also showed no correlation with halogen concentration between 15 ppt and 90 ppt.

It has been previously noted that other bromine species – likely HOBr – can recycle on inlet lines, forming Br_2 from halides residing on the surfaces of the inlet line [Neuman et al., 2010]. To minimize this, the 23 m long sampling line was rinsed with ~2 L of Milli-Q water between experiments. An aliquot of this water was reserved for analysis of Br^- and Cl^- content and the inlet line was heated and dried using ultra high purity nitrogen (Air Liquide). The line rinse samples showed no trend in halide content with either the length of use or the concentration of the halogens sampled through the line. Recycling was further tested in the field, along with line losses, by comparison between the concentrations measured through the sampling line and concentrations measured utilizing the ambient measurement method described by Liao et al. [2011], which minimizes interaction between the CIMS sampling interface and the Arctic air sample. The ambient inlet was rapidly changed to the clean 23 m long inlet line, which was then suspended at approximately the same height above the snowpack as the ambient inlet for a minimum of 10 minutes. An experiment was then conducted, which utilized the sampling line for 5-23 hours. At the end of the experiment, the sampling line was again suspended at the same height as the ambient inlet for a minimum of 10 minutes before the inlet was rapidly exchanged back to the ambient. This test was performed on six days in March and April 2016. A paired two-tailed t-test with 95% confidence showed no significant differences between the concentrations measured using the ambient method and the sampling line either at the beginning or end of an experiment.

Because line losses and recycling were never found to be significantly different from zero either in the laboratory or the field, halogen concentrations have not been corrected for line losses.

Br_2 and Cl_2 were measured using CIMS with hydrated iodide chemistry $I(H_2O)^-$. Br_2 was monitored as $I^{79}Br^{79}Br^-$ (287 amu) and $I^{79}Br^{81}Br^-$ (289 amu), Cl_2 was monitored as $I^{35}Cl^{35}Cl^-$ (197 amu) and $I^{35}Cl^{37}Cl^-$ (199 amu), and the reagent ion was monitored as $IH_2{}^{18}O$ (147 amu). For vertical profile measurements, all ions were monitored for 500 ms. CIMS details have previously been described by Liao et al.[2011, 2012], and Custard et al. [2016]. Calibrations were performed using Br_2 and Cl_2 permeation devices (VICI Metronics) at the beginning and end of every set of heights comprising a vertical profile. Background measurements were conducted at each height by passing the flow through a glass wool scrubber, which has previously been shown to remove >99% of molecular halogens [Neuman et al., 2010; Liao et al., 2011; Raso et al., 2017]. The standard deviation of background measurements resulted in 3σ LODs of 2 ppt and 0.8 ppt for Br_2 and Cl_2 respectively. The method uncertainty was ±(22%+LOD) for Br_2, and ±(21%+LOD) for Cl_2. Error bars in Figures are the standard deviation of the averaged data for the time period of the measurement, to allow for an understanding of the variability of the data. This was observed to be is independent of concentration and was 0.6 – 1 ppt for Br_2, and 0.4 – 1 ppt for Cl_2.

6.2.2 Tower and Auxiliary Measurements

Eight three-dimensional sonic anemometers (CSAT3, Campbell Scientific Inc.) were mounted at 0.5, 1.3, 2.7, 4.0, 5.7, 7.7, 9.7 and 11.6 m above the snowpack on a 12 m tower. Anemometers were mounted on booms facing upwind (~60°). Data was collected at a frequency of 10Hz. A power outage at 13:59 AKDT on March 21, 2016 interrupted measurements for the remainder of the day.

Hydrocarbon concentrations, ozone concentrations, and 2 m temperatures were obtained from the National Oceanic and Atmospheric Administration (NOAA) Global Monitoring Division (GMD) Barrow site, located approximately 5 km upwind from the CIMS measurement site over

flat tundra. Data can be obtained from their website (http://www.esrl.noaa.gov/gmd/). Aerosol halide concentrations were obtained from filter samples collected at the NOAA site, and are curtesy of Patricia Quinn (NOAA). For more information on filter aerosol analysis please see Quinn et al. [2002]. The NOAA-GMD site is downwind of a clean air sector containing undisturbed snow-covered tundra and sea ice. Lidar and microwave radiometer data from the Atmospheric Radiation Measurement (ARM) site in Barrow was used to obtain the wind speed and virtual temperature at the boundary layer height. The Atmospheric Radiation Measurement (ARM) site in Barrow is a climate research facility, and part of the U.S. department of energy (DOE). Data can be obtained online (https://www.arm.gov/data).

6.3 One-Dimensional Model

6.3.1 Model Overview

To examine the vertical structure of halogen chemistry above the snowpack, the 0-D model framework previously described by Wang and Pratt [2017] was extended in the vertical dimension as a 1-D model. The model consists of 20 layers from the snowpack surface (0 m) to 200 m, with 13 layers lower than 12 m above the snowpack. The heights of each layer are shown in Table 6.1. The model includes 6 fully coupled modules – i) gas and particle phase reactions, including photolysis, ii) heterogeneous reactions on aerosol, iii) phase transfer with the aerosol phase, iv) turbulent transport, v) deposition, and vi) emissions. The model solves a set of ordinary differential Equations describing the change in concentration of each species over time (Equation 6.1).

$$\frac{dC_g}{dt} = VT + P - L + E - D - k_t\left(C_g * LWC - \frac{C_p}{H*R*T}\right) \qquad \text{E6.1}$$

C_g is the concentration of the species of interest in the gas phase. VT is the net vertical transport term. P and L are the chemical production and loss rates, respectively, as described by the

chemical mechanism. E and D are the snowpack emission and dry deposition terms. The final term in Equation 6.1 describes the phase transfer of species from the gas to the particle phase, and is dependent on the phase transfer coefficient (k_t), concentration in the gas and particle phases (C_g and C_p), particle liquid water content (LWC), Henry's law coefficient (H), and temperature (T). The system of ordinary differential Equations is solved using Igor Pro 6 (Wavemetrics, Lake Oswego, Or, USA). Model spin up time was 48 hours.

Table 6.1 Model layer heights from the snowpack surface (0 m) to model top (200m)

Layer bottom	**Layer Mid-point**
0 m	5.00×10^{-6} m
1.00×10^{-5} m	5.00×10^{-5} m
1.00×10^{-4} m	5.00×10^{-4} m
1.00×10^{-3} m	5.00×10^{-3} m
1.00×10^{-2} m	5.00×10^{-2} m
0.100 m	0.200 m
0.300 m	0.420 m
0.540 m	0.870 m
1.20 m	1.95 m
2.70 m	3.17 m
3.60 m	4.65 m
5.70 m	6.67 m
7.70 m	8.67 m
9.70 m	10.6 m
11.60 m	13.3 m
15.0 m	17.5 m
20.0 m	25.0 m
30.0 m	40.0 m
50.0 m	80.0 m
110. m	155 m

6.3.2 Gas and Particle Phase Chemical Mechanism

The gas phase mechanism is based on Wang and Pratt [2017], and Thompson et al. [2015]. Reaction rate constants were updated to reflect Burkholder et al. [2015]. A full list of gas phase reactions and reaction rates can be found in Table 6.2. It contains a suite of bromine and chlorine chemistry, as well as HO_x, NO_y and hydrocarbon chemistry. Photolysis rates were calculated using the Tropospheric Ultraviolet Radiation model (TUV) produced by the National Center for Atmospheric Research (https://www2.acom.ucar.edu/modeling/tropospheric-ultraviolet-and-visible-tuv-radiation-model). Hydrocarbon and O_3 concentrations are constrained to measurements made on March 21, 2016, at the NOAA-GMD site. A full list of model constraints and initial concentrations can be found in Table 6.3.

Table 6.2 Base case gas phase chemistry mechanism. Photolysis rates were calculated using the National Center for Atmospheric Research (NCAR) tropospheric ultraviolet and visible radiation (TUV) model. Other reaction rates are based on Wang and Pratt [2017] and Thompson et al. [2015] with updated reactions from Burkholder et al. [2015]. The reaction of MEK and Cl is from Zhao et al. [2008]. Termolecular reactions are calculated as described in Burkholder et al. [2015].

Photolysis Species	Max photolysis rate constant (s^{-1})
Cl_2	$2.02x10^{-3}$
ClO	$9.24x10^{-6}$
OClO	$7.68x10^{-2}$
HOCl	$2.2x10^{-4}$
$ClNO_2$	$3.58x10^{-3}$
$ClNO_3 \rightarrow Cl + NO_3$	$2.9x10^{-5}$
$ClNO_3 \rightarrow ClO + NO_2$	$3.96x10^{-6}$
Br_2	$3.48x10^{-2}$
BrCl	$1.09x10^{2}$
BrO	$3.04x10^{-2}$
HOBr	$2.09x10^{-3}$
$BrNO_2$	$1.36x10^{-2}$
$BrNO_3 \rightarrow Br + NO_3$	$1.08x10^{-3}$
$BrNO_3 \rightarrow BrO + NO_2$	$1.9x10^{-4}$
O_3	$5.46x10^{-6}$
H_2O_2	$4.69x10^{-6}$
NO_2	$8.45x10^{-3}$
NO_3	$2.61x10^{-2}$
HONO	$1.38x10^{-3}$
N_2O_5	$2.77x10^{-5}$
HNO_3	$2.07x10^{-7}$
HNO_4	$3.79x10^{-6}$
PAN	$2.34x10^{-7}$
$HCHO \rightarrow CO + 2HO_2$	$1.93x10^{-5}$
$HCHO \rightarrow CO + H_2$	$3.54x10^{-5}$
CH_3OOH	$3.86x10^{-6}$
MEK	$2.04x10^{-6}$

	Reaction	Rate constant (cm^3 $molecule^{-1}$ s^{-1})
O	$O(^1D) + N_2 / O_2 \rightarrow O(3P)$	$3.3x10^{-11} * e^{\frac{55}{T}} * O_2 + 2.15x10^{-11} * e^{\frac{110}{T}} * N_2$
	$O(^3P) \rightarrow O_3$	$5.6x10^{-34} * \left(\frac{T}{300}\right)^{-2.6} * N_2 + 6.0x10^{-34} * \left(\frac{T}{300}\right)^{-2.6} * O_2$
H	$OH + O_3 \rightarrow HO_2$	$1.70x10^{-12} * e^{-\frac{940}{T}}$
	$OH + HO_2 \rightarrow$	$4.8x10^{-11} * e^{\frac{250}{T}}$
	$OH + H_2O_2 \rightarrow HO_2$	$2.9x10^{-11} * e^{-\frac{160}{T}}$
	$HO_2 + O_3 \rightarrow OH$	$1.0x10^{-14} * e^{-\frac{490}{T}}$
	$HO_2 + HO_2 \rightarrow H_2O_2$	$3.3x10^{-13} * e^{\frac{460}{T}} + 2.1x10^{-33} * e^{\frac{920}{T0}} * M$
N	$HO_2 + NO_3 \rightarrow HNO_3$	$4.0x10^{-12}$
	$NO + OH \rightarrow HONO$	$termolecular$ $k_0^{300} = 7.0x10^{-31}, n = 2.6, k_\infty^{300} = 3.6x10^{-11}, m = 0.1$
	$NO + HO_2 \rightarrow NO_2 + OH$	$3.45x10^{-12} * e^{\frac{270}{T}}$

Table 6.2 Continued.

	$NO + O_3 \rightarrow NO_2$	$\mathbf{3.0x10^{-12} * e^{-\frac{1500}{T}}}$
	$NO + NO_3 \rightarrow 2*NO_2$	$1.5x10^{-11} * e^{\frac{170}{T}}$
	$NO_2 + OH \rightarrow HNO_3$	$termolecular$ $k_0^{300} = 1.8x10^{-30}, n = 3, k_\infty^{300} = 2.8x10^{-11}, m = 0$
	$NO_2 + HO_2 \rightarrow HNO4$	$termolecular$ $k_0^{300} = 1.9x10^{-31}, n = 3.4, k_\infty^{300} = 4.0x10^{-12}, m = 0.3$
	$HNO4 \rightarrow NO_2 + HO_2$	$8.4x10^{-5}$
	$NO_2 + O_3 \rightarrow NO_3$	$1.2x10^{-13} * e^{-\frac{2450}{T}}$
	$NO_2 + NO_3 \rightarrow N_2O_5$	$termolecular$ $k_0^{300} = 2.410^{-30}, n = 3, k_\infty^{300} = 1.6x10^{-12}, m = -0.1$
	$N_2O_5 \rightarrow NO_2 + NO_3$	$termolecular$ $k_0^{300} = 2.4x10^{-30}, n = 3, k_\infty^{300} = 1.6x10^{-12}, m = -0.1$
	$NO_3 + NO_3 \rightarrow 2*NO_2$	$8.5x10^{-13} * e^{-\frac{2450}{T}}$
	$N_2O_5 \rightarrow 2*HNO_3$	$2.0x10^{-21} * H_2O$
	$HONO + OH \rightarrow NO_2$	$1.8x10^{-11} * e^{-\frac{390}{T}}$
	$HNO_3 + OH \rightarrow NO_3$	$3.4x10^{-13}$
	$HNO_4 + OH \rightarrow NO_2$	$3.2x10^{-13} * e^{\frac{690}{T}}$
C	$NO_2 + CH_3COOO \rightarrow PAN$	$1.2x10^{-11}$
	$PAN \rightarrow NO_2 + CH_3COOO$	$4.6x10^{-8}$
	$CO + OH \rightarrow HO_2$	$1.44x10^{-13} * (1 + \left(\frac{M}{4.2x10^{19}}\right))$
	$CH_4 + OH \rightarrow CH_3O_2$	$1.9x10^{-12} * e^{-\frac{1690}{T}}$
	$CH_3O_2 + NO \rightarrow NO_2 + HO_2 + HCHO$	$2.3x10^{-12} * e^{\frac{360}{T}}$
	$CH_3O_2 + HO_2 \rightarrow CH_3OOH$	$3.8x10^{-13} * e^{\frac{780}{T}} * (1 - \frac{1}{\left(1 + \left(498 * e^{-\frac{1160}{T}}\right)\right)})$
	$CH_3O_2 + CH_3O_2 \rightarrow 2*HCHO + 2*HO_2$	$2.06x10^{-13} * e^{\frac{365}{T}} * (1 - 7.18 * e^{-\frac{885}{T}})$
	$CH_3O_2 + CH_3COOO \rightarrow HCHO + CH_3O_2 + HO_2$	$2.0x10^{-12} * e^{\frac{500}{T}}$
	$C_2H_6 + OH \rightarrow C_2H_5O_2$	$6.9x10^{-12} * e^{-\frac{1000}{T}}$
	$C2H_5O_2 + NO \rightarrow NO_2 + CH_3CHO + HO_2$	$2.6x10^{-12} * e^{\frac{380}{T}}$
	$C2H_5O_2 + HO_2 \rightarrow C_2H_5OOH$	$4.3x10^{-13} * e^{\frac{870}{T}}$
	$C2H_5O_2 + CH_3O_2 \rightarrow CH_3CHO + HCHO + 2*HO_2$	$2 * \sqrt{1.0x10^{-13} * e^{\frac{365}{T}} * 6.4x10^{-14}}$
	$C2H_5O_2 + C_2H_5O_2 \rightarrow 2*CH_3CHO + 2*HO_2$	$2 * \sqrt{1.0x10^{-13} * e^{\frac{365}{T}} * 6.4x10^{-14}}$
	$C_2H_5O_2 + CH_3COOO \rightarrow CH_3CHO + CH_3O_2 + HO_2$	$2 * \sqrt{1.0x10^{-13} * e^{\frac{365}{T}} * 6.4x10^{-14}}$
	$C_3H_8 + OH \rightarrow nC_3H_7O_2$	$0.264 * 7.6x10^{-12} * e^{-\frac{585}{T}}$
	$C_3H_8 + OH \rightarrow iC_3H_7O_2$	$0.736 * 7.6x10^{-12} * e^{-\frac{585}{T}}$
	$nC_3H_7O_2 + NO \rightarrow NO_2 + Propanal$	$2.9x10^{-12} * e^{\frac{350}{T}}$
	$iC_3H_7O_2 + NO \rightarrow NO_2 + Acetone$	$2.7x10^{-12} * e^{\frac{360}{T}}$

Table 6.2 Continued.

$nC_3H_7O_2 + CH_3O_2 \rightarrow$ HCHO + Propanal + 2*HO_2	$\mathbf{3.9x10^{-13}}$
$nC_3H_7O_2 + CH_3O_2 \rightarrow$ Propanal + HCHO	$1.3x10^{-13}$
$nC_3H_7O_2 + CH_3O_2 \rightarrow$ HCHO + nC_3H_7OH	$1.3x10^{-13}$
$iC_3H_7O_2 + CH_3O_2 \rightarrow$ HCHO + Acetone + 2*HO_2	$0.6 * \sqrt{1.0x10^{-13} * e^{\frac{365}{T}} * 1.6x10^{-12} * e^{-\frac{220}{T}}}$
$iC_3H_7O_2 + CH_3O_2 \rightarrow$ Acetone + HCHO	$0.2 * \sqrt{1.0x10^{-13} * e^{\frac{365}{T}} * 1.6x10^{-12} * e^{-\frac{220}{T}}}$
$iC_3H_7O_2 + CH_3O_2 \rightarrow$ HCHO + iC_3H_7OH	$0.2 * \sqrt{1.0x10^{-13} * e^{\frac{365}{T}} * 1.6x10^{-12} * e^{-\frac{220}{T}}}$
$nC_3H_7O_2 + C_2H5O_2 \rightarrow$ CH_3CHO + Propanal + 2*HO_2	$3.9x10^{-13}$
$nC_3H_7O_2 + C_2H_5O_2 \rightarrow$ Propanal + CH_3CHO	$1.3x10^{-13}$
$nC_3H_7O_2 + C_2H_5O_2 \rightarrow$ CH_3CHO + nC_3H_7OH	$1.3x10^{-13}$
$iC_3H_7O_2 + C_2H_5O_2 \rightarrow$ CH_3CHO + Acetone + 2*HO_2	$0.6 * 2 * \sqrt{1.0x10^{-13} * e^{\frac{365}{T}} * 1.6x10^{-12} * e^{\frac{2200}{T}}}$
$iC_3H_7O_2 + C_2H_5O_2 \rightarrow$ Acetone + CH_3CHO	$0.2 * 2 * \sqrt{1.0x10^{-13} * e^{\frac{365}{T}} * 1.6x10^{-12} * e^{\frac{2200}{T}}}$
$iC_3H_7O_2 + C_2H_5O_2 \rightarrow$ CH_3CHO + iC_3H_7OH	$0.2 * 2 * \sqrt{1.0x10^{-13} * e^{\frac{365}{T}} * 1.6x10^{-12} * e^{\frac{2200}{T}}}$
$nC_4H_{10} + OH \rightarrow sC_4H_9O_2$	$0.873 * 9.8x10^{-12} * e^{-\frac{425}{T}}$
$nC_4H_{10} + OH \rightarrow nC_4H_9O_2$	$0.127 * 9.8x10^{-12} * e^{-\frac{425}{T}}$
$iC_4H_{10} + OH \rightarrow tC_4H_9O_2$	$0.794 * 1.2x10^{-17} * T^2 * e^{\frac{225}{T}}$
$iC_4H_{10} + OH \rightarrow iC_4H_9O_2$	$0.206 * 1.2x10^{-17} * T^2 * e^{\frac{225}{T}}$
$sC_4H_9O_2 + CH_3O_2 \rightarrow$ MEK + HCHO + 2*HO_2	$0.6 * 2.5x10^{-13}$
$sC_4H_9O_2 + CH_3O_2 \rightarrow$ MEK + HCHO	$0.2 * 2.5x10^{-13}$
$sC_4H_9O_2 + CH_3O_2 \rightarrow$ sC_4H_9OH + HCHO	$0.2 * 2.5x10^{-13}$
$nC_4H_9O_2 + CH_3O_2 \rightarrow$ Butanal + HCHO + 2*HO_2	$0.6 * 1.3x10^{-12}$
$nC_4H_9O_2 + CH_3O_2 \rightarrow$ Butanal + HCHO	$0.2 * 1.3x10^{-12}$
$nC_4H_9O_2 + CH_3O_2 \rightarrow$ nC_4H_9OH + HCHO	$0.2 * 1.3x10^{-12}$
$tC_4H_9O_2 + CH_3O_2 \rightarrow$ Acetone + CH_3O_2 + HCHO	$0.7 * 6.7x10^{-15}$
$tC_4H_9O_2 + CH_3O_2 \rightarrow$ tC_4H_9OOH + HCHO	$0.3 * 6.7x10^{-15}$
$tC_4H_9O_2 + C_2H_5O_2 \rightarrow$ Acetone + CH_3O_2 + CH_3CHO	$0.7 * 6.7x10^{-15}$
$tC_4H_9O_2 + C_2H_5O_2 \rightarrow$ tC_4H_9OOH + CH_3CHO	$0.3 * 6.7x10^{-15}$
$iC_4H_9O_2 + CH_3O_2 \rightarrow$ isobutanal + HCHO	$0.2 * 1.3x10^{-12}$

Table 6.2 Continued.

	$iC_4H_9O_2 + CH_3O_2 \rightarrow$ isobutanal + HCHO + 2*HO_2	$\mathbf{0.6 * 1.3x10^{-12}}$
	$iC_4H_9O_2 + CH_3O_2 \rightarrow$ iC4H9OH + HCHO	$0.2 * 1.3x10^{-12}$
	$iC_4H_9O_2 + C_2H_5O_2 \rightarrow$ isobutanal + CH_3CHO	$0.2 * 1.3x10^{-12}$
	$iC_4H_9O_2 + C_2H_5O_2 \rightarrow$ isobutanal + CH_3CHO + 2*HO_2	$0.6 * 1.3x10^{-12}$
	$iC_4H_9O_2 + C_2H_5O_2 \rightarrow$ iC_4H_9OH + CH_3CHO	$0.2 * 1.3x10^{-12}$
	MEK + OH→	$1.5x10^{-12} * e^{\frac{90}{T}}$
	Acetone + OH →	$8.8x10^{-12} * e^{-\frac{1320}{T}} + 1.7x10^{-14} * e^{\frac{423}{T}}$
	Propanal + OH →	$4.9x10^{-12} * e^{\frac{405}{T}}$
	Butanal + OH →	$6.0x10^{-12} * e^{\frac{410}{T}}$
	isobutanal + OH →	$6.8x10^{-12} * e^{\frac{410}{T}}$
	$CH_3OOH + OH \rightarrow HCHO + OH$	$0.4 * 5.3x10^{-12} * e^{\frac{190}{T}}$
	$CH_3OOH + OH \rightarrow CH_3O_2$	$0.6 * 5.3x10^{-12} * e^{\frac{190}{T}}$
	$HCHO + OH \rightarrow HO_2 + CO$	$5.4x10^{-12} * e^{\frac{135}{T}}$
	$CH_3CHO + OH \rightarrow CH_3COOO$	$4.7x10^{-12} * e^{\frac{345}{T}}$
	$CH_3COOO + NO \rightarrow CH_3O_2 + NO_2$	$7.5x10^{-12} * e^{\frac{290}{T}}$
	$CH_3COOO + HO_2 \rightarrow$ $CH_3COOH + O_3$	$5.2x10^{-13} * e^{\frac{980}{T}}$
	$CH_3COOO + CH_3COOO \rightarrow$ 2*CH_3COO	$2 * \sqrt{3.5x10^{-13} * 2.9x10^{-12} * e^{\frac{500}{T}}}$
Cl	$Cl_2 + OH \rightarrow HOCl + Cl$	$3.6x10^{-12} * e^{-\frac{1200}{T}}$
	$Cl + O_3 \rightarrow ClO$	$2.3x10^{-11} * e^{-\frac{200}{T}}$
	$Cl \rightarrow HCl$	$3.05x10^{-11} * e^{-\frac{2270}{T}} * H_2$
	$Cl + HO_2 \rightarrow HCl$	$1.4x10^{-11} * e^{\frac{270}{T}}$
	$Cl + HO_2 \rightarrow ClO + OH$	$3.6x10^{-11} * e^{\frac{375}{T}}$
	$Cl + H_2O_2 \rightarrow HCl + HO_2$	$1.1x10^{-11} * e^{-\frac{980}{T}}$
	$Cl + NO_3 \rightarrow ClO + NO_2$	$2.4x10^{-11}$
	$Cl + OClO \rightarrow$ 2*ClO	$3.2x10^{-11} * e^{\frac{170}{T}}$
	$Cl + ClNO_3 \rightarrow Cl_2 + NO_3$	$6.2x10^{-12} * e^{\frac{145}{T}}$
	$Cl + PAN \rightarrow HCl + HCHO + NO_3$	$1.0x10^{-14}$
	$Cl + HNO_3 \rightarrow HCl + NO_3$	$2.0x10^{-16}$
	$Cl + NO_2 \rightarrow ClNO_2$	$termolecular$ $k_0^{300} = 1.3x10^{-30}, n = 2, k_\infty^{300} = 1.0x10^{-10}, m = 1$ + $k_0^{300} = 1.8x10^{-31}, n = 2, k_\infty^{300} = 1x10^{-10}, m = 1$
	$ClO + O(^3P) \rightarrow Cl$	$2.8x10^{-11} * e^{\frac{85}{T}}$
	$ClO + OH \rightarrow Cl$	$7.4x10^{-12} * e^{\frac{270}{T}}$
	$ClO + OH \rightarrow HCl$	$6.0x10^{-13} * e^{\frac{230}{T}}$

Table 6.2 Continued.

	$ClO + HO_2 \rightarrow HOCl$	$\mathbf{2.6x10^{-12} * e^{\frac{290}{T}}}$
	$ClO + NO \rightarrow Cl + NO_2$	$6.2x10^{-12} * e^{\frac{295}{T}}$
	$ClO + NO_2 \rightarrow ClNO_3$	$termolecular$ $k_0^{300} = 1.8x10^{-31}, n = 3.4, k_\infty^{300} = 1.5x10^{-11}, m = 1.9$
	$ClO + ClO \rightarrow Cl_2$	$1.0x10^{-12} * e^{-\frac{1590}{T}}$
	$ClO + ClO \rightarrow 2*Cl$	$3.0x10^{-11} * e^{-\frac{2450}{T}}$
	$ClO + ClO \rightarrow Cl + OClO$	$3.5x10^{-13} * e^{-\frac{1370}{T}}$
	$OClO + OH \rightarrow HOCl$	$1.4x10^{-12} * e^{\frac{600}{T}}$
	$OClO + NO \rightarrow ClO + NO_2$	$2.5x10^{-12} * e^{-\frac{600}{T}}$
	$HOCl + OH \rightarrow ClO$	$3.0x10^{-12} * e^{-\frac{500}{T}}$
	$HCl + OH \rightarrow Cl$	$1.8x10^{-12} * e^{-\frac{240}{T}}$
	$ClNO_3 + OH \rightarrow HOCl + NO_3$	$1.2x10^{-12} * e^{-\frac{330}{T}}$
	$HOCl + O(^3P) \rightarrow ClO + OH$	$1.7x10^{-13}$
	$CH_4 + Cl \rightarrow CH_3O_2 + HCl$	$7.1x10^{-12} * e^{-\frac{1270}{T}}$
	$C_2H_6 + Cl \rightarrow C_2H_5O_2 + HCl$	$7.2x10^{-11} * e^{-\frac{70}{T}}$
	$C_3H_8 + Cl \rightarrow nC_3H_7O_2 + HCl$	$0.59 * 1.4x10^{-10} * e^{-\frac{90}{T}}$
	$C_3H_8 + Cl \rightarrow iC_3H_7O_2 + HCl$	$0.41 * 1.4x10^{-10} * e^{-\frac{90}{T}}$
	$nC_4H_{10} + Cl \rightarrow sC_4H_9O_2 + HCl$	$0.59 * 2.05x10^{-10} * e^{\frac{55}{T}}$
	$nC_4H_{10} + Cl \rightarrow nC_4H_9O_2 + HCl$	$0.41 * 2.05x10^{-10} * e^{\frac{55}{T}}$
	$iC_4H_{10} + Cl \rightarrow tC_4H_9O_2 + HCl$	$0.436 * 1.43x10^{-10}$
	$iC_4H_{10} + Cl \rightarrow iC_4H_9O_2 + HCl$	$0.564 * 1.43x10^{-10}$
	$Cl + HCHO \rightarrow HCl + HO_2 + CO$	$8.1x10^{-11} * e^{-\frac{30}{T}}$
	$Cl + CH_3CHO \rightarrow$ $HCl + CH_3COOO$	$8.0x10^{-11}$
	$Cl + Acetone \rightarrow HCl$	$1.6x10^{-11} * e^{-\frac{610}{T}}$
	$Cl + MEK \rightarrow HCl$	$2.8x10^{-11} * e^{\frac{76}{T}}$ †
	$Cl + CH_3OOH \rightarrow CH_3O_2 + HCl$	$5.7x10^{-11}$
	$ClO + CH_3O_2 \rightarrow$ $Cl + HCHO + HO_2$	$1.6x10^{-12}$
	$ClO + CH_3COOO \rightarrow Cl + CH_3O_2$	$2.0x10^{-12}$
Br	$Br + O_3 \rightarrow BrO$	$1.7x10^{-11} * e^{-\frac{800}{T}}$
	$Br_2 + OH \rightarrow HOBr + Br$	$2.1x10^{-11} * e^{\frac{240}{T}}$
	$Br + HO_2 \rightarrow HBr$	$4.8x10^{-12} * e^{-\frac{310}{T}}$
	$Br + NO_2 \rightarrow BrNO_2$	$termolecular$ $k_0^{300} = 4.2x10^{-31}, n = 2.4, k_\infty^{300} = 2.7x10^{-11}, m = 0$
	$Br + NO_2 \rightarrow BrONO$	$5.3x10^{-12}$
	$Br + BrNO_3 \rightarrow Br_2 + NO_3$	$1.78x10^{-11}8e^{\frac{365}{T}}$
	$Br + BrNO_2 \rightarrow Br_2 + NO_2$	$5x10^{-11}$
	$Br + BrONO \rightarrow Br_2 + NO_2$	$1x10^{-12}$
	$BrONO \rightarrow Br + NO_2$	$2x10^{-2}$
	$BrONO \rightarrow BrNO_2$	$1.4x10^{-2}$

Table 6.2 Continued.

$HOBr + O(^3P) \rightarrow BrO + OH$	$\mathbf{2.1x10^{-11}}$
$BrO + O(^3P) \rightarrow Br$	$1.9x10^{-11} * e^{\frac{230}{T}}$
$BrO + OH \rightarrow Br + HO_2$	$7.5x10^{-11}$
$BrO + HO_2 \rightarrow HOBr$	$3.4x10^{-12} * e^{\frac{540}{T}}$
$BrO + NO \rightarrow Br + NO_2$	$8.8x10^{-12} * e^{\frac{260}{T}}$
$BrO + NO_2 \rightarrow BrNO_3$	$termolecular$ $k_0^{300} = 5.4x10^{-31}, n = 3.1, k_\infty^{300} = 6.5x10^{-12}, m = 2.9$
$BrO + BrO \rightarrow 2*Br$	$2.4x10^{-12} * e^{\frac{40}{T}}$
$BrO + BrO \rightarrow Br_2$	$2.8x10^{-14} * e^{\frac{860}{T}}$
$BrO + HBr \rightarrow HOBr + Br$	$2.1x10^{-14}$
$HBr + OH \rightarrow Br$	$5.5x10^{-12} * e^{\frac{200}{T}}$
$HOBr + OH \rightarrow BrO$	$5.0x10^{-13}$
$HOBr + O(^3P) \rightarrow BrO + OH$	$2.1x10^{-11}$
$Br + OClO \rightarrow BrO + ClO$	$2.7x10^{-11} * e^{-\frac{1300}{T}}$
$HOBr + Cl \rightarrow BrCl + OH$	$8.0x10^{-11}$
$Cl + BrCl \rightarrow Br + Cl_2$	$1.5x10^{-11}$
$Br + Cl_2 \rightarrow Cl + BrCl$	$1.1x10^{-15}$
$Cl + Br_2 \rightarrow BrCl + Br$	$1.2x10^{-10}$
$BrCl + Br \rightarrow Cl + Br_2$	$3.3x10^{-15}$
$BrO + ClO \rightarrow Br + Cl$	$2.3x10^{-12} * e^{\frac{260}{T}}$
$BrO + ClO \rightarrow BrCl$	$4.1x10^{-13} * e^{\frac{290}{T}}$
$BrO + ClO \rightarrow Br + OClO$	$9.5x10^{-13} * e^{\frac{550}{T}}$
$Br + HCHO \rightarrow HBr + HO_2 + CO$	$7.9x10^{-12} * e^{-\frac{580}{T}}$
$Br + CH_3CHO \rightarrow$ $HBr + CH_3COOO$	$2.7x10^{-11} * e^{-\frac{567}{T}}$
$Br + Propanal \rightarrow HBr$	$5.8x10^{-11} * e^{-\frac{610}{T}}$
$Br + Butanal \rightarrow HBr$	$5.8x10^{-11} * e^{-\frac{540}{T}}$
$Br + isobutanal \rightarrow HBr$	$5.8x10^{-11} * e^{-\frac{540}{T}}$
$BrO + CH_3O_2 \rightarrow$ $Br + HCHO + HO_2$	$1.6x10^{-12}$
$BrO + CH_3O_2 \rightarrow HOBr + HCHO$	$4.1x10^{-12}$
$BrO + CH_3COOO \rightarrow Br + CH_3O_2$	$1.7x10^{-12}$

Table 6.3 Model constraints and initial conditions before 48-hour spin up.

Species	Initial concentration	Source
Br_2	8 ppt	CIMS measurements at 6am (sunrise)
Cl_2	0 ppt	CIMS measurements 12am – 6am
O_3	Constrained to measurements (Fig. S4)	[2015]
H_2O	82% RH	WUnderground (https://www.wunderground.com/history/airport/PABR)
NO_2	20 ppt	Villena et al., [2011]
HNO_3	30 ppt	Liang et al. [2011]
HONO	3 ppt	Thompson et al. [2015]
PAN	220 ppt	Thompson et al. [2015]
CO	Constant 147 ppb	Thompson et al. [2015]
CH_4	Constant 1.938 ppm	NOAA Observatory on March 21, 2016
C_2H_6	Constant 2.31 ppb	NOAA Observatory on March 21, 2016
C_3H_8	Constant 859 ppt	NOAA Observatory on March 21, 2016
nC_4H_{10}	Constant 248 ppt	NOAA Observatory on March 21, 2016
iC_4H_{10}	Constant 139 ppt	NOAA Observatory on March 21, 2016
HCHO	Constant 300 ppt	Thompson et al. [2015]
CH_3CHO	Constant 170 ppt	Thompson et al. [2015]
Acetone	Constant 78 ppt	Thompson et al. [2015]
MEK	Constant 159 ppt	Thompson et al. [2015]
Propanal	Constant 46 ppt	Thompson et al. [2015]
Butanal	Constant 13 ppt	Thompson et al. [2015]
isoButanal	Constant 13 ppt	Thompson et al. [2015]
H_2O_2	1 ppb	Thompson et al. [2015]
Bromide	Constant 2.5 ng/m^3	Patricia Quinn (NOAA)
Chloride	Constant 394 ng/m^3	Patricia Quinn (NOAA)
Nitrate	0.32 $\mu g/m^3$	Patricia Quinn (NOAA)

6.3.3 Heterogeneous Reactions and Phase Transfer with Aerosols

Heterogeneous reactions start with the uptake of gas phase species at a rate described by Equation 6.2 [Ammann et al., 2013].

$$k = \frac{1}{4} * \gamma * \bar{\nu} * SA \qquad \text{E6.2}$$

Here k is the pseudo-first order uptake rate coefficient (s^{-1}), γ is the dimensionless effective uptake coefficient, $\bar{\nu}$ is the mean molecular speed (m s^{-1}), and SA is the volumetric surface area of particles (μm^{-2} cm^{-3}). Table 6.4 contains a list of heterogeneous reactions in the model, and their effective uptake coefficients. Particle surface area is the 2013-2015 March mean SA from Utqiaġvik [Freud et al., 2017]. In our simulations we consider heterogeneous reactions with the particle to be in the aqueous phase.

Phase transfer between the gas and aerosol phases is controlled in the model by the phase transfer coefficient and the Henry's law constant. Phase transfer coefficients are calculated as described by Piot and von Glasow [Piot and von Glasow, 2008]. Table 6.5 contains the mass accommodation coefficients and Henry's law constants used to calculate the phase transfer coefficients. Particle phase reactions are based on Wang and Pratt [2017] and can be found in Table 6.6. Aerosol pH was held constant at 4.0. Aerosol bromide, chloride, and nitrate were held constant at concentrations of 2.5 ng/m^3, 394.2 ng/m^3, and 319.7 ng/m^3, respectively, which derive from the sum of submicron and supermicron aerosol measurements via filter samples collected at the NOAA-GMD site on March 21, 2016.

Table 6.4 Heterogeneous reactions in base case

	Reaction	Reactive uptake coefficient
N	$N_2O_{5(g)} \rightarrow NO_3^-{}_{(p)} + NO_3^-{}_{(p)}$	0.02 (Amman et al 2013)
Cl	$N_2O_{5(g)} + Cl^-{}_{(p)} \rightarrow ClNO_{2(g)}$	0.01 (Amman et al 2013)
	$ClNO_{3(g)} + Cl^-{}_{(p)} \rightarrow Cl_{2(g)} + NO_3^-{}_{(p)}$	0.024 (Deiber et al 2004)
Br	$N_2O_{5(g)} + Br^-{}_{(p)} \rightarrow BrNO_{2(g)}$	0.005 (Ammann et al 2013)
	$BrNO_{3(g)} + Br^-{}_{(p)} \rightarrow Br_{2(g)} + NO_3^-{}_{(p)}$	0.06 (Deiber et al 2004)
	$ClNO_{3(g)} + Br^-{}_{(p)} \rightarrow BrCl_{(g)} + NO_3^-{}_{(p)}$	0.041 (Deiber et al 2004)
	$Cl_{2(g)} + Br^-{}_{(p)} \rightarrow Cl^-{}_{(p)} + BrCl_{(g)}$	0.16 (Hu et al 1995)
	$BrCl_{(g)} + Br^-{}_{(p)} \rightarrow Br_{2(g)} + Cl^-{}_{(p)}$	0.018 (Huff and Abbatt 2000)

Table 6.5 Values used to calculate phase transfer coefficients. Phase transfer coefficients were calculated as in Piot and von Glasow [2008].

Species	Uptake coefficient (α)	Henrys law constant
$HNO_3 \rightarrow NO_3^-$	0.5	$1.7x10^5 * \exp\left(8694 * \left(\frac{1}{T} - \frac{1}{298.15}\right)\right) * \left(1 + \left(\frac{15}{[H^+]}\right)\right)$ (Lelieveld and Crutzen 1991)
Cl_2	0.038	$9.4x10^{-2} * \exp\left(2109 * \left(\frac{1}{T} - \frac{1}{298.15}\right)\right)$
$HCl \rightarrow Cl^-$	0.056	$1.2 * \exp\left(9001 * \left(\frac{1}{T} - \frac{1}{298.15}\right)\right) * \left(1 + \left(\frac{\left(1.7x10^6 * \exp\left(6896 * \left(\frac{1}{T} - \frac{1}{298.15}\right)\right)\right)}{[H^+]}\right)\right)$ (Brimblecombe and Clegg 1989)
HOCl	0.066	$6.6x10^2 * \exp\left(5900 * \left(\frac{1}{T} - \frac{1}{298.15}\right)\right) * \left(1 + \left(\frac{3.2x10^{-8}}{[H^+]}\right)\right)$
Br_2	0.038	$7.7x10^{-1} * \exp\left(229 * \left(\frac{1}{T} - \frac{1}{298.15}\right)\right)$
$HBr \rightarrow Br^-$	0.018	$1.3 * \exp\left(10239 * \left(\frac{1}{T} - \frac{1}{298.15}\right)\right) * \left(1 + \left(\frac{1x10^9}{[H^+]}\right)\right)$
HOBr	0.6	$6.1x10^3 * \left(1 + \left(\frac{\left(2.3x10^{-9} * \exp\left(-3091 * \left(\frac{1}{T} - \frac{1}{298.15}\right)\right)\right)}{[H^+]}\right)\right)$
BrCl	0.33	$9.4x10^{-1} * \exp\left(5629 * \left(\frac{1}{T} - \frac{1}{298.15}\right)\right)$

Table 6.6 Particle Phase Reactions

	Reaction	Reaction order (n)	Rate constant ($cm^{3(n-1)}$ $molecule^{1-n}$ s^{-1})
Cl	$Cl^- + HOCl \rightarrow Cl_2$	2	$2.2x10^4 * \exp\left(-3508 * \left(\frac{1}{T} - \frac{1}{298.15}\right)\right) * [H^+]$
	$Cl_2 \rightarrow Cl^- + HOCl$	1	$2.2x10^1$
Br	$Br^- + HOBr \rightarrow Br_2$	*2*	$1.6x10^{10} * [H^+]$
	$Br_2 \rightarrow Br^- + HOBr$	*1*	$9.7x10^1$
	$Cl^- + HOBr \rightarrow BrCl$	*2*	$2.3x10^{10} * [H^+]$
	$Br^- + HOCl \rightarrow BrCl$	2	$1.3x10^6 * [H^+]$
	$BrCl \rightarrow Cl^- + HOBr$	1	$3.0x10^6$

6.3.4 Turbulent Transport

The Yonsei University (YSU) model [Hong and Pan, 1996] is used to parameterize atmospheric vertical mixing. The mixing differentials within the surface and mixed layers are defined as:

$$\frac{\partial C}{\partial t} = \frac{\partial}{\partial z}\left[K_z\left(\frac{\partial C}{\partial z} - \gamma\right)\right] \quad \text{E6.3}$$

$\frac{\partial C}{\partial t}$ is the change of a species (C) with time (t) at a given height (z), ∂z is the change in height, taken to be the thickness of the model layer, K_z is the eddy diffusivity at the height z, and $\frac{\partial C}{\partial z}$ is the change in concentration with height. The counter-gradient mixing correction (γ) is calculated using the measured surface heat flux ($\overline{w'\theta'}$), the measured friction velocity (u^*), and a stability correction term (Φ_m).

$$\gamma = \frac{7.8\left(\overline{w'\theta'}\right)}{u^*/\Phi_m} \quad \text{E6.4}$$

The stability correction term (Φ_m) is the same used to calculate the eddy diffusivity (K_z), as described below.

Before the power outage, in-situ time, and height-resolved eddy diffusivities were calculated using a 12-m tower co-located with the halogen vertical profile measurements. A loss

of power at 13:59 AKDT on March 21, 2016, stopped measurements. Above the tower, and after the power outage, the YSU method was used to calculate eddy diffusivity. The tower was equipped with eight 3d sonic anemometers (CSAT3D, Campbell Scientific) at 0.54 m, 1.3 m, 2.7 m, 4 m, 5.7 m, 7.7 m, 9.7 m, and 11.6 m above the snowpack surface. The eddy diffusivity (K_z) was calculated using Equation 6.5.

$$K_z = -\frac{(\overline{u'w'})}{\partial U/\partial z} \quad \text{E6.5}$$

Here the momentum flux ($\overline{u'w'}$) and change in wind speed with height ($\frac{\partial U}{\partial z}$), were calculated at each sonic anemometer.

The eddy diffusivity is dependent on the boundary layer height (h), the height above the snowpack surface (z), and stability of the boundary layer, as expressed by the Obukhov length (L) (Equations 6.6 -6.9). Under stable conditions (L<0), eddy diffusivity is calculated using Equations 6.6 and 6.7 within the surface layer (z<0.1h), Equations 6.7 and 6.8 at the surface layer boundary (z=0.1h), and Equations 6.8 and 6.9 within the mixed layer (z>0.1h).

$$K_z = \frac{\kappa z u_*}{\Phi_m} \; for \; z < 0.1h \quad \text{E6.6}$$

$$\Phi_m = 1 + \frac{3.4(z/L)(1+z/L)^{1/3}}{1+0.31(z/L)} \; for \; z \leq 0.1h \quad \text{E6.7}$$

$$K_z = \frac{\kappa z u_*}{\Phi_m}\left(1 - \frac{z}{h}\right)^2 \; for \; z \geq 0.1h \quad \text{E6.8}$$

$$\Phi_m = 1 \; for \; z > 0.1h \quad \text{E6.9}$$

The boundary layer height (h) is calculated using Equation 6.10.

$$h = Rib_{cr}\frac{\theta_v |U(h)|^2}{g(\theta_v(h) - \theta_v)} \quad \text{E6.10}$$

Here Rib_{cr} is the critical Richardson number, and g is the gravitational constant. The virtual temperature (θ_v) is 2 m temperature from the NOAA-GMD site near Barrow. In dry conditions,

the virtual temperature, and the measured temperature can be treated as equal. The wind speed at the boundary layer height ($U(h)$) and virtual temperature at the boundary layer height ($\theta_v(h)$) were obtained from the ARM site in Barrow.

6.3.5 Snowpack Emissions and Deposition

Dry deposition to the snowpack was allowed from the lowest model layer. Table 6.7 contains 1st order dry deposition rate constants. The model also includes several surface emissions of species that have demonstrated photochemical production in the snowpack. The fluxes of NO_2 (maximum $1x10^9$ molecules cm^{-2} s^{-1}), H_2O_2 (maximum $1.6x10^9$ molecules cm^{-2} s^{-1}), and HONO (maximum $1x10^9$ molecules cm^{-2} s^{-1}) were scaled to their photolysis rates, so the maximum fluxes occurred with the maximum solar radiation. The NO_2 fluxes were sufficient to produce maximum modeled concentrations of 29 ppt at 1.95 m above the snowpack surface. Figure 6.1 shows NO_x with time and altitude.

In this work snowpack fluxes of Br_2 and Cl_2 were calculated using a steady state approximation.

$$X_2\ Flux = a * [X_2] * J * \sqrt{\frac{Kz}{J}} \qquad \text{E6.11}$$

Molecular halogen concentrations ($[X_2]$) were measured on March 20 2016 at ~1m above the snowpack surface following the methods of Liao et al. [2011, 2014]. a is a scaling parameter equal to two times the ratio of average March 21 molecular halogen concentrations over average March 20 molecular halogen concentrations. This flux assumes that photolysis is the only loss process for the molecular halogens, and thus J (the photolysis rate) is the zero-order loss rate, and the effective mixing height is $\sqrt{Kz/J}$ where Kz is the calculated eddy diffusivity at

Table 6.7 Dry deposition rates to the snowpack

Species	Dry deposition rate constant (s^{-1})
O_3	$2.8x10^{-5}$
NO	$12x10^{-5}$
NO_2	$12\ x10^{-5}$
HNO_4	$2.8\ x10^{-5}$
N_2O_5	$4.5\ x10^{-3}$
PAN	$4.5\ x10^{-3}$
NO_3	$4.5\ x10^{-3}$
HONO	$12\ x10^{-5}$
HNO_3	$4.5\ x10^{-3}$
CH_4	$1.0\ x10^{-5}$
C_2H_6	$1.0\ x10^{-5}$
C_3H_8	$1.0\ x10^{-5}$
nC_4H_{10}	$1.0\ x10^{-5}$
iC_4H_{10}	$1.0\ x10^{-5}$
HCHO	$1.0\ x10^{-5}$
CH_3CHO	$1.0\ x10^{-5}$
MEK	$1.0\ x10^{-5}$
Acetone	$1.0\ x10^{-5}$
Propanal	$1.0\ x10^{-5}$
Butanal	$1.0\ x10^{-5}$
isobutanal	$1.0\ x10^{-5}$
CH_3O_2	$2.8\ x10^{-5}$
$C_2H_5O_2$	$2.8\ x10^{-5}$
$nC_3H_7O_2$	$2.8\ x10^{-5}$
$iC_3H_7O_2$	$2.8\ x10^{-5}$
$sC_4H_9O_2$	$2.8\ x10^{-5}$
$nC_4H_9O_2$	$2.8\ x10^{-5}$
$tC_4H_9O_2$	$2.8\ x10^{-5}$
$iC_4H_9O_2$	$2.8\ x10^{-5}$
CH3OOH	$2.8\ x10^{-5}$
CH3COOH	$2.8\ x10^{-5}$
Cl_2	$2.8\ x10^{-5}$
HCl	$4.5\ x10^{-3}$
HOCl	$2.8\ x10^{-5}$
$ClNO_2$	$2.8\ x10^{-5}$
$ClNO_3$	$4.5\ x10^{-3}$
Br_2	$2.8\ x10^{-5}$
BrCl	$2.8\ x10^{-5}$
HBr	$4.5\ x10^{-3}$
HOBr	$2.8\ x10^{-5}$
BrONO	$2.8\ x10^{-5}$
$BrNO_2$	$2.8\ x10^{-5}$
$BrNO_3$	$4.5\ x10^{-3}$

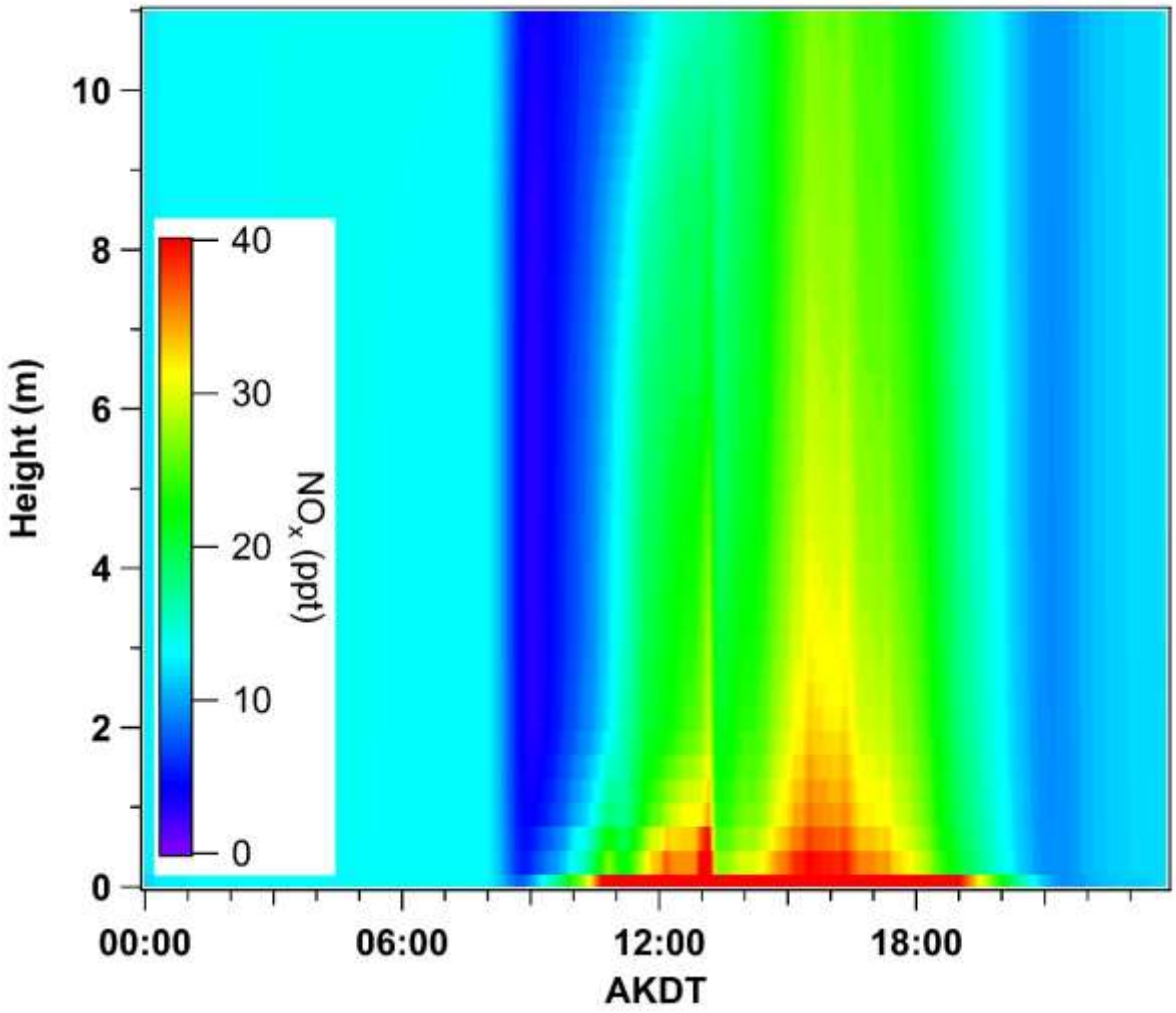

Figure 6.1 Modeled NO_x for 0-11 m for the base case. NO_2 at 1.95 m is up to 29 ppt.

1m above the snowpack surface. A plot of March 20 molecular halogen concentrations, effective mixing heights, and calculated fluxes can be seen in Figure 6.2. This method results in maximum Br_2 and Cl_2 fluxes of $11x10^8$ and $2.4x10^8$ molecules cm^{-2} s^{-1} respectively. These fluxes are consistent with the fluxes reported by Custard et al. [2017] ($0.7\text{-}12x10^8$ molecules cm^{-2} s^{-1} and $0.16\text{-}14x10^8$ molecules cm^{-2} s^{-1} for Br_2 and Cl_2, respectively), and in chapter 5 of this work ($1.8x10^8$ for Cl_2).

While BrCl fluxes have not been reported from the snowpack, Custard et al. [2017] did observe the photochemical production of BrCl within the snowpack following similar patterns to those of Br_2, at ~1/10 of the concentrations. Therefore, in this work, the BrCl fluxes are 1/10 of the calculated Br_2 fluxes

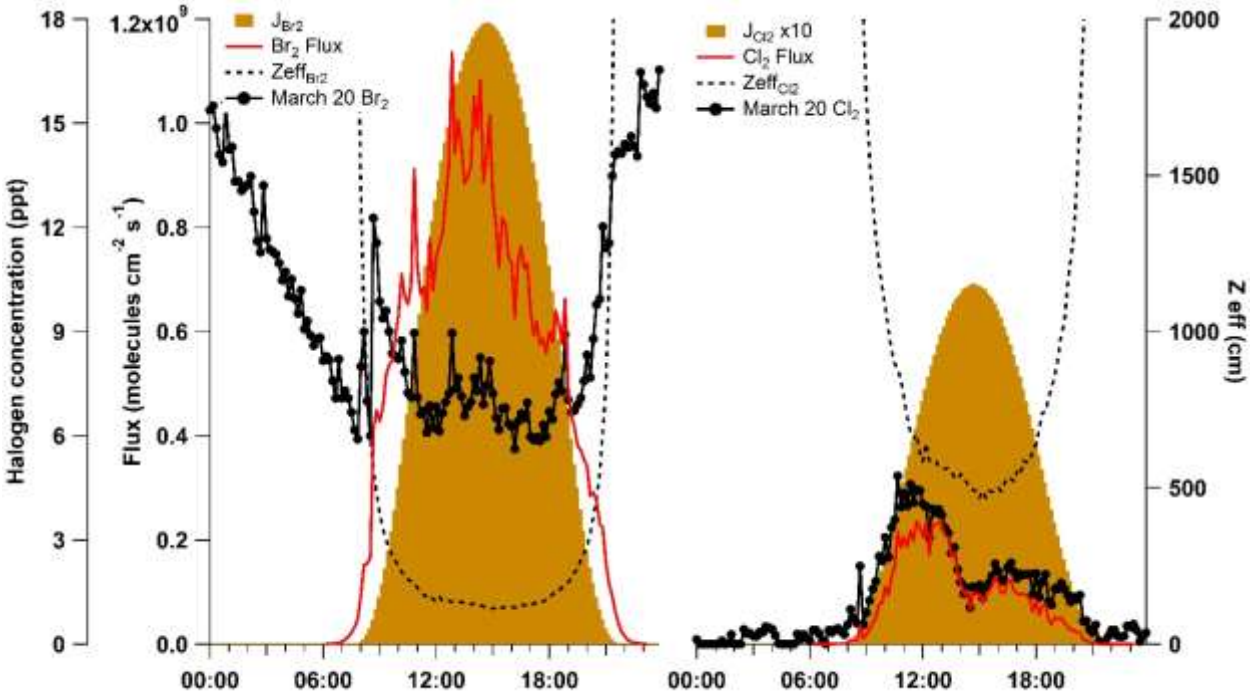

Figure 6.2 Halogen concentrations from March 20, 2016, used to calculate Br_2 and Cl_2 fluxes. Prescribed fluxes are shown as solid lines, effective mixing heights (Z_{eff}) are shown as small dashed lines, and halogen concentrations from March 20, 2016, are shown as large dashes.

6.3.6 Model Runs

Table 6.8 contains a description of model runs. The base case mixing is a hybrid of in-situ measurements and the YSU parameterization. March 21, 2016, showed both intermittent turbulence and stratification. The effects of intermittent turbulence and layering within the atmosphere on bromine chemistry was tested by simulating mixing using the YSU method during

the daytime period when tower measurements were available (07:30 – 13:00 AKDT). The hybridized base case was then compared with the fully parameterized YSU case.

For the sensitivity test including iodine chemistry, gas phase reactions are found in Table 6.9 and are based on Raso et al. [2017] and Thompson et al. [2015]. Iodide heterogeneous reactions are found in Table 6.10, phase transfer details are found in Table 6.11, and particle phase reactions are found in Table 6.12; they are analogous to bromine particle-phase reaction, with the exception of the deposition of gas phase hydroiodic acid (HIO_3) to the particle phase and iodate (IO_3^-) which is based on Pechtl et al. [2007]. Iodide in the particle phase was constrained to the Na^+/I^- ratio of seawater [Waite et al., 2006], and sodium filter measurements (NOAA-GMD). The maximum snowpack flux of I_2 ($7.2x10^8$ molecules cm^{-2} s^{-1}) was scaled to radiation.

Table 6.8 Description of Model Runs.

Model Run	Description
Base Case	See text
YSU Mixing	The YSU mixing parameterization is used for all times and heights.
No Heterogeneous Recycling	Gas phase bromine species can deposit to aerosols, but Br_2 is not generated from multiphase reactions.
Photochemical Br^- Oxidation	Br_2 equal to the HBr deposition rate is emitted from the aerosol phase.
Iodine	Iodine chemistry is included.

Table 6.9 Iodine gas phase chemistry mechanism used for iodine sensitivity test. Photolysis rates were calculated using the National Center for Atmospheric Research (NCAR) tropospheric ultraviolet and visible radiation (TUV) model (https://www2.acom.ucar.edu/modeling/tropospheric-ultraviolet-and-visible-tuv-radiation-model). Other reaction rates are primarily from Thompson et al. [2015], Burkholder et al. [2015], and Atkinson et al. [2007]. Termolecular reactions are calculated as described in Burkholder et al. [2015].

Photolysis	
Species	Max photolysis rate (s^{-1})
I_2	$1.3x10^{-1}$
ICl	$1.9x10^{-2}$
IBr	$5.9x10^{-2}$
INO	$7.3x10^{-2}$
INO_2	$1.9x10^{-3}$
$INO_3 \rightarrow IO + NO_2$	$6.2x10^{-4}$
$INO_3 \rightarrow I + NO_3$	$2.5x10^{-4}$
$I_2O_2 \rightarrow 2I$	$1.3x10^{-2}$
$I_2O_2 \rightarrow 2IO$	$1.3x10^{-2}$
HOI	$8.35x10^{-3}$
IO	$2x10^{-1}$
$OIO \rightarrow I$	$2.8x10^{-2}$
$OIO \rightarrow IO + O(^3P)$	$1.32x10^{-3}$
Reaction	Rate constant
$I_2 + O(^3P) \rightarrow IO + I$	$1.4x10^{-10}$
$I_2 + NO_3 \rightarrow I + INO_3$	$1.5x10^{-12}$
$I_2 + OH \rightarrow HOI + I$	$1.8x10^{-10}$
$HI + OH \rightarrow I$	$3.0x10^{-11}$
$I + HO_2 \rightarrow HI$	$1.5x10^{-11} * e^{-\frac{1090}{T}}$
$I + O_3 \rightarrow IO$	$1.3x10^{-33} * e^{-\frac{870}{T}}$
$I + NO \rightarrow INO$	$termolecular$ $k_0^{300} = 1.8x10^{-32}, n = 1, k_\infty^{300} = 1.7x10^{-11}, m = 0$
$I + NO_2 \rightarrow INO_2$	$termolecular$ $k_0^{300} = 3.0x10^{-31}, n = 1, k_\infty^{300} = 6.6x10^{-11}, m = 0$
$I + NO_3 \rightarrow IO + NO_2$	$1.0x10^{-10}$
$I_2O_2 \rightarrow 2*IO$	$1.3x10^{-4}$
$I_2O_2 \rightarrow OIO + I$	$2.1x0^{-1}$
$I_2O_2 + O_3 \rightarrow I_2O_3$	$1.0x10^{-12}$
$HOI + OH \rightarrow IO$	$2.3x10^{-13}$
$IO + O(^3P) \rightarrow I$	$1.2x10^{-10}$
$IO + HO_2 \rightarrow HI$	$1.3x10^{-11} * e^{\frac{570}{T}}$
$IO + NO \rightarrow I + NO_2$	$9.1x10^{-12} * e^{\frac{240}{T}}$
$IO + NO_2 \rightarrow INO_3$	$termolecular$ $k_0^{300} = 7.5x10^{-31}, n = 3.5, k_\infty^{300} = 7.6x10^{-12}, m = 1.5$
$IO + NO_3 \rightarrow OIO + NO_2$	$9.0x10^{-12}$
$IO + HO_2 \rightarrow HOI$	$1.4x10^{-11} * e^{\frac{540}{T}}$
$IO + ClO \rightarrow ICl$	$3.2x10^{-12}$
$IO + ClO \rightarrow I + Cl$	$4.0x10^{-12}$
$IO + ClO \rightarrow I + OClO$	$8.7x10^{-12}$
$IO + BrO \rightarrow IBr$	$4.3x10^{-11}$

Table 6.9 Continued.

IO + BrO → I + Br	$\mathbf{7.2x10^{-12}}$
IO + BrO → OIO + Br	$9.4x10^{-11}$
IO + IO → 2*I	$1.8x10^{-11}$
IO + IO → I + OIO	$4.4x10^{-11}$
IO + IO → I_2O_2	$5.3x10^{-11}$
IO + OIO → I_2O_3	$1.5x10^{-10}$
OIO + NO → IO + NO_2	$9.7x10^{-12}$
OIO + OH → HOI	$6.0x10^{-12}$
OIO + OIO → I_2O_4	$1.0x10^{-10}$
I_2O_3 + O_3 → I_2O_4	$1.0x10^{-12}$
I_2O_4 → 2*OIO	$4.4x10^{-4}$
I_2O_4 + O_3 → I_2O_5	$1.0x10^{-12}$
OIO + OH → HIO_3	$5.8x10^{-10}$
I_2O_5 → 2*HIO_3	$5.2x10^{-24} * [H_2O]$
HIO_3 + HIO_3 → I_2O_5	$5.0x10^{-25}$

Table 6.10 Iodine heterogeneous reactions, and reactive uptake coefficients used for iodine sensitivity test

Reaction	**Reactive uptake coefficient**
$INO_{3(g)} + Cl^-_{(p)} \rightarrow ICl_{(g)} + NO_3^-{}_{(p)}$	0.04
$INO_{3(g)} + Br^-_{(p)} \rightarrow IBr_{(g)} + NO_3^-{}_{(p)}$	0.05 (Holmes et al. [2001])
$ICl_{(g)} + I^-_{(p)} \rightarrow I_{2(g)} + Cl^-_{(p)}$	0.01
$ICl_{(g)} + Br^-_{(p)} \rightarrow IBr_{(g)} + Cl^-_{(p)}$	0.018 (Holmes et al. [2001])
$IBr_{(g)} + I^-_{(p)} \rightarrow I_{2(g)} + Br^-_{(p)}$	2e-3 (Braban et al. [2007])
$Br_{2(g)} + I^-_{(p)} \rightarrow IBr_{(g)} + Br^-_{(p)}$	0.33 (Hu et al. [1995])
$BrCl_{(g)} + I^-_{(p)} \rightarrow IBr_{(g)} + Cl^-_{(p)}$	0.018
$BrCl_{(g)} + I^-_{(p)} \rightarrow ICl_{(g)} + Br^-_{(p)}$	0.018
$Cl_{2(g)} + I^-_{(p)} \rightarrow ICl_{(g)} + Cl^-_{(p)}$	0.20 (Hu et al. [1995])

Table 6.11 Values used to calculate phase transfer coefficients for iodine species in iodine sensitivity test. Phase transfer coefficients were calculated as in Piot and von Glasow [2008].

Species	**A**	**Henrys law**
I_2	0.02	3
ICl	0.018	$1.1x10^2$
IBr	0.018	$2.4x10^1$
$HI \rightarrow I^-$	$6.35x10^{-9} * \exp\left(\frac{4519}{T}\right)$	$2.5x10^7 * \exp\left(9800 * \left(\frac{1}{T} - \frac{1}{298.15}\right)\right) * \left(1 + \left(\frac{3.16x10^9}{[H^+]}\right)\right)$
HOI	0.6	$4x10^4$
$HIO_3 \rightarrow IO_3^-$	0.01	$2.5x10^7 * \exp\left(9800 * \left(\frac{1}{T} - \frac{1}{298.15}\right)\right) * \left(1 + \left(\frac{0.16}{[H^+]}\right)\right)$

Table 6.12 Iodine particle phase chemistry used in iodine sensitivity test.

Reaction	**Rate constant (cm^3 $molecule^{-1}$ s^{-1})**
$I^- + HOI \rightarrow I_2$	$4.4x10^{12} * [H^+]$
$I_2 \rightarrow I^- + HOI$	3
$Cl^- + HOI \rightarrow ICl$	$2.9x10^{10} * [H^+]$
$ICl \rightarrow Cl^- + HOI$	$2.4x10^6$
$Br^- + HOI \rightarrow IBr$	$4.1x10^{12} * [H^+]$
$IBr \rightarrow Br^- + HOI$	$8.0x10^5$
$I^- + HOCl \rightarrow ICl$	$3.5x10^{11} * [H^+]$
$I^- + HOBr \rightarrow IBr$	$1.2x10^{13} * [H^+]$

The importance of bromine explosion chemistry on aerosols was determined by stopping multiphase recycling of bromine on aerosols. In this case bromine species were allowed to deposit into the aerosols, but re-emissions of Br_2, BrCl, and $BrNO_2$ were not allowed. This did not limit the uptake of bromine species to the particle phase or change the particle phase concentration of halides, as halides in the particle phase are constrained to measurements.

To test photochemical oxidation of snowpack-derived bromine on the particle phase, Br_2 emissions were added to each layer of the model. The emissions for each layer were calculated to equal the rate at which HBr replenished aerosol Br^-. This is shown in Equation 6.12 below

$$Aerosol\ Production = \frac{1}{2} * \frac{J}{J_{max}} * k_t \left([HBr] * LWC - \frac{Br^-}{H*R*T} \right) \quad \text{E6.12}$$

Here, ½ is the stoichiometric coefficient for the conversion from Br^- to Br_2. The photolysis rate fraction is to account for the proposed photochemical nature of Br^- oxidation, and the rest of the term is the phase transfer of HBr to Br^-. This did not affect aerosol Br^- content, as Br^- was constrained to measurements (Table 6.4).

6.4 Results and Discussion

6.4.1 The Vertical Evolution of Halogens Above the Snowpack

To investigate the impact of snowpack derived bromine on the vertical evolution of molecular halogens in the Arctic, we simulated the case day of March 21, 2016, during the PHOX:MELT campaign in Utqiaġvik, Alaska. The resulting modeled vertical profiles for Br_2 and Cl_2, shown in Figure 6.3, display an exponential decay typical of a short-lived species with a surface source. The measured profiles of Cl_2 show a similar shape to the modeled profiles, with the highest concentrations at the lowest height measured (1 m) and decreasing

Figure 6.3 (a-d) Modeled (lines) and measured (lines with markers) vertical profiles of Br_2 (blue) and Cl_2 (green) for four time periods on March 21, 2016, near Utqiaġvik, Ak. Model results are a composite of times to match the time of the measurement at the same height. Scaled vertical profiles (dashed lines and unfilled markers) are scaled to the 1 m measurement and the 0.87 m layer for the model. Measurement error bars are the standard deviation of the average for the measurement at that height. Modeled mole ratios are off the scale at the bottom of each vertical profile, where maximum values (at $5x10^{-6}$ m) a) Br_2 – 55 ppt Cl_2 – 6 ppt b) Br_2 – 60. ppt Cl_2 – 29 ppt c) Br_2 – 62 ppt Cl_2 – 23 ppt d) Br_2 – 64 ppt Cl_2 – 16 ppt

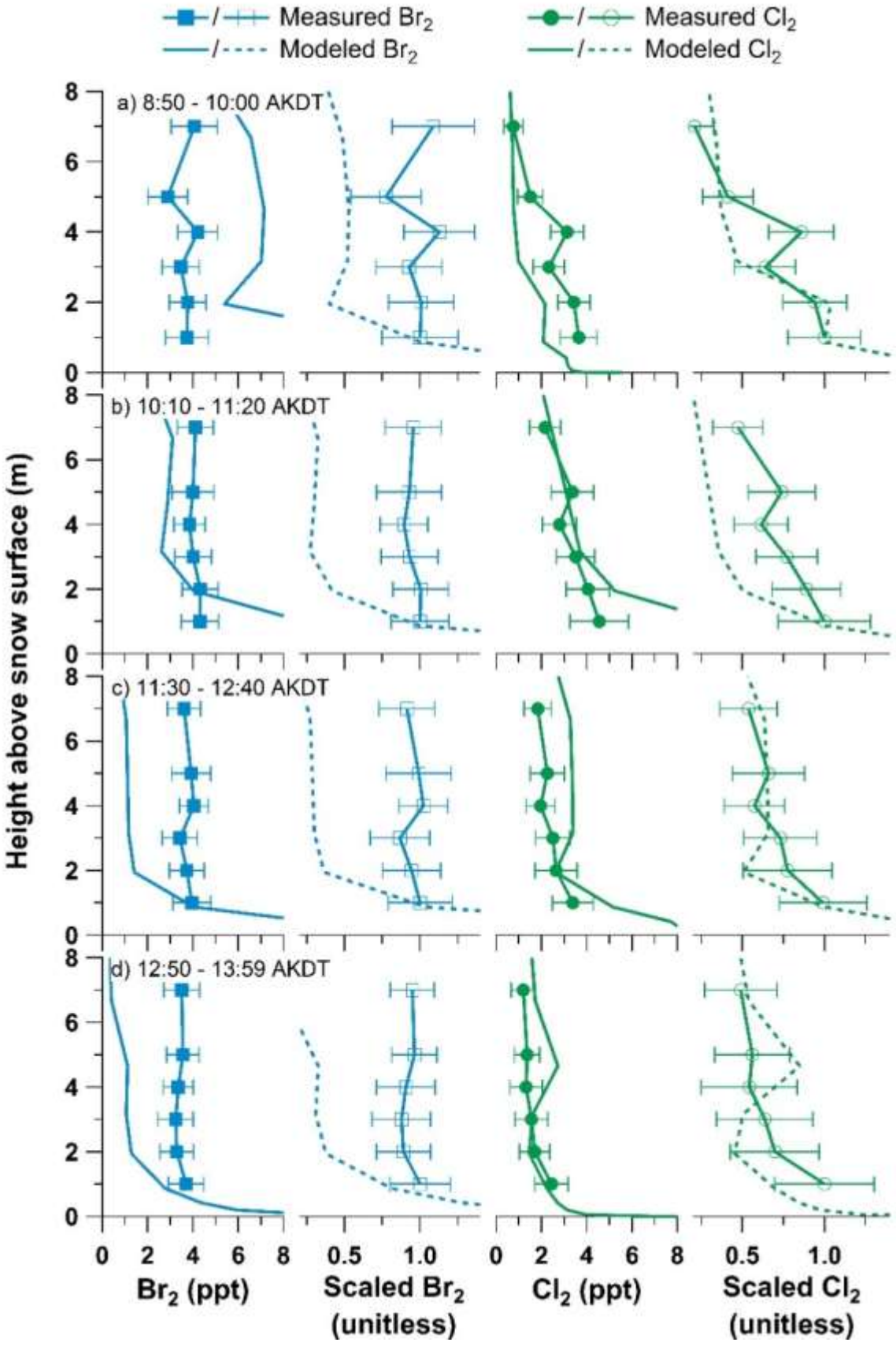
Measured Br_2
Modeled Br_2
Measured Cl_2
Modeled Cl_2
a) 8:50 - 10:00 AKDT
b) 10:10 - 11:20 AKDT
c) 11:30 - 12:40 AKDT
d) 12:50 - 13:59 AKDT
Height above snow surface (m)
Br_2 (ppt)
Scaled Br_2 (unitless)
Cl_2 (ppt)
Scaled Cl_2 (unitless)

concentrations with height. This remains true throughout the time period observed, with both measured and observed concentrations of Cl_2 reaching as low as 20% of the 1 m measurement by 7 m above the snowpack. In contrast, the measured profiles of Br_2 remain relatively constant with height throughout the measurement period. The lack of Br_2 concentration variation with height during the daytime was also observed under various meteorological conditions for vertical profiles measured on April 6, April 12, April 18, April 25, April 27, and April 30, 2016 (Figure 6.4). Cl_2 vertical profiles were not measured on these days as Cl_2 was below the CIMS limit of detection (0.8 ppt). The constant Br_2 concentrations with height are most consistent with the model results in the morning (8:50 – 10:00 AKDT, Figure 6.3a). Due to the lack of photolysis, Br_2 has a long lifetime overnight and becomes well mixed. It remains relatively well mixed until 8:00 AKDT (Figure 6.5b). After 8:00 AKDT, first the surface flux, then atmospheric radiation begins to rapidly increase, causing a spike followed by a rapid decrease in Br_2 concentration starting in the bottom layer of the model and spreading up. The vertical profiles simulated from 10:10 – 11:20 AKDT (Figure 6.3b) show high concentrations of Br_2, with the highest concentrations near the snowpack and an exponential decay to 3.2 m above the snowpack, after which a concentration of ~3 ppt is maintained to 8 m. The apparent stop of the exponential decay at 3.2 m in the case of Figure 6.3b is caused by the order the measurements were taken, and rapidly changing concentrations. Finally, throughout the daytime hours (11:30 – 21:00 AKDT) the model predicts an exponential decay, with very low (<2 ppt) Br_2 concentrations at heights greater than 2 m above the snowpack. While the modeled vertical profiles reflect the diurnal profile of Br_2 described above, the measured Br_2 vertical profiles do not decay with height. Rather, the measured Br_2 profiles are consistently ~4 ppt throughout the time period observed (8:50- 13:59 AKDT).

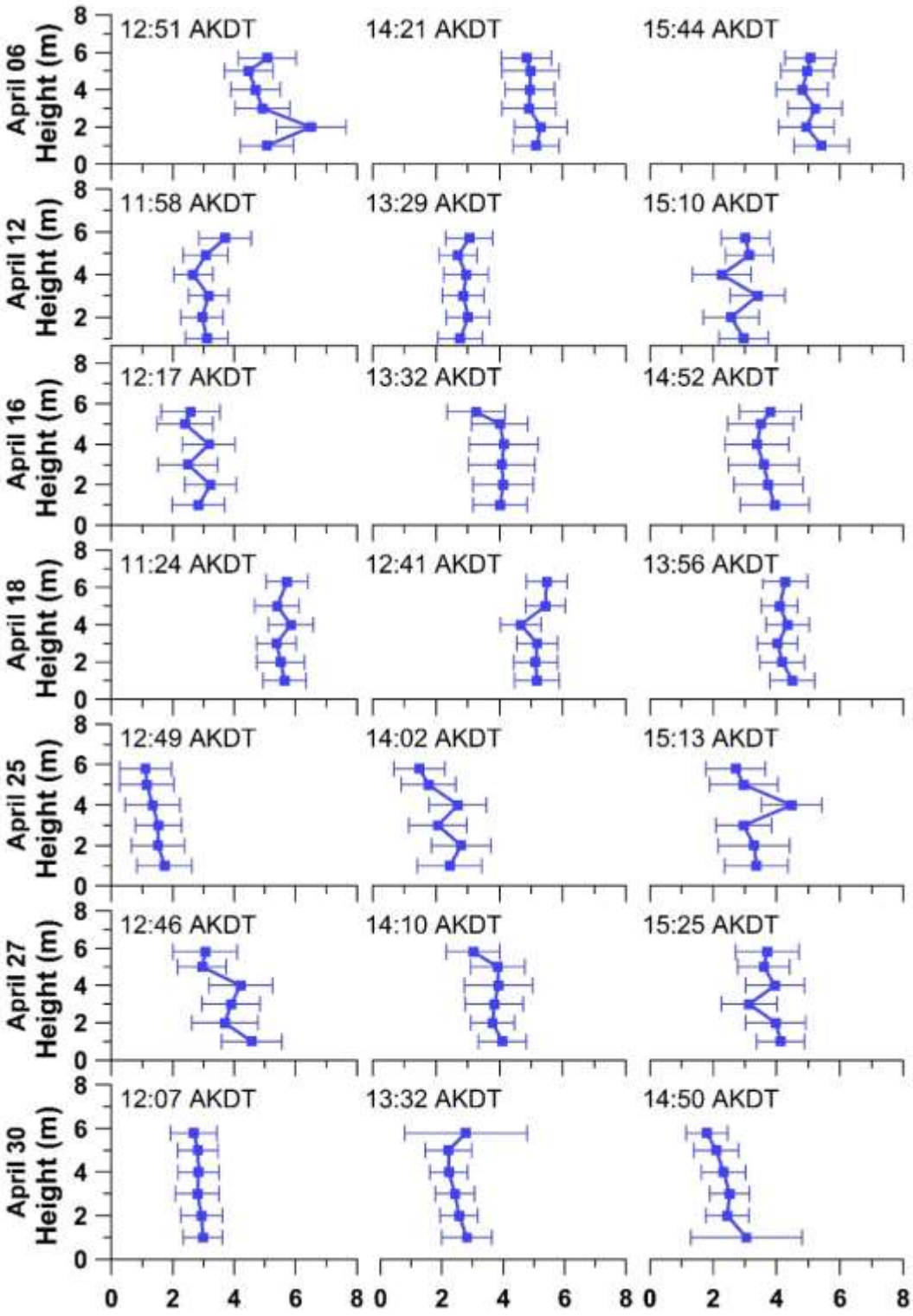

Figure 6.4 Measured Br_2 vertical profiles on April 6, April 12, April 16, April 18, April 25, April 27, and April 30, 2016. Times noted on each vertical profile are the middle of each ~1 h long measurement. Each error bars shown is the standard deviation of the average for each height.

Figure 6.5 Daytime (07:30-21:00) model results for March 21, 2016, near Utqiaġvik, AK. a) Eddy diffusivity. The black box indicates eddy diffusivities that were calculated discretely using tower data. Outside of the box eddy diffusivity was calculated using the YSU method. b) Br_2. Colored circles show measured Br_2 concentrations measured at 1 m on March 20, 2016. c) BrO. d) Br atoms. e) reactive Bromine - the sum of Br, BrO, HOBr, 2*Br_2, BrCl, $BrNO_2$ and $BrNO_3$.

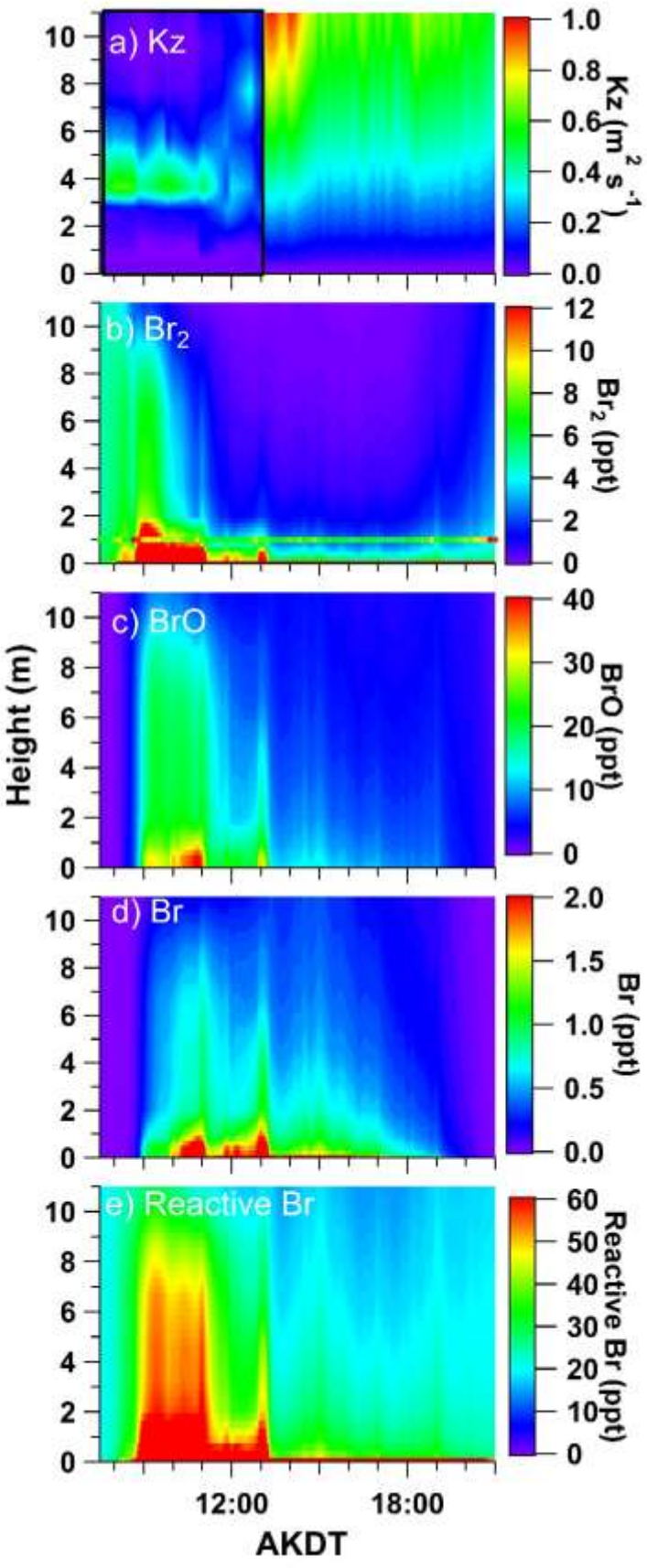
a) Kz
Kz (m^2 s^{-1})
b) Br$_2$
Br$_2$ (ppt)
c) BrO
BrO (ppt)
d) Br
Br (ppt)
e) Reactive Br
Reactive Br (ppt)
Height (m)
12:00
18:00
AKDT

The differences between the ability of the model to predict the observed Br_2 and Cl_2 vertical profiles is possibly indicative of the very different chemistry these species experience. While bromine and chlorine undergo similar reactions, the relative rates, and thus relative importance of each of these reactions can be very different. Bromine undergoes fast and efficient recycling between species, with only 5-10% of Br reactions at 1.95 m leading to the production of HBr (Figure 6.6), which is the major sink of reactive bromine in the atmosphere. In contrast, 60-78% of Cl reactions produce HCl (Figure 6.6). The relative production ratios of HBr and HCl suggest that gas-phase recycling of bromine is more efficient than it is for chlorine. The other main sink of both bromine and chlorine atoms is the propagation reaction with O_3, to form BrO or ClO (reaction 6.2). The variation of the HBr and HCl production proportion with time is largely

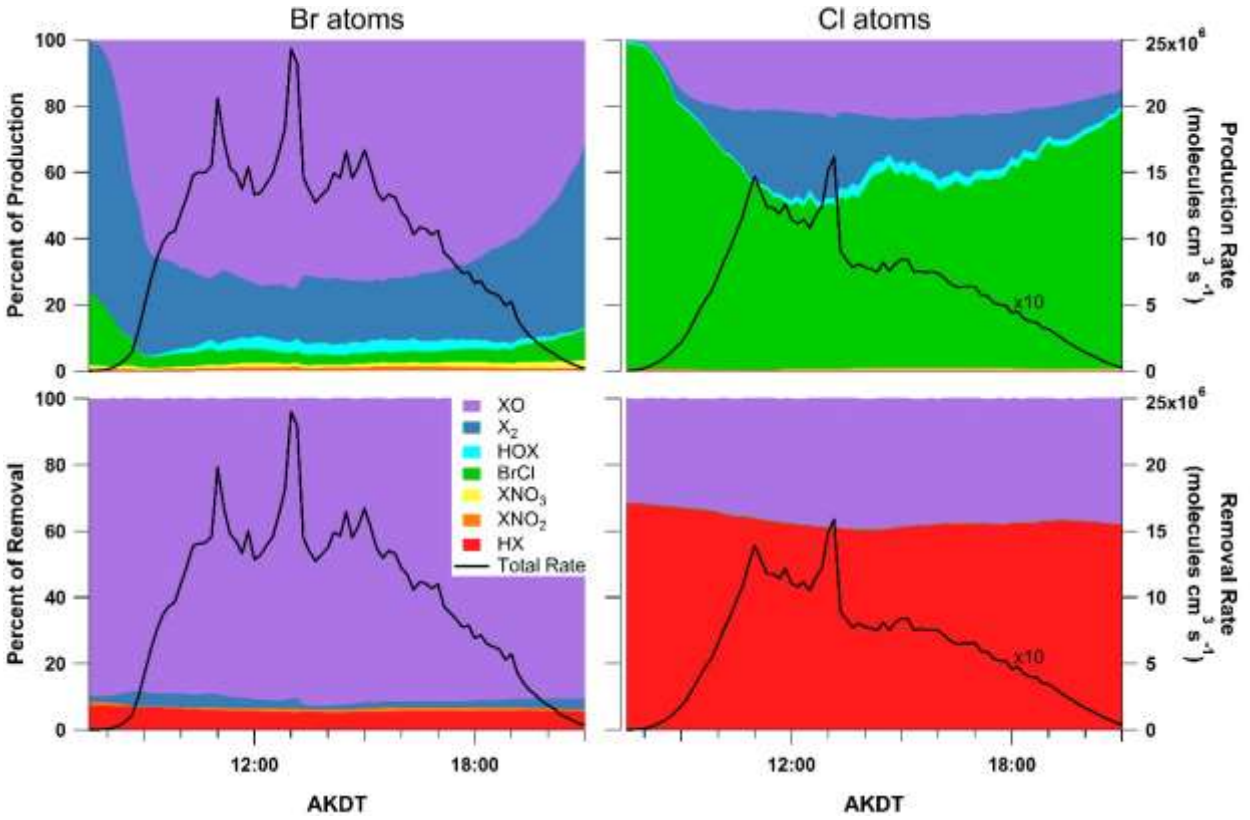

Figure 6.6 Br (left) and Cl (right) atom chemical production (top) and removal (bottom) at 1.95 m. Black lines show total production and removal rates (right axis). Cl_2 total production has been multiplied by 10 for clarity. Colors represent mole percent of production and removal that corresponding to various halogen species (XO, X_2, HOX, BrCl, XNO_3, XNO_2, HX.

dependent on the BrO production rate, and thus the O_3 concentration, which was increasing throughout the day (Figure 6.7). The activity of bromine recycling can also be seen in the sources of Br and Cl (Figure 6.6). During the daytime, 65-70% of Br production is from BrO, either through BrO photolysis or the reaction of BrO with itself. In contrast, a maximum of 20% of daytime Cl production is from ClO, and ~60% of production is from BrCl photolysis. The relative sources and sinks of Br and Cl demonstrate that bromine and chlorine chemistry are distinct from each other.

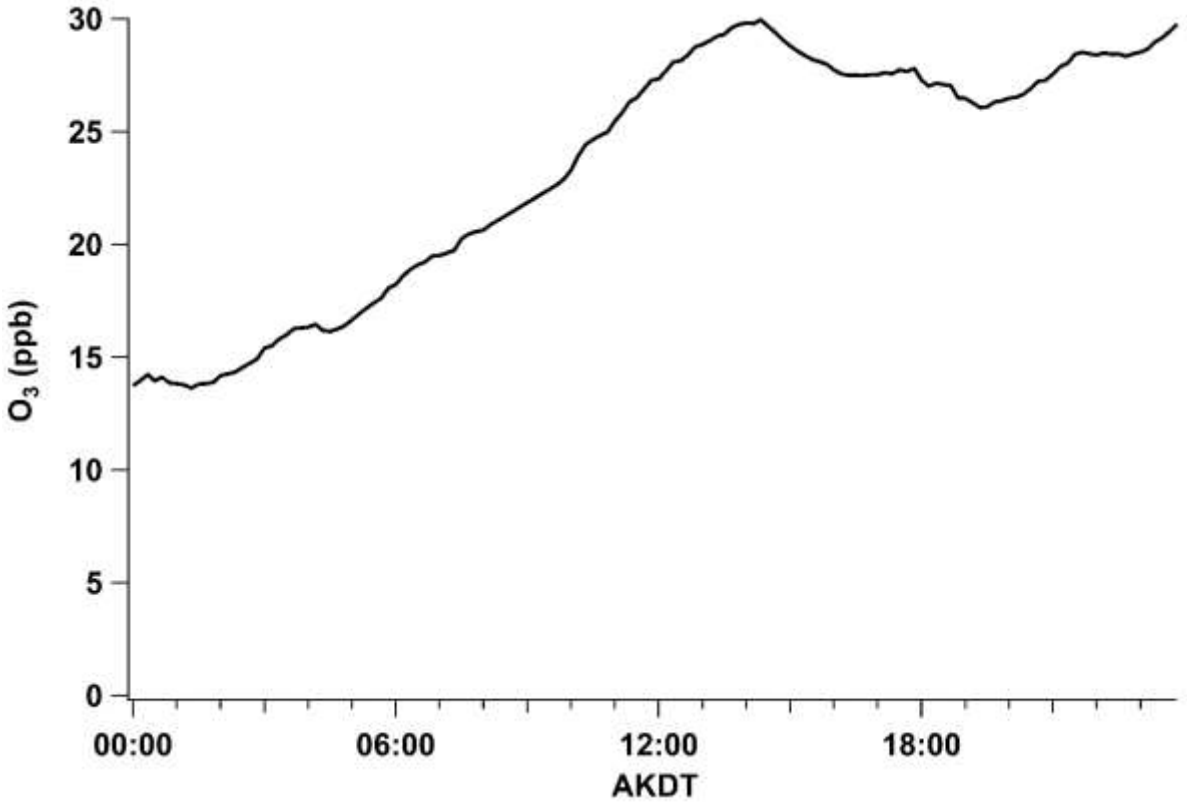

Figure 6.7 Ozone concentration on March 21, 2016, as measured at the NOAA GMD station in Utqiaġvik, AK. The model is constrained to measured ozone.

6.4.2 The Effects of Atmospheric Mixing on Vertical Propagation

Reaction rates are directly dependent on the concentrations of the reactants. This is especially relevant to reactions between species that are heavily dependent on each other. The second propagation step in the O_3 depletion chain reaction is the self-reaction of BrO with BrO (reaction 6.3). This reaction rate increases as the square of BrO, not linearly with reactive bromine concentration (Figure 6.8). The multiphase bromine reactions, such as the bromine explosion, are also highly dependent on the collision rate with particles, and thus concentration in the gas phase. At 0.87 m above the snowpack surface, where daytime reactive bromine is 50-

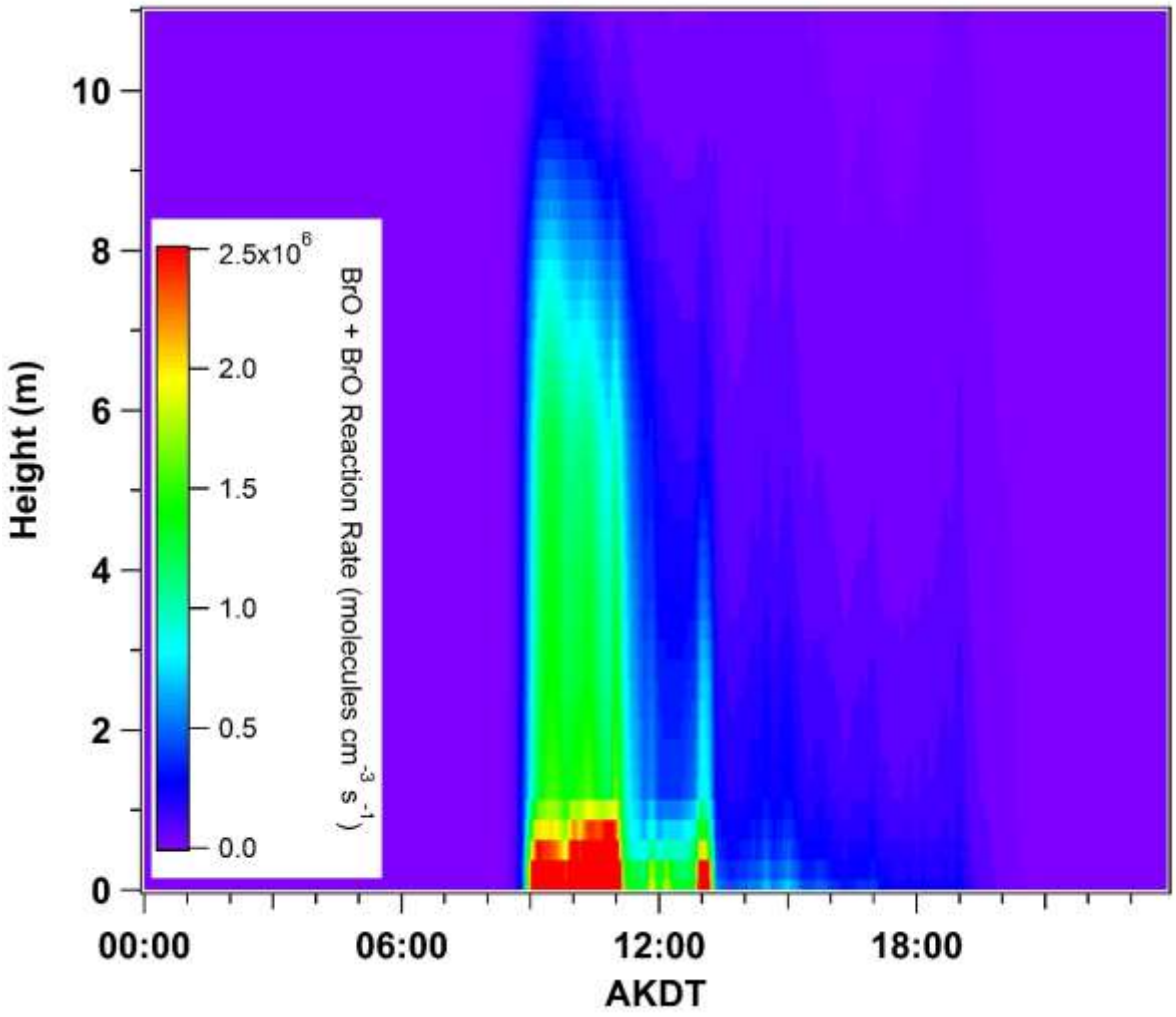

Figure 6.8 The BrO + BrO reaction rate. This reaction scales as the square of BrO concentration.

70 ppt, the formation rate of Br_2 from reaction 6.8 is 5-7x10^3 molecules cm^{-3} s^{-1}, while at 10.6 m above the snowpack, where reactive bromine is more than halved (20-26 ppt), the formation rate of Br_2 is also halved (~3x10^3 molecules cm^{-3} s^{-1}). In the stable polar boundary layer, the effective mixing volume, the volume over which species are distributed, not only controls the concentration of the species itself, but also the rate at which recycling, and bromine explosion occurs. The effective mixing volume is controlled by the intensity of atmospheric turbulence, and the method used to calculate the rate of atmospheric mixing can have a large impact on model predictions of both the distribution and total amount of bromine within the boundary layer.

Modeling of atmospheric vertical mixing under stable conditions is difficult [Mahrt, 1999], and eddy diffusivities from different models diverge [Dyer, 1974; Andreas, 2002]. The eddy diffusivity calculated within the tower height (black box, Figure 6.5), shows an unusual pattern, with peak values at 4 m above the snowpack surface. This is indicative of stratification within the boundary layer that cannot be captured by current atmospheric mixing parameterizations, which rely on Monin-Obukhov similarity theory, and thus predict monotonically increasing mixing throughout the surface layer. Figure 6.9a shows the calculated eddy diffusivity (base case), the eddy diffusivity calculated using the Yonsei University model (YSU), and the difference between the calculated and modeled eddy diffusivity. During the time period of the measurements, the surface layer height (estimated as one-tenth of the boundary layer height) was between 15 and 41 m above the snowpack surface. Therefore, the modeled eddy diffusivity shown in Figure 6.9a increases linearly with height but varies with time as described in Equation 6.8. The YSU model overpredicts eddy diffusivity by up to 6400%, and only under predicts mixing by 41% in the turbulent layer which occurs ~4m. This overprediction of mixing leads to lower concentrations of bromine species within the bottom 11.6 m of the boundary layer.

Br_2 shows the largest height dependence for change in concentrations between the two cases (Figure 6.9b), with greater mixing causing decreased Br_2 near the surface in the YSU case. Higher concentrations of reactive bromine tend to favor Br_2 over other species because of nonlinear production mechanisms (e.g., reaction 6.3). Reactive bromine (the sum of Br, BrO, HOBr, 2*Br_2, BrCl, $BrNO_3$, and $BrNO_2$) is reduced by up to 72%, as shown in Figure 6.9e. Br_2 and reactive bromine concentrations are most reduced close to the snowpack surface. Above the highest tower measurement (11.6 m) reactive bromine concentrations are slightly increased, and the column reactive bromine over the 200 m model domain is nearly the same as the base case (increased up to 4%, Figure 6.10b). Figure 6.9d shows that the decrease of Br (up to 83%) in the bottom 11.6 m due to increased mixing is larger than the decrease in reactive bromine, suggesting that lower concentrations of reactive bromine shifts the distribution away from Br. Less Br relative to reactive bromine slows HBr production. HBr is the main sink of reactive bromine in the atmosphere, so the shift away from Br towards other reactive species leads to slightly higher total column reactive bromine. In the base case, low mixing traps a larger fraction of the reactive bromine in the bottom 11.6 m of the atmosphere (Fig. 6.9c).

While this does slightly enhance the reactive bromine sink, the balance shift of reactive bromine towards Br may also make the atmosphere more reactive and increase removal rates of O_3. Additionally, high concentrations of bromine near the snowpack surface may be necessary to cause the bromine explosion within the snowpack and create the fluxes that are prescribed in the model.

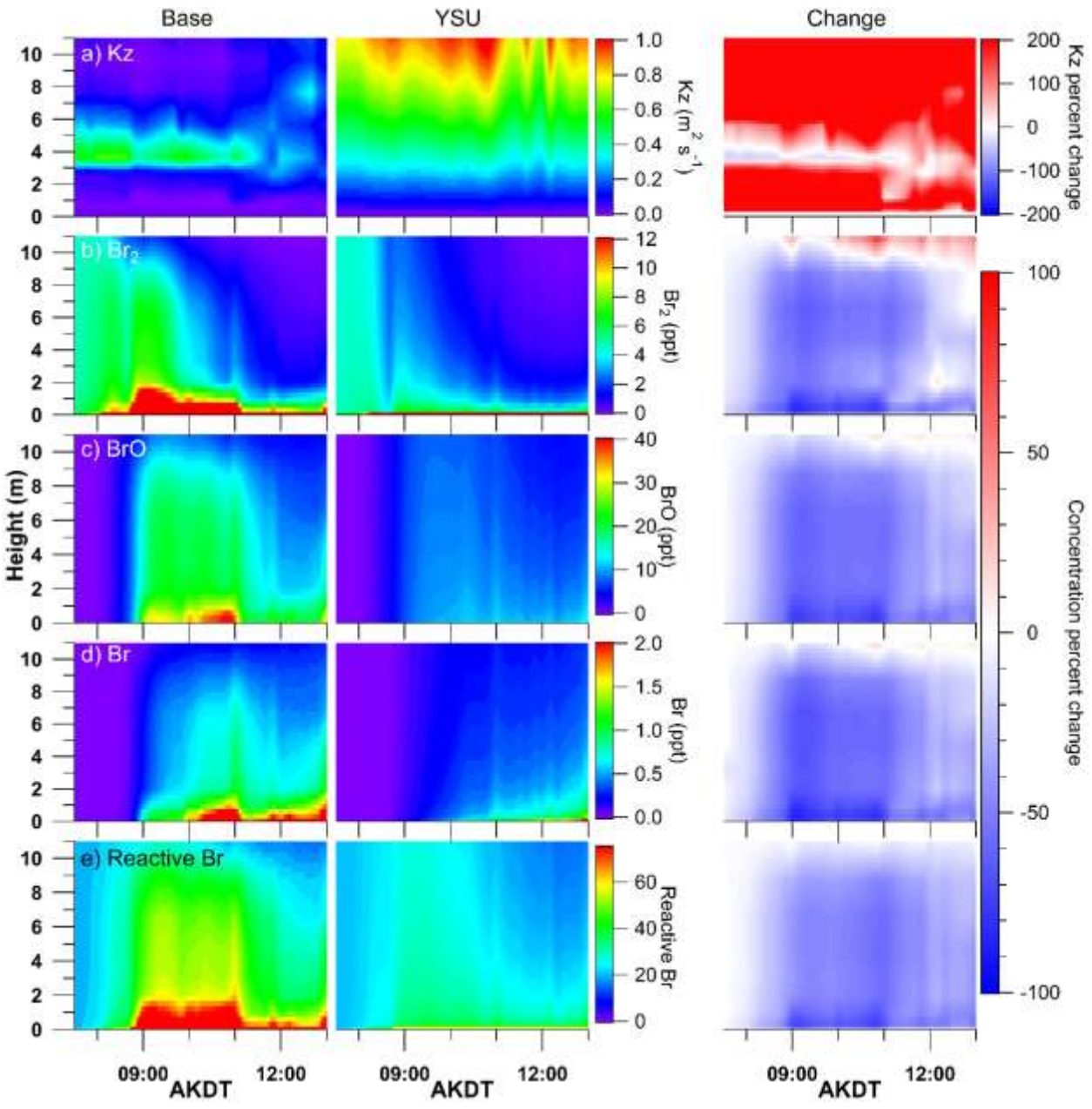

Figure 6.9 Model results for the base case and YSU mixing, as well as percent change ($100 * (YSU - Base)/Base$) for the period of daytime tower measurements (07:30 – 13:00 AKDT) on March 21, 2016, near Utqiaġvik, AK. The difference in eddy diffusivity is off scale, up to 6400%.

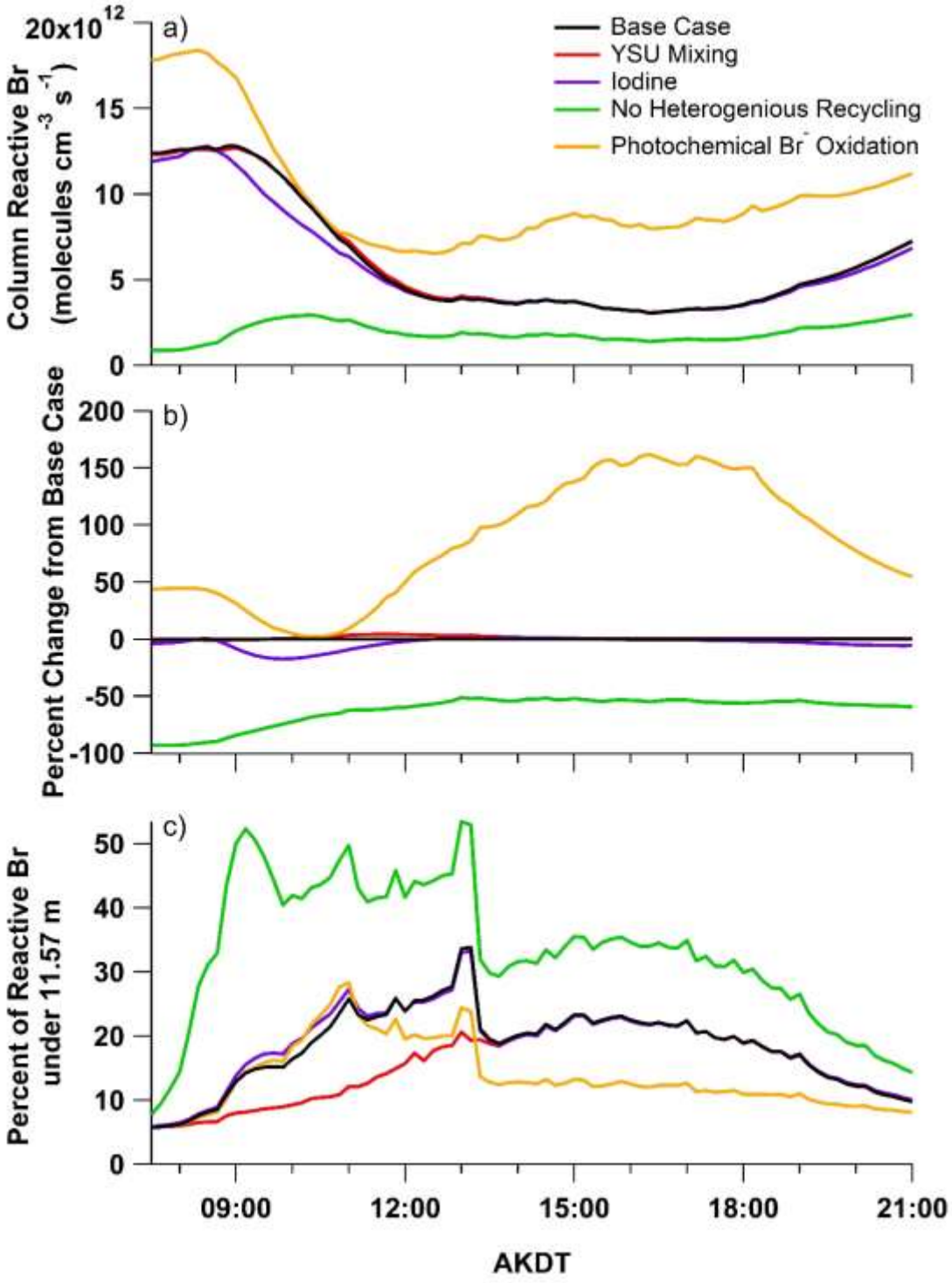

Figure 6.10 a) Column reactive bromine over the 200 m model domain on March 21, 2016 (07:30-21:00) for the Base case, YSU mixing case, iodine sensitivity test, sensitivity test without multiphase recycling, and sensitivity test with photochemical Br- production in the aerosol phase. b) change in reactive bromine (the sum of Br, BrO, HOBr, 2*Br_2, BrCl, $BrNO_3$, and $BrNO_2$) relative to the Base case. c) Percent of the column reactive bromine present below 11.6 m, of the full 200 m column.

6.4.3 Bromine Explosion and Photochemical Oxidation of Bromide

Each oxidation of aerosol or snowpack Br^- by HOBr or $BrNO_3$ increases the amount of gas phase reactive bromine in the boundary layer. Bromine explosion chemistry not only increases the total reactive bromine within the boundary layer, but it also allows for a more even distribution of reactive bromine with height. To test the importance of bromine explosion chemistry a sensitivity test was performed which removed Br_2 production from multiphase reactions (Figure 6.11). The change in Br_2 from the base case shows the highest dependence on height, with near zero difference between the cases near the snowpack surface, where most Br_2 is generated via the snowpack flux, and 62.4% less Br_2 at 11.6 m above the snowpack surface at 9:10 AKDT. As the day continues the effect of multiphase recycling on Br_2 concentrations decrease. This is likely due to the increasing mixing of snowpack sourced Br_2 throughout the day within the model (Figure 6.5a). Bromine production via multiphase aerosol recycling mechanisms in the model produces primarily Br_2, though BrCl and $BrNO_2$ can also be produced via multiphase reactions. Daytime concentrations of reactive bromine are reduced by up to 67.7% in the bottom 11.6 m (Figure 6.10d), and daytime column reactive bromine is reduced by ~50% (Figure 6.10b) in the absence of heterogeneous Br_2 production. The absence of aerosol phase bromine explosion chemistry increases the fraction of reactive bromine below 11.6 m by 20% during the daytime (Figure 6.10c., 09:00-13:00 AKDT). While aerosol recycling is very important to the vertical propagation of bromine within the boundary layer, another source of Br_2 above the snowpack is required to explain the observed vertical profiles. Within the model, the main sink of reactive bromine is the formation of HBr, which is subsequently lost to aerosols or the surface. This Br^- is then available to be oxidized to Br_2. Previous models have included photochemical oxidation in the aerosol phase [Thomas et al., 2011; Toyota et al., 2014], but they have not explicitly tested the effect of photochemical oxidation on the vertical propagation of bromine chemistry. To test the effect of

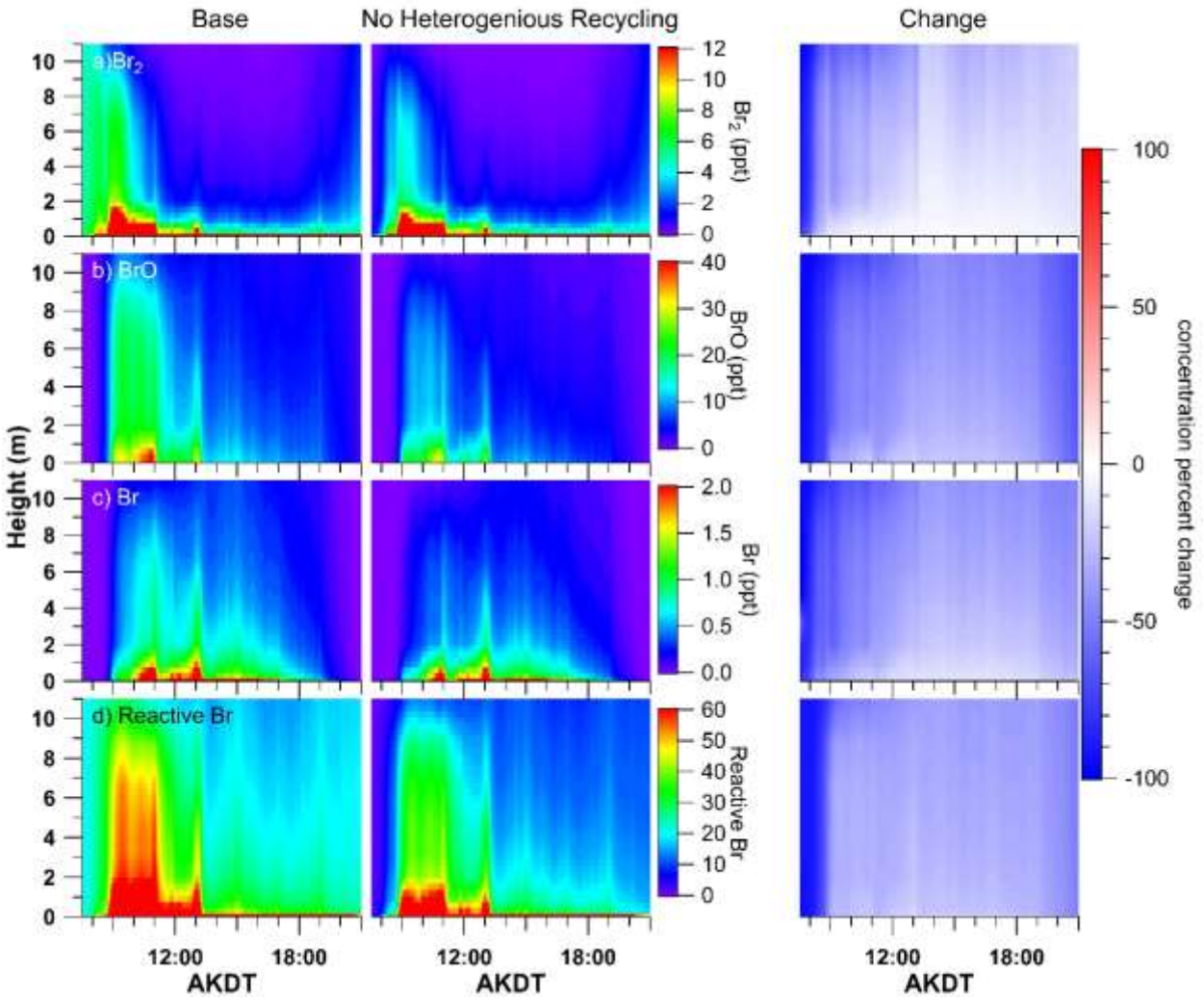

Figure 6.11 Daytime (07:30 – 21:00 AKDT) model results on March 21, 2016, near Utqiaġvik, AK in the base case, without aerosol phase bromine explosion reactions and percent change. Br_2 formation in the aerosol phase, and from heterogeneous reactions was stopped, but loss of bromine species due to these reactions was allowed.

oxidation of Br^- to Br_2 in the aerosol phase via photochemical oxidation, a sensitivity test was performed where HBr deposited to the aerosol phase was added back to the model as a Br_2 emission factor. The emission factor was scaled to photolysis rates to simulate the photochemical nature of the proposed oxidation mechanism. Figure 6.12 shows Br_2, reactive bromine, HBr, and the Br_2 emission rate. The change in Br_2 concentration shows a strong dependence on mixing, with the highest changes in concentration occurring where the least mixing occurs during the morning. During the afternoon, the percent

change in Br_2 is higher with altitude, as the influence of the snowpack declines. The increase of reactive bromine concentrations shows less dependence on height, especially in the afternoon. The emissions of Br_2 increased column reactive bromine by 160% (Figure 6.10b). Because Br_2 emissions are more evenly distributed (Figure 6.13) the percent of reactive bromine which is below 11.6 m is reduced by ~10% throughout the afternoon (Figure 10c). Despite the Br_2 emission rate being consistent with height above ~0.5 m, there is still a steep gradient of Br_2 concentrations within the bottom 11.6 m of the atmosphere. Unlike reactive bromine species, which are most concentrated closest to the snowpack surface, HBr is most concentrated slightly higher in the atmosphere but shows little other variation with height in the bottom 11.6 m, because it is not reactive in the gas phase. Following the same pattern, the Br_2 emission rate also varies little over the bottom 11.6 m. However, actual emissions of Br_2 due to photochemical oxidation would be related to Br^- aerosol content, which may vary with height. Currently, no observed vertical profiles of aerosol Br^- concentration in the Arctic exist. Aerosol Br^- at all heights within our model is constrained by observations, which are averaged for the day, and measured at a single height. A better understanding of the diurnal and vertical variation of the Br^- content of aerosols would allow

a better simulation of the potential effect of photochemical oxidation of aerosol Br^-, which could explain the measured Br_2 profile.

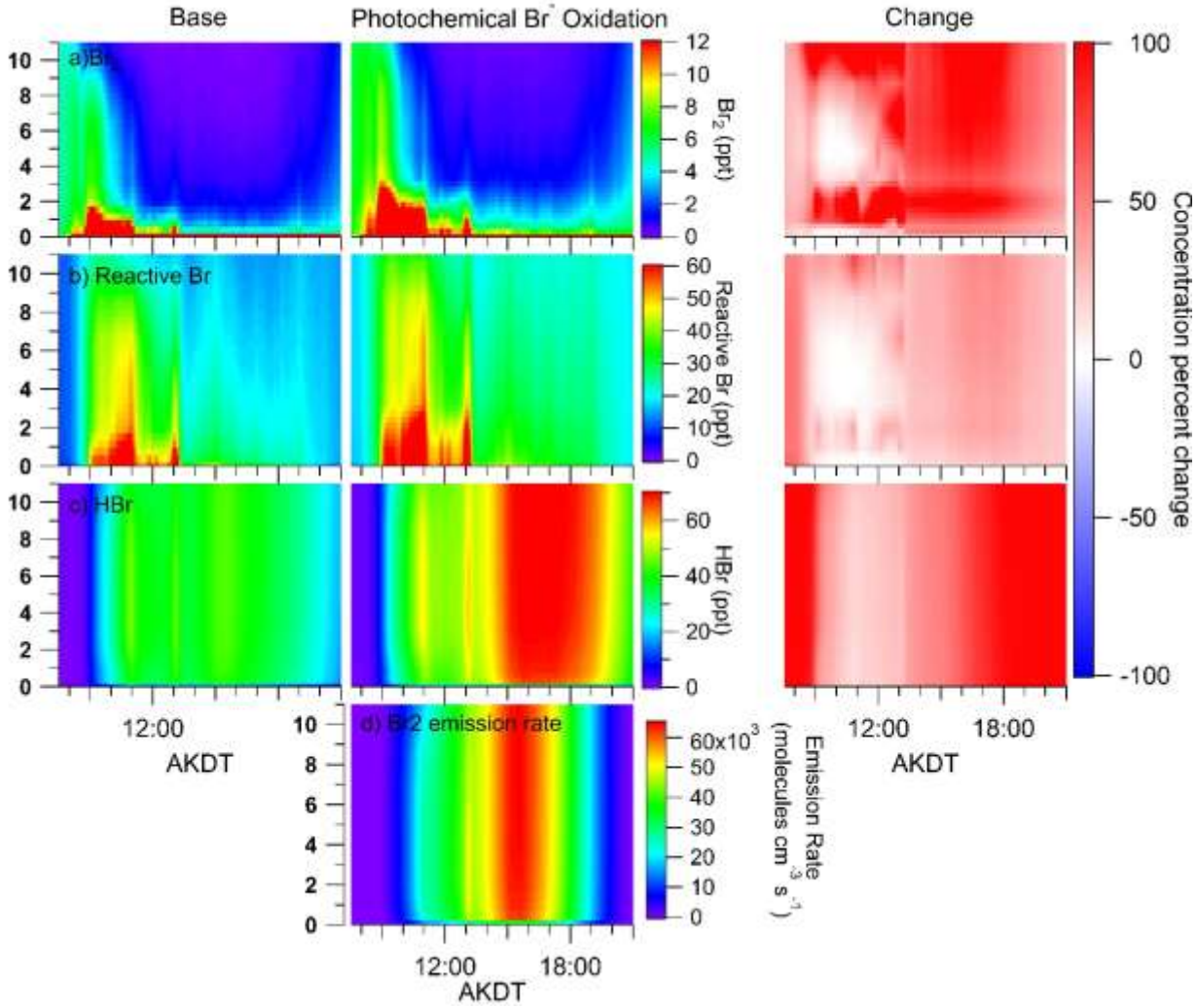

Figure 6.12 Daytime (07:30 – 21:00 AKDT) model results showing the results of photochemical oxidation of Br^- deposited to the aerosol phase from HBr.

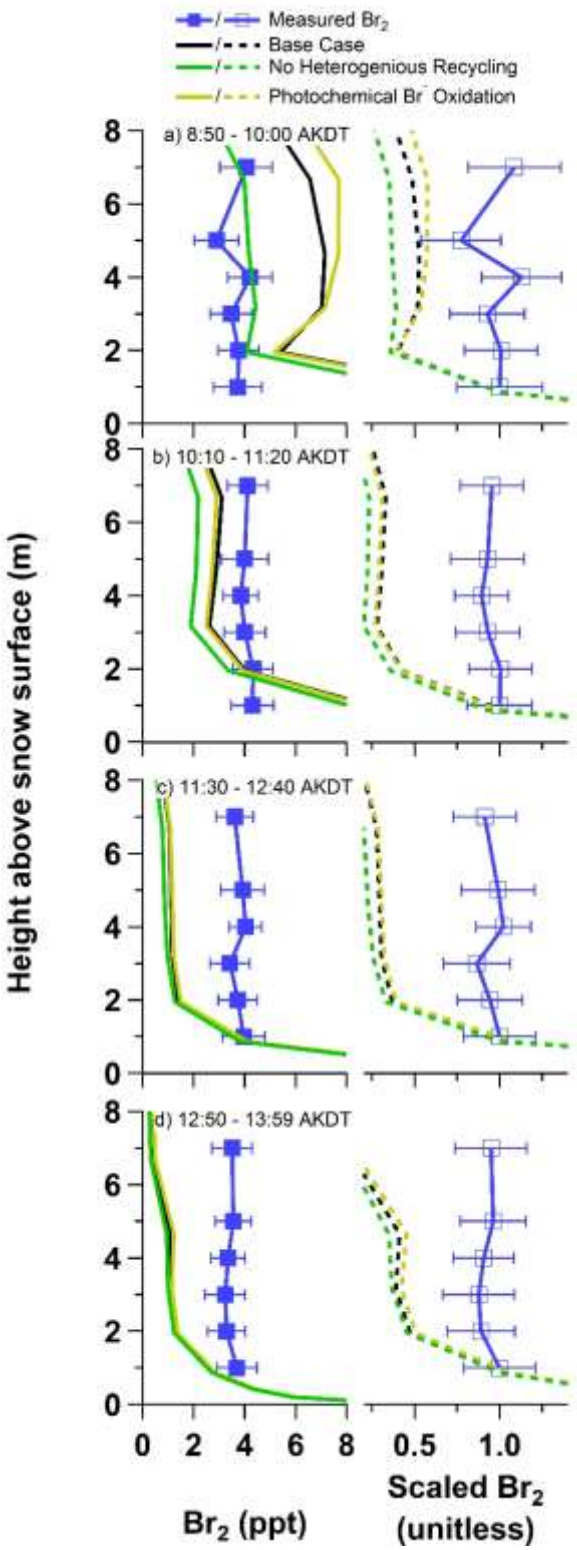

Figure 6.13 Measured vertical profiles (lines with markers) and modeled vertical profiles for the base case (black), case without heterogeneous chemistry (green), and with photochemical oxidation of aerosol bromide (yellow). Profiles on the right have been scaled to the 1 m measurement or the modeled value at 0.87 m.

6.4.4 Iodine Chemistry

Recent observations of active iodine chemistry in the Arctic [Sipilä et al., 2016; Raso et al., 2017] make clear the need for examination of the vertical extent of iodine chemistry, and its effect on the vertical extent of bromine chemistry in the Arctic. Previous models have suggested that iodine chemistry may have a significant impact on both the chain length of the bromine radical reaction [Thompson et al., 2017], and the ability of models to simulate the O_3 depletion rate [Thompson et al., 2015; Raso et al., 2017]. However, observations of gas phase inorganic iodine in the Arctic remain sparse, and there has yet to be a one-dimensional simulation of iodine chemistry in the Arctic. Figure 6.14 shows the vertical and diurnal evolution of iodine chemistry for key iodine species with a radiation-dependent snowpack flux. Molecular iodine (I_2) (Figure 6.14a) shows a steep vertical dependence. This is not unexpected, as the photolysis lifetime of I_2 is very short (7.7 seconds midday), and the midday effective mixing height for iodine is only ~1 m (Zeff for Br_2 and Cl_2 are ~2 m and ~8 m respectively). Simulated I_2 concentrations (Figure 6.14a) at 1 m (0.3 – 0.5 ppt) are similar to the only reported measurements [Raso et al., 2017] during the daytime (~0.3 ppt). Iodine monoxide has also only been observed once in the high Arctic, at concentrations less than 1 ppt [Zielcke, 2015]. The modeled IO concentrations (< 0.2 ppt, Figure 6.14b) are consistent with this, even close to the snowpack surface. The only other observation of gas phase inorganic iodine in the Arctic has been of HIO_3, which may be an important new particle formation precursor [Sipilä et al., 2016]. HIO_3 was simulated to occur at concentrations of less than 0.20 ppt (Figure 6.14c), which is significantly less than the reported observation, from northern Greenland [Sipilä et al., 2016]. Even with low concentrations of other iodine species, the model predicts that the concentration of iodine atoms is quite high (up to 60 ppt). There are many uncertainties in iodine chemistry, which may account for both the apparent underprediction of HIO_3 and the high concentration of iodine atoms in the model. However, little

is known about the temporal and spatial distribution of iodine chemistry in the Arctic. The possible underestimation of HIO_3 production in the model could be due to unknown reactions or reaction rate constants with high uncertainties. Under nondepleted O_3 conditions (14-30 ppb), and with low iodine concentrations, iodine chemistry had only a small effect on the vertical evolution and speciation of bromine (Figure 6.15), reducing reactive bromine concentrations by up to 14% in the bottom 11.6 m of the boundary layer (Figure 6.10c).

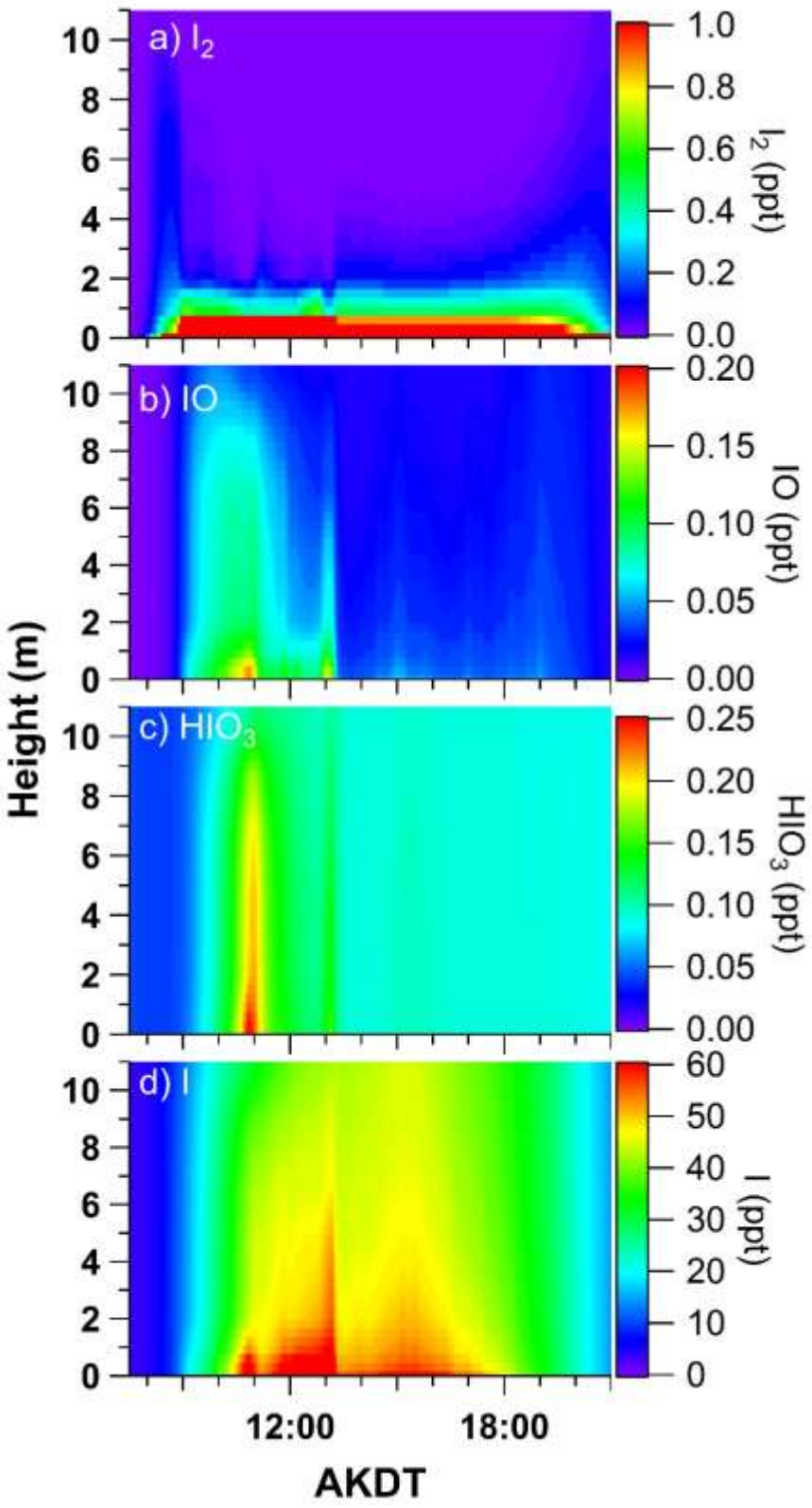

Figure 6.14 Daytime (07:30 – 21:00 AKDT) model results showing the vertical extent of iodine chemistry.

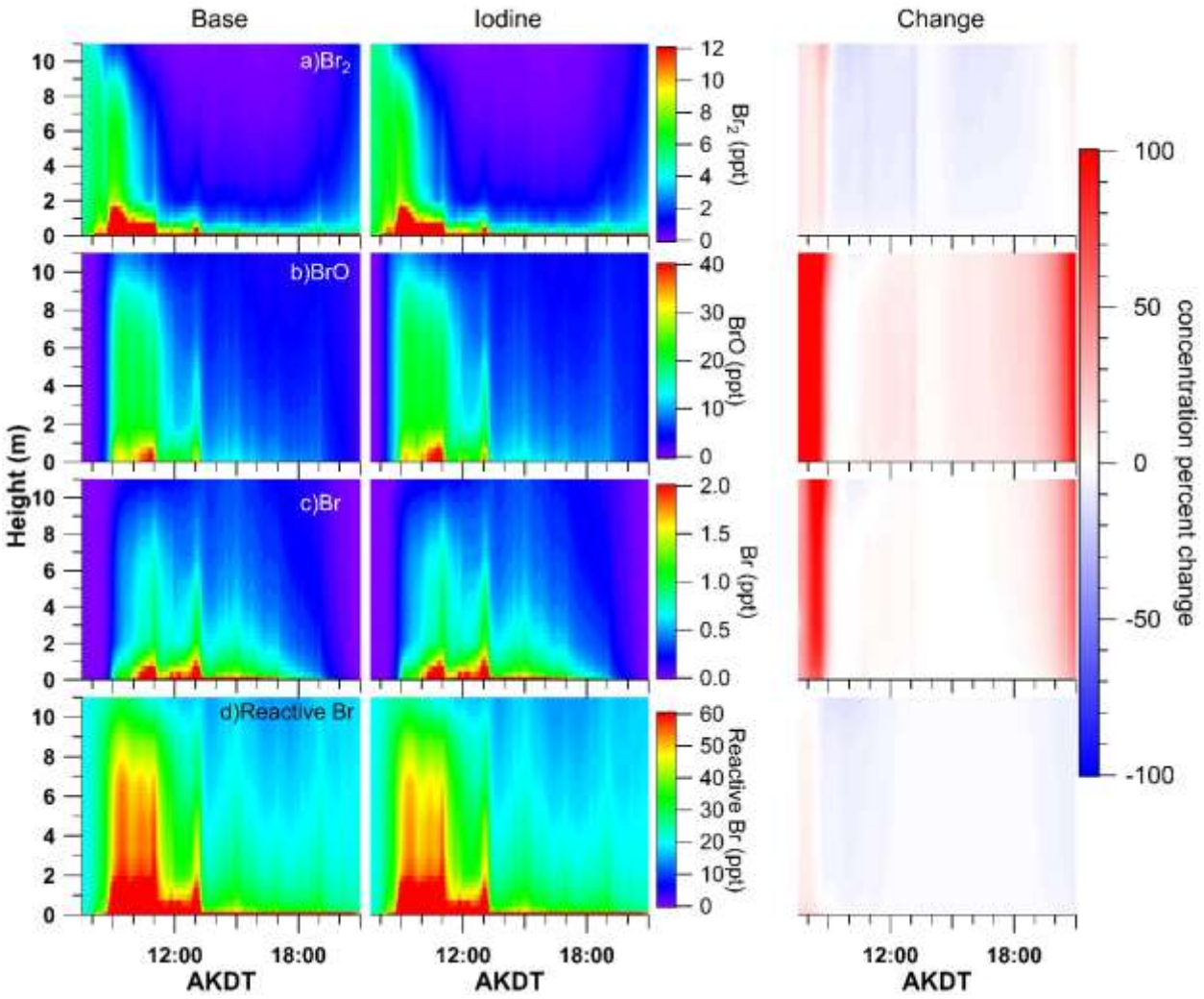

Figure 6.15 Daytime modeled bromine for sensitivity test with iodine chemistry.

6.5 Conclusions

A one-dimensional model was used to investigate the impact of snowpack emissions on the vertical scale of halogen chemistry in the Arctic. The first reported measured vertical profiles of Br_2 show nearly no dependence on height above the snowpack between 1 and 7 m. The one-dimensional model results are inconsistent with these measurements, even when in-situ mixing is accounted for, suggesting that significant uncertainties exist in our understanding of the sources and sinks of bromine chemistry in the Arctic. We have examined several areas of uncertainty using the one-dimensional model. First, atmospheric mixing in the Arctic is challenging to parameterize, yet the mixing of species near the snowpack can have substantial effects on the oxidation capacity of the Arctic. A better theoretical understanding of turbulence in stably stratified boundary layers will allow for better parameterization of currently unpredictable intermittent and layered turbulence. Second, the oxidation of aerosol Br^- to Br_2 is undoubtedly one of the most important processes for the vertical propagation of bromine chemistry. But the distribution of aerosol Br^-, and thus the importance of Br^- oxidation, vertically through the boundary layer is not known. Simulated heterogeneous recycling of HOBr and $BrONO_2$ increases atmospheric bromine concentrations at 11.6 m by up to 70% in the daytime, assuming an even vertical distribution of Br^-. Photochemical oxidation of Br^- may be as significant a source of bromine to the atmosphere as heterogeneous recycling. However it is not known whether the OH radical oxidation of Br^- that occurs in laboratory experiments [Wren et al., 2013; Halfacre et al., 2018] occurs in atmospheric aerosol. Here we tested the photochemical oxidation of Br^- deposited locally from HBr. However, we do not understand the distribution of aerosol Br^-in the atmosphere well enough to thoroughly test this hypothesis given that no vertically resolved measurements of aerosol Br^- during the Arctic springtime exist. This is a crucial measurement to understanding the processes that control oxidation throughout the Arctic boundary layer. Finally, despite the impact

iodine may have on the speed and chain length of bromine recycling reaction, its potential impact on the vertical extent of iodine chemistry is dwarfed by other uncertainties in our understanding of bromine chemistry. The community's current understanding of the sources, sinks, and vertical propagation of bromine within the boundary layer is not sufficient to explain the observed vertical profiles of Br_2 between 1 and 7 m.

CHAPTER 7. CONCLUSIONS AND FUTURE DIRECTIONS

The work presented in this dissertation was conducted with the goal of further understanding the impact of snowpack halogen production on the oxidation capacity of the Arctic atmosphere. The beginning of this work posed six scientific questions to further the community's understanding of Arctic halogen chemistry.

1. Is I_2 present at detectable concentrations in the Arctic atmosphere?
2. Is I_2, like Br_2, BrCl, and Cl_2, produced photochemically in the coastal snowpack?
3. What is the impact of I_2 on ozone depletion in the Arctic boundary layer?
4. What is the rate of halogen emissions from the snowpack?
5. What is the vertical extent of bromine and chlorine chemistry in the Arctic boundary layer?
6. Does our current understanding of halogen sources, sinks and recycling explain observations of the vertical evolution of Br_2 and Cl_2?

Here we discuss the answers to these questions and pose further questions raised by the results.

The first and second questions were addressed in chapter 2. While it had been observed for many decades that iodine is enriched in Arctic aerosols, it is not until lately that observations of gas phase iodine have been reported in the Arctic [Zielcke, 2015; Sipilä et al., 2016]. In chapter 2, and the corresponding publication, Raso et al. [2017], I present the first measurement of I_2 in the Arctic. I_2 was present in low concentrations (0.30-1.0 ppt) above the snowpack, and much higher concentrations (up to 22 ppt) in the snowpack interstitial air. Despite two orders of magnitude lower I^- concentrations (0.5-15 nM) than Br^- concentrations (0.06-0.8 μM), I_2 concentrations within the snowpack interstitial air showed peak concentrations similar to those of

Br_2. This suggests that I^-, consistent with its oxidation potential, is more easily oxidized than Br^-, however no measurements of the rate constant of I- with $OH^\cdot$ have previously been reported. I_2 concentrations in the snowpack interstitial air showed a strong dependence on radiation, leading to the conclusion that a photochemical production mechanism in snow is responsible for I_2 production. The profiles of I_2 and Br_2 in and above the snowpack show significant differences, suggesting that the air-snow multiphase chemistry of iodine might be different from that of bromine.

Photochemical I_2 production is further supported by the observed vertical profiles of iodide (I^-) enrichment in the snowpack shown in chapter 3. I^- was highly enriched relative to the seawater I^-/Na^+ ratio at all depths in the Arctic coastal snowpack, but enrichment was smallest close to the surface. The relative lack of I^- close the snowpack – boundary layer interface suggests that iodine has been lost from the snowpack to the boundary layer. Differences in the snowpack depth profiles of Br^- and I^- agree with the evidence from vertical profiles of I_2 and Br_2 within the snowpack interstitial air that there must be significant differences in bromine and iodine multiphase chemistry in the snowpack and snowpack interstitial air. Almost all the iodine present in Arctic snow is inorganic (I^- and IO_3^-), suggesting that in the snowpack phase measurements of total iodine may continue to be a good proxy for I^- in the Arctic. The near constant concentrations of I^- with depth below the surface layer, along with high wintertime concentrations of iodine in the snow and aerosol phase, shows that the source of iodine to the snowpack does not decrease significantly in the fall and winter. This observation rules out local enrichment via a radiation dependent mechanism, such as biological activity or photochemistry. It seems likely that iodine enrichment in the arctic comes from an unknown source. Additional studies may provide further evidence of the exact source of iodine to the Arctic environment. First, previous work has shown that while

iodine enrichment of aerosols is not seasonally dependent at coastal sites, at inland sites there is some seasonality [Sturges and Barrie, 1988]. Measurements of iodine enrichment in aerosols has not been reported in recent decades, while the Arctic has been rapidly changing. First, reobservation of the seasonality of aerosol iodine enrichment should be shown. Coupling measurements of iodine in aerosols from various Arctic sites with air mass back-trajectories could allow for analysis of the exact locations iodine enriched aerosols are transported from and explain the apparent variability of iodine enrichment between coastal and inland sites. A similar study was recently conducted by Freud et al. [2017] who conducted back-trajectories to understand where aerosol mass at several Arctic sites originated, but did not include analysis of aerosol chemical composition. Second, the chemical composition, including iodine speciation, and morphology of iodine enriched aerosols in the Arctic may show evidence of their origin. It is unknown if all of the observations of iodine enriched particles observed in the Arctic are formed from iodine induced new particle events, as observed by Sipilä et al. [2016] and Allan et al. [2014], or if or if some of the iodine partitions from the gas phase to already formed particles. Iodine speciation, along with the iodine to oxygen ratio within the particle phase, could provide evidence to answer this question.

In contrast to the Arctic samples, Antarctic snow showed large concentrations of an unidentified iodine species, which is likely bound in an organic molecule. These contrasting results suggest that caution is required when considering iodine enrichment mechanisms. Chemically specific measurements, should be conducted to confirm that the unknown peak is an organic iodine compound. Ion chromatography, coupled with high resolution mass spectrometry or MS-MS, would allow for chemical identification of the unknown peak. Recently Yang et al. [2016] reported the identification of twelve previously unobserved organic iodine compounds from

seaweed using a similar method to the one suggested above. While the limits of detection reported for the high resolution orbitrap mass spectrometer (4.0-0.1 nM) were higher than those for ICPMS (50-200 pM), they should be low enough for identification of the unknown compound. Finally, while in the midlatitudes it is accepted that biological enrichment is the main source of I_2 to the atmosphere, and it has been postulated that sea ice diatoms can release I_2 to the atmosphere [Saiz-Lopez et al., 2015], it has not been shown that ice diatoms do in fact form I_2.

The third question was addressed using 0-D modeling. In chapter 4 it is shown that even at sub-ppt levels in the Arctic atmosphere, I_2 can have significant impacts on atmospheric boundary layer oxidation capacity and composition. The inclusion of observed molar ratios of I_2 in a 0-D model increases the ability of the model to simulate the initial rate of an observed ozone depletion event and produces IO concentrations consistent with recent observations [Zielcke, 2015]. In the snowpack interstitial air, I_2 has a modest impact on the destruction of O_3 due to the large concentrations of Br_2 present in the case examined. These first measurements of Arctic snowpack I^-, snowpack interstitial air I_2, and ambient I_2, combined with photochemical modeling show that not only is I_2 present in the boundary layer but that even the small amounts of I_2 present (<1 ppt) are important to understanding the ongoing chemistry of the springtime Arctic atmosphere.

The fourth question is partially addressed in chapter 5. The eddy covariance fluxes of Cl_2 at Utqiaġvik from the tundra snowpack ranged from -0.1×10^8 to 1.8×10^8 molecules cm^{-2} s^{-1}. These are within the range reported by Custard et al. [2017] ($0.16\text{-}14 \times 10^8$ molecules cm^{-2} s^{-1}) despite the differences in the measurement dates. Significantly different from zero Br_2 fluxes were not observed. However, the Br_2 flux limit of detection was determined to be 6.5×10^7 molecules cm^{-2} s^{-1}. The method used to calculate this value assumed that there was no flux present on March 09 and 10, and thus likely is an overestimate of the limit of detection rather than an underestimate.

Still, the calculated limit of detection is smaller than the Br_2 fluxes calculated by Custard et al. [2017] ($0.69 – 12x10^8$ molecules cm^{-2} s^{-1}), and those that have been used in models [Lehrer et al., 2004; Piot and von Glasow, 2008; Piot and Glasow, 2010; Thomas et al., 2011; Toyota et al., 2014] ($9.0 x10^7 – 2.7x10^9$ molecules cm^{-2} s^{-1}) suggesting that measurements of the Br_2 flux would have been possible in other years. The lack of observations of fluxes that were significantly different from zero is likely due to a combination of underestimation of other sources of Br_2 in models, as suggested by chapter 6, and unusually low snowpack bromine production in 2016 which is was indicated by observations of low bromine concentrations [Swanson et al., 2017].

The fluxes calculated in chapter 5 show the feasibility of future calculations of Arctic halogen fluxes using the eddy covariance method. Future fluxes using the eddy covariance method in the Arctic should be attempted, as they could have a large impact on the field's understanding of the sources and sinks of halogens in the Arctic. Concurrent fluxes of chlorine and nitrogen species may yield significant insight to the episodic nature of Cl_2 production in the Arctic. Using CIMS, Kim et al. [2014] recently reported fluxes of $ClNO_2$ above the seawater, finding deposition to the ocean surface, rather than production. Their use of a time-of-flight (TOF) mass analyzer allowed for higher frequency and higher precision then the measurements described in chapter 5, which utilized a CIMS with a quadrupole mass analyzer. Increased frequency and precision would reduce uncertainties and decrease the flux limit of detection yielding better measurements of the flux. Even without use of a TOF mass analyzer, yielding lower limits of detection, future measurements of Br_2 and Cl_2 fluxes in the Arctic following the methods outlined in chapter 5 should be attempted given the likelihood that future years will have higher fluxes than 2016, given bromine concentrations observed in other years [Liao et al., 2012; Peterson et al., 2016; Swanson et al., 2017].

The fifth and sixth questions are addressed in chapter 6. The first vertical profile measurements of Br_2 and Cl_2 between 1 and 7 m above the snow surface showed results very different than expected. Vertical profiles of Br_2 show nearly no dependence on height, while the vertical profiles of Cl_2 show dependence on height. A one-dimensional model was used to investigate the expected evolution of Br_2 and Cl_2 above the snowpack surface, given the community's current understanding of vertical mixing, and the sources, sinks, and recycling of halogens in the Arctic. The one-dimensional model results are inconsistent with the measurements for Br_2, suggesting that significant uncertainties exist in our understanding of the sources and sinks of bromine chemistry in the Arctic. The Cl_2 measurements and modeling agreed well, suggesting that chlorine chemistry is well described by a snowpack Cl_2 source coupled with gas and aerosol multiphase recycling. In contrast similar processes cannot explain the observed vertical profiles of Br_2, suggesting that additional production or recycling mechanisms are necessary to understand bromine chemistry in the air close to (<7 m above) the snowpack surface.

We examined several areas of uncertainty using the one-dimensional model. These areas of uncertainty present several opportunities for future measurements which would increase our understanding of bromine sources, sinks, and recycling. First, further studies of the processes that control mixing and stratification in the Arctic are necessary. Modeling of stable boundary layers is difficult at best, and studies of its processes have been sparse. Second, the vertical profiles of aerosol Br^- should be obtained. The oxidation of aerosol Br^- to Br_2 is undoubtedly one of the most important processes for the vertical propagation of bromine chemistry. This conclusion has previously been supported by measurements of $BrO^\cdot$ transport being sustained on aerosols [Peterson et al., 2017]. One possible explanation for the inability of the one-dimensional model to reproduce the observed vertical profiles of Br_2 is variability of bromine recycling on and

production from aerosols with height above the snowpack. Recycling and production of bromine on aerosols is likely highly dependent on bromide concentration. However, no measurements of the vertical profile of bromide in Arctic aerosols has been reported. Height resolved measurements of aerosol halide content could be obtained by collecting simultaneous filter samples with inlets positioned at various heights. While it is likely that the profile varies diurnally, even the daily averaged data that would be yielded by this method would be a vast improvement over the current lack of measurements. Finally, despite the impact iodine may have on the speed and chain length of bromine recycling reaction, its potential impact on the vertical extent of bromine chemistry is dwarfed by other uncertainties in our understanding. However, iodine chemistry likely has a large impact on new particle formation [Sipilä et al., 2016], and model results suggest that iodine atom concentrations might be relatively high (up to 60 ppt). Therefore, measurements of iodine atom concentrations should be attempted, using the CIMS instrument during future field campaigns.

The work presented in this dissertation has made a significant advancement in understanding Arctic halogen chemistry. The presence of active iodine photochemistry in the Arctic is a recent discovery, with potential ramifications for atmospheric boundary layer oxidation and composition, and the impacts on pollutant fate and particle formation are likely significant. Additionally, the evidence presented that the community's understanding of bromine sources, sinks, and recycling is insufficient to explain the observed vertical profiles poses a substantial challenge for future work. As the Arctic continues to warm halogen chemistry may undergo significant changes. With warmer temperatures the snowpack will be below the $NaCl \cdot 2H_2O$ eutectic point (251 K) less often, likely bringing higher concentrations of chlorine species and lower concentrations of bromine. As sea ice covers less of the Arctic ocean, more sea salt aerosols

will be deposited into the snow, increasing the concentration of halides. Additionally, more oil and gas extraction (leading to anthropogenic emissions) may cause greater production of acidic aerosols, acidifying the snowpack and increasing halogen production. The multiphase chemistry of halogens in the Arctic is complex, and both warming, and more anthropogenic activity, will likely have profound effects on an already incompletely understood system.

REFERENCES

Abbatt, J. P. D., N. Oldridge, A. Symington, V. Chukalovskiy, R. D. McWhinney, S. Sjostedt, and R. A. Cox (2010), Release of gas-phase halogens by photolytic generation of OH in frozen halide-nitrate solutions: an active halogen formation mechanism?, *J. Phys. Chem. A*, *114*(23), 6527–6533.

Abbatt, J. P. D., J. L. Thomas, K. Abrahamsson, C. Boxe, A. Granfors, A. E. Jones, M. D. King, A. Saiz-Lopez, P. B. Shepson, J. Sodeau, D. W. Toohey, C. Toubin. R. von Glasow, S. N. Wren, and X. Yang (2012), Halogen activation via interactions with environmental ice and snow in the polar lower troposphere and other regions, *Atmos. Chem. Phys.*, *12*, 6237–6271, doi:10.5194/acp-12-6237-2012.

Adams, J. W., N. S. Holmes, and J. N. Crowley (2002), Uptake and reaction of HOBr on frozen and dry NaCl / NaBr surfaces between 253 and 233 K, *Atmos. Chem. Phys.*, *2*, 79–91.

Albert, M. R., and E. F. Shultz (2002), Snow and firn properties and air-snow transport processes at Summit, Greenland, *Atmos. Environ.*, *36*, 2789–2797, doi:10.1016/S1352-2310(02)00119-X.

Albert, M. R., A. M. Grannas, J. Bottenheim, P. B. Shepson, and F. E. Perron (2002), Processes and properties of snow-air transfer in the high Arctic with application to interstitial ozone at Alert, Canada, *Atmos. Environ.*, *36*(15–16), 2779–2787, doi:10.1016/S1352-2310(02)00118-8.

Allan, J. D., P. I. Williams, J. Najera, J. D. Whitehead, M. J. Flynn, J. W. Taylor, D. Liu, E. Darbyshire, L. J. Carpenter, R. Chance, and G. McFiggans (2014), Iodine observed in new particle formation events in the Arctic atmosphere during ACCACIA, *Atmos. Chem. Phys.*, *14*(21), 28949–28972, doi:10.5194/acpd-14-28949-2014.

Ammann, M., R. A. Cox, J. N. Crowley, M. E. Jenkin, A. Mellouki, M. J. Rossi, J. Troe, and T. J. Wallington (2013), Evaluated kinetic and photochemical data for atmospheric chemistry : Volume VI – heterogeneous reactions with liquid, *Atmos. Chem. Phys.*, 8045–8228, doi:10.5194/acp-13-8045-2013.

Anderson, P. S., and W. D. Neff (2008), Boundary layer physics over snow and ice, *Atmos. Chem. Phys.*, *8*(2001), 3563–3582.

Andreas, E. L. (2002), Parameterizing Scalar Transfer over Snow and Ice: A Review, *J. Hydrometeorol.*, 417–432.

Ashworth, S. H., B. J. Allan, and J. M. C. Plane (2002), High resolution spectroscopy of the OIO radical: Implications for the ozone-depleting potential of iodine, *Geophys. Res. Lett.*, *29*(10), 95-1-95–4, doi:10.1029/2001GL013851.

Atkinson, H. M., R.-J. Huang, R. Chance, H. K. Roscoe, C. Hughes, B. Davidson, A. Schönhardt, A. S. Mahajan, A. Saiz-Lopez, T. Hoffmann, and P. S. Liss (2012), Iodine emissions from the sea ice of the Weddell Sea, *Atmos. Chem. Phys.*, *12*(22), 11229–11244, doi:10.5194/acp-12-11229-2012.

Atkinson, R., D. L. Baulch, R. A. Cox, J. N. Crowley, R. F. Hampson, R. G. Hynes, M. E. Jenkin, M. J. Rossi, and J. Troe (2004), Evaluated kinetic and photochemical data for atmospheric chemistry: Volume I – gas phase reactions of O_x, HO_x, NO_x and SO_x species, *Atmos. Chem. Phys.*, *4*, 1461–1738, doi:10.5194/acp-4-1461-2004.

Atkinson, R., D. L. Baulch, R. A. Cox, J. N. Crowley, R. F. Hampson, R. G. Hynes, M. E. Jenkin, M. J. Rossi, and J. Troe (2007), Evaluated kinetic and photochemical data for atmospheric chemistry : Volume III – gas phase reactions of inorganic halogens, *Atmos. Chem. Phys.*, *7*, 981–1191.

Baldocchi, D. (2013), A brief history on eddy covariance flux measurements : A Personal Perspective, *FluxLetter Newsl. Fluxnet*, *5*(2).

Barrie, L. A., and U. Platt (1997), Arctic tropospheric chemistry: an overview, *Tellus, Ser. B Chem. Phys. Meteorol.*, *49B*.

Barrie, L. A., J. W. Bottenheim, R. C. Schnell, P. J. Crutzen, and R. A. Rasmussen (1988), Ozone destruction and photochemical reactions at polar sunrise in the lower Arctic atmosphere, *Nature*, *334*, 138–141.

Barrie, L. A., G. den Hartog, J. W. Bottenheim, and S. Landsberger (1989), Anthroprogenic aerosols and gases in the lower troposphere at Alert Canada in April 1986, *J. Atmos. Chem.*, *9*, 101–127.

Barrie, L. A., S. Li, D. L. Toom, S. Landsberger, and W. T. Sturges (1994), Lower tropospheric measurements of halogens , nitrates , and sulphur oxides during Polar Sunrise Experiment 1992, *J. Geophys. Res.*, *99*(94), 25453–25468.

Bartels-Rausch, T., H.-W. Jacobi, T. F. Kahan, J. L. Thomas, E. S. Thomson, J. P. D. Abbatt, M. Ammann, J. R. Blackford, H. Bluhm, C. Boxe, F. Domine, M. M. Frey, I. Gladich, M. I. Guzmán, D. Heger, Th. Huthwelker, P. Klán, W. F. Kuhs, M. H. Kuo, S. Maus, S. G. Moussa, V. F. McNeill, J. T. Newberg, J. B. C. Pettersson, M. Roeselová, and J. R. Sodeau (2014), A review of air-ice chemical and physical interactions (AICI): Liquids, quasi-liquids, and solids in snow, *Atmos. Chem. Phys.*, *14*(3), 1587–1633, doi:10.5194/acp-14-1587-2014.

Bauer, D., S. A. Ingham, S. A. Carl, G. K. Moortgat, and J. N. Crowley (1998), Ultraviolet-Visible Absorption Cross Sections of Gaseous HOI and Its Photolysis at 355 nm, *J. Phys. Chem. A*, *102*, 2857–2864.

Beckwith, R. C., T. X. Wang, and D. W. Margerum (1996), Equilibrium and Kinetics of Bromine Hydrolysis, *Inorg. Chem.*, *35*, 995–1000.

Berg, W. W., and P. D. Sperry (1983), Atmospheric Bromine in the Arctic, *J. Geophys. Res.*, *88*(C11), 6719–6736.

Bloss, W. J., M. Camredon, J. D. Lee, D. E. Heard, J. M. C. Plane, A. Saiz-Lopez, S. J. Bauguitte, R. A. Salmon, and A. E. Jones (2010), Coupling of HO_x, NO_x and halogen chemistry in the antarctic boundary layer, *Atmos. Chem. Phys.*, *10*, 10187–10209, doi:10.5194/acp-10-10187-2010.

Bongartz, A., J. Kames, F. Welter, and U. Schurath (1991), Near-UV Absorption Cross Sections and Trans/Cis Equilibrium of Nitrous Acid, *J. Phys. Chem.*, *95*, 1076–1082.

Bongartz, A., J. Kames, U. Schurath, C. George, P. Mirabel, and J. L. Ponche (1994), Experimental Determination of HONO Mass Accommodation Coefficients Using Two Different Techniques, *J. Atmos. Chem.*, *18*, 149.

Bottenheim, J. W., A. G. Gallant, and K. A. Brice (1986), Measurements of NO Y species and O 3 at 82° N latitude, *Geophys. Res. Lett.*, *13*(2), 113–116, doi:10.1029/GL013i002p00113.

Boudries, H., and J. W. Bottenheim (2000), CI and Br Atom Concentrations During a Surface Boundary Layer Ozone Depletion Event in the Canadian High Arctic, *Geophys. Res. Lett.*, *27*(4), 517–520.

Braban, C. F., J. W. Adams, D. Rodriguez, R. A. Cox, J. N. Crowley, and G. Schuster (2007), Heterogeneous reactions of HOI , ICl and IBr on sea salt and sea salt proxies, *Phys. Chem. Chem. Phys.*, *9*, 3136–3148, doi:10.1039/b700829e.

Brost, R. A., and J. C. Wyngaard (1978), A model study of the stably stratified planetary boundary layer, *J. Atmos. Sci.*, *35*, 1427–1440.

Burba, G. (2005), *Eddy Covariance Method*, edited by J. Goodding, J. Kathilankal, and I. Begashaw, LI-COR Biosciences, Lincoln, Nebraska.

Burkholder, J. B. (1993), Ultraviolet Absorption Spectrum of HOCl, *J. Geophys. Res.*, *98*, 2963–2974.

Burkholder, J. B., R. K. Talukdar, A. R. Ravishankara, and S. Solomon (1993), Temperature Dependence of the HNO_3 UV Absorption Cross Sections, *J. Geophys. Res.*, *98*, 22937–22948.

Burkholder, J. B., S. P. Sander, J. P. D. Abbatt, J. R. Barker, R. E. Huie, C. E. Kolb, M. J. Kurylo, V. L. Orkin, D. M. Wilmouth, and P. H. Wine (2015), Chemical Kinetics and Photochemical Data for use in Atmospheric Studies, Evaluation No. 18, *NASA, JPL*, (18).

Calvert, J. G., and S. E. Lindberg (2004), Potential influence of iodine-containing compounds on the chemistry of the troposphere in the polar spring. I. Ozone depletion, *Atmos. Environ.*, *38*(30), 5087–5104, doi:10.1016/j.atmosenv.2004.05.049.

Campbell, K., C. J. Mundy, M. Gosselin, J. C. Landy, A. Delaforge, and S. Rysgaard (2017), Net community prodction in the bottomom of first-year sea ice over the Arctic spring bloom, *J. Geophys. Res.*, 8971–8978, doi:10.1002/2017GL074602.

Cao, L., H. Sihler, U. Platt, and E. Gutheil (2014), Numerical analysis of the chemical kinetic mechanisms of ozone depletion and halogen release in the polar troposphere, *Atmos. Chem. Phys.*, *14*, 3771–3787, doi:10.5194/acp-14-3771-2014.

Carpenter, L. J., S. M. MacDonald, M. D. Shaw, R. Kumar, R. W. Saunders, R. Parthipan, J. Wilson, and J. M. C. Plane (2013), Atmospheric iodine levels influenced by sea surface emissions of inorganic iodine, *Nat. Geosci.*, *6*(2), 108–111, doi:10.1038/ngeo1687.

Custard, K. D., C. R. Thompson, K. A. Pratt, P. B. Shepson, J. Liao, L. G. Huey, and J. J. Orlando (2015), The NO_x dependence of bromine chemistry in the Arctic, *Atmos. Chem. Phys.*, 10799–10809, doi:10.5194/acp-15-10799-2015.

Custard, K. D., K. A. Pratt, S. Wang, and P. B. Shepson (2016), Constraints on Arctic atmospheric chlorine production through measurements and simulations of Cl_2 and ClO, *Environ. Sci. Technol.*, *50*, acs.est.6b03909, doi:10.1021/acs.est.6b03909.

Custard, K. D., A. R. W. Raso, P. B. Shepson, R. M. Staebler, and K. A. Pratt (2017), Production and Release of Molecular Bromine and Chlorine from the Arctic Coastal Snowpack, *ACS Earth Sp. Chem.*, *1*(3), doi:10.1021/acsearthspacechem.7b00014.

Van Dam, B., D. Helmig, C. Toro, P. Doskey, L. Kramer, K. Murray, L. Ganzeveld, and B. Seok (2015), Dynamics of ozone and nitrogen oxides at Summit, Greenland: I. Multi-year observations in the snowpack, *Atmos. Environ.*, *123*, 268–284, doi:10.1016/j.atmosenv.2015.09.060.

Dassau, T. M., P. B. Shepson, J. W. Bottenheim, and K. M. Ford (2004), Peroxyacetyl nitrate photochemistry and interactions with the Arctic surface, *J. Geophys. Res. Atmos.*, *109*(18), doi:10.1029/2004JD004562.

Deiber, G., C. George, and S. Le Calv (2004), Uptake study of $ClONO_2$ and $BrONO_2$ by Halide containing droplets, *Atmos. Chem. Phys.*, 1291–1299.

DeMore, W. B., S. P. Sander, D. M. Golden, R. F. Hampson, M. J. Kurylo, C. J. Howard, A. R. Ravishankara, C. E. Kolb, and M. J. Molina (1997), *Chemical Kinetics and Photochemical Data for Use in Stratospheric Modeling, Evaluation Number 12*, Pasadena, California.

Domine, F., J. Bock, D. Voisin, and D. J. Donaldson (2013), Can we model snow photochemistry? Problems with the current approaches., *J. Phys. Chem. A*, *117*(23), 4733–49, doi:10.1021/jp3123314.

Donahue, N. M., J. G. Anderson, and K. L. Demerjian (1998), New Rate Constants for Ten OH Alkane Reactions from 300 to 400 K : An Assessment of Accuracy, *J. Phys. Chem. A*, *102*, 3121–3126.

Duce, R. A., J. W. Winchester, and T. W. Van Nahl (1965), Iodine, Bromine, and Chlorine in the Hawaiian Marine Atmosphere, *J. Geophys. Res.*, *70*(8).

Duce, R. A., J. W. Winchester, T. W. Van Nahl, R. A. Duce, J. W. Winchester, and T. W. Van Nahl (1966), Iodine , bromine , and chlorine in winter aerosols and snow from Barrow , Alaska, *Tellus*, *18*(2–3), 238–248, doi:10.3402/tellusa.v18i2-3.9630.

Duce, R. A., W. H. Zoller, and J. L. Moyers (1973), Particulate and gaseous halogens in the Antarctic atmosphere, *J. Geophys. Res.*, *78*(33), 7802–7811.

Dunlea, E. J., and A. R. Ravishankara (2004), Kinetic studies of the reactions of $O(^1D)$ with several atmospheric molecules, *Phys. Chem. Chem. Phys.*, *6*, 2152–2161.

Dyer, A. J. (1974), A Review of Flux-Profile Relationships, *Boundary-Layer Meteorol.*, *7*, 363–372.

Eberhard, J., and C. J. Howard (1996), Temperature Dependent Kinetics Studies of the Reactions of $C_2H_5O_2$ and n-$C_3H_7O_2$ Radicals with NO, *Int. J. Chem. Kinet.*, *28*, 731–740.

Fan, S.-M., and D. J. Jacob (1992), Surface ozone depletion in the Arctic spring sustained by bromine reactions on aerosols, *Nature*, *360*, 522–524.

Farman, J. C., B. G. Gardiner, and J. D. Shanklin (1985), Large losses of total ozone in Antarctica reveal seasonal ClO_x/NO_x interaction, *Nature*, *315*(6016), 207–210, doi:10.1038/315207a0.

Finlayson-Pitts, B. J., and J. N. J. Pitts (2000), *Chemistry of the Upper and Lower Atmosphere*, Academic Press, London.

Forte, E., H. Hippler, and H. Van Den Bergh (1981), INO thermodynamic properties and ultraviolet spectrum, *Int. J. Chem. Kinet.*, *13*(12), 1227–1233, doi:10.1002/kin.550131203.

Foster, K. L., R. A. Plastridge, J. W. Bottenheim, P. B. Shepson, B. J. Finlayson-Pitts, and C. W. Spicer (2001), The role of Br_2 and BrCl in surface ozone destruction at polar sunrise, *Science (80-.).*, *291*, 471–474.

France, J. L., H. J. Reay, M. D. King, D. Voisin, H. W. Jacobi, F. Domine, H. J. Beine, C. Anastasio, and A. Macarthur (2012), Hydroxyl radical and NO_x production rates , black carbon concentrations and light-absorbing impurities in snow from field measurements of light penetration and nadir reflectivity of onshore and offshore coastal Alaskan snow, *J. Geophys. Res.*, *117*(D14), doi:10.1029/2011JD016639.

Freud, E., R. Krejci, P. Tunved, R. Leaitch, Q. T. Nguyen, and A. Massling (2017), Pan-Arctic aerosol number size distributions : seasonality and transport patterns, *Atmos. Chem. Phys.*, 8101–8128.

Frieß, U., T. Wagner, I. Pundt, K. Pfeilsticker, and U. Platt (2001), Spectroscopic measurements of tropospheric iodine oxide at Neumayer Station, Antarctica, *Geophys. Res. Lett.*, *28*(10), 1941–1944, doi:10.1029/2000GL012784.

Frieß, U., T. Deutschmann, B. S. Gilfedder, R. Weller, and U. Platt (2010), Iodine monoxide in the Antarctic snowpack, *Atmos. Chem. Phys.*, *10*(5), 2439–2456.

Frieß, U., H. Sihler, R. Sander, D. Phler, S. Yilmaz, and U. Platt (2011), The vertical distribution of BrO and aerosols in the Arctic: Measurements by active and passive differential optical absorption spectroscopy, *J. Geophys. Res. Atmos.*, *116*(18), 1–19, doi:10.1029/2011JD015938.

Gálvez, O., M. T. Baeza-romero, M. Sanz, and A. Saiz-Lopez (2016), Photolysis of frozen iodate salts as a source of active iodine in the polar environment, *Atmos. Chem. Phys.*, *16*, 12703–12713, doi:10.5194/acp-16-12703-2016.

George, I. J., and C. Anastasio (2007), Release of gaseous bromine from the photolysis of nitrate and hydrogen peroxide in simulated sea-salt solutions, *Atmos. Environ.*, *41*(3), 543–553, doi:10.1016/j.atmosenv.2006.08.022.

Ghosh, B., D. K. Papanastasiou, R. K. Talukdar, J. M. Roberts, and J. B. Burkholder (2012), Nitryl Chloride ($ClNO_2$): UV / Vis Absorption Spectrum between 210 and 296 K and $O(^3P)$ Quantum Yield at 193 and 248 nm, *J. Phys. Chem. A*, *116*, 5796–5805.

Gilfedder, B. S., M. Petri, and H. Biester (2007a), Iodine and bromine speciation in snow and the effect of orographically induced precipitation, *Atmos. Chem. Phys.*, *7*(10), 2661–2669, doi:10.5194/acp-7-2661-2007.

Gilfedder, B. S., M. Petri, and H. Biester (2007b), Iodine speciation in rain and snow: Implications for the atmospheric iodine sink., *J. Geophys. Res.*, *112*(D7), D07301, doi:10.1029/2006JD007356.

Gilfedder, B. S., S. C. Lai, M. Petri, and T. Hoffmann (2008), Iodine speciation in rain, snow and aerosols, *Atmos. Chem. Phys.*, *8*, 6069–6084.

Gómez Martín, J. C., P. Spietz, and J. P. Burrows (2005), Spectroscopic studies of the I_2/O_3 photochemistry, *J. Photochem. Photobiol. A Chem.*, *176*(1–3), 15–38, doi:10.1016/j.jphotochem.2005.09.024.

Grachev, A. A., E. L. Andreas, C. W. Fairall, P. S. Guest, and P. O. G. Persson (2007), SHEBA flux-profile relationships in the stable atmospheric boundary layer, *Boundary-Layer Meteorol.*, *124*, 315–333, doi:10.1007/s10546-007-9177-6.

Graham, R. A., and H. S. Johnston (1978), The Photochemistry of NO_3 and the Kinetics of the N_2O_5 - O_3 System, *J. Phys. Chem.*, *82*(3), 254–268.

Guenther, A., C. Nicholas, R. Fall, L. Klinger, W. A. Mckay, and B. Scholes (1995), A global model of natural volatile organic compound emissions s Raja the balance Triangle changes in the atmospheric accumulation rates of greenhouse Triangle Several inventories of natural and Exposure Assessment global scales have been two classes Fores, *J. Geophys. Res.*, *100*(94), 8873–8892.

Halfacre, J. W., T. N. Knepp, P. B. Shepson, C. R. Thompson, K. A. Pratt, B. Li, P. K. Peterson, S. J. Walsh, W. R. Simpson, P. A. Matrai, J. W. Bottenheim, S. Netcheva, D. K. Perovich, and A. Richter (2014), Temporal and spatial characteristics of ozone depletion events from measurements in the Arctic, *Atmos. Chem. Phys.*, *14*(10), 4875–4894, doi:10.5194/acp-14-4875-2014.

Halfacre, J. W., P. B. Shepson, and K. A. Pratt (2018), pH- Dependent Production of Molecular Chlorine, Bromine, and Iodine from Frozen Saline Surfaces, *Atmos. Chem. Phys. Discuss.*

Harris, S. J., and J. A. Kerr (1988), Relative rate measurements of some reactions of hydroxyl radicals with alkanes studied under atmospheric conditions, *Int. J. Chem. Kinet.*, *20*(12), 939–955, doi:10.1002/kin.550201203.

Harwood, M. H., J. B. Burkholder, and A. R. Ravishankara (1998), Photo- dissociation of $BrONO_2$ and N_2O_5: Quantum Yields for NO_3 Production at 284, 308, and 352.5 nm, *J. Phys. Chem. A*, *102*(1309–1317).

Hausmann, M., and U. Platt (1994), measurement of bromine oxide and ozone in the high Arctic during Polar Sunrise Experiment 1992, *J. Geophys. Res.*, *99*(2), 25399, doi:10.1029/94JD01314.

Heumann, K. G., M. Gall, and H. Weiss (1987), Geochemical investigations to explain iodine-overabundances in Antarctic meteorites, *Geochim. Cosmochim. Acta*, *51*, 2541–2547.

Hewson, J. C., and M. Bollig (1996), Reduced mechanisms for NO_x emissions from hydrocarbon diffusion flames, *Twenty-Sixth Symp. Combust. / Combust. Inst.*, (2), 2171–2179.

Holmes, N. S., J. W. Adams, and J. N. Crowley (2001), Uptake and reaction of HOI and IONO on frozen and dry NaCl / NaBr surfaces and H2SO4, *Phys. Chem. Chem. Phys.*, 1679–1687.

Hong, S.-Y., and H.-L. Pan (1996), Nonlocal Boundary Layer Vertical Diffusion in a Medium-Range Forecast Model, *Mon. Weather Rev.*, *124*, 2322–2339.

Honrath, R. E., M. C. Peterson, S. Guo, J. E. Dibb, P. B. Shepson, and B. Campbell (1999), Evidence of NO_x Production Within or Upon Ice Particles in the Greenland Snowpack, *Geophys. Res. Lett.*, *26*(6), 695–698.

Hooshiyar, P. A., and H. Niki (1995), Rate Constants for the Gas-Phse Reactions of Cl-atoms with C2-C8 Alkanes at T = 296 K, *Int. J. Chem. Kinet.*, *27*, 1197–1206.

Howell, J. F. (1995), Identifying Sudden Changes in Data, *Mon. Weather Rev.*, *123*, 1207–1212.

Hu, J. H., Q. Shi, P. Davidovits, D. R. Worsnop, M. S. Zahniser, and C. E. Kolb (1995), Reactive Uptake of $Cl_{2(g)}$ and $Br_{2(g)}$ by Aqueous Surfaces as a Function of Br^- and I^- Ion Concentration: The Effect of Chemical Reaction at the Interface, *J. Phys. Chem*, *2*(4), 8768–8776.

Huff, A. K., and J. P. D. Abbatt (2002), Kinetics and Product Yields in the Heterogeneous Reactions of HOBr with Ice Surfaces Containing NaBr and NaCl, *J. Phys. Chem. A*, *106*, 5279–5287.

Impey, G. A., P. B. Shepson, D. R. Hastie, and L. A. Bartie (1997), Measurement technique for the determination of photolyzable chlorine and bromine in the atmosphere, *J. Geophys. Res.*, *102*, 15999–16004.

Ingham, T., D. Bauer, J. Landgraf, and J. N. Crowley (1998), Ultraviolet-Visible Absorption Cross Sections of Gaseous HOBr, *J. Phys. Chem. A*, *102*, 3293–3298.

Jacob, D. J. (2000), Heterogeneous chemistry and tropospheric ozone, *Atmos. Environ.*, *34*(12–14), 2131–2159, doi:10.1016/S1352-2310(99)00462-8.

Jobson, B. T., H. Niki, Y. Yokouchi, J. W. Bottenheim, F. Hopper, and R. Leaitch (1994), Measurements of C2 -C6 hydrocarbons during the Polar Sunrise1992 Experiment: Evidence for Cl atom and Br atom chemistry, *J. Geophys. Res.*, *99*(D12), 25355, doi:10.1029/94JD01243.

Jones, A. E., P. S. Anderson, M. Begoin, N. Brough, M. A. Hutterli, G. J. Marshall, A. Richter, H. K. Roscoe, and E. W. Wolff (2009), BrO , blizzards , and drivers of polar tropospheric ozone depletion events, *Atmos. Chem. Phys.*, *9*(2), 4639–4652, doi:10.5194/acpd-9-8903-2009.

Kaimal, J. C., and J. J. Finnigan (1994), *Atmospheric Boundary Layer Flows: Their Structure and Measurement.*, Oxford University Press.

Kamboures, M. A., J. C. Hansen, and J. S. Francisco (2002), A study of the kinetics and mechanisms involved in the atmospheric degradation of bromoform by atomic chlorine, *Chem. Phys. Lett.*, *353*, 335–344.

Keil, A. D., and P. B. Shepson (2006), Chlorine and bromine atom ratios in the springtime Arctic troposphere as determined from measurements of halogenated volatile organic compounds, *J. Geophys. Res. Atmos.*, *111*(17), 1–11, doi:10.1029/2006JD007119.

Keith, S. A., A. P. Kerswell, and S. R. Connolly (2014), Global diversity of marine macroalgae : environmental conditions explain less variation in the tropics, *Glob. Ecol. Biogeogr.*, *23*, 517–529, doi:10.1111/geb.12132.

Kim, K., A. Yabushita, M. Okumura, A. Saiz-Lopez, A. Carlos, C. S. Blaszczak-Boxe, D. W. Min, H. Yoon, and W. Choi (2016), Production of molecular iodine and triiodide in the frozen solution of iodide: implication for polar atmosphere, *Environ. Sci. Technol.*, *50*(3), 1280–1287.

Kim, M. J., D. K. Farmer, and T. H. Bertram (2014), A controlling role for the air − sea interface in the chemical processing of reactive nitrogen in the coastal marine boundary layer, *PNAS*, *111*(11), doi:10.1073/pnas.1318694111.

King, M. D., and W. R. Simpson (2001), Extinction of UV radiation in Arctic snow at Alert, Canada, *J. Geophys. Res.*, *106*(D12), 12499–12507.

Kirchner, F., and W. R. Stockwell (1996), Effect of peroxy radical reactions on the predicted concentrations of ozone, nitrogenous compounds and radicals, *J. Geophys. Res. - Atmos.*, *101*(D15), 21007–21022.

Komabayasi, M. (1962), Enrichment of inorganic ions with increasing atomic weight in aerosol, rainwater, and snow in comparison with sea water, *J. Meteorol. Soc. Japan*, *40*, 25–38.

Koop, T., A. Kapilashrami, L. T. Molina, and M. J. Molina (2000), Phase transitions of sea-salt/water mixtures at low temperatures: Implications for ozone chemistry in the polar marine boundary layer, *J. Geophys. Res.*, *105*(D21), 393–402.

Kristensen, L., J. Mann, S. P. Oncley, and J. C. Wyngaard (1997), How close is close enough when measuring scalar fluxes with displaced sensors?, *J. Atmos. Ocean. Technol.*, *14*(4), 814–821, doi:10.1175/1520-0426(1997)014<0814:HCICEW>2.0.CO;2.

Laszlo, B., M. J. Kurylo, and R. E. Huie (1995), Absorption Cros Sections, Kinetics of Formation, and Self-Reaction of the IO Radical Produced via the Laser Photolysis of $N_2O/I_2/N_2$ Mixtures, *J. Phys. Chem.*, *99*, 11701–11707.

Lee, X., and A. Black (1994), Relating eddy correlation sensible heat flux to horizontal sensor separation in the unstable atmospheric surface layer, *J. Geophys. Res.*, *99*, 18545–18553.

Lehrer, E., G. Hönninger, and U. Platt (2004), A one dimensional model study of the mechanism of halogen liberation and vertical transport in the polar troposphere, *Atmos. Chem. Phys.*, *4*, 2427–2440, doi:10.5194/acp-4-2427-2004.

Li, S., Y. Yokouchi, L. A. Barrie, K. Muthuramu, P. B. Shepson, J. W. Bottenheim, W. T. Sturges, and S. Landsberger (1994), Organic and inorganic bromine compounds and their composition in the Arctic troposphere during polar sunrise increased gradually from about m -3 during the dark period m -3 during the light period , with a marked peak of 120 ng (Br) m -3 corresponding t, *Atmos. Chem. Phys.*, *99*.

Liao, J., H. Sihler, L. G. Huey, J. A. Neuman, D. J. Tanner, U. Frieß, U. Platt, F. M. Flocke, J. J. Orlando, P. B. Shepson, H. J. Beine, A. J. Weinheimer, S. J. Sjostedt, J. B. Nowak, D. J. Knapp, R. M Staebler, W. Zheng, R. Sander, S. R. Hall, and K. Ullmann (2011), A comparison of Arctic BrO measurements by chemical ionization mass spectrometry and long path-differential optical absorption spectroscopy, *J. Geophys. Res.*, *116*(D14), D00R02, doi:10.1029/2010JD014788.

Liao, J., L. G. Huey, D. J. Huey, D. J. Tanner, F. M. Flocke, J. J. Orlando, J. A. Neuman, J. B. Nowak, A. J. Weinheimer, S. R. Hall, J. N. Smith, A. Fried, R. M. Staebler, Y. Wang, J.-H. Koo, C. A. Cantrell, P. Weibring, J. Walega, D. J. Knapp, P. B. Shepson, and C. R. Stephens (2012), Observations of inorganic bromine (HOBr, BrO, and Br_2) speciation at Barrow, Alaska, in spring 2009, *J. Geophys. Res.*, *117*(D14), D00R16, doi:10.1029/2011JD016641.

Liao, J., L. G. Huey, Z. Liu, D. J. Tanner, C. A. Cantrell, J. J. Orlando, F. M. Flocke, P. B. Shepson, A. J. Weinheimer, S. R. Hall, K. Ullmann, H. J. Beine, Y. Wang, E. D. Ingall, C. R. Stephens, R. S. Hornbrook, E. C. Apel, D. Riemer, A. Fried, R. L. Maudlin III, J. N. Smith, R. M. Staebler, J. A. Neuman, and J. B. Nowak (2014), High levels of molecular chlorine in the Arctic atmosphere, *Nat. Geosci.*, *7*(2), 91–94, doi:10.1038/ngeo2046.

Lightfoot, P. D., R. A. Cox, J. N. Crowley, M. Destriau, G. D. Hayman, M. E. Jenkin, G. K. Moortgat, and F. Zabel (1992), Organic peroxy radicals: Kinetics, spectroscopy and tropospheric chemistry, *Atmos. Environ.*, *26*(10), 1805–1961.

Lin, X., M. Trainer, and S. C. Liu (1988), On the Nonlinearity of the Tropospheric Ozone Production, *J. Geophys. Res.*, *93*(88), 879–888.

Lurmann, F. W., A. C. Lloyd, and R. Atkinson (1986), A chemical mechanism for use in long-range transport/acid deposition computer modeling, *J. Geophys. Res. - Atmos.*, *91*(D10), 905–936, doi:10.1029/JD091iD10p10905.

Macdonald, R. W., L. A. Barrie, T. F. Bidleman, M. L. Diamond, D. J. Gregor, R. G. Semkin, W. M. J. Strachan, Y. F. Li, F. Wania, M. Alaee, L. B, Alexeeva, S. M. Backus, R. Bailey, J. M. Bewers, C. Gobeil, C. J. Halsall, T. Harner, J. T. Hoff, L. M. M. Jantunen, W. L. Lockhart, D. Mackay, D. C. G. Muir, J. Pudykeiwicz, K. J. Reimer, J. N. Smith, G. A. Stern, W. H. Schroeder, R. Wagemann, and M. B. Yunker (2000), Contaminants in the Canadian Arctic : 5 years of progress in understanding sources , occurrence and pathways, *Sci. Total Environ.*, *254*, 93–234.

Mahajan, A. S., M. Shaw, H. Oetjen, K. E. Hornsby, L. J. Carpenter, L. Kaleschke, X. Tian-Kunze, J. D. Lee, S. J. Moller, P. Edwards, R. Commane, T. Ingham, D. E. Heard, and J. M. C. Plane (2010), Evidence of reactive iodine chemistry in the Arctic boundary layer, *J. Geophys. Res.*, *115*(D20), D20303, doi:10.1029/2009JD013665.

Mahrt, L. (1999), Stratified atmospheric boundary layers, *Boundary-Layer Meteorol.*, (May 1998), 375–396.

Maric, D., J. P. Burrows, and G. K. Moortgat (1994), A study of the UV-visible spectra of Br_2 and BrCl, *J. Photochem. Photobiol. A Chem.*, *83*, 179–192.

Martinez, R. D., A. A. Buitrago, N. W. Howell, C. H. Hearn, and J. A. Joens (1992), The Near U. V. Absorption Spectra of Several Aliphatic Aldehydes and Ketones at 300 K, *Atmos. Environ.*, *26A*, 785–792.

Massman, W. J., and A. Ibrom (2008), Attenuation of concentration fluctuations of water vapor and other trace gases in turbulent tube flow, *Atmos. Chem. Phys.*, *8*, 6245–6259, doi:10.5194/acpd-8-9819-2008.

Mauder, M., M. Cuntz, C. Drüe, A. Graf, C. Rebmann, H. Peter, M. Schmidt, and R. Steinbrecher (2013), A strategy for quality and uncertainty assessment of long-term eddy-covariance measurements, *Agric. For. Meteorol.*, *169*, 122–135, doi:10.1016/j.agrformet.2012.09.006.

Mazzola, M., F. Tampieri, A. P. Viola, C. Lanconelli, and T. Choi (2016), Stable boundary layer vertical scales in the Arctic : observations and analysis at Ny Alesund , Svalbard, *Q. J. R. Meteorol. Soc.*, (April), 1250–1258, doi:10.1002/qj.2727.

McConnell, J. C., G. S. Henderson, L. A. Barrie, J. W. Bottenheim, H. Niki, C. H. Langford, and E. M. J. Templeton (1992), Photochemical bromine production implicated in Arctic boundary-layer ozone depletion, *Nature*, *355*, 150–152.

McFiggans, G. (2002), Active chlorine release from marine aerosols: Roles for reactive iodine and nitrogen species, *J. Geophys. Res.*, *107*(D15), 4271, doi:10.1029/2001JD000383.

McFiggans, G., H. Coe, R. Burgess, J. Allan, M. Cubison, M. R. Alfarra, R. Saunders, A. Saiz-Lopez, J. M. C. Plane, D. J. Wevill, L. J. Carpenter, A. R. Rickard, and P. S. Monks (2004), Direct evidence for coastal iodine particles from Laminaria macroalgae – linkage to emissions of molecular iodine, *Atmos. Chem. Phys. Atmos. Chem. Phys.*, *4*(2), 701–713, doi:10.5194/acp-4-701-2004.

Mcnamara, S. M., A. R. W. Raso, S. Wang, S. Thanekar, J. D. Fuentes, P. B. Shepson, and K. A. Pratt (n.d.), Observations of Nitrogen Oxide-Influenced Chlorine Chemistry in the Alaskan Arctic, *In Prep.*

Michalowski, B. A., J. S. Francisco, S. M. Li, L. A. Barrie, J. W. Bottenheim, and P. B. Shepson (2000), A computer model study of multiphase chemistry in the Arctic boundary layer during polar sunrise, *J. Geophys. Res. Atmos.*, *105*(D12), 15131–15145.

Molina, L. T., and M. J. Molina (1986), Absolute Absorption Cross Sections of Ozone in the 185-350 nm Wavelength Range, *J. Geophys. Res.*, *91*, 14501–14508.

Molina, L. T., S. Madronich, J. S. Gaffney, E. Apel, B. De Foy, J. Fast, R. Ferrare, S. Herndon, and J. L. Jimenez (2010), An overview of the MILAGRO 2006 Campaign : Mexico City emissions and their transport and transformation, *Atmos. Chem. Phys.*, *10*, 8697–8760, doi:10.5194/acp-10-8697-2010.

Molina, M. J., and F. S. Rowland (1974), Stratospheric sink for chlorofluoromethanes: chlorine atomc-atalysed destruction of ozone, *Nature*, *249*(5460), 810–812, doi:10.1038/249810a0.

Mossinger, J. C., D. M. Rowley, and R. A. Cox (2002), The UV-visible absorption cross-sections of $IONO_2$, *Atmos. Chem. Phys.*, (2), 227–234.

Neuman, J. A., J. B. Nowak, L. G. Huey, J. B. Burkholder, J. E. Dibb, J. S. Holloway, J. Liao, J. Peischl, J. M. Roberts, T. B. Ryerson, E. Scheuer, H. Stark, R. E. Stickel, D. J. Tanner, and Weinheimer (2010), Bromine measurements in ozone depleted air over the Arctic Ocean, *Atmos. Chem. Phys.*, *10*(14), 6503–6514, doi:10.5194/acp-10-6503-2010.

Nicovich, J. M., and P. H. Wine (1990), Kinetics of the reactions of $O(^3P)$ and $Cl(^2P)$ with HBr and Br_2, *Int. J. Chem. Kinet.*, *22*(4), 379–397, doi:10.1002/kin.550220406.

O'Dowd, C. D., G. McFiggans, D. J. Creasey, L. Pirjola, C. Hoell, M. H. Smith, B. J. Allan, J. M. C. Plane, D. E. Heard, J. D. Lee, M. J. Pilling, and M. Kulmala (1999), On the photochemical production of new particles in the coastal boundary layer, *Geophys. Res. Lett.*, *26*(12), 1707, doi:10.1029/1999GL900335.

O'Dowd, C. D., J. L. Jimenez, R. Bahreini, R. C. Flagan, J. H. Seinfeld, K. Hameri, L. Pirjola, M. Kulmala, S. G. Jennings, and T. Hoffmann (2002), Marine aerosol formation from biogenic iodine emissions, *Nature*, *417*, 632–636, doi:10.1038/nature00773.1.2.3.4.5.6.7.8.9.10.

Oldridge, N. W., and J. P. D. Abbatt (2011), Formation of gas-phase bromine from interaction of ozone with frozen and liquid NaCl/NaBr solutions: Quantitative separation of surficial chemistry from bulk-phase reaction, *J. Phys. Chem. A*, *115*(12), 2590–2598, doi:10.1021/jp200074u.

Oltmans, S. J. (1981), Surface Ozone Measurements in Clean Air, *J. Geophys. Res.*, *86*(C2), 1174–1180.

Oltmans, S. J., and W. D. Komhyr (1986), Surface ozone distributions and variations from 1973–1984: Measurements at the NOAA Geophysical Monitoring for Climatic Change Baseline Observatories, *J. Geophys. Res.*, *91*(D4), 5229, doi:10.1029/JD091iD04p05229.

Pechtl, S., G. Schmitz, and R. Von Glasow (2007), Modelling iodide – iodate speciation in atmospheric aerosol : Contributions of inorganic and organic iodine chemistry, *Atmos. Chem. Phys.*, (2005), 1381–1393.

Peterson, M. C., and R. E. Honrath (2001), Observations of Rapid Photochemical Destruction of Ozone in Snowpack Interstitial Air, *Geophys. Res. Lett.*, *28*(3), 511–514.

Peterson, P. K., W. R. Simpson, K. A. Pratt, P. B. Shepson, U. Frieß, J. Zielcke, U. Platt, S. J. Walsh, and S. V. Nghiem (2015), Dependence of the vertical distribution of bromine monoxide in the lower troposphere on meteorological factors such as wind speed and stability, *Atmos. Chem. Phys.*, *15*, 2119–2137, doi:10.5194/acp-15-2119-2015.

Peterson, P. K., W. R. Simpson, and S. V Nghiem (2016), Variability of bromine monoxide at Barrow , Alaska , over four halogen activation (March – May) seasons and at two on-ice locations, *J. Geophys. Res.*, 1381–1396, doi:10.1002/2015JD024094.Received.

Peterson, P. K., D. Pöhler, H. Sihler, J. Zielcke, S. General, U. Frieß, U. Platt, W. R. Simpson, S. V. Nghiem, P. B. Shepson, B. H. Stirm, S. Dhaniyala, T. Wagner, D. R. Caulton, J. D. Fuentes, and K. A. Pratt (2017), Observations of bromine monoxide transport in the Arctic sustained on aerosol particles, *Atmos. Chem. Phys.*, 7567–7579.

Piot, M., and R. von Glasow (2008), The potential importance of frost flowers , recycling on snow , and open leads for ozone depletion events, *Atmos. Chem. Phys.*, *8*, 2437–2467, doi:10.5194/acp-8-2437-2008.

Piot, M., and R. Von Glasow (2010), Modelling the multiphase near-surface chemistry related to ozone depletions in polar spring, *J. Atmos. Chem.*, *64*(2–3), 77–105, doi:10.1007/s10874-010-9170-1.

Platt, U., and G. Honniger (2003), The role of halogen species in the troposphere, *Chemosphere*, *52*, 325–338, doi:10.1016/S0045-6535(03)00216-9.

Pratt, K. A., K. D. Custard, P. B. Shepson, T. A. Douglas, D. Pöhler, S. General, J. Zielcke, W. R. Simpson, U. Platt, D. J. Tanner, L. G. Huey, M. Carlsen, and B. H. Stirm (2013), Photochemical production of molecular bromine in Arctic surface snowpacks, *Nat. Geosci.*, *6*(5), 351–356, doi:10.1038/ngeo1779.

Quinn, P. K., T. L. Miller, T. S. Bates, and G. E. Shaw (2002), A 3-year record of simultaneously measured aerosol chemical and optical properties at Barrow , Alaska, *J. Geophys. Res.*, *107*(D11).

Quinn, P. K., G. Shaw, E. Andrews, E. G. Dutton, T. Ruoho-Airola, and S. L. Gong (2007), Arctic haze: Current trends and knowledge gaps, *Tellus, Ser. B Chem. Phys. Meteorol.*, *59*(1), 99–114, doi:10.1111/j.1600-0889.2006.00238.x.

Quinn, P. K., T. S. Bates, K. Schulz, and G. E. Shaw (2009), Decadal trends in aerosol chemical composition at Barrow, AK: 1976–2008, *Atmos. Chem. Phys. Discuss.*, *9*(5), 18727–18743, doi:10.5194/acpd-9-18727-2009.

Rahn, K. A., and R. D. Borys (1977), The Asian source of Arctic haze bands, *Nature*, *268*, 713–715.

Rankin, A. M., E. W. Wolff, and S. Martin (2002), Frost flowers : Implications for tropospheric chemistry and ice core interpretation, *J. Geophys. Res.*, *107*, doi:10.1029/2002JD002492.

Rannik, Ü., O. Peltola, and I. Mammarella (2016), Random uncertainties of flux measurements by the eddy covariance technique, *Atmos. Meas. Tech. Discuss.*, *4*(February), 1–31, doi:10.5194/amt-2016-31.

Raso, A. R. W., K. D. Custard, N. W. May, D. J. Tanner, M. K. Newburn, L. Walker, R. J. Moore, L. G. Huey, L. M. Alexander, P. B. Shepson, and K. A. Pratt (2017), Active Molecular Iodine Photochemistry in the Arctic, *Proc. Natl. Acad. Sci. U. S. A.*, *114*(38), 10053–10058.

Ravishankara, A. R., G. J. Smith, and D. D. Davis (1988), A kinetics study of the reaction of Cl with NO_2, *Int. J. Chem. Kinet.*, *20*(10), 811–814, doi:10.1002/kin.550201005.

Roscoe, H. K., A. E. Jones, N. Brough, R. Weller, A. Saiz-Lopez, A. S. Mahajan, A. Schoenhardt, J. P. Burrows, and Z. L. Fleming (2015), Particles and iodine compounds in coastal Antarctica, *J. Geophys. Res. Atmos.*, 7144–7156, doi:10.1002/2015JD023301.Received.

Rowley, D. M., W. J. Bloss, R. A. Cox, and R. L. Jones (2001), Kinetics and Products of the IO + BrO Reaction, *J. Phys. Chem. A*, *105*(33), 7855–7864, doi:10.1021/jp004494y.

Saiz-Lopez, A., and C. S. Blaszczak-Boxe (2016), The polar iodine paradox, *Atmos. Environ.*, *145*, 72–73, doi:10.1016/j.atmosenv.2016.09.019.

Saiz-Lopez, A., and J. M. C. Plane (2004), Novel iodine chemistry in the marine boundary layer, *Geophys. Res. Lett.*, *31*(4), L04112, doi:10.1029/2003GL019215.

Saiz-Lopez, A., R. W. Saunders, D. M. Joseph, S. H. Ashworth, and J. M. C. Plane (2004), Absolute absorption cross-section and photolysis rate of I_2, *Atmos. Chem. Phys.*, *4*, 1443–1450.

Saiz-Lopez, A., J. M. C. Plane, G. McFiggans, P. I. Williams, S. M. Ball, M. Bitter, R. L. Jones, C. Hongwei, and T. Hoffmann (2006), Modelling molecular iodine emissions in a coastal marine environment: the link to new particle formation, *Atmos. Chem. Phys.*, *6*, 883–895.

Saiz-Lopez, A., A. S. Mahajan, R. A. Salmon, S. J. Bauguitte, A. E. Jones, H. K. Roscoe, and J. M. C. Plane (2007a), Boundary Layer Halogens in Coastal Antarctica, *Science (80-.).*, *317*, 348–351.

Saiz-Lopez, A., K. Chance, X. Liu, T. P. Kurosu, and S. P. Sander (2007b), First observations of iodine oxide from space, *Geophys. Res. Lett.*, *34*(12), L12812, doi:10.1029/2007GL030111.

Saiz-Lopez, A., J. M. C. Plane, A. S. Mahajan, P. S. Anderson, S. J.-B. Baugiutte, A. E. Jones, H. K. Roscoe, R. A. Salmon, W. J. Bloss, J. D. Lee, and D. E. Heard (2008), On the vertical distribution of boundary layer halogens over coastal Antarctica : implications for O_3, HO_x, NO_x and the Hg lifetime, *Atmos. Chem. Phys.*, (8), 887–900.

Saiz-Lopez, A., J. M. C. Plane, A. R. Baker, L. J. Carpenter, R. von Glasow, J. C. Gómez Martín, G. McFiggans, and R. W. Saunders (2012), Atmospheric chemistry of iodine, *Chem. Rev.*, *112*, 1773–1804.

Saiz-Lopez, A., R. P. Fernandez, C. Ordóñez, D. E. Kinnison, J. C. G. Martín, J. F. Lamarque, and S. Tilmes (2014), Iodine chemistry in the troposphere and its effect on ozone, *Atmos. Chem. Phys.*, *14*(23), 13119–13143, doi:10.5194/acp-14-13119-2014.

Saiz-Lopez, A., C. S. Blaszczak-Boxe, and L. J. Carpenter (2015), A mechanism for biologically-induced iodine emissions from sea-ice, *Atmos. Chem. Phys.*, *15*(7), 10257–10297, doi:10.5194/acpd-15-10257-2015.

Sander, R. (2015), Compilation of Henry's law constants (version 4.0) for water as solvent, *Atmos. Chem. Phys.*, *15*(8), 4399–4981, doi:10.5194/acp-15-4399-2015.

Sander, R., and P. J. Crutzen (1996), Model study indicating halogen activation and ozone destruction in polluted air masses transported to the sea, *J. Geophys. Res. - Atmos.*, *101*(D4), 9121–9138.

Sander, S. P., A. R. Ravishankara, D. M. Golden, C. E. Kolb, M. J. Kurylo, M. J. Molina, G. K. Moortgat, B. J. Finlayson-Pitts, P. H. Wine, R. E. Huie, and V. L. Orkin (2006), Chemical Kinetics and Photochemical Data for Use in Atmospheric Studies, Evaluation Number 15, *NASA, JPL*.

Saunders, R. W., and J. M. C. Plane (2005), Formation Pathways and Composition of Iodine Oxide Ultra-Fine Particles, *Environ. Chem.*, *2*(4), 299, doi:10.1071/EN05079.

Scheffler, D., H. Grothe, H. Willner, A. Frenzel, and C. Zetzsch (1997), Properties of Pure Nitryl Bromide . Thermal Behavior , UV / Vis and FTIR Spectra , and Photoisomerization to trans -BrONO in an Argon Matrix, *Inorg. Chem.*, *36*, 335–338.

Schneider, W., G. K. Moortgat, G. S. Tyndall, and J. P. Burrows (1987), Absorption Cross-Sections of NO_2 in the UV and Visible Region (200-700nm) at 298K, *J. Photochem. Photobiol. A Chem.*, *40*, 195–217.

Schnell, R. C. (1984), Arctic Haze and the Arctic Gas and Aerosol Sampling Program (AGASP), *Geophys. Res. Lett.*, *11*(5), 361–364.

Schonhardt, A., A. Richter, F. Wittrock, H. Kirk, H. Oetjen, H. K. Roscoe, and J. P. Burrows (2008), Observations of iodine monoxide columns from satellite, *Atmos. Chem. Phys.*, *8*, 637–653.

Schroeder, W. H., K. G. Anlauf, L. A. Barrie, J. Y. Lu, A. Steffen, D. R. Schneeberger, and T. Berg (1998), Arctic springtime depletion of mercury, *Nature*, *394*, 16–17.

Seery, D. J., and D. Britton (1964), The Continuous Absorption Spectra of Chlorine, Bromine, Bromine Chloride, Iodine Chloride, and Iodine Bromide, *J. Phys. Chem.*, *68*(8), 2263–2268.

Simon, H., A. Re, B. Wells, J. Xing, and N. Frank (2015), Ozone Trends Across the United States over a Period of Decreasing NO_x and VOC Emissions, *Environ. Sci. Technol.*, *49*, 186–195, doi:10.1021/es504514z.

Simpson, W. R., L. Alvarez-aviles, T. A. Douglas, M. Sturm, and F. Domine (2005), Halogens in the coastal snow pack near Barrow , Alaska : Evidence for active bromine air-snow chemistry during springtime, *Geophys. Res. Lett.*, *32*, 2–5, doi:10.1029/2004GL021748.

Simpson, W. R., S. S. Brown, A. Saiz-Lopez, J. A. Thornton, and R. Von Glasow (2015), Tropospheric Halogen Chemistry: Sources, Cycling, and Impacts, *Chem. Rev.*, 4035–62, doi:10.1021/cr5006638.

Simpson, W. R., P. K. Peterson, U. Frieß, H. Sihler, J. Lampel, U. Platt, C. Moore, K. A. Pratt, P. B. Shepson, J. W. Halfacre, and S. V. Nghiem (2017), Horizontal and vertical structure of reactive bromine events probed by bromine monoxide MAX-DOAS, *Atmos. Chem. Phys.*, 9291–9309.

Singer, R. J., J. N. Crowley, J. P. Burrows, W. Schneider, and G. K. Moortgat (1989), Measurement of the Absorption Cross-Section of Peroxynitric Acid between 210 and 330 nm in the Range 253-298 K, *J. Photochem. Photobiol. A Chem.*, *48*, 17–32.

Sipilä, M., N. Sarnela, T. Jokinen, H. Henschel, H. Junninen, J. Kontkanen, S. Richters, J. Kangasluoma, A. Franchin, O. Peräkylä, M. P. Rissanen, M. Ehn. H. Vehkamäki, T. Kurten, T. Berndt, T. Petäjä, D. Worsnop, D. Ceburnis, V.-M. Kerminen, M. Kulmala, and C. D. O'Dowd (2016), Molecular-scale evidence of aerosol particle formation via sequential addition of HIO_3: Supplementary information, *Nature*, *537*(7621), 532–534, doi:10.1038/nature.

Sjostedt, S. J., and J. P. D. Abbatt (2008), Release of gas-phase halogens from sodium halide substrates: heterogeneous oxidation of frozen solutions and desiccated salts by hydroxyl radicals, *Environ. Res. Lett.*, *3*(4), 45007, doi:10.1088/1748-9326/3/4/045007.

Skov, H., J. H. Christensen, M. E. Goodsite, N. Z. Heidam, B. Jensen, P. Wåhlin, and G. Geernaert (2004), Fate of Elemental Mercury in the Arctic during Atmospheric Mercury Depletion Episodes and the Load of Atmospheric Mercury to the Arctic, *Environ. Sci. Technol.*, *38*(8), 2373–2382, doi:10.1021/es030080h.

Solomon, S., D. J. Ivy, D. Kinnison, M. J. Mills, R. R. N. Iii, and A. Schmidt (2016), Emergence of healing in the Antarctic ozone layer, *Science (80-.).*, *61*(June), 1–13.

Sommariva, R., W. J. Bloss, and R. von Glasow (2012), Uncertainties in gas-phase atmospheric iodine chemistry, *Atmos. Environ.*, *57*, 219–232, doi:10.1016/j.atmosenv.2012.04.032.

Spicer, C. W., R. A. Plastridge, K. L. Foster, B. J. Finlayson-Pitts, J. W. Bottenheim, A. M. Grannas, and P. B. Shepson (2002), Molecular halogens before and during ozone depletion events in the Arctic at polar sunrise : concentrations and sources, *Atmos. Environ.*, *36*, 2721–2731.

Steffen, A., T. Douglas, M. Amyot, P. Ariya, K. Aspmo, T. Berg, J. Bottenheim, S. Brooks, and F. Cobbett (2008), A synthesis of atmospheric mercury depletion event chemistry in the atmosphere and snow, *Atmos. Chem. Phys.*, *8*, 1445–1482.

Steffen, A., I. Lehnherr, A. Cole, P. Ariya, A. Dastoor, D. Durnford, J. Kirk, and M. Pilote (2015), Atmospheric mercury in the Canadian Arctic. Part I: A review of recent field measurements, *Sci. Total Environ.*, *509–510*, 3–15, doi:10.1016/j.scitotenv.2014.10.109.

Stephens, C. R., P. B. Shepson, A. Steffen, J. W. Bottenheim, J. Liao, L. G. Huey, E. Apel, A. Weinheimer, S. R. Hall, C. Cantrell, B. C. Sive, D. J. Knapp, D. D. Montzka, and R. S. Hornbrook (2012), The relative importance of chlorine and bromine radicals in the oxidation of atmospheric mercury at Barrow , Alaska, *J. Geophys. Res.*, *117*, 1–16, doi:10.1029/2011JD016649.

Stull, R. B. (1988), *An Introduction to Boundary Layer Meteorology*, edited by A. Berger et al., Kluwer Academic Publishers, Norwell, MA.

Sturges, W. T., and L. A. Barrie (1988), CHLORINE , BROMINE, AND IODINE IN ARCTIC AEROSOLS, *Atmos. Environ.*, *22*(6), 1179–1194, doi:10.1016/0004-6981(88)90349-6.

Sumner, A. L., and P. B. Shepson (1999), Snowpack production of formaldehyde and its effect on the Arctic troposphere, *Nature*, *398*, 230–233.

Swanson, W., K. A. Graham, C. Holmes, J. W. Halfacre, and W. R. Simpson (n.d.), Seasonal and Regional Differences in Reactive Bromine Abundance near the North Pole, the Beaufort Gyre, and at Utqiaġvik (Barrow), Alaska, *2017 fall Meet. Am. Geophys. Union*.

Tackett, P. J., A. E. Cavender, A. D. Keil, P. B. Shepson, J. W. Bottenheim, S. Morin, J. Deary, A. Steffen, and C. Doerge (2007), A study of the vertical scale of halogen chemistry in the Arctic troposphere during Polar Sunrise at Barrow, Alaska, *J. Geophys. Res. Atmos.*, *112*(7), 1–13, doi:10.1029/2006JD007785.

Talukdar, R. K., J. B. Burkholder, A.-M. Schmoltner, J. M. Roberts, R. R. Wilson, and A. R. Ravishankara (1995), Investigation of the Loss Processes for Peroxyacetyl Nitrate in the Atmosphere: UV Photolysis and Reaction with OH, *J. Geophys. Res.*, *100*, 14163–14173.

Thomas, J. L., J. Stutz, B. Lefer, L. G. Huey, K. Toyota, J. E. Dibb, and R. von Glasow (2011), Modeling chemistry in and above snow at Summit, Greenland – Part 1: Model description and results, *Atmos. Chem. Phys.*, *11*(10), 4899–4914, doi:10.5194/acp-11-4899-2011.

Thomas, J. L., J. E. Dibb, L. G. Huey, J. Liao, D. J. Tanner, B. Lefer, R. von Glasow, and J. Stutz (2012), Modeling chemistry in and above snow at Summit, Greenland – Part 2: Impact of snowpack chemistry on the oxidation capacity of the boundary layer, *Atmos. Chem. Phys.*, *12*(14), 6537–6554, doi:10.5194/acp-12-6537-2012.

Thompson, A. M. (1992), The Oxidizing Capacity of the Earth's Atmosphere: Probable Past and Future Changes, *Science (80-.).*, *256*(5060), 1157–1165.

Thompson, C. R., P. B. Shepson, J. Liao, L. G. Huey, E. C. Apel, C. A. Cantrell, F. Flocke, J. Orlando, A. Fried, S. R. Hall, R. S. Hornbrook, D. J. Knapp, R. L. Mauldin III, D. D. Montzka, B. C. Sive, K. Ullmann, P. Weibring, and A. Weinheimer (2015), Interactions of bromine, chlorine, and iodine photochemistry during ozone depletions in Barrow, Alaska, *Atmos. Chem. Phys.*, *15*(16), 9651–9679, doi:10.5194/acp-15-9651-2015.

Thompson, C. R., P. B. Shepson, J. Liao, L. G. Huey, C. A. Cantrell, and F. Flocke (2017), Bromine atom production and chain propagation during springtime Arctic ozone depletion events in Barrow , Alaska, *Atmos. Chem. Phys.*, 3401–3421, doi:10.5194/acp-17-3401-2017.

Toyota, K., J. C. McConnell, R. M. Staebler, and A. P. Dastoor (2014), Air–snowpack exchange of bromine, ozone and mercury in the springtime Arctic simulated by the 1-D model PHANTAS – Part 1: In-snow bromine activation and its impact on ozone, *Atmos. Chem. Phys.*, *14*(8), 4101–4133, doi:10.5194/acp-14-4101-2014.

Troy, R. C., M. D. Kelley, J. C. Nagy, and D. W. Margerum (1991), Non-Metal Redox Kinetics: Iodine Monobromide Reaction with Iodide Ion and the Hydrolysis of IBr, *Inorg. Chem.*, *30*(25), 4838–4845.

Tsalkani, N., A. Mellouki, G. Poulet, G. Toupance, and G. Le Bras (1988), Rate constant measurement for the reactions of OH and Cl with peroxyacetyl nitrate at 298 K, *J. Atmos. Chem.*, *7*(4), 409–419, doi:10.1007/BF00058713.

Tuckermann, M., R. Ackermann, C. Golz, H. Lorenzen-Schmidt, T. Seene, J. Stutz, B. Trost, W. Unold, and U. Platt (2017), DOAS-observation of halogen radical-catalysed arctic boundary layer ozone destruction during the ARCTOC-campaigns 1995 and 1996 in Ny-Alesund, Spitsbergen, *Tellus, Ser. B Chem. Phys. Meteorol.*, *889*, doi:10.3402/tellusb.v49i5.16005.

Tyndall, G. S., J. J. Orlando, T. J. Wallington, M. Dill, and E. W. Kaiser (1997), Kinetics and Mechanisms of the Reactions of Chlorine Atoms with Ethane , Propane , and n -Butane, *Int. J. Chem. Kinet.*, *29*, 43–55.

Vaghjiani, G. L., and A. R. Ravishankara (1989), Absorption Cross Sections of CH_3OOH, H_2O_2 and D_2O_2 Vapors between 210 and 365 nm at 297 K, *J. Geophys. Res.*, *94*, 3487–3492.

Vakhtin, A. B., J. E. Murphy, and S. R. Leone (2003), Low-Temperature Kinetics of Reactions of OH Radical with Ethene, Propene, and 1-Butene, *J. Phys. Chem. A*, *107*(47), 10055–10062, doi:10.1021/jp030230a.

Wahner, A., G. S. Tyndall, and A. R. Ravishankara (1987), Absorption Cross Sections for OClO as a Function of Temperature in the Wavelength Range 240-480 nm, *J. Phys. Chem.*, *91*, 2734–2738.

Waite, T. J., V. W. Truesdale, and J. Olafsson (2006), The distribution of dissolved inorganic iodine in the seas around Iceland, *Mar. Chem.*, *101*, 54–67, doi:10.1016/j.marchem.2006.01.003.

Wallington, T. J., L. M. Skewes, W. O. Seigl, C.-H. Wu, and S. M. Japar (1988), Gas Phase Reaction of Cl Atoms with a Series of Oxygenated Organic Species at 295K, *Int. J. Chem. Kinet.*, *20*, 867–875.

Wang, S., and K. A. Pratt (2017), Molecular Halogens Above the Arctic Snowpack: Emissions, Diurnal Variations, and Recycling Mechanisms, *J. Geophys. Res. Atmos.*, *122*(21), 11,991-12,007, doi:10.1002/2017JD027175.

Wennberg, P. O. (1999), Bromine explosion, *Nature*, *397*(6717), 299–301, doi:10.1038/16805.

Wine, P. H., J. R. Wells, and J. M. Nicovich (1988), Kinetics of the reactions of atomic fluorine(2P) and atomic chlorine(2P) with nitric acid, *J. Phys. Chem.*, *92*(8), 2223–2228, doi:10.1021/j100319a028.

Wofsy, A. S. C., M. L. Goulden, J. W. Munger, S. Fan, P. S. Bakwin, B. C. Daube, S. L. Bassow, and F. A. Bazzaz (1993), Net Exchange of CO_2 in a Mid-Latitude Forest, *Science (80-.).*, *260*(5112), 1314–1317.

Worthy, D. E. J., N. B. A. Trivctt, J. F. Hopper, J. W. Bottcnhcim, and I. Levin (1994), Analysis of long-range transport events at Alert , Northwest Territories , during the Polar Sunrise Experiment transport episodes European Measurements of the radon daughter, *J. Geophys. Res.*, *99*, 25,329-25344.

Wrede, E., S. Laubach, S. Schulenburg, A. Brown, E. R. Wouters, A. J. Orr-Ewing, and M. N. R. Ashfold (2001), Continuum state spectroscopy: A high resolution ion imaging study of IBr photolysis in the wavelength range 440–685 nm, *J. Chem. Phys.*, *114*(6), 2629, doi:10.1063/1.1337049.

Wren, S. N., D. J. Donaldson, and J. P. D. Abbatt (2013), Photochemical chlorine and bromine activation from artificial saline snow, *Atmos. Chem. Phys.*, *13*(19), 9789–9800, doi:10.5194/acp-13-9789-2013.

Xu, W., M. Tenuta, and F. Wang (2016), Bromide and chloride distribution across the snow-sea-

ice-ocean interface: A comparative study between an Arctic coastal marine site and an experimental sea ice mesocosm, *J. Geophys. Res. Ocean.*, *121*(8), 1063–1084, doi:10.1002/2015JC010796.Received.

Yang, X., J. A. Pyle, and R. A. Cox (2008), Sea salt aerosol production and bromine release: Role of snow on sea ice, *Geophys. Res. Lett.*, *35*(16), 1–5, doi:10.1029/2008GL034536.

Yang, X., J. A. Pyle, R. A. Cox, N. Theys, and M. Van Roozendael (2010), Snow-sourced bromine and its implications for polar tropospheric ozone, *Atmos. Chem. Phys.*, *10*(16), 7763–7773, doi:10.5194/acp-10-7763-2010.

Yang, Y., Q. Chang, C. Dan, W. Guo, and Y. Wang (2016), Selective Identification of Organic Iodine Compounds Using Liquid Chromatography − High Resolution Mass Spectrometry, *Anal. Chem.*, *88*, 1275–1280, doi:10.1021/acs.analchem.5b03694.

Yokelson, R. J., J. B. Burkholder, R. W. Fox, and A. R. Ravishankara (1997), Photodissociation of $ClONO_2$: 2. Time-Resolved Absorption Studies of Product Quantum Yields, *J. Phys. Chem. A*, *101*, 6667–6678.

Zhao, Z., D. T. Huskey, J. M. Nicovich, and P. H. Wine (2008), Kinetics Study of the Gas-Phase Reactions of atomic chlorine with acetone, 2-butanone, and 3-Pentanone, *Int. J. Chem. Kinet.*, doi:10.1002/kin.

Zielcke, J. (2015), Observations of reactive bromine, iodine and chlorine species in the Arctic and Antarctic with Differential Optical Absorption Spectroscopy, Ruperto-Carola University of Heidelberg.

Zona, D., B. Gioli, R. Commane, J. Lindaas, S. C. Wofsy, and C. E. Miller (2016), Cold season emissions dominate the Arctic tundra methane budget, *Proc. Natl. Acad. Sci. U. S. A.*, *113*(1), 40–45, doi:10.1073/pnas.1516017113.

PUBLICATION

Active molecular iodine photochemistry in the Arctic

Angela R. W. Raso[a,b], Kyle D. Custard[a], Nathaniel W. May[b], David Tanner[c], Matt K. Newburn[d], Lawrence Walker[d], Ronald J. Moore[d], L. G. Huey[c], Liz Alexander[d], Paul B. Shepson[a,e,f], and Kerri A. Pratt[b,g,1]

[a]Department of Chemistry, Purdue University, West Lafayette, IN 47907; [b]Department of Chemistry, University of Michigan, Ann Arbor, MI 48109; [c]School of Earth and Atmospheric Sciences, Georgia Institute of Technology, Atlanta, GA 30332; [d]Environmental Molecular Sciences Laboratory, Pacific Northwest National Laboratory, Richland, WA 99352; [e]Department of Earth, Atmospheric, and Planetary Sciences, Purdue University, West Lafayette, IN 47907; [f]Purdue Climate Change Research Center, Purdue University, West Lafayette, IN 47907; and [g]Department of Earth & Environmental Sciences, University of Michigan, Ann Arbor, MI 48109

Edited by Mark H. Thiemens, University of California, San Diego, La Jolla, CA, and approved August 15, 2017 (received for review February 17, 2017)

During springtime, the Arctic atmospheric boundary layer undergoes frequent rapid depletions in ozone and gaseous elemental mercury due to reactions with halogen atoms, influencing atmospheric composition and pollutant fate. Although bromine chemistry has been shown to initiate ozone depletion events, and it has long been hypothesized that iodine chemistry may contribute, no previous measurements of molecular iodine (I_2) have been reported in the Arctic. Iodine chemistry also contributes to atmospheric new particle formation and therefore cloud properties and radiative forcing. Here we present Arctic atmospheric I_2 and snowpack iodide (I^-) measurements, which were conducted near Utqiaġvik, AK, in February 2014. Using chemical ionization mass spectrometry, I_2 was observed in the atmosphere at mole ratios of 0.3–1.0 ppt, and in the snowpack interstitial air at mole ratios up to 22 ppt under natural sunlit conditions and up to 35 ppt when the snowpack surface was artificially irradiated, suggesting a photochemical production mechanism. Further, snow meltwater I^- measurements showed enrichments of up to ∼1,900 times above the seawater ratio of I^-/Na^+, consistent with iodine activation and recycling. Modeling shows that observed I_2 levels are able to significantly increase ozone depletion rates, while also producing iodine monoxide (IO) at levels recently observed in the Arctic. These results emphasize the significance of iodine chemistry and the role of snowpack photochemistry in Arctic atmospheric composition, and imply that I_2 is likely a dominant source of iodine atoms in the Arctic.

atmosphere | iodine | cryosphere | snowpack | photochemistry

Atmospheric boundary layer ozone depletion events (ODEs), during which ozone (O_3) in the lower troposphere rapidly drops from background levels of 30–40 ppb to below 10 ppb, have been observed during springtime in the polar regions for several decades (1, 2). Early measurements of filterable halogens (bromine, chlorine, and iodine) (3) showed a particularly strong correlation between filterable bromine and O_3 concentrations, suggesting the catalytic destruction of O_3 by bromine atoms (4). Subsequent observations of inorganic bromine (Br_2, BrO, HOBr) in the polar regions (5–10) have elucidated the "bromine explosion" chemical mechanism (11, 12). Still, modeling studies suggest that this system is far from fully understood, and bromine chemistry alone cannot explain the full extent of ODEs that occur (13–16). The presence of iodine compounds, even at small mole ratios (moles of analyte/mole of air), may significantly increase the rate of O_3 destruction during ODEs (13, 17, 18), due to the relatively large rate constant for the reaction of BrO with IO [$k = 9.4 \times 10^{-11}$ $cm^3 \cdot molecule^{-1} \cdot s^{-1}$ (19)] compared with the BrO self-reaction [$k = 9.3 \times 10^{-13}$ $cm^3 \cdot molecule^{-1} \cdot s^{-1}$ (20)] (R31, 33; Fig. 1). Recently, inorganic chlorine (Cl_2, ClO) (21, 22) and iodine (IO, HIO_3) (23, 24) have been observed in the Arctic, adding support to signs of the importance of iodine chemistry from early aerosol measurements (3). Although molecular iodine (I_2) has not previously been observed in the Arctic, it has been observed at several midlatitude marine and coastal sites (25) and along the Antarctic coast (26), and IO has been observed in the Antarctic (16, 27, 28), and in the sub-Arctic (29). During recent measurements at Alert, Canada, IO was observed at levels up to 1.5 ppt (23). Iodine has recently been observed to contribute to atmospheric new particle formation (30) through the sequential addition of iodic acid (HIO_3) at maximum Arctic mole ratios of ∼1 ppt (24), giving further evidence to the presence and importance of Arctic iodine chemistry.

Although there is a clear indication of iodine chemistry in the Arctic, the source of the inorganic iodine has not been clear. In most midlatitude observations of I_2 and IO, the source of inorganic iodine is believed to be macroalgae under oxidative stress, such as during low tide (31–33). In the Antarctic, observations have previously been ascribed to I_2 production by sea ice diatoms, which are commonly found on the underside of both Arctic and Antarctic sea ice, followed by I_2 diffusion through open brine channels to the sea ice surface (25, 34, 35). However, although the diffusion of I_2 through brine channels has been modeled (34), it has not been directly observed. Whether iodine precursors in the Arctic are emitted from the open ocean (23, 29) or from sea ice-covered regions (24) has remained unclear. There are potential mechanistic pathways for both sources. Br_2, Cl_2, and BrCl production via photochemical reactions has been demonstrated in the Arctic saline snowpack (7, 9, 36) and from frozen substrates in laboratory experiments (37–44). I_2 and triiodide (I_3^-) have recently been shown to be photochemically produced in Antarctic snow spiked with iodide (1–1,000 μM) (45), and iodate (IO_3^-) has also been shown to be photochemically active in frozen solutions (46). These studies show condensed phase iodine photochemistry, and although previous samples have lacked the physical and chemical characteristics of authentic snow, they suggest that photochemical production of I_2, similar to that of Br_2, Cl_2, and BrCl production in the Arctic surface snowpack (7, 36), is probable. However, neither atmospheric I_2 nor the production of I_2 from snow samples with natural iodide (I^-) levels has ever been reported.

Significance

We report here the first measurements of molecular iodine (I_2) in the Arctic atmosphere and iodide (I^-) in the Arctic snowpack. Although iodine chemistry is expected to have significant impacts on Arctic atmospheric ozone destruction and new particle production, sparse measurements of atmospheric iodine have limited our ability to examine sources and impacts. We show, through sunlit and artificially irradiated snowpack experiments, that the coastal Arctic snowpack is capable of photochemical production and release of I_2 to the boundary layer. This is supported by enrichment of the snowpack in I^- compared with that expected from sea spray influence alone. Through photochemical modeling, we demonstrate that, at observed I_2 levels, snowpack production can have a significant impact on Arctic atmospheric chemistry.

Author contributions: A.R.W.R., K.D.C., P.B.S., and K.A.P. designed research; A.R.W.R., K.D.C., N.W.M., M.K.N., L.W., R.J.M., L.A., and K.A.P. performed measurements; D.T. and L.G.H. contributed new analytic tools; A.R.W.R., N.W.M., and K.A.P. analyzed data; and A.R.W.R. and K.A.P. wrote the paper.

The authors declare no conflict of interest.

This article is a PNAS Direct Submission.

[1]To whom correspondence should be addressed. Email: prattka@umich.edu.

This article contains supporting information online at www.pnas.org/lookup/suppl/doi:10.1073/pnas.1702803114/-/DCSupplemental.

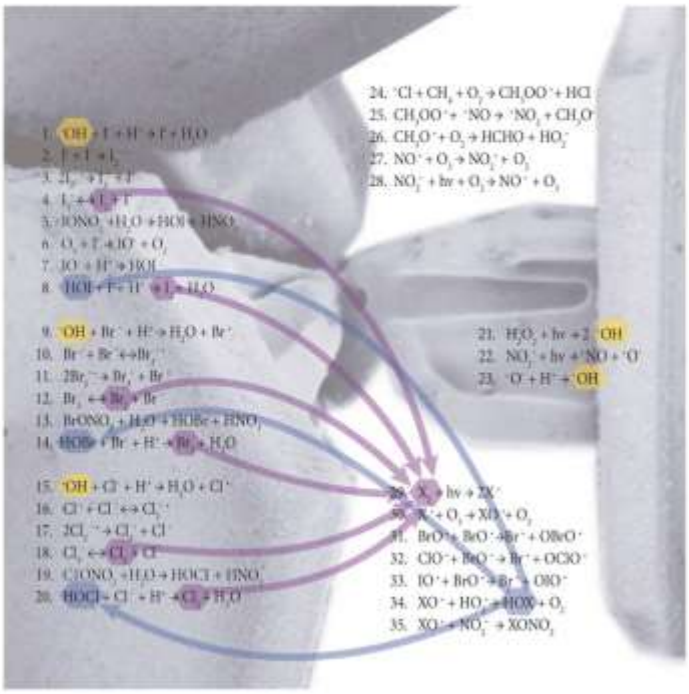

Fig. 1. Snowpack halogen production and interstitial air halogen reactions. Major halogen reactions proposed to occur in the interstitial snowpack air and within the snow surface are shown. Oxidation of I^- in the dark (R6–R8) is based on Carpenter et al. (47). Photochemical oxidation of Br^- (R9–R12) is based on Abbatt et al. (38). Cl^- and I^- photochemical oxidation reactions (R15–R18 and R1–R4, respectively) are suggested to be analogous. Snow crystal SEM image is an open source image from the Electron and Confocal Microscopy Laboratory, Agricultural Research Service, US Department of Agriculture.

Given the expected importance of iodine chemistry in the atmosphere (24, 25), snowpack iodine chemistry was investigated near Utqiaġvik, AK, in February 2014. Here, we report Arctic I_2 measurements, in both the tropospheric boundary layer and snowpack interstitial air, coupled with measurements of I^- in Arctic snow. The effect of radiation on halogen mole ratios in the snowpack interstitial air was examined through sunlit experiments, artificial irradiation experiments, and snowpack vertical profiles. In addition, the sensitivity of ozone depletion rates and IO mole ratios to tropospheric I_2 was examined using a zero-dimensional photochemical model.

Results and Discussion

Snowpack Molecular Iodine Production. Here we report observations of I_2 and snowpack I^- in the Arctic. Gas-phase I_2 was observed in the snowpack interstitial air at 10 cm below the sunlit snowpack surface on February 1 and 2, 2014, near Utqiaġvik, AK (Fig. 2). I_2 mole ratios in the snowpack interstitial air peaked at 2.7–5.1 ppt in the early afternoon, just following the solar radiation maxima (Fig. 2). Coincident with these daytime maxima, I_2 was observed in the boundary layer, 1 m above the snowpack surface, at mole ratios of ~0.3–1.0 ppt (Fig. 2). Significantly more I_2 was observed in the snowpack interstitial air on February 2 (maximum I_2 5.1 ppt), which was sunny and clear (maximum radiation 172 W/m^2), compared with February 1 (maximum I_2 2.7 ppt), which was overcast (maximum radiation 18 W/m^2), further supporting a photochemical production mechanism. Laboratory studies have shown that I_2 can be produced from aqueous samples containing I^- in the presence of O_3 without light, via reactions 6–8 (Fig. 1) (47). During the night of February 1–2, average wind speeds rose from 2.0 m·s^{-1} to 5.9 m·s^{-1}, leading to increased wind pumping, resulting in increasing O_3 from 5 to 25 ppb in the snowpack interstitial air over the course of ~30 min [22:00–22:30 Alaska Standard Time (AKST)] (Fig. 2). This presents an opportunity to examine the influence of O_3 on dark oxidation and subsequent I_2 formation. However, although an apparent small increase in I_2 signal at a snowpack depth of 10 cm was observed during this time (Fig. 2), the I_2 levels were never statistically significant different from zero. Therefore, these observations suggest that snowpack photochemical reactions were the predominant source of the observed I_2 in the Arctic boundary layer.

The photochemical nature of I_2 production in the snowpack is further demonstrated by the differences in the vertical profiles of I_2 and molecular bromine (Br_2) within the snowpack interstitial air (Fig. 3). Gas-phase I_2 and Br_2 were simultaneously quantified at mole ratios up to 22 and 43 ppt, respectively, under sunlit conditions in the snowpack interstitial air, as shown in Fig. 3. Br_2 showed peak mole ratios (43 ppt) just below the snowpack/atmosphere interface (within the top ~10 cm) (Fig. 3 and Fig. S1). This is consistent with previous measurements, which showed a maximum in Br_2 mole ratios within the top 7 cm of the snowpack air at Alert, Canada (9). In contrast, the I_2 peak mole ratio (22 ppt) was observed at ~40 cm below the snowpack surface, at least 30 cm deeper than the Br_2 maximum (Fig. 3). At this snow depth, ambient light was attenuated (at 40 cm, ~2% of 400 nm light remains) (48). The difference in behavior between I_2 and Br_2 with depth reflects two factors. First, I_2 photolyzes nearly four times faster than Br_2 (I_2 $J_{max} = 2.9 \times 10^{-3}$ s^{-1} vs. Br_2 $J_{max} = 8.6 \times 10^{-4}$ s^{-1} for above the snowpack on February 2, 2014). Second, whereas bromide (Br^-) shows no consistent enrichment (relative to the seawater Br^-/Na^+ ratio) with depth (Fig. S2), I^- was increasingly enriched with depth in January and February 2014 snow meltwater (Fig. 3). I^- was observed at concentrations of 1.4–4.3 nM (Fig. S2) that are greatly enriched relative to sodium (Na^+), at up to ~1,900 times the seawater ratio (I^-/Na^+) (Fig. 3). The I^- concentrations in the surface snowpack (top 7 cm) meltwater (2.0 ± 0.6 nM; Fig. S2) were sufficient to produce ~1,600 ppt of I_2, if I^- were completely converted to I_2 and contained in the snowpack interstitial air (*SI Methods*). In comparison, snow meltwater Br^- ranged from partially depleted to double that in

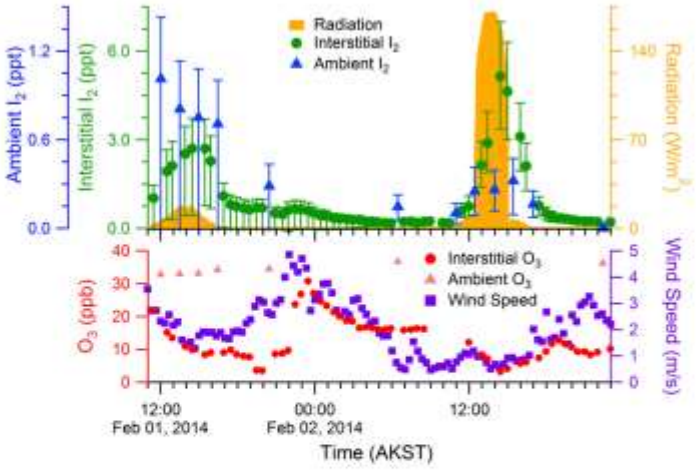

Fig. 2. I_2, O_3, radiation, and wind speeds during February 1–2, 2014. The diurnal profiles for I_2 and O_3 mole ratios, as well as the radiation and wind speeds, are shown as 20-min averages from February 1 to 2, 2014. Error bars are propagated uncertainties (*SI Methods*). Ambient measurements were conducted 1 m above the snowpack surface. Interstitial air measurements were conducted 10 cm below the snowpack surface. Fluctuations in interstitial air O_3 mole ratios correlate with high wind speeds and are therefore likely due to wind pumping.

seawater (0.58–2.0 times the seawater Br^-/Na^+ ratio; Fig. S2). Previous measurements of Br^-/Na^+ ratios in coastal surface snow have shown bromide enrichments, relative to seawater, to increase from late winter (1.5–5 times the seawater Br^-/Na^+ ratio) through early spring (20–72 times the Br^-/Na^+ ratio in seawater), which is consistent with active heterogeneous recycling of bromine on the snowpack (49, 50). The much greater snowpack enrichment factor for I^- suggests production and transport of iodine compounds from upwind snowpack; ocean or saline sea ice environments; or aerosols, and subsequent deposition on the downwind coastal snowpack. The exact source of I^- to the snowpack remains undetermined, but the increasing enrichment of I^- with depth indicates that iodine near the surface has migrated, either redepositing deeper in snowpack and/or being lost from the snowpack surface to the atmosphere, perhaps following polar sunrise. Although the source of I^- enrichment in the Arctic snowpack requires further investigation, deposition of gas or particle phase iodine is consistent with earlier findings of enriched iodine in the aerosol phase (3). Future measurements of the spatial and temporal heterogeneity of snowpack I^- enrichment are needed to elucidate the migration of iodine in the Arctic system.

To further investigate photochemical I_2 production, the snowpack was exposed to artificial UV light (Fig. 4). This experiment was conducted during the night and morning when solar radiation was low (<20 W/m^2). When exposed to artificial light, the snowpack rapidly produced up to 35 ppt of gas-phase I_2 at a depth of 10 cm (Fig. 4). The radiation spectrum of the lights used (Fig. S3) is adequate for the photolytic production of hydroxyl radicals from hydrogen peroxide and nitrite (Fig. 1, R21–R23), but not for significant I_2 photolysis, which occurs most efficiently at wavelengths greater than 400 nm (20, 51). Upon snow illumination, Br_2 was also quickly produced in the snowpack interstitial air, yielding mole ratios of 40–80 ppt (Fig. 4). With halogen production in the snowpack, O_3 decayed rapidly, via the chemistry shown in Fig. 1. When the lights were turned off, both Br_2 and I_2 mole ratios decayed, and O_3 partially recovered. This molecular halogen decline was likely controlled by dilution with ambient air (wind pumping), a lack of photochemical halogen production, and adsorption/desorption of halogen species onto the snow. Although snow grain chemical composition and exchange processes are complex (52), the rate of desorption from aqueous surfaces is often described as inversely proportional to the Henry's Law constant for that species (53). Because I_2 is more soluble (k_H = 41.9 M/atm at −20 °C) than Br_2 (k_H = 8.4 M/atm at −20 °C) (54), its rate of desorption from the disordered snow interface is expected to be slower, as shown in Fig. 4 by the slower decay in I_2 mole ratios after illumination ceases, and from the slower initial rise in I_2 mole ratios upon illumination. I_2 and Br_2 were again observed upon snowpack reillumination (Fig. 4). This demonstrates that I_2 and Br_2 are both characterized by condensed-phase photochemical production mechanisms.

The I_2 multiphase photochemical production mechanism proposed here (Fig. 1) is analogous to that for Br_2 production, which occurs first by condensed-phase photochemistry and then is greatly enhanced by gas-phase recycling of Br atoms in the presence of O_3 (7, 37). The suggested mechanism for I_2 production begins in the disordered interface of the aqueous phase on the snow grain surface (52) with oxidation of I^- to an iodide radical by a photochemically produced oxidant (R1), likely the hydroxyl radical, produced by nitrite photolysis in Utqiaġvik snow (R22–R23)

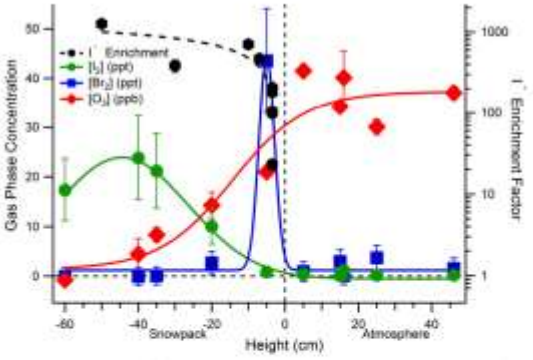

Fig. 3. Vertical profiles of near-surface atmospheric and snowpack interstitial air I_2, Br_2, and O_3 mole ratios, as well as snow I^- enrichment. Gas-phase measurements were made during daylight from 12:22 to 16:23 AKST on February 4, 2014, at heights above (positive) and below (negative) the snowpack surface. Error bars for species measured with CIMS (I_2 and Br_2) are propagated uncertainties (*SI Methods*). Error bars on the O_3 measurements are the SDs of 9- to 22-min averages at each height. I^- enrichment factors (the ratio of I^- to Na^+ in snow meltwater relative to the same ratio in seawater) are shown for snow samples collected from January 27 to February 5, 2014. I^- enrichment factor error bars are the propagated error from three measurements of the I^- concentration in a single sample. See Fig. S1 for an additional set of vertical profile measurements from February 3, 2014.

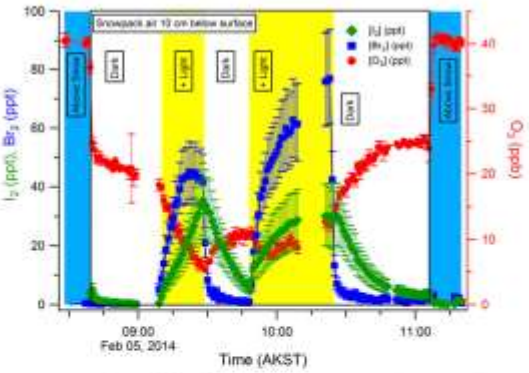

Fig. 4. Snowpack artificial irradiation experiment. Snowpack interstitial air Br_2, I_2, and O_3 mole ratios are shown as 1-min averages for dark and artificial light measurement periods during an experiment on February 5, 2014. Error bars for I_2 and Br_2 are propagated uncertainties (*SI Methods*). The interstitial air measurements were bracketed by near-surface (5 cm above the snowpack surface) measurements of boundary-layer air. The duration of the experiment occurred before the sun rose, allowing for near-complete darkness when the artificial lights were off.

(55). The iodide radical then further reacts in solution to form I_3^- (R2–R3), which has been recently observed in snow samples spiked with I^- (45). I_3^- then decomposes, forming I_2 (R4). I_2 can then be released from the condensed phase to the gas phase, where it rapidly photolyzes in the presence of sunlight. The resulting iodine atoms react with O_3 to form IO (R30). IO can then react with HO_2 to form HOI (R34) or NO_2 to form $IONO_2$ (R35), which can each then be redeposited onto the snow grain surface to reproduce I_2 in a catalytic cycle similar to the bromine explosion (56). Interhalogen reactions may also participate in the production of molecular halogens. HOBr has also been shown to oxidize Cl^- on frozen surfaces to form BrCl when the Br^-/Cl^- ratio is low (37, 39, 40). Similarly, HOI and $IONO_2$ can react on frozen surfaces with Br^- and Cl^- to form IBr and ICl (57). The production of IBr via the reaction of HOI and Br^- is up to ~200 times faster ($k = 3.3 \times 10^{12}\ M^{-2}{\cdot}s^{-1}$) (58) than the production of Br_2 via the reaction of HOBr and Br^- ($k = 1.6 \times 10^{10}\ M^{-2}{\cdot}s^{-1}$) (59). Although the interactions between halogen species in the gas phase have received some study, the condensed-phase interactions of halogens have been significantly understudied (56).

Simulations of Arctic Ozone Destruction. Because even small levels of I_2 can significantly impact Arctic atmospheric chemistry, a zero-dimensional photochemical model was used to simulate O_3 depletion and IO production. Because an ODE was not observed during the January to February 2014 study [ODEs typically begin in March in Utqiaġvik (2)], previous observations of atmospheric Br_2, Cl_2, and HOBr from the same location on March 11, 2012 were used to constrain the model (Fig. S4). On this day, atmospheric O_3 decreased from ~20 ppb to <1 ppb over the course of 7 h (Fig. 5*A*), with winds blowing from north to northeast over the consolidated snow-covered ice on the Beaufort Sea. The overall observed ozone depletion rate (3.0 ppb·h^{-1} over the 7-h period) is typical of a large number of ODEs observed over the snow-covered sea ice on the Arctic Ocean (average of 3.5 ppb·h^{-1}) (60). The initial depletion (from 14:00–16:10 AKST) occurred at a rate of 2.2 ppb·h^{-1} and was interrupted by a local atmospheric mixing event (16:10–18:00 AKST), which is not possible to simulate with a zero-dimensional model.

Given that I_2 was only measured in early February in this study, it is plausible that higher mole ratios are present in March, when ODEs regularly occur. Therefore, the model was used to test the sensitivity of O_3 depletion rates to I_2 mole ratios from 0–2.4 ppt (Fig. 5*A*). Without the inclusion of iodine chemistry, O_3 was simulated to deplete initially (14:00–16:10 AKST) at a rate of 1.3 ppb·h^{-1} (Fig. 5*A*), mostly from bromine atom chemistry. However, as shown in Fig. 5*A*, the addition of 0.3 ppt of I_2 (as observed on February 2, 2014) increases the initial rate of ozone depletion by 31%, to 1.7 ppb·h^{-1}. The best fit to the observed initial ozone depletion rate (2.2 ppb·h^{-1}) corresponds to the inclusion of 0.6 ppt of I_2 (within the range of our observations), which causes the model to simulate the initial depletion at a rate of at 2.1 ppb·h^{-1}. The significant increase in the simulated ozone depletion rate with the inclusion of only 0.6 ppt I_2 demonstrates the importance of even a small amount of iodine on the depletion of boundary layer O_3. Higher, but still very modest and plausible, I_2 mole ratios (compared with the ~18 ppt of Br_2 present) have a pronounced effect on the predicted O_3. The addition of 2.4 ppt of I_2 triples the rate of O_3 depletion for the initial period (14:00–16:10 AKST) to 4.0 ppb·h^{-1}.

The sensitivity of simulated IO concentrations to varying amounts of I_2 on March 11, 2012 was also examined (Fig. 5*B*). The simulation containing 2.4 ppt of I_2 produced a maximum of 1.6 ppt of IO, which is near the highest mole ratios observed (1.5 ppt) in Alert, Canada (23). The simulation with 0.3 ppt of I_2 (February 2, 2014, maximum mole ratio) revealed IO mole ratios similar to those most commonly observed at Alert (~0.3 ppt) (23). It should be noted, however, that there are significant uncertainties associated with modeling gas-phase iodine chemistry. Variations in the branching ratio for the products of the reaction of IO with itself can significantly change predicted IO mole ratios. The branching ratios used here (38% I + OIO, 16% I + I, 46% IOOI) may cause overestimation of IO by up to ~10% (61). Additionally, because the photolysis of higher-order iodine oxides (I_2O_3 and larger) could cause the simulated O_3 ratios shown here to be overestimated by up to 18% (17), sub-parts per trillion levels of I_2 may result in even greater ozone depletion rates than predicted here. Even with these uncertainties in simulating iodine chemistry, our snowpack and ambient I_2 observations along

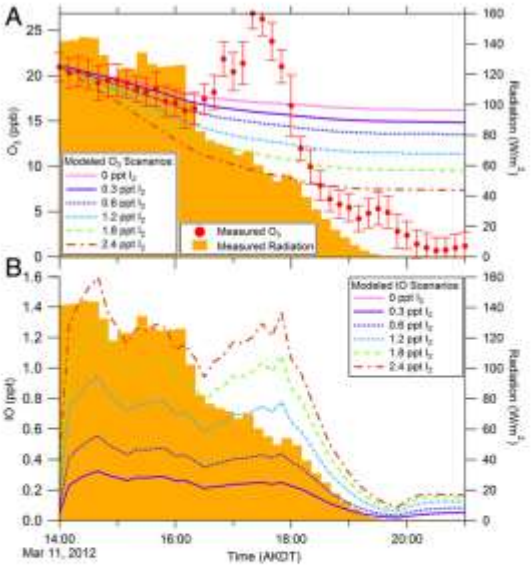

Fig. 5. Model results show the influence of I_2 on (*A*) tropospheric ozone depletion rates and (*B*) IO mole ratios. An ozone depletion event occurring on March 11, 2012 was simulated with I_2 mole ratios between 0 and 2.4 ppt. Cl_2, Br_2, and HOBr were constrained to measurements as shown in Fig. S4. (*A*) Measured O_3 with SDs of the 10-min average, and model results showing simulated O_3 mole ratios. (*B*) Simulated IO mole ratios during the same period.

with our model results demonstrate that even a small amount of I_2, at the observed levels, can significantly increase O_3 depletion rates, while also producing realistic IO mole ratios.

Conclusions

Here we report measurements of I_2 in the Arctic. Low mole ratios (0.3–1.0 ppt) of I_2 in the boundary layer air coupled with elevated I_2 mole ratios in the snowpack interstitial air suggest that the snowpack is a source of I_2 to the Arctic boundary layer. These results are supported by Arctic snowpack measurements of I$^-$, which was greatly enriched relative to seawater, and more so with increasing depth. I_2 is observed in the snowpack interstitial air under naturally sunlit conditions, and under artificial irradiation, but not in the dark, suggesting a photochemical production mechanism. The inclusion of observed molar ratios of I_2 in a zero-dimensional model increases the ability of the model to simulate the initial rate of an observed ozone depletion event, and produces IO concentrations consistent with recent observations. Differences in the snowpack depth profiles of bromine and iodine species within both the snow phase (Br$^-$ and I$^-$) and snowpack interstitial air (Br_2 and I_2) suggest that there are significant differences in bromine and iodine multiphase chemistry. The assumption that these species act similarly may be an oversimplification—one that can only be remedied through further measurements of production examining important chemical mechanisms and fundamental reaction rates and yields under both laboratory and field conditions.

The community's challenge to properly simulate the chemical and physical processes that occur within and on the surface of snow grains (62) is especially daunting, because we do not currently understand the physical nature of the phase in which the chemistry is occurring (52, 62). New methodology is required to examine the chemical composition of ambient snow grain surfaces in situ. Although we lack comprehensive knowledge about the heterogeneous chemical processes of halogens on snow, we benefit greatly from real-world observations, such as those described herein. Multiphase interhalogen chemistry may also be important; however, there are no reported ambient measurements of the iodine molecular interhalogens (IBr and ICl). It is also unclear how the likely increasingly saline surface snowpack (from increasing first-year sea ice, sea spray production, and potentially decreasing snow depth), combined with increasing Arctic development (which may be changing acid deposition), are influencing springtime halogen chemistry. Iodine chemistry may have an especially large impact on atmospheric composition as the Arctic warms, given the prevalence of iodine chemistry in the marine midlatitudes (25).

Even at sub-parts per trillion levels of I_2 in the Arctic atmosphere, iodine chemistry has significant impacts on atmospheric boundary layer oxidation capacity and composition, impacting pollutant fate and particle formation. Further simultaneous measurements of aerosol I$^-$, snowpack I$^-$, and I_2 are needed to examine the movement of iodine between the aerosol, gas, and the snowpack phases. We now know that the coastal Arctic snowpack is a source of photochemically reactive inorganic iodine. This provides an abiotic source of iodine for new particle formation, expanding the potential importance of this chemical process to impacts on clouds (24, 25, 63). Given the dramatic impact of iodine on Arctic atmospheric composition, there is a need for further measurements of I_2 in the ambient atmosphere to connect and elucidate the full cycling of iodine in the Arctic system.

Methods

Trace halogen gases were measured using chemical ionization mass spectrometry (CIMS), as described by Liao et al. (5, 64), Peterson et al. (8), and Custard et al. (22), on the Barrow Environmental Observatory (BEO), 5 km inland over tundra snowpack near Utqiaġvik, AK, on March 11, 2012, and February 1–5, 2014. A detailed description of the sampling, calibrations, background measurements, line loss tests, and uncertainties are described in *SI Methods*. Briefly, in 2012, CIMS, using H_3O^+ as the reagent ion, measured Br_2, Cl_2, and HOBr at ∼1 m above the snowpack surface [Peterson et al. (8), Custard et al. (22); *SI Methods*]. For 2014 measurements, the CIMS instrument was modified by the addition of an 18-cm-long PTFE-coated flow tube to the original 4.5-cm flow tube. CIMS measurements in 2014 were made using SF_6^- as the reagent ion; masses 254 amu ($^{127}I_2^-$), 160 amu ($^{81}Br^{79}Br^-$), and 158 amu ($^{79}Br_2^-$) were monitored. Calibrations were performed using I_2 and Br_2 permeation devices (VICI) every 30 min to 2 h. Background measurements were performed every 20 min to 1 h, for 7–20 min, by passing the airflow through a glass wool scrubber, which quantitatively destroyed (>99%) the molecular halogens. For the I_2 measurements, an apparent interference caused higher backgrounds when measuring in the snowpack interstitial air; therefore, only background measurements made above the snowpack were used. This uncertainty in the background is accounted for in the mole ratio uncertainties shown. In 2014, SDs of background signals resulted in 3σ limits of detection (LODs) for Br_2 ranging from 1.5 to 3.9 ppt and for I_2 ranging from 0.2 to 0.5 ppt. The method uncertainty in the I_2 and Br_2 mole ratios was (−33%/+35% + LOD) and (−19%/+21% + LOD), respectively. The 2014 and 2016 CIMS molecular halogen data are available through the NSF Arctic Data Center.

Interstitial snowpack air and depth profile sampling was conducted using a 380-cm-long, 1.3-cm ID FEP-Teflon line heated to 25 °C, which was attached directly to the CIMS sampling inlet. Estimated line losses, based on laboratory and field testing of the lines with permeation devices, were accounted for in the method uncertainties (*SI Methods*). To prevent heterogeneous recycling (65), the line was rinsed with Milli-Q water and dried with N_2 before each experiment. A custom machined PTFE snow probe (Fig. S5) was used to prevent snow from entering the sampling line. A custom-built 61 × 61 cm Acrylite OP-4 cover (80% transmittance at 300 nm and ∼92% at 395 nm) with a 7.6-cm aluminum lip was pressed into the snow surface to prevent ambient air from being pulled directly into the snowpack and mixing with the interstitial air being sampled below (Fig. S6). Although dilution of the snowpack interstitial air by ambient air will occur to some extent, the O_3 mole ratios measured during in-snowpack experiments were consistently much lower than those observed in the air above the snowpack and agreed with previous snowpack O_3 observations (66, 67), suggesting that the mixing of ambient air into the snowpack was minimal. Any mixing of air within the snowpack due to high sampling rates would be expected to lessen the gradients shown in Fig. 3 and Fig. S1. O_3 was measured using a 2B Technologies model 205 dual-beam O_3 monitor. Artificial light was supplied by six Q-Lab UVA-340 halogen light bulbs (68) housed in a custom-built heated and insulated fixture. The light exited the fixture through a sheet of Acrylite OP-4, which insulated the light bulbs from the cold environment. The lamp housing was suspended ∼10 cm above the snow cover (Fig. S6).

Snow samples were collected ∼50 m upwind (north to northeast) of the CIMS sampling site on the BEO using a polypropylene scoop, which was rinsed with ACS-grade methanol and air dried before sampling. Samples were stored frozen (−10 °C to −40 °C) in polyethylene bags until the day of analysis. An Agilent Technologies 1200 series ion chromatograph (IC) was paired with a Thermo Scientific Element XR inductively coupled plasma mass spectrometer (ICP-MS) for quantitation of I$^-$ in snowmelt samples. The 3σ limits of detection for iodide (I$^-$) were 1.2–5.2 pM. Na^+, Cl^-, and Br^- were determined using Dionex ICS-1100 and ICS-2100 chromatography systems, respectively, with conductivity detectors. Additional IC and IC-ICP-MS analysis details can be found in *SI Methods*. I$^-$ enrichment factors relative to seawater were calculated using the ratio of I$^-$ to Na^+ in seawater off the coast of Iceland ($I^-/Na^+ = 6.2 \times 10^{-8}$) (69). Br^- enrichment factors were calculated based on seawater off the coast of Utqiaġvik ($Br^-/Na^+ = 2.0 \times 10^{-3}$) (49).

Boundary layer modeling was constrained using Br_2, HOBr, O_3, and radiation data from a 7-h period on March 11, 2012, during the Bromine Ozone and Mercury Experiment (BROMEX) (Fig. S4) (7, 8, 22, 70). The zero-dimensional model is a series of explicit gas-phase reactions (Tables S1 and S2) and ref. 13. Initial gas-phase mole ratios (for species not constrained to observations) and photolysis rate constants are shown in Tables S1 and S3. Photolysis rate constants were obtained using the National Center for Atmospheric Research Tropospheric and UV (TUV) Radiation Model (https://www2.acom.ucar.edu/modeling/tropospheric-ultraviolet-and-visible-tuv-radiation-model) and scaled to radiation measurements from the NOAA Global Monitoring Division Earth Systems Research Laboratory (https://esrl.noaa.gov/gmd).

ACKNOWLEDGMENTS. We thank the staff of the Jonathan Amy Facility for Chemical Instrumentation at Purdue University for building the snow cover and light fixture. Solar radiation data were acquired by and obtained from the National Oceanic & Atmospheric Administration, Earth System Research Laboratory, Global Monitoring Division Solar Radiation group. Photolysis rates were obtained using the TUV model from the National Center for Atmospheric Research, Atmospheric Chemistry Division, Chemical Processes and Regional Modeling group. We also thank Ukpeagvik Iñupiat Corporation Science and CH2MHILL Polar Services for field logistical support and T. Miller (Birck Nanotechnology Center) for nano-pure water for chromatography. P. Burroff-Murr (Purdue University) consulted on the graphic design of Fig. 1. Financial support was provided by NSF Division of Polar Programs ARC-1107695,

PLR-1417906, and PLR-1417668. For the 2012 measurements, K.A.P. was supported by NSF Postdoctoral Fellowship in Polar Regions Research ARC-1103423. IC-ICPMS analyses were performed at the Environmental Molecular Sciences Laboratory, a national scientific user facility located at the Pacific Northwest National Laboratory (PNNL) and sponsored by the Office of Biological and Environmental Research of the US Department of Energy (DOE). PNNL is operated for the DOE by Battelle Memorial Institute under Contract DE-AC06-76RL0 1830.

1. Barrie LA, Bottenheim JW, Schnell RC, Crutzen PJ, Rasmussen RA (1988) Ozone destruction and photochemical reactions at polar sunrise in the lower Arctic atmosphere. *Nature* 334:138–141.
2. Oltmans SJ (1981) Surface ozone measurements in clean air. *J Geophys Res* 86:1174–1180.
3. Sturges WT, Barrie LA (1988) Chlorine, bromine, and iodine in Arctic aerosols. *Atmos Environ* 22:1179–1194.
4. Barrie LA, den Hartog G, Bottenheim JW, Landsberger S (1989) Anthropogenic aerosols and gases in the lower troposphere at Alert Canada in April 1986. *J Atmos Chem* 9:101–127.
5. Liao J, et al. (2012) Observations of inorganic bromine (HOBr, BrO, and Br2) speciation at Barrow, Alaska, in spring 2009. *J Geophys Res* 117:D00R16.
6. Hausmann M, Platt U (1994) Spectroscopic measurement of bromine oxide and ozone in the high Arctic during Polar Sunrise Experiment 1992. *J Geophys Res* 99:25399–25413.
7. Pratt KA, et al. (2013) Photochemical production of molecular bromine in Arctic surface snowpacks. *Nat Geosci* 6:351–356.
8. Peterson PK, et al. (2015) Dependence of the vertical distribution of bromine monoxide in the lower troposphere on meteorological factors such as wind speed and stability. *Atmos Chem Phys* 15:2119–2137.
9. Foster KL, et al. (2001) The role of Br2 and BrCl in surface ozone destruction at polar sunrise. *Science* 291:471–474.
10. Hönninger G, Platt U (2002) Observations of BrO and its vertical distribution during surface ozone depletion at Alert. *Atmos Environ* 36:2481–2489.
11. Simpson WR, et al. (2007) Halogens and their role in polar boundary-layer ozone depletion. *Atmos Chem Phys* 7:4375–4418.
12. Wennberg PO (1999) Bromine explosion. *Nature* 397:299–301.
13. Thompson CR, et al. (2015) Interactions of bromine, chlorine, and iodine photochemistry during ozone depletions in Barrow, Alaska. *Atmos Chem Phys* 15:9651–9679.
14. Toyota K, McConnell JC, Staebler RM, Dastoor AP (2014) Air-snowpack exchange of bromine, ozone and mercury in the springtime Arctic simulated by the 1-D model PHANTAS – Part 1: In-snow bromine activation and its impact on ozone. *Atmos Chem Phys* 14:4101–4133.
15. Thomas JL, et al. (2011) Modeling chemistry in and above snow at Summit, Greenland – Part 1: Model description and results. *Atmos Chem Phys* 11:4899–4914.
16. Saiz-Lopez A, et al. (2007) Boundary layer halogens in coastal Antarctica. *Science* 317:348–351.
17. Saiz-Lopez A, et al. (2014) Iodine chemistry in the troposphere and its effect on ozone. *Atmos Chem Phys* 14:13119–13143.
18. Calvert JG, Lindberg SE (2004) Potential influence of iodine-containing compounds on the chemistry of the troposphere in the polar spring. I. Ozone depletion. *Atmos Environ* 38:5087–5104.
19. Rowley DM, Bloss WJ, Cox RA, Jones RL (2001) Kinetics and products of the IO + BrO reaction. *J Phys Chem A* 105:7855–7864.
20. Sander SP, et al. (2006) Chemical kinetics and photochemical data for use in atmospheric studies (Jet Propulsion Lab, NASA, Pasadena, CA), Evaluation no. 15.
21. Liao J, et al. (2014) High levels of molecular chlorine in the Arctic atmosphere. *Nat Geosci* 7:91–94.
22. Custard KD, Pratt KA, Wang S, Shepson PB (2016) Constraints on Arctic atmospheric chlorine production through measurements and simulations of Cl 2 and ClO. *Environ Sci Technol* 50:acs.est.6b03909.
23. Zielcke J (2015) Observations of reactive bromine, iodine and chlorine species in the Arctic and Antarctic with differential optical absorption spectroscopy. PhD dissertation (Ruperto-Carola University, Heidelberg), 10.11 7/CBO9781107415324.004.
24. Sipilä M, et al. (2016) Molecular-scale evidence of aerosol particle formation via sequential addition of HIO3. *Nature* 537:532–534.
25. Saiz-Lopez A, et al. (2012) Atmospheric chemistry of iodine. *Chem Rev* 112:1773–1804.
26. Atkinson HM, et al. (2012) Iodine emissions from the sea ice of the Weddell Sea. *Atmos Chem Phys* 12:11229–11244.
27. Saiz-Lopez A, Chance K, Liu X, Kurosu TP, Sander SP (2007) First observations of iodine oxide from space. *Geophys Res Lett* 34:L12812.
28. Frieß U, Deutschmann T, Gilfedder BS, Weller R, Platt U (2010) Iodine monoxide in the Antarctic snowpack. *Atmos Chem Phys* 10:2439–2456.
29. Mahajan AS, et al. (2010) Evidence of reactive iodine chemistry in the Arctic boundary layer. *J Geophys Res* 115:D20303.
30. Allan JD, et al. (2014) Iodine observed in new particle formation events in the Arctic atmosphere during ACCACIA. *Atmos Chem Phys* 14:28949–28972.
31. Saiz-Lopez A, Plane JMC (2004) Novel iodine chemistry in the marine boundary layer. *Geophys Res Lett* 31:L04112.
32. Mcfiggans G, et al. (2004) Direct evidence for coastal iodine particles from Laminaria macroalgae – linkage to emissions of molecular iodine. *Atmos Chem Phys Atmos Chem Phys* 4:701–713.
33. Saiz-Lopez A, et al. (2006) Modelling molecular iodine emissions in a coastal marine environment: The link to new particle formation. *Atmos Chem Phys* 6:883–895.
34. Saiz-Lopez A, Blaszczak-Boxe CS, Carpenter LJ (2015) A mechanism for biologically-induced iodine emissions from sea-ice. *Atmos Chem Phys* 15:10257–10297.
35. Saiz-Lopez A, Blaszczak-Boxe CS (2016) The polar iodine paradox. *Atmos Environ* 145:72–73.
36. Custard KD, Raso ARW, Shepson PB, Staebler RM, Pratt KA (2017) Production and release of molecular bromine and chlorine from the Arctic coastal snowpack. *ACS Earth Sp Chem* 1:10.1021/acsearthspacechem.7b00014.
37. Wren SN, Donaldson DJ, Abbatt JPD (2013) Photochemical chlorine and bromine activation from artificial saline snow. *Atmos Chem Phys* 13:9789–9800.
38. Abbatt J, et al. (2010) Release of gas-phase halogens by photolytic generation of OH in frozen halide-nitrate solutions: An active halogen formation mechanism? *J Phys Chem A* 114:6527–6533.
39. Adams JW, Holmes NS, Crowley JN (2002) Uptake and reaction of HOBr on frozen and dry NaCl/NaBr surfaces between 253 and 233 K. *Atmos Chem Phys* 2:79–91.
40. Huff AK, Abbatt JPD (2002) Kinetics and product yields in the heterogeneous reactions of HOBr with ice surfaces containing NaBr and NaCl. *J Phys Chem A* 106:5279–5287.
41. Kirchner U, Benter T, Schindler RN (1997) Experimental verification of gas phase bromine enrichment in reaction of HOBr with sea salt doped ice surfaces. *Berichte der Bunsengesellschaft für Phys Chemie* 97:975–977.
42. Oldridge NW, Abbatt JPD (2011) Formation of gas-phase bromine from interaction of ozone with frozen and liquid NaCl/NaBr solutions: Quantitative separation of surficial chemistry from bulk-phase reaction. *J Phys Chem A* 115:2590–2598.
43. Oum KW, Lakin MJ, Finlayson-Pitts BJ (1998) Bromine activation in the troposphere by the dark reaction of O_3 with seawater ice. *Geophys Res Lett* 25:3923–3926.
44. Sjostedt SJ, Abbatt JPD (2008) Release of gas-phase halogens from sodium halide substrates: Heterogeneous oxidation of frozen solutions and desiccated salts by hydroxyl radicals. *Environ Res Lett*, 10.1088/1748-9326/3/4/045007.
45. Kim K, et al. (2016) Production of molecular iodine and triiodide in the frozen solution of iodide: Implication for polar atmosphere. *Environ Sci Technol* 50:1280–1287.
46. Gálvez O, Baeza-romero MT, Sanz M, Saiz-Lopez A (2016) Photolysis of frozen iodate salts as a source of active iodine in the polar environment. *Atmos Chem Phys* 16:12703–12713.
47. Carpenter LJ, et al. (2013) Atmospheric iodine levels influenced by sea surface emissions of inorganic iodine. *Nat Geosci* 6:108–111.
48. King MD, Simpson WR (2001) Extinction of UV radiation in Arctic snow at Alert, Canada. *J Geophys Res* 106:12499–12507.
49. Simpson WR, Alvarez-aviles L, Douglas TA, Sturm M, Domine F (2005) Halogens in the coastal snow pack near Barrow, Alaska: Evidence for active bromine air-snow chemistry during springtime. *Geophys Res Lett* 32:2–5.
50. Xu W, Tenuta M, Wang F (2013) Bromide and chloride distribution across the snow-sea-ice-ocean interface: A comparative study between an Arctic coastal marine site and an experimental sea ice mesocosm. *J Geophys Res Ocean* 121:1063–1084.
51. Saiz-Lopez A, Saunders RW, Joseph DM, Ashworth SH, Plane JMC (2004) Absolute absorption cross-section and photolysis rate of I2. *Atmos Chem Phys* 4:1443–1450.
52. Bartels-Rausch T, et al. (2014) A review of air-ice chemical and physical interactions (AIC): Liquids, quasi-liquids, and solids in snow. *Atmos Chem Phys* 14:1587–1633.
53. Jacob DJ (2000) Heterogeneous chemistry and tropospheric ozone. *Atmos Environ* 34:2131–2159.
54. Sander R (2015) Compilation of Henry's law constants (version 4.0) for water as solvent. *Atmos Chem Phys* 15:4399–4981.
55. France JL, et al. (2012) Hydroxyl radical and NOx production rates, black carbon concentrations and light-absorbing impurities in snow from field measurements of light penetration and nadir reflectivity on onshore and offshore coastal Alaskan snow. *J Geophys Res*, 10.1029/2011JD016639.
56. Simpson WR, Brown SS, Saiz-Lopez A, Thornton JA, Glasow Rv (2015) Tropospheric halogen chemistry: Sources, cycling, and impacts. *Chem Rev* 115:4035–4062.
57. Holmes NS, Adams JW, Crowley JN (2001) Uptake and reaction of HOI and IONO2 on frozen and dry NaCl/NaBr surfaces and H2SO4. *Phys Chem Chem Phys* 3:1679–1687.
58. Troy RC, Kelley MD, Nagy JC, Margerum DW (1991) Non-metal redox kinetics: Iodine monobromide reaction with iodide ion and the hydrolysis of IBr. *Inorg Chem* 30:4838–4845.
59. Beckwith RC, Wang TX, Margerum DW (1996) Equilibrium and kinetics of bromine hydrolysis. *Inorg Chem* 35:995–1000.
60. Halfacre JW, et al. (2014) Temporal and spatial characteristics of ozone depletion events from measurements in the Arctic. *Atmos Chem Phys* 14:4875–4894.
61. Sommariva R, Bloss WJ, von Glasow R (2012) Uncertainties in gas-phase atmospheric iodine chemistry. *Atmos Environ* 57:219–232.
62. Domine F, Bock J, Voisin D, Donaldson DJ (2013) Can we model snow photochemistry? Problems with the current approaches. *J Phys Chem A* 117:4733–4749.
63. Saiz-Lopez A, et al. (2012) Estimating the climate significance of halogen-driven ozone loss in the tropical marine troposphere. *Atmos Chem Phys* 12:3939–3949.
64. Liao J, et al. (2011) A comparison of Arctic BrO measurements by chemical ionization mass spectrometry and long path-differential optical absorption spectroscopy. *J Geophys Res* 116:D00R02.
65. Neuman JA, et al. (2010) Bromine measurements in ozone depleted air over the Arctic Ocean. *Atmos Chem Phys* 10:6503–6514.
66. Peterson MC, Honrath RE (2001) Observations of rapid photochemical destruction of ozone in snowpack interstitial air. *Geophys Res Lett* 28:511–514.
67. Van Dam B, et al. (2015) Dynamics of ozone and nitrogen oxides at Summit, Greenland: I. Multi-year observations in the snowpack. *Atmos Environ* 123:268–284.
68. Q-Lab Corporation (2011) Spectral power distribution for QUV with UVA-340 fluorescent lamps. Technical Bulletin LU-8052. Available at www.q-lab.com/products/lamps-optical-filters/lamps-and-optical-filters. Accessed December 3, 2014.
69. Waite TJ, Truesdale VW, Olafsson J (2006) The distribution of dissolved inorganic iodine in the seas around Iceland. *Mar Chem* 101:54–67.
70. Nghiem SV, et al. (2012) Studying bromine, ozone, and mercury chemistry in the Arctic. *Eos (Wash DC)* 94:2012–2013.